15386

NATIONAL LIBRARY
OTTAWA

CANADA

BIBLIOTHÈQUE NATIONALE
OTTAWA

NAME OF AUTHOR...EL-SAYED AHMED IBRAHIM YOUSSEF

TITLE OF THESIS...A UNIFORMLY TWISTED ELECTROSTATIC QUADRUPOLE FOR GUIDING AND IMAGING CHARGED PARTICLES

UNIVERSITY...U. of Alberta...

DEGREE FOR WHICH THESIS WAS PRESENTED...Ph.D...

YEAR THIS DEGREE GRANTED...SPRING, 1973...

Permission is hereby granted to THE NATIONAL LIBRARY OF CANADA to microfilm this thesis and to lend or sell copies of the film.

The author reserves other publication rights, and neither the thesis nor extensive extracts from it may be printed or otherwise reproduced without the author's written permission.

(Signed)...E-S Youssef...

PERMANENT ADDRESS:

#806, Vanier House
Michener Park
Edmonton 70, Alberta
Canada

DATED...Nov., 15th...19 72

NL-91 (10-68)

THE UNIVERSITY OF ALBERTA

A UNIFORMLY TWISTED ELECTROSTATIC QUADRUPOLE FOR GUIDING AND IMAGING CHARGED PARTICLES

by

Ⓒ EL-SAYED AHMED IBRAHIM YOUSSEF

A THESIS
SUBMITTED TO THE FACULTY OF GRADUATE STUDIES AND RESEARCH
IN PARTIAL FULFILMENT OF THE REQUIREMENTS FOR THE DEGREE OF
DOCTOR OF PHILOSPHY

DEPARTMENT OF ELECTRICAL ENGINEERING

EDMONTON, ALBERTA

SPRING,1973

UNIVERSITY OF ALBERTA

FACULTY OF GRADUATE STUDIES AND RESEARCH

The undersigned certify that they have read, and recommend to the Faculty of Graduate Studies and Research, a thesis entitled "A Uniformly Twisted Electrostatic Quadrupole For Guiding and Imaging Charged Particles" submitted by El-Sayed Ahmed Ibrahim Youssef in partial fulfilment of the requirements for the degree of Doctor of Philosophy.

....
Supervisor

F. E. Vermeulen
Supervisor

P. A. Goud

C. R. James

C. E. Capjack

G. A. Moss

G. D. Moore
External Examiner

Date ...10 Nov. 72...

ABSTRACT

A study is made of the guiding properties of a long electrostatic quadrupole that has been uniformly twisted about its axis. Analytic solutions have been developed for particle trajectories and they show that stable orbits exist if the structure parameters are properly chosen. A confinement criterion, which sets the acceptance limits of the twisted structure, has been derived using the analytic solutions. The accuracy of the analytic solutions and the validity of the confinement criterion are examined by comparing the analytically computed trajectories with those computed by numerical integration. The acceptance limits of the twisted quadrupole structure are compared to those of the classical electrostatic quadrupole channel. Twisted electrostatic quadrupole structures of finite lengths are found to be capable of identically reproducing the injection conditions of a system of particles. Such lenses have been fabricated and their imaging properties have been tested using a beam of contact charged microparticles. The experimental results are in good agreement with the theoretical analysis. A study has also been made of the effect of bending the axis of the twisted structure, and it was found that stable orbits can exist.

ACKNOWLEDGEMENTS

The author wishes to express his gratitude to Dr. F.S. Chute and Dr. F.E. Vermeulen, the supervisors of this project, for their invaluable encouragement and guidance throughout the course of this study.

The interest shown and many suggestions made by members of the faculty and the technical staff of the Department of Electrical Engineering at the University of Alberta, are gratefully acknowledged. Particular thanks are due to Mr. E. Buck.

The author also wishes to thank the Department of Electrical Engineering, University of Alexandria, Egypt, for permitting him the study leave to do this project. Thanks are also due to the National Research Council of Canada, the Izaak Walton Killam Memorial Fellowship Trust, and the Department of Electrical Engineering for the financial support during the course of this work.

The author owes a debt of gratitude to his wife, Mrs. Zeinab Youssef, for her encouragement and understanding during this work and also for checking the manuscript. Mrs. Maureen K. Mounteer is to be thanked for typing the manuscript.

TABLE OF CONTENTS

Page

1. INTRODUCTION 1

1.1 Background 1

1.2 Some Existing Electric Field Focusing Devices 5

1.2.1 Foils and Grids 6

1.2.2 Rectangular Drift Tubes, Rotated Grids and Finger Structures 7

1.2.3 Weak Electrostatic Focusing 10

1.2.4 Electrostatic Quadrupole Lenses 12

1.3 The Present Study 17

2. PARTICLE DYNAMICS IN THE UNIFORMLY TWISTED ELECTROSTATIC QUADRUPOLE STRUCTURE 22

2.1 Coordinate Systems and Potential Distribution 22

2.2 The Hamiltonian and the Equations of Motion 25

2.3 Solution of the Equations of Motion by Contact Transformation 30

2.4 Solution of the Equations of Motion by Matrix Techniques 39

3. GUIDING PROPERTIES 49

3.1 Stability 49

3.2 Particle Confinement 50

3.3 Special Cases of Injection 53
  3.3.1 Parallel Beam 53
  3.3.2 Point Source 57
  3.3.3 Injection on the X-Axis with X-Directed Momentum 60
  3.3.4 Injection on the Y-Axis with Y-Directed Momentum 62
  3.3.5 Point Source at a Distance d from Input Plane 64

4. AN EVALUATION OF THE ANALYTIC SOLUTION 68
4.1 Introduction 68
4.2 Comparison of the Analytic and the Runge-Kutta Trajectories 72
4.3 The Axial Velocity $\dot{Z}$ 94
4.4 Spatial Modes 99

5. EFFECT OF EARTH'S GRAVITY ON PARTICLE TRAJECTORIES 104
5.1 Particle Motion 104

6. COMPARISON OF THE PROPERTIES OF THE UNIFORMLY TWISTED ELECTROSTATIC QUADRUPOLE STRUCTURE AND THE CLASSICAL ELECTROSTATIC QUADRUPOLE CHANNEL 112
6.1 Introduction 112
6.2 Acceptance Limits 115
  6.2.1 The Classical Structure 115
  6.2.2 The Twisted Structure 120

6.3 Acceptance Comparison 126

6.4 The Focusing Strength 138

7. THE ELECTROSTATIC TWISTED QUADRUPOLE AS A NOVEL IMAGING LENS 143

7.1 Introduction 143

7.2 Particle Imaging 144

7.3 Results 152

7.4 Effect of Detuning s About Its Imaging Value 164

8. EXPERIMENTAL INVESTIGATIONS OF THE IMAGING PROPERTIES OF THE TWISTED ELECTROSTATIC LENS 180

8.1 High Vacuum System 180

8.2 The Microparticle Charger 182

  8.2.1 Testing of the Charger 187

  8.2.2 Charge Detection 189

8.3 The Uniformly Twisted Quadrupole Structure 192

  8.3.1 The Electrode Shapes 192

  8.3.2 Structure Parameters 193

  8.3.3 Fabrication of the Twisted Structure 193

8.4 Experiments 198

  8.4.1 Experimental Results 207

    (a) Single Twisted Electrostatic Quadrupole Lens 207

    (b) Two Oppositely Twisted Equal Sections 214

9. THE CIRCULAR UNIFORMLY TWISTED ELECTROSTATIC QUADRUPOLE 219

9.1 Introduction 219

9.2 The Hamiltonian of the Motion 221

9.3 The Equations of Motion 225

10. CONCLUSION 230

REFERENCES 233

APPENDIX A POTENTIAL DISTRIBUTION IN THE UNIFORMLY TWISTED ELECTROSTATIC QUADRUPOLE 237

APPENDIX B THE AXIAL VELOCITY $\dot{Z}$ 242

APPENDIX C DERIVATION OF THE MATRIX FORM OF THE ANALYTIC SOLUTION 247

APPENDIX D COMPUTATION OF ACCEPTANCE FOR POINT SOURCE INJECTION. 252

APPENDIX E COMPUTER PROGRAM LISTINGS 255

APPENDIX F SPATIAL MODES OF THE MOTION ALONG THE TWISTED STRUCTURE 271

LIST OF ILLUSTRATIONS

Figure		Page
1.1	Accelerating Gaps and Drift Tubes of a Heavy Ion Linear Accelerator.	2
1.2	Field Distribution Across a Typical Accelerating Gap.	3
1.3	Field Distribution Across a Gap Between Drift Tubes with a Thin Foil on the Entrance of the Right Tube.	6
1.4a	Rectangular Drift Tubes.	7
1.4b	Electric Field Distribution Across the Gap Between Rectangular Drift Tubes in the X-Z and the Y-Z Transverse Planes.	8
1.5	Circular Drift Tubes with Two Parallel Wire Grids.	9
1.6	Drift Tubes with "Fingers".	10
1.7	A Unipotential Electrostatic Lens.	11
1.8	Symmetrical Hyperbolic Electrodes.	12
1.9	Symmetrical Quadrupole Triplet.	14
1.10	Classical Quadrupole Channel.	17
1.11	The Uniformly Twisted Electrostatic Quadrupole Structure.	19
2.1	Coordinate System for the Uniformly Twisted Quadrupole Structure.	23
3.1	Acceptance in the Normalized $\frac{X_0}{a} - \frac{Y_0}{a}$ Transverse Coordinate Plane for Parallel Beam Injection.	55
3.2	Acceptance in the Normalized $\frac{P_{X_0}}{P_{Z_0}} - \frac{P_{Y_0}}{P_{Z_0}}$ Transverse Momentum Plane for Point Source Injection.	58

3.3 Acceptance in the $\frac{X_o}{a} - \frac{P_{X_o}}{P_{Z_o}}$ Phase Plane for Injection on the X-Axis with X-Directed Transverse Momentum. 61

3.4 Acceptance in the $\frac{Y_o}{a} - \frac{P_{Y_o}}{P_{Z_o}}$ Phase Plane for Injection on the Y-Axis with Y-Directed Transverse Momentum. 63

3.5 Acceptance in the Normalized $\frac{P_{X_o}}{P_{Z_o}} - \frac{P_{Y_o}}{P_{Z_o}}$ Transverse Momenta Plane for Injection from a Point Source at a Distance d from the Injection Plane. 66

4.1 The X-Z, Y-Z and X-Y Projections of the Numerical (Runge-Kutta) and Analytical Trajectories, when (X_o = 0.1 cm, Y_o = 0.2 cm, $\frac{P_{X_o}}{P_{Z_o}} = 0.02$, $\frac{P_{Y_o}}{P_{Z_o}} = 0.02$). 73

4.2 As in Figure (4.1) when (X_o = 0.3 cm, Y_o = 0.2 cm, $\frac{P_{X_o}}{P_{Z_o}} = 0.01$ and $\frac{P_{Y_o}}{P_{Z_o}} = 0.01$). 74

4.3 As in Figure (4.1) for Parallel Injection when (X_o = 0.45 cm, Y_o = 0). 75

4.4 As in Figure (4.1) for Parallel Injection when (X_o = .337 cm, Y_o = .079 cm). 76

4.5 As in Figure (4.1) for Parallel Injection when (X_o = 0.225 cm, Y_o = 0.159 cm). 77

4.6 As in Figure (4.1) for Point Source Injection when ($\frac{P_{X_o}}{P_{Z_o}} = 0.016$, $\frac{P_{Y_o}}{P_{Z_o}} = 0.011$). 78

4.7 As in Figure (4.1) for Point Source Injection when ($\frac{P_{X_o}}{P_{Z_o}} = 0.007$, $\frac{P_{Y_o}}{P_{Z_o}} = 0.022$). 79

4.8 As in Figure (4.1) for Parallel Injection when (X_o = 0.675 cm, Y_o = 0.159 cm). 81

4.9 As in Figure (4.1) for Parallel Injection when (X_0 = 0 cm, Y_0 = 0.53 cm). 82

4.10 As in Figure (4.1) for Point Source Injection when ($\frac{P_{X_0}}{P_{Z_0}}$ = 0.017, $\frac{P_{Y_0}}{P_{Z_0}}$ = 0.051). 83

4.11 As in Figure (4.1) for Point Source Injection when ($\frac{P_{X_0}}{P_{Z_0}}$ = 0.047, $\frac{P_{Y_0}}{P_{Z_0}}$ = 0.012). 84

4.12 As in Figure (4.1) for Parallel Injection at the Limiting Acceptance Point (X_0 = a = 1.5 cm, Y_0 = 0). 86

4.13 As in Figure (4.1) for Parallel Injection at the Limiting Acceptance Point (X_0 = 1.125 cm, Y_0 = 0.265 cm). 87

4.14 As in Figure (4.1) for Parallel Injection at the Limiting Acceptance Point (X_0 = 0.187 cm, Y_0 = 0.928 cm). 88

4.15 As in Figure (4.1) for Point Source Injection at the Limiting Acceptance Point ($\frac{P_{X_0}}{P_{Z_0}}$ = 0.0599, $\frac{P_{Y_0}}{P_{Z_0}}$ = 0). 89

4.16 As in Figure (4.1) for Point Source Injection at the Limiting Acceptance Point ($\frac{P_{X_0}}{P_{Z_0}}$ = 0.052, $\frac{P_{Y_0}}{P_{Z_0}}$ = 0.038). 90

4.17 As in Figure (4.1) for Point Source Injection at the Limiting Acceptance Point ($\frac{P_{X_0}}{P_{Z_0}}$ = 0, $\frac{P_{Y_0}}{P_{Z_0}}$ = 0.079). 91

4.18 Plots of ($\dot{Z}_Z/U_{Z_0}$) versus Z. 95

4.19 Analytical Trajectory Projections for a Particle when (X_0 = 0.9 cm, Y_0 = 0.4 cm, P_{X_0} = 0, P_{Y_0} = 0). 97

5.1 The Mean Orbit of Particle Motion when the Effect of Gravitational Forces is Taken into Consideration. 109

6.1 A Schematic Diagram of the Twisted and Classical Structures to be compared. 113

6.2 The Acceptance Areas in the X-X' and Y-Y' Phase Planes. 127

6.3 The Acceptance Limits in the X-X' Phase Plane. 129

6.4 The Acceptance Limits in the Y-Y' Phase Plane. 130

6.5 Effect of Drift Space on the X-X' Acceptance Limits of Classical Structures. 131

6.6 Effect of Drift Space on the Y-Y' Acceptance Limits of Classical Structures. 132

6.7 Effect of Drift Space on the $\frac{X}{a} - \frac{Y}{a}$ Acceptance Limits of Classical Structures. 134

6.8 Effect of Drift Space on the X'-Y' Acceptance Limits of Classical Structures. 136

6.9 The Y-Z Projections of the Trajectory of a Particle Along the Twisted Structure and Along the Classical Structure with $\frac{d}{\ell} = 0$, when $(X_0 = 0, Y_0 = 0, X'_0 = 0, Y'_0 = 0.07)$. 140

6.10 The X-Z Projections of the Trajectory of a Particle Along the Twisted Structure and Along the Classical Structure with $\frac{d}{\ell} = 0$, when $(X_0 = \frac{a}{2} = 0.75$ cm, $Y_0 = 0, X'_0 = 0, Y'_0 = 0)$. 141

7.1a X and Y versus Z for Point Source Injection. 155

7.1b Injection and Exit Momenta for Point Source Injection. 156

7.2a X and Y versus Z for Parallel Beam Injection. 157

7.2b Injection and Exit Coordinates for Parallel Beam Injection. 158

7.3a Injection and Exit Coordinates for a Single Twisted Lens Section. 160

7.3b Injection and Exit Momenta Corresponding to the Coordinates of Figure (7.3a) for a Single Twisted Lens. 161

7.4a Injection and Exit Coordinates for Two Adjoining Lens Sections of Equal Length but Opposite Twist. 162

7.4b Injection and Exit Momenta Corresponding to the Coordinates of Figure (7.4a) for Two Adjoining Lens Sections of Equal Length but Opposite Twist. 163

7.5a Schematic of the Arrangement Used for Studying the Effect of Detuning s. 166

7.5b Lens Equivalent at Imaging Values of s. 166

7.6 Exit Coordinates of Particles at the Lens Exit Plane ($\ell_e = 0$). 174

7.7 The Coordinates of Particles at a Distance $\ell_e = 1$ cm, Beyond the Lens Exit Plane. 175

7.8 As in Figure (7.7) Except at a Distance $\ell_e = 2$ cm Beyond the Lens Exit Plane. 176

7.9 As in Figure (7.7) Except at a Distance $\ell_e = 3$ cm Beyond the Lens Exit Plane. 177

8.1 High Vacuum System. 181

8.2 The Microparticle Charger. 184

8.3 Exploded Front View of the Charging Mechanism. 186

8.4 Exploded Rear View of the Charging Mechanism. 186

8.5 Microparticle Charger and Tapping Mechanism. 188

8.6 Sketch of the Charge Detection Arrangement. 188

8.7 Photographs of Oscilloscope Trace of Typical Output from the Charge-Sensitive Amplifier. 191

8.8 The Mould that was used to Fabricate the Twisted Electrodes. 194

8.9a A Clockwise Twisted Electrode Before Painting. 196

8.9b Front and Side Views of the Clockwise, β - ve, Twisted Lens Before Painting. 196

8.9c The Uniformly, Clockwise, Twisted Lens After Painting. 197

8.10 Circuit Diagram of the Quadrupole Focusing Voltage Supply. 199

8.11 Sketch and Photograph of the Experimental Arrangement Used to Test the Imaging Properties of the Twisted Lens Structures. 200

8.12 The Injected Beam Shaping Aperture. 202

8.13a Sketch of the Experimental Arrangement Used to Test the Injected Beam Cross-Section. 202

8.13b Photograph of Injected Microparticle Beam Cross-Section at the Plane of the Shaping Aperture E. 203

8.13c Photograph of the Injected Beam Cross-Section at the Lens Injection Plane. 203

8.14 Beam Cross-Section at the Exit Plane of the CounterClockwise, β + ve, Twisted Lens at V_0 = 1210 Volts. 209

8.15 As in (8.14) for the Clockwise, β - ve, Twisted Lens. 209

8.16 Beam Cross-Sections at the Exit Plane of the CounterClockwise Twisted Lens for Different Values of V_0. 210

8.17 Beam Cross-Sections at the Exit Plane of the Clockwise Twisted Lens for Different Values of V_0. 210

8.18 Beam Cross-Sections at a Distance $d_3 = 7$ mm Beyond the Exit Plane of the Clockwise Twisted Lens for Different Values of V_0. 212

8.19 Exit Beam Cross-Sections at a Distance $d_3 = 17.5$ mm Beyond the Exit Plane of the Clockwise Twisted Lens for Different Values of V_0. 212

8.20 Exit Beam Cross-Sections at a Distance $d_3 = 33$ mm Beyond the Exit Plane of the Clockwise Twisted Lens for Different Values of V_0. 213

8.21 Photograph of the Lens Structure that Consists of Two Adjoining Sections of Equal Length but Opposite Twist. 215

8.22 Beam Cross-Sections at the Exit Plane of the Lens Structure shown in Figure (8.21) for Different Values of V_0. 215

9.1 Coordinate System for the Circular Uniformly Twisted Quadrupole Structure. 220

9.2 The Mean Orbit of Particles Along the Circular Twisted Structure. 228

A.1 Symmetry Properties of the Twisted Structure. 238

CHAPTER 1

1.1 Background

During the past few years an increased interest has developed in the acceleration of very heavy charged particles. Serious efforts are now being made to ionize and accelerate elements as heavy as argon(1-5). The interest in obtaining energetic heavy ions is largely directed towards the emerging field of nucleosynthesis. However, the interaction of such particles with atomic, molecular and biological systems promises to yield much vital information in such areas as the study of radiation damage in solids and the investigation of cellular disorders. Also recently, attention has been focused on charged micron-sized solid and liquid particles. When accelerated to high velocities the applications for such particles range from sprayed ink jets for extremely high speed printing(6) to mass expulsion systems for spacecraft propulsion(7). It has even been suggested(8) that micron-sized particles moving at velocities of the order of 10^4 kilometers/sec could trigger thermonuclear reactions in a controllable manner. A further use of these macroscopic particles, which is of particular interest at the University of Alberta, is for the simulation of micrometeoroids with velocities up to several tens of kilometers per second. Such artificial micrometeoroids can be used to study impact phenomena and the resulting hazards to men and equipment outside the earth's atmosphere. For example, high velocity aluminum particles, of approximately 4 micron diameter, have been used to investigate the abrasion of optical surfaces exposed to micrometeoroid bombardment(9).

Radio-frequency linear accelerators have been suggested as the most suitable machines for producing very energetic heavy particles(10). In such accelerators an r.f. source is used to establish an electric field across a linear array of accelerating gaps, as shown schematically in figure (1.1).

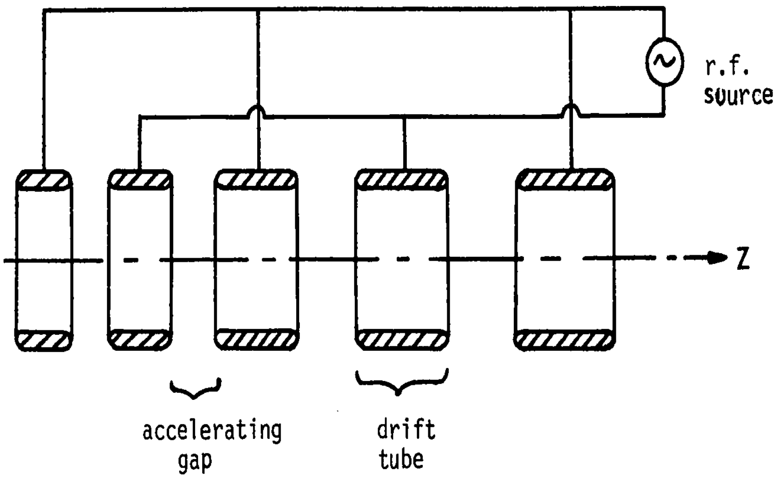

Figure (1.1) Accelerating Gaps and Drift Tubes of a Heavy Ion Linear Accelerator

As particles pass along the axis of the structure they experience an essentially field free region within each drift tube. However, the dimensions of the drift tubes and of the accelerating gaps are so adjusted that the particles reach each successive gap at a time when they will be accelerated by the electric field. The field across a typical accelerating gap is illustrated in figure (1.2).

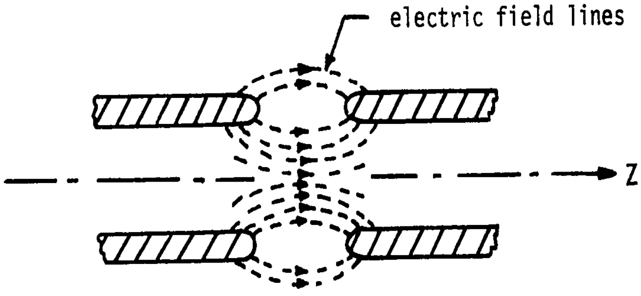

Figure (1.2) Field Distribution Across a Typical Accelerating Gap

Note that in the first half of the gap the radial component of the electric field will exert a force on particles that is towards the axis of the accelerator. In the second half of the gap the particles will experience a defocusing force away from the axis. Since the accelerated particles will spend less time in the second half of the gap, one might imagine that the net effect would be a focusing force action tending to keep the particles near the axis of the structure. Unfortunately, to ensure longitudinal stability of the motion, particles must pass through the gap when the amplitude of the r.f. field is increasing(11). This increase in the field is sufficient that the defocusing forces are increased to the point where the net effect of the accelerating gap is to deflect particles away from the axis of the machine. Space charge forces, stray fields, and misalignments have the effect of further defocusing the particles. In a long accelerator it becomes essential to compensate for these defocusing actions as well as to make provisions for handling particles that enter the structure with non-zero transverse momenta.

In electron and proton accelerators this compensation is almost invariably provided either by axial magnetic fields or by magnetic quadrupole lenses. Such focusing devices work well as long as the charge-to-mass ratios of the particles are large. However, as the charge-to-mass ratio, $\frac{q}{M}$, decreases, the required magnetic fields can become excessive. Even the lightest of heavy ions have values of charge-to-mass ratios that are several orders of magnitude smaller than that of an electron. Singly charged argon for example has a charge-to-mass ratio of only 2.39×10^6 coulombs/kilogram. The values of $\frac{q}{M}$ for typical solid or liquid microparticles are much smaller still and may range from as small as 0.001 coulombs/kilogram to an upper limit of approximately 500,000 coulombs/kilogram(12-13). The use of magnetic fields to guide and contain beams of such heavy particles is quite impractical. Consider, for example, the problem of using an axial magnetic field to confine a particle with a transverse velocity of u = 1000 meter/sec. The particle has a charge-to-mass ratio of 1000 coulombs/kilogram and is to be confined within a cylindrical aperture of radius, R = 2 cm. The required magnetic field is easily calculated from

$$B = \frac{Mu}{qR}$$

In this case B = 500 kilogauss. At the present state of technology, magnetic fields of this magnitude are almost impossible to maintain, especially over large apertures(14). Moreover, the ohmic losses associated with the large magnet currents are prohibitively high. The power requirements can be reduced using superconducting magnets but only at the expense of costly cryogenic installations. On the other hand, electric field focusing devices consume almost no power and the required fields can be established in reasonably sized structures at modest voltages. In the preceding example, an electric field of only 500 volts/cm is needed to produce a force equal to that exerted on the particle by the magnetic field.

The purpose of the present thesis is to present the analysis, design and testing of a novel electrostatic system for guiding and focusing very heavy charged particles. It is intended that the structure be compatible with the micrometeoroid simulator under construction at the University of Alberta.

1.2 Some Existing Electric Field Focusing Devices

In conjunction with the development of heavy ion linear accelerators two approaches have been proposed that use electric fields to provide the necessary focusing forces(15). The first approach is to simply modify the radio frequency fields in the accelerating gaps so that the net effect of the gaps will be a focusing action. Such modification of the r.f. fields can be achieved through fitting the successive circular drift tubes with foils, grids or fingers or by using rectangular drift tubes which are rotated 90° with respect to each other. In the second approach the focusing action is provided by external electrostatic focusing devices which are placed within the drift tubes. These devices almost always consist of some form of electrostatic quadrupole.

1.2.1 Foils and Grids

When the entrance to the right hand drift tube of figure (1.2) is closed by a metal foil thin enough for the beam to penetrate without damage, electric field lines in the accelerating gap are as shown in figure (1.3)(16).

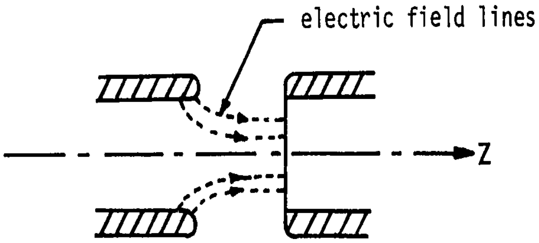

Figure (1.3) Field Distribution Across a Gap Between Drift Tubes with a Thin Foil on the Entrance of the Right Tube

It can be seen that the defocusing radial component in the second half of the gap has disappeared and the whole of the gap is therefore convergent. In practice it has been found that the foils cause unacceptable scattering of the beam and cannot withstand even occasional breakdown between the drift tubes. Moreover, the ability of the foils to dissipate thermal energy is very low and the beam density is therefore extremely limited.

It was then found that fitting the entrance of the right hand side drift tube in figure (1.2) with a metal grid, which closes only a portion of the aperture, modifies the r.f. electric field in a manner similar to that of the foil. Several grid configurations have been suggested and used successfully(17).

1.2.2 Rectangular Drift Tubes, Rotated Grids and Finger Structures

To obtain focusing in the radial direction while maintaining the longitudinal stability of the motion, linear accelerators with drift tubes of rectangular cross-sections have been proposed(18),(19). The successive rectangular drift tubes are rotated 90° with respect to each other, as shown in figure (1.4a).

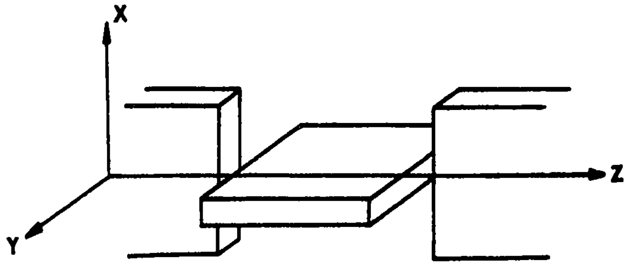

Figure (1.4a) Rectangular Drift Tubes

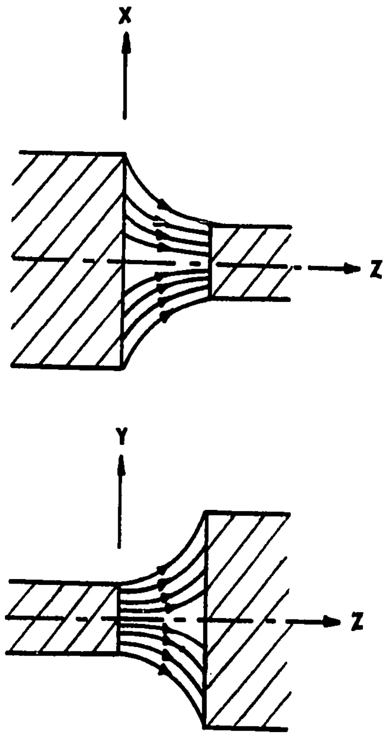

Figure (1.4b) Electric Field Distribution Across the Gap Between Rectangular Drift Tubes in the X-Z and the Y-Z Transverse Planes

As illustrated in figure (1.4b), the shape of the lines of force of the r.f. field in a gap is such that there is focusing in one transverse direction and defocusing in the other transverse direction. This action is reversed from one gap to the next. Thus, as the particle travels along the accelerator it will alternately experience focusing and defocusing forces, in both the X-Z and the Y-Z planes of figures (1.4a) and (1.4b). With proper choice of dimensions and accelerating voltages, this alternating force action can lead to net focusing in both transverse directions.

A similar alternating force can be obtained when using circular drift tubes whose entrances are fitted with two parallel wire grids. From one drift tube to the next the direction of the grids is altered by 90°, as shown in figure (1.5)(20).

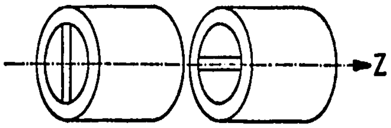

Figure (1.5) Circular Drift Tubes with Two Parallel Wire Grids

Another structure that can provide an alternating force can be constructed by fitting the entrances and the exits of the circular drift tubes with fingers as shown in figure (1.6)(21). The difference in potential between the successive drift tubes,and hence between the fingers,will exert focusing forces on a particle traversing the gap in one transverse direction and defocusing forces in the other transverse direction. Across the next gap the action is reversed, hence the particle will experience, in either one of the two transverse directions, alternating focusing and defocusing forces. Proper choice of the dimensions and the accelerating voltages again leads to a net focusing

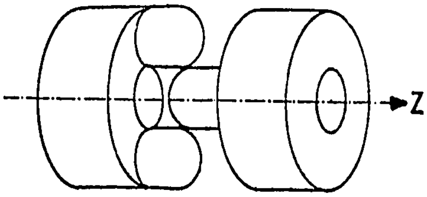

Figure (1.6) Drift Tubes with "Fingers"

action in both transverse directions.

The alternating force action provided by the structures described above is known as alternating gradient focusing. Such action can also be provided using external focusing devices as will be explained in detail in Section 1.2.4.

1.2.3 Weak Electrostatic Lenses

Weak electrostatic lenses consist of two or more cylindrical electrodes which are at different constant potentials. The focusing action is provided by the weak radial components of the d.c. electric field in the gap or gaps between the electrodes together with the small accelerating or decelerating action of these gaps. One of the weak

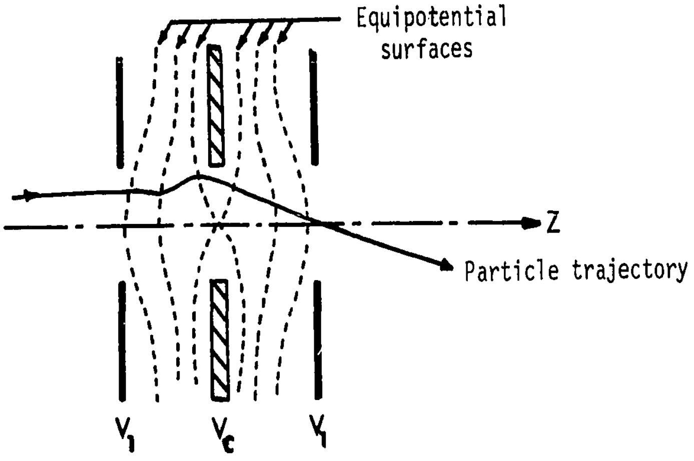

V_1 and V_C are the electrode potentials

Figure (1.7) A Unipotential Electrostatic Lens

electrostatic lenses used in linear accelerators is the unipotential lens which may be in the form shown in figure (1.7)(22). The beam entering the lens is allowed to spread out and then is bent toward the lens axis, with the focal spot near the end of the lens. To provide such action, the electrode potentials should be comparable to the beam accelerating potential. Such weak lenses often are used for shaping the input beam for heavy ion accelerators(23).

Although this type of lens does not have widespread applications for guiding heavy particles it is widely used for shaping and focusing electron beams in electronic devices such as the cathode-ray tube or the electron microscope.

1.2.4 Electrostatic Quadrupole Lenses

The basic principle of alternating gradient focusing, mentioned in Section 1.2.2, was first introduced(24) as it applied to magnetic quadrupole focusing. The principle was later extended to electrostatic quadrupoles. Since then, quadrupole structures have become an almost universal feature of beam transport systems. Since the principle of operation of the classical quadrupole structure is quite similar to that of the lens system described in this thesis, its operation will be reviewed in some detail.

The fields of a quadrupole section are provided by four symmetrical electrodes, as shown in figure (1.8).

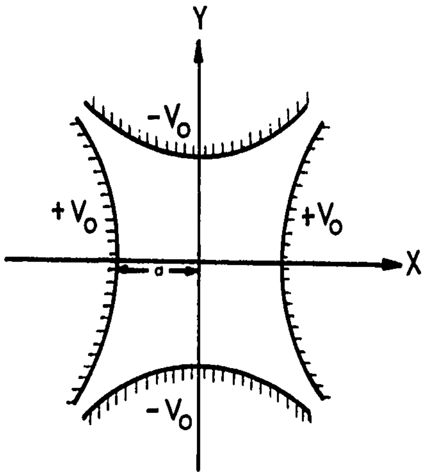

Figure (1.8) Symmetrical Hyperbolic Electrodes

The operation of an electrostatic quadrupole is based on having the potential distribution within the aperture in the form

$$V = k(X^2 - Y^2) \qquad (1.1)$$

which gives the fields as

$$E_X = -2kX \quad ,$$

and $$E_Y = 2kY \quad . \tag{1.2}$$

Such a potential distribution is obtained when hyperbolically shaped electrodes extending to infinity are used, in which case $k = \frac{V_o}{a^2}$ where V_o is the electrode focusing voltage and a is the aperture radius(25). Extensive investigations of the fields from electrodes of shapes other than hyperbolic have shown that electrodes which are parts of cylindrical cylinders give much the same field variation as that of equations (1.2), over a limited portion of the aperture. More complex electrode shapes also have been investigated and have been found to give suitable fields over limited apertures(26).

Equations (1.2) show that each quadrupole section will provide focusing forces in one transverse direction and defocusing forces in the other transverse direction. To provide focusing action in both directions, doublet, triplet and multiplet combinations are used. These classical combinations have a series of sections placed end to end with the potentials reversed on alternate sections. Thus, a particle travelling along any of these combinations will be acted upon, in both transverse directions, by alternate focusing and defocusing forces. Through proper choice of the parameters the net action on the particle in both transverse directions can be focusing.

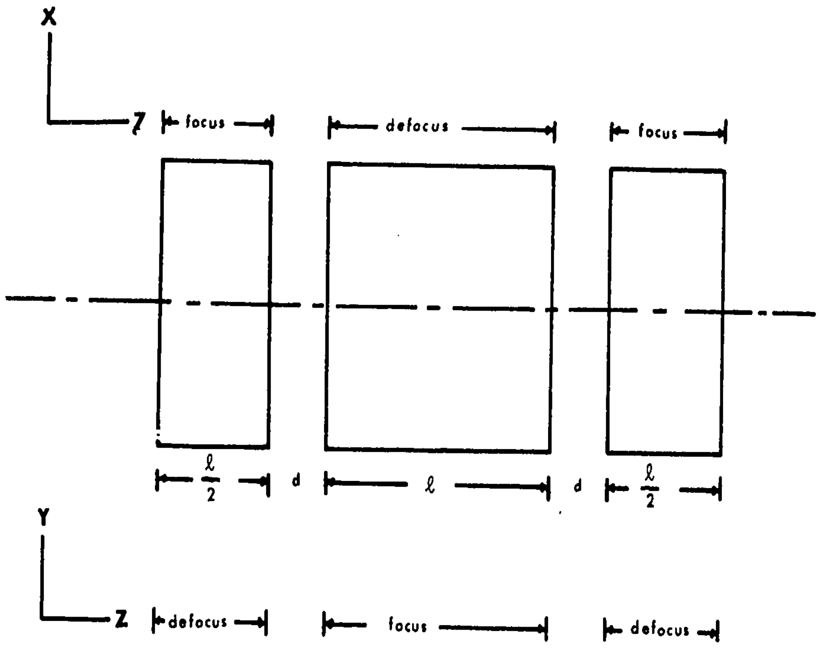

Figure (1.9) Symmetrical Quadrupole Triplet

Figure (1.9) shows a symmetrical quadrupole triplet which consists of a straight quadrupole section of length $\ell/2$ followed by a drift space of length d, then a second straight quadrupole section of length ℓ on which the potentials have been reversed with respect to the first section. The reversal of the potential is equivalent to having rotated the second section through 90° while leaving its electrode potentials unchanged. The second quadrupole is followed by another drift space of length d, and a third quadrupole of length $\frac{\ell}{2}$,which is rotated a further 90° with respect to the second quadrupole section. The first quadrupole section is oriented such that its positive electrodes are aligned symmetrically about the X-axis of a fixed (X,Y,Z) coordinate sytem. Thus,the forces exerted on a positively charged particle at $Z = 0$ are focusing forces in the X-direction and defocusing forces in the Y-direction. Therefore,the X - Z plane can be referred to as the initially focusing plane of the triplet and the Y - Z plane can be referred to as the initially defocusing plane of the triplet.

If the axial momentum of a particle travelling along the triplet is assumed constant, the projections of the particle motion on the X - Z and the Y - Z planes are uncoupled. Therefore,these projections can be independently analyzed. In analyzing the motion it must be noticed that the basis of operation of the quadrupole combinations as guiding and focusing structures is the linear increase of the forces, focusing or defocusing, with the increase of the distance from the Z axis.

Consider the motion of a particle along a triplet with properly chosen parameters. A particle injected in the X - Z plane will experience focusing forces during its travel along the first quadrupole section. These focusing forces will decrease the X directed transverse momentum of the particle and will tend to deflect it towards the Z axis. Due to the action of these focusing forces, the particle, after coasting across the first drift space, will enter the middle quadrupole section at a point closer to the Z axis than if the focusing forces were absent. Hence, the defocusing forces that the particle experiences as it travels along the second quadrupole section are smaller than they might have been if the focusing forces of the first section were absent. The defocusing forces of the middle quadrupole section will deflect the particle away from the Z axis so that the particle, after traversing the second drift space, will experience large focusing forces as it travels along the third quadrupole section. Thus, the particle will experience alternating focusing and defocusing forces as it passes along the triplet. However, if the triplet parameters are properly chosen, the particle finds itself farther displaced from the Z axis while experiencing focusing forces than when experiencing defocusing forces. Since the fields and hence the forces increase linearly with the distance from the Z axis, the effect of the alternating forces will be a net focusing action on the particle.

A similar action occurs when a particle is injected in the Y - Z plane. The particle will first experience defocusing forces that will deflect it away from the Z axis so as the particle travels along the middle quadrupole section it will experience large focusing forces. These large focusing forces will tend to deflect the particle towards the Z axis so that it experiences small defocusing forces as it travels along the third quadrupole section. It has been found that the choice of parameters that produces net focusing action in the X - Z plane will also produce net focusing action in the Y - Z plane(27).

Most beam transport and focusing systems in accelerators are chains of triplets similar to that in figure (1.9). A chain of symmetrical triplets, referred to as a classical quadrupole channel, is shown in figure (1.10).

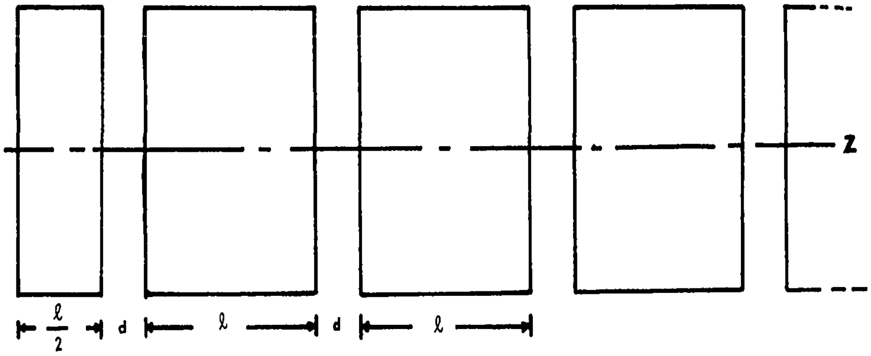

Figure (1.10) A Classical Quadrupole Channel

An infinitely long classical channel will consist of a straight quadrupole section of length $\ell/2$ followed by a succession of drift spaces of length, d, and quadrupole sections of length, ℓ. The successive quadrupole sections will be rotated 90° with respect to each other. The mathematical treatment of the particle motion along such a classical channel will be outlined in Chapter 6.

1.3 The Present Study

Recently, studies have been carried out for incrementally rotated magnetic quadrupole channels for which the angle of rotation between the successive straight quadrupole sections was equal to $\frac{180°}{n}$ where $n = 3, 4, 5, \ldots$ (28-29). These studies showed that the focusing strength of the structure is improved as the angle of rotation between the successive straight quadrupole sections is decreased. Preliminary investigations of continuously twisted magnetic quadrupole structures(30-31) have shown that such structures provide better focusing action than either the classical or the incrementally rotated magnetic quadrupole structures.

The purpose of the present study, as mentioned in Section 1.1, is to develop a guiding and focusing system for heavy charged microparticles. It is intended that the structure be compatible with the micrometeoroid simulator under construction at the University of Alberta. The focusing and guiding system must be an electrostatic structure if it is to be capable of guiding the artificial micrometeoroids whose charge-to-mass ratios are very low. In view of the results obtained by previous authors(30-31) during their investigations of the guiding properties of uniformly twisted magnetic quadrupole structures, it was expected that a uniformly twisted electrostatic quadrupole structure would provide good focusing and guiding of heavy particle beams. Therefore, it was decided to investigate, both theoretically and experimentally, the guiding and focusing properties of a uniformly twisted electrostatic quadrupole structure designed to handle beams of charged microparticles with very low and variable charge-to-mass ratios.

The twisted quadrupole structure consists of four hyperbolically shaped electrodes which have been uniformly and slowly twisted about the structure axis as shown in figure (1.11). The radius of the circular aperture of the twisted structure is much smaller than the periodic length of twist of the electrodes. Each two nonadjacent electrodes are electrically connected. Two nonadjacent electrodes are at a positive potential, + V_0,

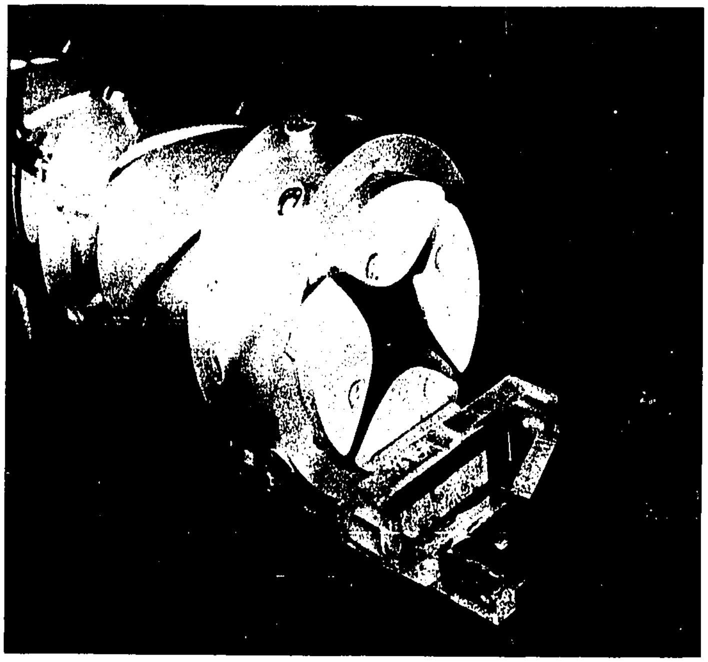

Figure (1.11) The Uniformly Twisted Electrostatic Quadrupole Structure

while the other two are at a negative potential, - V_0. Thus, the force exerted on a positive particle on the axis of the first electrode pair is a focusing force while the force exerted on a particle on the axis of the second electrode pair is a defocusing force.

In classical or incrementally rotated quadrupole structures the change in the direction of the focusing and defocusing forces occurs suddenly as the particle leaves one straight quadrupole section to enter the next. In the twisted structure as the particle travels along the structure, the particle experiences forces that change gradually from focusing to defocusing and so on. However, as in the case of the classical triplet, the particle while experiencing the focusing forces will be farther displaced from the structure axis than while experiencing defocusing forces. Thus, the net action of these gradually alternating focusing and defocusing forces will be a focusing action and the twisted structure will be capable of guiding the particles.

Beside its present application as a guiding and focusing system for heavy charged microparticles, the twisted electrostatic quadrupole structure could also be used to guide electrostatically sprayed liquids used in non-impact electrostatic printing(6) as well as for guiding exhaust streams of colloidal propulsion devices(7).

The work of this thesis is described in the chapters which follow. The theoretical analysis of charged particle motion along the slowly and uniformly twisted electrostatic structure is developed in Chapter 2. Then, Chapter 3 presents the derivation of the acceptance limits of an infinitely long structure and these limits are discussed for some special cases of injection. To examine the accuracy of the analytic solution developed in Chapter 2, particle trajectories computed using the analytical solution are compared, in Chapter 4, with the trajectories computed using numerical integration of the original equations of motion. The effect of earth's gravity on the motion of the heavy microparticles is studied in Chapter 5. The guiding properties of the twisted electrostatic quadrupole structure are compared,in Chapter 6,with those of a classical electrostatic quadrupole channel.

A theoretical study of the imaging properties of a twisted electrostatic quadrupole structure of finite length is presented in Chapter 7, showing that the structure acts as a novel identical imaging device, provided the structure parameters are chosen properly. This imaging device is capable of identically imaging the injection coordinates and momenta of a beam of particles and the imaging occurs with very small aberration. The imaging properties of a structure constructed from two equal but oppositely twisted electrostatic quadrupole sections are also studied in Chapter 7, showing this structure provides identical imaging with less aberration than a single twisted section. The theoretical studies are followed by experimental investigations of the imaging and guiding properties of the twisted channel. A high density beam of charged 3 micron carbonyl iron microparticles was used in the experimental investigations. The descriptions and the results of the experimental investigations are in Chapter 8.

Finally, Chapter 9 presents the analysis of the motion of a charged particle as it travels along a twisted electrostatic quadrupole structure whose axis is bent in a circle. This analysis is relevant to beam bending devices and to storage rings of heavy charged particle beams.

CHAPTER 2

PARTICLE DYNAMICS IN THE UNIFORMLY TWISTED ELECTROSTATIC QUADRUPOLE STRUCTURE

The structure consists of a long electrostatic quadrupole whose four hyperbolic shaped electrodes have been uniformly twisted about the structure axis at the rate of β radians per meter. The objective of this chapter is to determine the analytic solutions for the motion of charged particles travelling along the structure so that the guiding properties of the structure can be easily established. Only non-relativistic solutions are considered since the main objective is to provide a guiding system for microparticles, which simulate micrometeoroids whose velocities range from a fraction of a kilometer per second up to 72 kilometers per second(32).

2.1 Coordinate Systems and Potential Distribution

Figure (2.1) shows the four hyperbolic shaped electrodes of the structure. The distance a is the radius of the quadrupole aperture in meters and V_0 is the magnitude of the d.c. focusing voltage applied to each of the electrodes in volts. The polarities of the d.c. focusing voltages are shown in figure (2.1). In the analysis of the charged particle motion along the structure two rectangular coordinate systems are used, namely the (X,Y,Z) and the (x,y,z) coordinate systems.

The quadrupole structure axis is taken as the Z-axis of the fixed

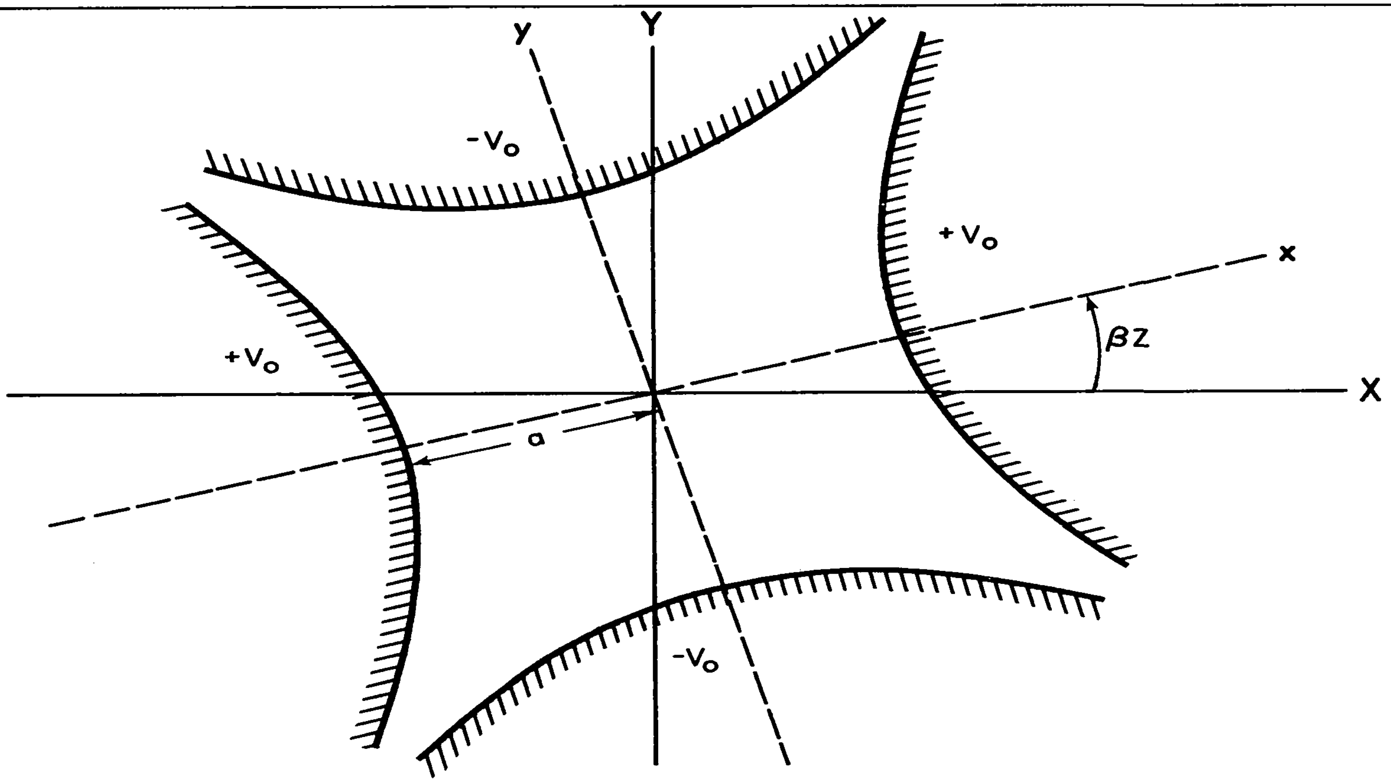
y
Y
$-V_o$
$+V_o$
x
βZ
X
$+V_o$
a
$-V_o$

Figure (2.1) Coordinate System for the Uniformly Twisted Quadrupole Structure.

rectangular coordinate system (X,Y,Z). The axes (X,Y) coincide with the electrode axes at the input plane of the structure, Z = 0. The (x,y,z) coordinate system is a rotating coordinate system whose axes (x,y) rotate, as z increases, at the rate of β radians per meter so that the axes (x,y) always coincide with the electrode axes at any distance z. The Z and z axes of the two coordinate systems coincide. Figure (2.1) shows the orientation of the quadrupole electrodes and the axes (x,y) with respect to the fixed axes (X,Y) at a distance Z from the input plane of the quadrupole structure.

It is shown in Appendix A that if the electrodes are slowly twisted so that the pitch length $L = \frac{2\pi}{\beta}$ is much greater than the aperture radius a, that is $(\beta a)^2 << 1$, then for hyperbolic shaped electrodes and for points within the aperture, the potential distribution is given by

$$V = k[\{X^2 - Y^2\}\cos 2\beta Z + \{2XY\}\sin 2\beta Z] \tag{2.1a}$$

or

$$V = k\{x^2 - y^2\} \tag{2.1b}$$

where $k = \frac{V_0}{a^2}$.

Equation (2.1b) shows that at any cross section of the twisted structure the potential at points within the aperture in terms of the rotating coordinates (x,y,z) is simply that of a conventional quadrupole and is unaffected by the twisting action provided that

$$(\beta a)^2 << 1. \tag{2.2}$$

2.2 The Hamiltonian and the Equations of Motion

Particle dynamics in the uniformly twisted straight electrostatic quadrupole can be conveniently discussed in terms of the Hamiltonian of particle motion, H. In the present case, H is a constant of the motion since the potential and hence the fields do not depend explicitly on time(33). In terms of the fixed coordinate system (X,Y,Z), H is simply the sum of the kinetic energy of the particle, T, and its potential energy(33), qV, where V is the electric potential given by either equation (2.1a) or equation (2.1b). Thus the Hamiltonian is

$$H = T + qV$$

or,

$$H = \frac{1}{2M}\,[P_X{}^2 + P_Y{}^2 + P_Z{}^2] + qV(X,Y,Z) \qquad (2.3)$$

where q is the charge of the particle in coulombs and M is the mass of the particle in kilograms. P_X, P_Y and P_Z are the mechanical momenta canonically conjugate to the (X,Y,Z) coordinates and are given by

$$\begin{aligned} P_X &= M\dot{X} \quad , \\ P_Y &= M\dot{Y} \quad , \\ P_Z &= M\dot{Z} \quad , \end{aligned} \qquad (2.4)$$

where the dot notation represents the total time derivative.

Substituting for the potential V, using equation (2.1a), H is given by

$$H = \frac{1}{2M}[P_X{}^2 + P_Y{}^2 + P_Z{}^2]$$

$$+ qk[\{X^2 - Y^2\}\cos 2\beta Z + \{2XY\} \sin 2\beta Z] \qquad (2.5)$$

Using the canonical equations of Hamilton(34), the equations of motion in the (X,Y,Z) coordinate system are found to be:

$$\ddot{X} = -\frac{2qk}{M}[X \cos 2\beta Z + Y \sin 2\beta Z] \quad ,$$

$$\ddot{Y} = -\frac{2qk}{M}[X \sin 2\beta Z - Y \cos 2\beta Z] \quad ,$$

$$\ddot{Z} = -\frac{2qk}{M}\beta[\{2XY\} \cos 2\beta Z - \{X^2 - Y^2\}\sin 2\beta Z] \quad . \qquad (2.6)$$

These are three coupled nonlinear second order differential equations for which no direct analytical solutions seem to exist.

At this stage the problem can be simplified by expressing H in terms of the rotating coordinates (x,y,z) and the corresponding conjugate momenta (p_x, p_y, p_z). The coordinates of the fixed and the rotating coordinate systems are interrelated through the following equations

$$X = x \cos \beta z - y \sin \beta z \quad ,$$
$$Y = x \sin \beta z + y \cos \beta z \quad ,$$
$$Z = z \quad . \qquad (2.7)$$

Differentiating with respect to time gives:

$$\dot{X} = \frac{P_X}{M} = \{\dot{x} \cos \beta z - \dot{y} \sin \beta z\} - \beta\dot{z}\{x \sin \beta z + y \cos \beta z\} \quad ,$$

$$\dot{Y} = \frac{P_Y}{M} = \{\dot{x} \sin \beta z + \dot{y} \cos \beta z\} + \beta\dot{z}\{x \cos \beta z - y \sin \beta z\} \quad ,$$

$$\dot{Z} = \frac{P_Z}{M} = \dot{z} \quad . \qquad (2.8)$$

Using equations (2.8), the kinetic energy of the particle is given by

$$T = \frac{1}{2M}[P_X{}^2 + P_Y{}^2 + P_Z{}^2]$$

$$T = \frac{M}{2}[\dot{x}^2 + \dot{y}^2 + 2\beta\dot{z}\{x\dot{y} - y\dot{x}\} + \beta^2\dot{z}^2\{x^2 + y^2\} + \dot{z}^2] \qquad (2.9)$$

Since the potential energy, $qV = qk(x^2 - y^2)$, is velocity independent, the momenta (p_x, p_y, p_z) adjoint to the rotating coordinates are(34),

$$p_x = \frac{\partial T}{\partial \dot{x}} = M[\dot{x} - \beta\dot{z}y] \quad ,$$

$$p_y = \frac{\partial T}{\partial \dot{y}} = M[\dot{y} + \beta\dot{z}x] \quad ,$$

$$p_z = \frac{\partial T}{\partial \dot{z}} = M[\dot{z} + \beta(x\dot{y} - y\dot{x}) + \beta^2(x^2 + y^2)\dot{z}] = M\dot{z} + \beta(x\, p_y - y\, p_x) \quad .$$

$$(2.10)$$

Using equations (2.9) and (2.10), the kinetic energy of the particle in terms of the rotating coordinates (x,y,z) and their adjoint momenta (p_x, p_y, p_z) is given by

$$T = \frac{1}{2M} [p_x{}^2 + p_y{}^2 + \{p_z - \beta(x\,p_y - y\,p_x)\}^2] \quad .$$

Hence, in the rotating coordinate system the Hamiltonian is given by,

$$H = \frac{1}{2M} [p_x{}^2 + p_y{}^2 + \{p_z - \beta(x\,p_y - y\,p_x)\}^2]$$

$$+ qk(x^2 - y^2) \quad . \tag{2.11}$$

Examination of (2.11) shows that H is independent of z. Thus z is a cyclic coordinate and p_z is a constant of the motion given by

$$p_z = M\dot{z} + \beta(x\,p_y - y\,p_x). \tag{2.12}$$

Using equations (2.7), (2.8) and (2.12) it can be shown that the momenta (p_x, p_y, p_z), in terms of the fixed coordinates (X,Y,Z) and their adjoint mechanical momenta (P_X, P_Y, P_Z), are given by

$$p_x = P_X \cos \beta Z + P_Y \sin \beta Z \quad ,$$

$$p_y = - P_X \sin \beta Z + P_Y \cos \beta Z \quad ,$$

$$p_z = P_Z + \beta(X\,P_Y - Y\,P_X) \quad . \tag{2.13}$$

Using the Hamiltonian given by equation (2.11), the equations of motion in the rotating coordinate system are given as,

$$\dot{p}_x = -\frac{\partial H}{\partial x} = \frac{\beta p_y}{M}[p_z - \beta(x\,p_y - y\,p_x)] - 2qkx \quad ,$$

$$\dot{p}_y = -\frac{\partial H}{\partial y} = -\frac{\beta p_x}{M}[p_z - \beta(x\,p_y - y\,p_x)] + 2qky \quad ,$$

$$\dot{x} = \frac{\partial H}{\partial p_x} = \frac{1}{M}[p_x + \beta y\{p_z - \beta(x\,p_y - y\,p_x)\}] \quad ,$$

$$\dot{y} = \frac{\partial H}{\partial p_y} = \frac{1}{M}[p_y - \beta x\{p_z - \beta(x\,p_y - y\,p_x)\}] \quad . \qquad (2.14)$$

Equations (2.14) are four first order nonlinear coupled equations in x, y, p_x and p_y and they can be used to obtain two second order nonlinear coupled differential equations in x and y alone.

The nonlinear nature of equations (2.14) is removed when the transverse momenta conjugate to the rotating coordinates are such that

$$\left(\frac{p_x}{p_z}\right)^2 \text{ and } \left(\frac{p_y}{p_z}\right)^2 << 1. \qquad (2.15)$$

It will be shown later, in Chapter 3, that these inequalities are satisfied for all particles successfully guided by the structure, provided $(\beta a)^2 << 1$. Under the conditions of equation (2.15), the Hamiltonian can be reduced to

$$H = \frac{1}{2M}[p_x^{\,2} + p_y^{\,2} + p_z^{\,2} - 2\beta p_z(x\,p_y - y\,p_x)] + qk(x^2 - y^2) \qquad (2.16)$$

This Hamiltonian can be used to generate the following linear, but coupled, equations of motion

$$\dot{p}_x = \frac{1}{M}[\beta p_z\, p_y - 2Mqk\, x] \quad ,$$

$$\dot{p}_y = \frac{1}{M}[-\beta p_z\, p_x + 2Mqky] \quad ,$$

$$\dot{x} = \frac{1}{M}[p_x + \beta p_z\, y] \quad ,$$

$$\dot{y} = \frac{1}{M}[p_y - \beta p_z\, x] \quad . \tag{2.17}$$

There are two approaches for solving these four linear coupled first order differential equations. The first approach is to resort once more to Hamiltonian mechanics to generate, through contact transformation, a new coordinate system in which the equations of motion are uncoupled. The second approach is to put equations (2.17) in a matrix form and then to solve the resulting linear first order vector differential equation. Both of these approaches are used and described in the two sections which follow.

2.3 Solution of the Equations of Motion by Contact Transformation

The difficulty encountered in solving equations (2.17) is due to the fact that these equations are coupled. However, uncoupled equations of motion can be obtained through contact transformation to a new set of variables $(\bar{x},\bar{y})$ and $(\bar{p}_x, \bar{p}_y)$. The appropriate generating function$^{(34)}$ is found to be

$$G_1 = x\,\bar{p}_x + y\,\bar{p}_y - \gamma\,\bar{p}_x\,\bar{p}_y \tag{2.18}$$

when the factor γ is chosen properly.

Since G_1 is time independent, the value of the Hamiltonian remains unchanged$^{(34)}$. The canonical variables of the rotating coordinate system (x, y, p_x, p_y) and those of the new coordinate system $(\bar{x}, \bar{y}, \bar{p}_x, \bar{p}_y)$ are related as follows$^{(34)}$:

$$
\begin{aligned}
p_x &= \frac{\partial G_1}{\partial x} = \bar{p}_x \quad , \\
p_y &= \frac{\partial G_1}{\partial y} = \bar{p}_y \quad , \\
\bar{x} &= \frac{\partial G_1}{\partial \bar{p}_x} = x - \gamma\, \bar{p}_y \quad , \\
\bar{y} &= \frac{\partial G_1}{\partial \bar{p}_y} = y - \gamma\, \bar{p}_x \quad .
\end{aligned}
\tag{2.19}
$$

The Hamiltonian of equation (2.16), when expressed in terms of $(\bar{x}, \bar{y}, \bar{p}_x, \bar{p}_y)$ becomes:

$$
\begin{aligned}
H = \frac{p_z^{\,2}}{2M} &+ \frac{1}{2M}\left[\bar{p}_x^{\,2}\{1 + 2\beta p_z\gamma - 2qkM\gamma^2\} + 2qkM\bar{x}^2\right] \\
&- \frac{1}{2M}\left[\bar{p}_y^{\,2}\{-1 + 2\beta p_z\gamma - 2qkM\gamma^2\} + 2qkM\bar{y}^2\right] \\
&+ \frac{1}{2M}\left[4qkM\gamma - 2\beta p_z\right]\left[\bar{x}\,\bar{p}_y - \bar{y}\,\bar{p}_x\right] \quad .
\end{aligned}
\tag{2.20}
$$

The coupling between the variables $(\bar{x},\bar{y})$ is represented by the last term in equation (2.20) and in order to avoid such coupling the coefficient of $\{\bar{x}\,\bar{p}_y - \bar{y}\,\bar{p}_x\}$ should vanish. Thus, the proper choice of γ is

$$\gamma = \frac{\beta p_z}{2qkM} \quad . \tag{2.21}$$

The contact transformation generating function becomes

$$G_1 = x\,\bar{p}_x + y\,\bar{p}_y - \frac{\beta p_z}{2qkM}\,\bar{p}_x\,\bar{p}_y \quad , \tag{2.22}$$

and the transformation equations become

$$\bar{x} = x - \frac{\beta p_z}{2qkM}\; p_y \quad ,$$

$$\bar{y} = y - \frac{\beta p_z}{2qkM}\; p_x \quad ,$$

$$\bar{p}_x = p_x \quad ,$$

$$\bar{p}_y = p_y \quad . \tag{2.23}$$

From (2.20) and (2.21) the transformed Hamiltonian becomes:

$$H = \frac{1}{2M}\,[p_z{}^2 + \{\bar{p}_x{}^2(s + 1) + 2qkM\,\bar{x}^2\}$$

$$- \{\bar{p}_y{}^2(s - 1) + 2qkM\,\bar{y}^2\}] \quad , \tag{2.24}$$

where $s = \frac{\beta^2 p_z{}^2}{2qkM}$. (2.25)

This Hamiltonian represents uncoupled motion in both the $\bar{x}$ and $\bar{y}$ directions and the equations of motion are

$$\dot{\bar{x}} = \frac{1}{M}\,\bar{p}_x(s + 1) \quad ,$$

$$\dot{\bar{y}} = -\frac{1}{M}\,\bar{p}_y(s - 1) \quad ,$$

$$\dot{\bar{p}}_x = -\,2qk\,\bar{x} \quad ,$$

$$\dot{\bar{p}}_y = 2qk\,\bar{y} \quad . \tag{2.26}$$

Hence,the uncoupled differential equations in x, y are

$$\ddot{\bar{x}} + \frac{2qk}{M}\,(s + 1)\bar{x} = 0 \quad ,$$

$$\ddot{\bar{y}} + \frac{2qk}{M}\,(s - 1)\bar{y} = 0 \quad . \tag{2.27}$$

Equation (2.25) shows that the sign of s is independent of the sign of β. Taking the above into consideration,it is clear from equations (2.24) and (2.27) that the motion of the particle in the $(\bar{x}, \bar{y}, \bar{p}_x, \bar{p}_y)$ coordinate system is independent of the sign of β. On the other hand, equation (2.25) shows that the sign of s is dependent on the sign of the charge of the particle, q. For a particle with a negative charge,-q,the factor s will be related to that of a particle with a positive charge,+q,as,

$$s_{-q} = \frac{\beta^2 p_z^{\,2}}{2(-q)kM} = -\,s_{+q} \quad .$$

Substituting s_{-q} into the Hamiltonian of equation (2.24) gives

$$H_{-q} = \frac{1}{2M}\,[p_z^{\,2} + \{\bar{p}_x^{\,2}(-s_{+q} + 1) + 2(-q)kM\,\bar{x}^2\}$$

$$- \{\bar{p}_y^{\,2}(-s_{+q} - 1) + 2(-q)kM\,\bar{y}^2\}]$$

or

$$H_{-q} = \frac{1}{2M}\,[p_z^{\,2} - \{\bar{p}_x^{\,2}(s_{+q} - 1) + 2qkM\,\bar{x}^2\}$$

$$+ \{\bar{p}_y^{\,2}(s_{+q} + 1) + 2qkM\,\bar{y}^2\}] \quad .$$

and the equations of motion of the negatively charged particle, obtained by substituting s_{-q} into equations (2.27), are

$$\ddot{\bar{x}} + \frac{2qk}{M}\,(s_{+q} - 1)\bar{x} = 0 \quad ,$$

$$\ddot{\bar{y}} + \frac{2qk}{M}\,(s_{+q} + 1)\bar{y} = 0 \quad .$$

Comparison of H_{-q} and the last two equations with equations (2.24) and (2.27) shows that the change of the particle charge from +q to -q corresponds to an interchange of $\bar{x}$ into $\bar{y}$ and $\bar{y}$ into $\bar{x}$.

Equations (2.27) represent stable harmonic motion with respect to $\bar{x}$ and $\bar{y}$ provided the factor s, which will be referred to as the stability factor, satisfies the following condition:

$$|s| = \left|\frac{\beta^2 p_z^{\,2}}{2qkM}\right| > 1.0 \qquad (2.28)$$

The solutions for $\bar{x}$, $\bar{y}$, $\bar{p}_x$ and $\bar{p}_y$ are found to be

$$\bar{x} = C_1 \cos F_1 \quad ,$$

$$\bar{y} = C_2 \cos F_2 \quad ,$$

$$\bar{p}_x = -\, p_z \frac{\beta\, C_1(-1)^n}{\sqrt{s}\sqrt{s+1}} \sin F_1 \quad ,$$

$$\bar{p}_y = +\, p_z \frac{\beta\, C_2(-1)^n}{\sqrt{s}\sqrt{s-1}} \sin F_2 \quad . \tag{2.29}$$

The solutions for $\bar{x}$ and $\bar{y}$ are direct solutions for equations (2.27). The solutions for $\bar{p}_x$ and $\bar{p}_y$ were derived by differentiating the solutions for $\bar{x}$ and $\bar{y}$ with respect to time, then substituting the resulting expressions for $\dot{\bar{x}}$ and $\dot{\bar{y}}$ into the first two equations of (2.26). In equations (2.29), $n = 0$ for β positive, corresponding to a counter-clockwise twist of the electrodes, and $n = 1$ for β negative, corresponding to a clockwise twist of the electrodes. The other parameters in equations (2.29) are

$$F_1 = f_1 t + \alpha_1 \quad ,$$

$$F_2 = f_2 t + \alpha_2 \quad ,$$

$$f_1 = \sqrt{\frac{2qk}{M}}\sqrt{s+1} \quad ,$$

$$f_2 = \sqrt{\frac{2qk}{M}}\sqrt{s-1} \quad . \tag{2.30}$$

The values of the constants C_1, C_2, α_1 and α_2 depend upon the conditions of the particle at injection. Notice that in equations (2.29), (2.30) and in all equations to follow a positive square root will be assumed.

Thus, from equations (2.23) and (2.29) the motion of a charged particle in terms of the rotating coordinates (x,y) and their adjoint momenta (p_x, p_y) is given by

$$x = C_1 \cos F_1 + \frac{\sqrt{s}}{\sqrt{s - 1}} (-1)^n C_2 \sin F_2 \quad ,$$

$$y = C_2 \cos F_2 - \frac{\sqrt{s}}{\sqrt{s + 1}} (-1)^n C_1 \sin F_1 \quad ,$$

$$p_x = - p_z \frac{\beta(-1)^n}{\sqrt{s}\sqrt{s + 1}} C_1 \sin F_1 \quad ,$$

$$p_y = + p_z \frac{\beta(-1)^n}{\sqrt{s}\sqrt{s - 1}} C_2 \sin F_2 \quad , \qquad (2.31)$$

provided that the inequalities expressed by (2.15) are satisfied. These equations give the rotating transverse coordinates and their adjoint momenta as functions of the time t, where t = 0 at the instant of injection of the particle into the structure at Z = 0.

For the particle trajectories to be completely determined it is necessary to find the axial distance Z as a function of the time t and the injection conditions of the particle. Equation (2.12) gives the axial velocity $\dot{Z}$ as

$$\dot{Z} = \dot{z} = \frac{p_z}{M} - \frac{\beta}{M}(x\, p_y - y\, p_x) \qquad (2.32)$$

The constant of the motion, p_z, can be expressed in terms of the injection conditions of the particle by using equation (2.13) as,

$$p_z = P_{Z_0} + \beta(X_0 P_{Y_0} - Y_0 P_{X_0})$$

$$= M\, U_{Z_0}[1 + (\beta a)(\frac{X_0}{a}\frac{P_{Y_0}}{P_{Z_0}} - \frac{Y_0}{a}\frac{P_{X_0}}{P_{Z_0}})] \qquad (2.33)$$

where (X_0, Y_0) are the coordinates of the particle at injection, and where $(P_{X_0}, P_{Y_0}, P_{Z_0})$ are the components of the momentum of the particle at injection. U_{Z_0} is the axial velocity at injection. As shown in Appendix B, equations (2.31), (2.32) and (2.33) give $\dot{Z}$ as a function of the injection conditions and the time t as

$$\begin{aligned}\dot{Z} = \dot{z} = U_{Z_0}&[1 + \beta a\{\frac{X_0}{a}\frac{P_{Y_0}}{P_{Z_0}} - \frac{Y_0}{a}\frac{P_{X_0}}{P_{Z_0}}\}]\\ &+ \frac{\beta^2}{2}\frac{p_z}{M}[\frac{C_1^{\,2}}{(s+1)} - \frac{C_2^{\,2}}{(s-1)}]\\ &+ \frac{\beta}{2}\frac{C_1 C_2}{\sqrt{s^2 - 1}}(f_1 - f_2)\sin(F_1 - F_2)\\ &- \frac{\beta}{2}\frac{C_1 C_2}{\sqrt{s^2 - 1}}(f_1 + f_2)\sin(F_1 + F_2)\\ &+ \frac{\beta^2}{2}\frac{p_z}{M}[\frac{C_2^{\,2}}{(s-1)}\cos 2F_2 - \frac{C_1^{\,2}}{(s+1)}\cos 2F_1]. \qquad (2.34)\end{aligned}$$

Integrating equation (2.34) with respect to time gives the axial distance traversed by the particle as a function of the time t as,

$$Z = z = \int_0^t \dot{Z}\, dt$$

$$
\begin{aligned}
&= [1 + \beta a\{\frac{X_0}{a}\,\frac{P_{Y_0}}{P_{Z_0}} - \frac{Y_0}{a}\,\frac{P_{X_0}}{P_{Z_0}}\}] \,.\\
&\quad [1 + \frac{\beta^2}{2}\{\frac{C_1^{\,2}}{s + 1} - \frac{C_2^{\,2}}{s - 1}\}]U_{Z_0}\, t\\
&\quad + \frac{\beta}{2}\frac{C_1\, C_2}{\sqrt{s^2 - 1}}\,[\cos(F_1 + F_2) - \cos(F_1 - F_2)]\\
&\quad + (-1)^n\,\frac{\beta}{4}\,\sqrt{s}[\frac{C_2^{\,2}}{(s - 1)^{3/2}}\,\sin 2F_2 - \frac{C_1^{\,2}}{(s + 1)^{3/2}}\,\sin 2F_1]\\
&\quad - \frac{\beta}{2}\frac{C_1\, C_2}{\sqrt{s^2 - 1}}\,[\cos(\alpha_1 + \alpha_2) - \cos(\alpha_1 - \alpha_2)]\\
&\quad - (-1)^n\,\frac{\beta}{4}\,\sqrt{s}[\frac{C_2^{\,2}}{(s - 1)^{3/2}}\,\sin 2\alpha_2 - \frac{C_1^{\,2}}{(s + 1)^{3/2}}\,\sin 2\alpha_1] \,.
\end{aligned}
\tag{2.35}
$$

Equations (2.31) together with equation (2.35) completely specify the particle trajectory in the rotating (x,y,z) coordinate system, with $n = 0$ for β positive and $n = 1$ for β negative. The equations specifying the trajectories in the fixed (X,Y,Z) coordinate system are obtained from equations (2.31) by using the transform equations (2.7)

The constants C_1, C_2, α_1 and α_2 can be evaluated in terms of the injection conditions of the particle. Setting $t = 0$ in equations (2.7) and (2.13), the relationships between the rotating and the fixed coordinate systems are

$$x_0 = X_0 \quad , \quad y_0 = Y_0 \quad , \quad z_0 = Z_0 = 0 \quad ,$$

$$p_{X_0} = P_{X_0} \quad , \quad p_{y_0} = P_{Y_0} \quad ,$$

$$p_Z = P_{Z_0} + \beta\{X_0 P_{Y_0} - Y_0 P_{X_0}\} \quad . \tag{2.36}$$

Setting t = 0 in equations (2.31) and using the relations (2.36), the constants C_1, C_2, α_1 and α_2 are found to be

$$C_1{}^2 = [X_0 - \frac{s}{\beta} \frac{P_{Y_0}}{p_z}]^2 + \frac{s(s+1)}{\beta^2} \frac{P_{X_0}{}^2}{p_z{}^2} \quad ,$$

$$C_2{}^2 = [Y_0 - \frac{s}{\beta} \frac{P_{X_0}}{p_z}]^2 + \frac{s(s-1)}{\beta^2} \frac{P_{Y_0}{}^2}{p_z{}^2} \quad ,$$

$$\alpha_1 = \tan^{-1} \left[\frac{-\frac{\sqrt{s}\sqrt{s+1}}{(-1)^{n}\beta} \{\frac{P_{X_0}}{p_z}\}}{\{X_0 - \frac{s}{\beta} \frac{P_{Y_0}}{p_z}\}} \right] \quad ,$$

$$\alpha_2 = \tan^{-1} \left[\frac{\frac{\sqrt{s}\sqrt{s-1}}{(-1)^{n}\beta} \{\frac{P_{Y_0}}{P_z}\}}{\{Y_0 - \frac{s}{\beta} \frac{P_{X_0}}{p_z}\}} \right] \quad . \tag{2.37}$$

2.4 Solution of the Equations of Motion by Matrix Techniques

The second approach to finding an analytical solution for the particle trajectories utilizes a matrix formulation of the equations of motion, (2.17). Thus,

$$\begin{bmatrix} \dot{x} \\ \dot{y} \\ \dot{p}_x \\ \dot{p}_y \end{bmatrix} = \begin{bmatrix} T \end{bmatrix} \begin{bmatrix} x \\ y \\ p_x \\ p_y \end{bmatrix} \qquad (2.38)$$

where,

$$[T] = \begin{bmatrix} 0 & \frac{\beta p_z}{M} & \frac{1}{M} & 0 \\ -\frac{\beta p_z}{M} & 0 & 0 & \frac{1}{M} \\ -2qk & 0 & 0 & \frac{\beta p_z}{M} \\ 0 & 2qk & -\frac{\beta p_z}{M} & 0 \end{bmatrix} \qquad (2.39)$$

Equation (2.38) is a first order linear vector differential equation of the form,

$$\dot{\overline{\eta(t)}} = [T]\overline{\eta(t)} \qquad (2.40)$$

where

$$\overline{\eta(t)} = \begin{bmatrix} x \\ y \\ p_x \\ p_y \end{bmatrix} \qquad (2.41)$$

For the case where the eigenvalues of [T] are distinct, the solution of equation (2.40) is known to be(35)

$$\overline{\eta(t)} = A_1 \overline{\eta_1} e^{\lambda_1 t} + A_2 \overline{\eta_2} e^{\lambda_2 t} + A_3 \overline{\eta_3} e^{\lambda_3 t} + A_4 \overline{\eta_4} e^{\lambda_4 t} \qquad (2.42)$$

where λ_1, λ_2, λ_3 and λ_4 are the four eigenvalues of the transform matrix [T] and $\overline{\eta_1}$, $\overline{\eta_2}$, $\overline{\eta_3}$ and $\overline{\eta_4}$ are the corresponding four eigenvectors. The values of the constants A_1, A_2, A_3 and A_4 depend on the components of $\overline{\eta(t)}$ at $t = 0$, that is they depend on the injection values of x, y, p_x and p_y.

The four eigenvalues of [T] are the roots of the equation

$$|T - \lambda I| = 0 \qquad \text{where I is the 4x4 unit matrix.}$$

Substituting for [T], the above equation becomes

$$\begin{bmatrix} -\lambda & \frac{\beta p_z}{M} & \frac{1}{M} & 0 \\ -\frac{\beta p_z}{M} & -\lambda & 0 & \frac{1}{M} \\ -2qk & 0 & -\lambda & \frac{\beta p_z}{M} \\ 0 & 2qk & -\frac{\beta p_z}{M} & -\lambda \end{bmatrix} = 0$$

giving,

$$\lambda^4 + 2\left(\frac{\beta p_z}{M}\right)^2 \lambda^2 + \left\{\left(\frac{\beta p_z}{M}\right)^4 - \left(\frac{2qk}{M}\right)^2\right\} = 0$$

The solution of this equation gives the four eigenvalues as

$$\lambda_1 = j[(\frac{\beta p_z}{M})^2 - \frac{2qk}{M}]^{1/2} = jf_2 \quad ,$$

$$\lambda_2 = - \lambda_1 = - jf_2 \quad ,$$

$$\lambda_3 = j[(\frac{\beta p_z}{M})^2 + \frac{2qk}{M}]^{1/2} = jf_1 \quad ,$$

$$\lambda_4 = -\lambda_3 = -jf_1 \quad , \qquad (2.43)$$

where f_1 and f_2 are the same as defined by equations (2.30). In other words,

$$f_1 = \sqrt{\frac{2qk}{M}}\sqrt{s + 1} \quad ,$$

$$f_2 = \sqrt{\frac{2qk}{M}}\sqrt{s - 1} \quad .$$

Each of the eigenvectors $\overline{\eta_i}$, i = 1,2,3,4 satisfies the four algebraic simultaneous equations,

$$\begin{array}{lllll}
- \lambda_i \gamma_{1i} & + \frac{\beta p_z}{M} \gamma_{2i} & + \frac{1}{M} \gamma_{3i} & & = 0 \quad , \\
- \frac{\beta p_z}{M} \gamma_{1i} & - \lambda_i \gamma_{2i} & & + \frac{1}{M} \gamma_{4i} & = 0 \quad , \\
- 2qk \gamma_{1i} & & - \lambda_i \gamma_{3i} & + \frac{\beta p_z}{M} \gamma_{4i} & = 0 \quad , \\
 & + 2qk \gamma_{2i} & - \frac{\beta p_z}{M} \gamma_{3i} & - \lambda_i \gamma_{4i} & = 0 \quad .
\end{array} \qquad (2.44)$$

where

$$\overline{\eta_i} = \begin{bmatrix} \gamma_{1i} \\ \gamma_{2i} \\ \gamma_{3i} \\ \gamma_{4i} \end{bmatrix}$$

Solving equations (2.44) for each of the eigenvalues gives the four eigenvectors as,

$$\overline{\eta_1} = \begin{bmatrix} 1 \\ \frac{\lambda_1 M}{\beta p_z} \\ 0 \\ \frac{2qkM}{\beta p_z} \end{bmatrix}, \qquad \overline{\eta_2} = \begin{bmatrix} 1 \\ \frac{\lambda_2 M}{\beta p_z} \\ 0 \\ \frac{2qkM}{\beta p_z} \end{bmatrix},$$

$$\overline{\eta_3} = \begin{bmatrix} -\frac{\lambda_3 M}{\beta p_z} \\ 1 \\ \frac{2qkM}{\beta p_z} \\ 0 \end{bmatrix}, \qquad \overline{\eta_4} = \begin{bmatrix} -\frac{\lambda_4 M}{\beta p_z} \\ 1 \\ \frac{2qkM}{\beta p_z} \\ 0 \end{bmatrix}. \tag{2.45}$$

Substituting equations (2.43) and (2.45) into (2.42) gives the solution of equation (2.38) as

$$\begin{bmatrix} x \\ y \\ p_x \\ p_y \end{bmatrix} = A_1 \begin{bmatrix} 1 \\ j\,\frac{f_2M}{\beta p_z} \\ 0 \\ \frac{2qkM}{\beta p_z} \end{bmatrix} e^{jf_2t} + A_2 \begin{bmatrix} 1 \\ -j\,\frac{f_2M}{\beta p_z} \\ 0 \\ \frac{2qkM}{\beta p_z} \end{bmatrix} e^{-jf_2t}$$

$$+ A_3 \begin{bmatrix} -j\,\frac{f_1M}{\beta p_z} \\ 1 \\ \frac{2qkM}{\beta p_z} \\ 0 \end{bmatrix} e^{jf_1t} + A_4 \begin{bmatrix} j\,\frac{f_1M}{\beta p_z} \\ 1 \\ \frac{2qkM}{\beta p_z} \\ 0 \end{bmatrix} e^{-jf_1t} \qquad (2.46)$$

Stability of the solution implies real values for f_1 and f_2. It is apparent that f_1 and f_2 are real provided

$$|s| = \left|\frac{\beta^2 p_z^{\ 2}}{2qkM}\right| > 1.0$$

This stability criterion is the same as that given in (2.28).

To evaluate the constants A_1, A_2, A_3 and A_4 consider equations (2.36) rearranged in a vector form as

$$\begin{bmatrix} x \\ y \\ p_x \\ p_y \end{bmatrix}_{t=0} = \begin{bmatrix} x_o \\ y_o \\ p_{x_o} \\ p_{y_o} \end{bmatrix} = \begin{bmatrix} X_o \\ Y_o \\ P_{X_o} \\ P_{Y_o} \end{bmatrix} \qquad (2.47)$$

Setting t = 0 in equations (2.46) and substituting from equation (2.47) gives

$$X_o = A_1 + A_2 - j\,\frac{f_1 M}{\beta p_z}\,(A_3 - A_4) \quad ,$$

$$Y_o = A_3 + A_4 + j\,\frac{f_2 M}{\beta p_z}\,(A_1 - A_2) \quad ,$$

$$P_{X_o} = \frac{2qkM}{\beta p_z}\,(A_3 + A_4) \quad ,$$

$$P_{Y_o} = \frac{2qkM}{\beta p_z}\,(A_1 + A_2) \quad .$$

Solving these four algebraic equations, the constants A_1, A_2, A_3 and A_4 in terms of the injection conditions are:

$$A_1 = \frac{1}{2}\,\frac{\beta p_z}{2qkM}\,P_{Y_o} - j\,\frac{1}{2}\,\frac{\beta p_z}{Mf_2}\left[Y_o - \frac{\beta p_z}{2qkM}\,P_{X_o}\right] \quad ,$$

$$A_2 = \frac{1}{2}\,\frac{\beta p_z}{2qkM}\,P_{Y_o} + j\,\frac{1}{2}\,\frac{\beta p_z}{Mf_2}\left[Y_o - \frac{\beta p_z}{2qkM}\,P_{X_o}\right] \quad ,$$

$$A_3 = \frac{1}{2}\frac{\beta p_z}{2qkM}P_{X_0} + j\,\frac{1}{2}\frac{\beta p_z}{Mf_1}\left[X_0 - \frac{\beta p_z}{2qkM}P_{Y_0}\right] \quad ,$$

$$A_4 = \frac{1}{2}\frac{\beta p_z}{2qkM}P_{X_0} - j\,\frac{1}{2}\frac{\beta p_z}{Mf_1}\left[X_0 - \frac{\beta p_z}{2qkM}P_{Y_0}\right] \quad . \qquad (2.48)$$

As shown in Appendix C by substituting equations (2.48) into equations (2.46) and by rearranging the terms, the equations describing the trajectories of the particle in the rotating coordinate system are obtained as functions of the injection conditions in the matrix form:

$$\begin{bmatrix} x \\ y \\ p_x \\ p_y \end{bmatrix} = [Q(t)] \begin{bmatrix} x_0 \\ y_0 \\ p_{x_0} \\ p_{y_0} \end{bmatrix} = [Q(t)] \begin{bmatrix} X_0 \\ Y_0 \\ P_{X_0} \\ P_{Y_0} \end{bmatrix} \quad , \qquad (2.49)$$

where the matrix Q(t) is given by

$$Q(t) = \left[\begin{array}{c|c|c|c}
\cos f_1 t & \frac{\beta p_z}{\sqrt{2Mqk}} \frac{\sin f_2 t}{\sqrt{s-1}} & \frac{\sqrt{s+1}}{\sqrt{2Mqk}} \sin f_1 t - \frac{s}{\sqrt{2Mqk}} \frac{\sin f_2 t}{\sqrt{s-1}} & \frac{\beta p_z}{2Mqk} (\cos f_2 t - \cos f_1 t) \\
\hline
- \frac{\beta p_z}{\sqrt{2Mqk}} \frac{\sin f_1 t}{\sqrt{s+1}} & \cos f_2 t & \frac{\beta p_z}{2Mqk} (\cos f_1 t - \cos f_2 t) & \frac{s}{\sqrt{2Mqk}} \frac{\sin f_1 t}{\sqrt{s+1}} - \frac{\sqrt{s-1}}{\sqrt{2Mqk}} \sin f_2 t \\
\hline
- \frac{\sqrt{2Mqk}}{\sqrt{s+1}} \sin f_1 t & 0 & \cos f_1 t & \frac{\beta p_z}{\sqrt{2Mqk}} \frac{\sin f_1 t}{\sqrt{s+1}} \\
\hline
0 & \frac{\sqrt{2Mqk}}{\sqrt{s-1}} \sin f_2 t & - \frac{\beta p_z}{\sqrt{2Mqk}} \frac{\sin f_2 t}{\sqrt{s-1}} & \cos f_2 t
\end{array}\right] \tag{2.50}$$

Appendix C shows that the solution given by equations (2.49) and (2.50) is obtainable directly from equations (2.31) and (2.37) through the expansion of the trignometric terms and the evaluation of the constants C_1, C_2, α_1 and α_2 in terms of the injection conditions. One feature of the matrix approach is that it circumvents the need for determining a suitable contact transformation.

The first form of the solution, given by equations (2.31) and (2.37) is very useful for investigating the guiding properties of a long uniformly twisted electrostatic quadrupole beam transport system. Equations (2.31) can be easily used to obtain an expression for the radial displacement of the particle and by imposing the condition that the maximum radial displacement must be less than or equal to the aperture radius, it is possible to derive the acceptance limits of the structure.

The matrix form of the solution is useful for studying the imaging properties of the twisted structure. By inspecting the different elements of the transfer matrix, it is possible to investigate the parametric changes required to obtain specific transformation properties for a structure of finite length. For example, in Chapter 7 it is shown that it is possible for $Q(t)$ to be a unit matrix.

CHAPTER 3

GUIDING PROPERTIES

3.1 Stability

The analytical expressions for the particle motion, either equations (2.31) or equations (2.49) and (2.50), show that the harmonic motion of the particle will be bounded and stable if the two frequencies f_1 and f_2 are real, that is

$$f_1^2 = \frac{2qk}{M}(s + 1) > 0 \quad ,$$

and $$f_2^2 = \frac{2qk}{M}(s - 1) > 0 \quad .$$

These two conditions show that the motion of the particle is bounded and stable if s satisfies the condition,

$$|s| = \left|\frac{\beta^2 p_z^{\,2}}{2qkM}\right| > 1.0 \tag{3.1}$$

Substitution for p_z from equation (2.33) gives this stability condition in terms of the structure parameters and the particle injection conditions as,

$$|s| = \left|\frac{\beta^2 P_{Z_0}^{\;2}}{2qkM}\right|[1 + (\beta a)\{\frac{X_0}{a}\frac{P_{Y_0}}{P_{Z_0}} - \frac{Y_0}{a}\frac{P_{X_0}}{P_{Z_0}}\}]^2 > 1.0 \qquad (3.2)$$

For particles which prior to injection have been axially accelerated from rest through a potential V, the axial momentum is given by $P_{Z_0} = \sqrt{2qMV}$. For such particles equation (3.2) takes the form

$$|s| = (\beta a)^2\left|\frac{V}{V_0}\right|[1 + (\beta a)\{\frac{X_0}{a}\frac{P_{Y_0}}{P_{Z_0}} - \frac{Y_0}{a}\frac{P_{X_0}}{P_{Z_0}}\}]^2 > 1.0 \qquad (3.3)$$

3.2 Particle Confinement

So far it has been shown that particle motion along the uniformly twisted quadrupole structure will be stable and oscillatory provided that the stability condition as well as the inequalities (2.2) and (2.15) are satisfied. However, these conditions are not sufficient to ensure that a particle will remain bounded within the aperture of the structure. For a particle to be successfully guided, its maximum transverse displacement from the axis of the structure must never exceed the aperture radius a. In terms of the rotating coordinates

$$r^2 = (x^2 + y^2) \leq a^2 \qquad (3.4)$$

Substitution using equations (2.31) gives

$$r^2 = C_1^2 \cos^2 F_1 + 2(-1)^n\sqrt{\frac{s}{s-1}}\, C_1C_2 \sin F_2 \cos F_1$$

$$+ \frac{s}{s-1} C_2^2 \sin^2 F_2 + C_2^2 \cos^2 F_2$$

$$- 2(-1)^n \sqrt{\frac{s}{s + 1}}\, C_1 C_2 \sin F_1 \cos F_2 + \frac{s}{s + 1} C_1^2 \sin^2 F_1$$

$$= C_1^2[\cos^2 F_1 + \frac{s}{s + 1} \sin^2 F_1]$$

$$+ \frac{s}{s - 1} C_2^2[\frac{s - 1}{s} \cos^2 F_2 + \sin^2 F_2]$$

$$+ 2(-1)^n C_1 C_2 \sqrt{\frac{s}{s - 1}}\, [\sin F_2 \cos F_1 - \sqrt{\frac{s - 1}{s + 1}} \sin F_1 \cos F_2].$$

However, each of the three terms between brackets can only have a magnitude equal to or less than unity. Thus,

$$r^2 \leq C_1^2 + \frac{s}{s - 1} C_2^2 + 2\sqrt{\frac{s}{s - 1}}\, |C_1||C_2|$$

or

$$r \leq |C_1| + \sqrt{\frac{s}{s - 1}}\, |C_2| \qquad (3.5)$$

Hence, to ensure successful guiding of the particle by the twisted structure, $|C_1|$ and $|C_2|$ should be such that the maximum radial displacement satisfies the confinement criterion

$$r_{max} = |C_1| + \sqrt{\frac{s}{s - 1}}\, |C_2| \leq a \qquad (3.6)$$

This inequality sets the limits for the maximum values that $|C_1|$ and $|C_2|$ can have as

$$|C_1|_{max} = a \quad \text{when} \quad |C_2| = 0.0$$

and $$|C_2|_{max} = \sqrt{\frac{s - 1}{s}}\, a \quad \text{when} \quad |C_1| = 0.0 \tag{3.7}$$

In Chapter 2, the solutions for the particle motion were based on the assumption that $(\frac{p_x}{p_z})^2$ and $(\frac{p_y}{p_z})^2$ are much less than unity. Consideration of equations (2.31) shows that the peak values that $(\frac{p_x}{p_z})^2$ and $(\frac{p_y}{p_z})^2$ can have are:

$$(\frac{p_x}{p_z})^2_{max} = \frac{\beta^2}{s(s + 1)} C_1^2 \quad ,$$

$$(\frac{p_y}{p_z})^2_{max} = \frac{\beta^2}{s(s - 1)} C_2^2 \quad . \tag{3.8}$$

Substitution of the maximum values of C_1 and C_2 from equations (3.7) into equation (3.8) yields:

$$(\frac{p_x}{p_z})^2_{max} \leq \frac{(\beta a)^2}{s(s + 1)} < \frac{\beta^2 a^2}{s^2}$$

and

$$(\frac{p_y}{p_z})^2_{max} \leq \frac{\beta^2}{s(s - 1)} \quad \frac{(s - 1)}{s} a^2 = \frac{\beta^2 a^2}{s^2}$$

Thus, for any particle whose stable motion has a maximum radial displacement less than the aperture radius,

$$(\frac{p_x}{p_z})^2 < (\frac{p_y}{p_z})^2 < (\frac{\beta a}{s})^2 \tag{3.9}$$

Since $(\beta a)^2 << 1.0$ and $|s| > 1.0$ for stability considerations, equation (3.9) shows that the inequality (2.15) is satisfied as long as the inequalities (3.1) and (3.6) are satisfied.

Substituting the values of $|C_1|$ and $|C_2|$, given in equations (2.37), into equation (3.6) gives the confinement criterion in terms of the structure parameters and the particle injection conditions. Thus,

$$\left|\left\{\left[X_0 - \frac{s}{\beta}\frac{P_{Y_0}}{P_z}\right]^2 + \frac{s(s+1)}{\beta^2}\frac{P_{X_0}^2}{P_z^2}\right\}^{1/2}\right| + \sqrt{\frac{s}{s-1}}\left|\left\{\left[Y_0 - \frac{s}{\beta}\frac{P_{X_0}}{P_z}\right]^2 + \frac{s(s-1)}{\beta^2}\frac{P_{Y_0}^2}{P_z^2}\right\}^{1/2}\right| \leq a \tag{3.10}$$

When the injection conditions of a particle are such that this confinement criterion is satisfied it will be successfully guided by the structure without being intercepted by any of the four twisted electrodes. A general discussion of these injection limitations is difficult and only some special cases of injection are considered.

3.3 Special Cases of Injection

3.3.1 Parallel Beam

When a charged particle is injected parallel to the structure axis, the Z-axis, its transverse momenta P_{X_0} and P_{Y_0} are zero and its initial transverse displacements are given by X_0 and Y_0. Equations (2.37) under these conditions show that,

$$|C_1| = |X_0| \quad , \quad |C_2| = |Y_0| \tag{3.11}$$

Consideration of equation (3.10) shows that particles will be contained by the uniformly twisted structure when X_0 and Y_0 are within the parallelogram - shaped region depicted by figure (3.1) (plotted for $s = 2.0$ and $(\beta a)^2 = 0.1$). This region is bounded by the straight lines

$$\left|\frac{Y_0}{a}\right| = - \left|\frac{X_0}{a}\right| \frac{\sqrt{s - 1}}{\sqrt{s}} + \frac{\sqrt{s - 1}}{\sqrt{s}} \tag{3.12}$$

Equation (3.12) shows that the maximum allowable value of X_0, when $Y_0 = 0$, is equal to the aperture radius irrespective of the value of s. Equation (3.12) also shows the maximum acceptable value of Y_0 when $X_0 = 0$ is equal to $\sqrt{\frac{s - 1}{s}}\, a$. Thus $Y_{0_{max}}$ increases from zero to a maximum value equal to the aperture radius as s increases from 1.0 to infinity.

It is clear from equation (3.3) that for parallel injection

$$|s| = (\beta a)^2 \left|\frac{V}{V_0}\right| \quad .$$

For a given structure and fixed (βa), increasing s for a particular particle corresponds to an increase of its accelerating potential at injection or to a decrease of the quadrupole focusing voltage, V_0.

Study of figure (3.1) shows that the twisted structure exhibits a feature common to classical quadrupole structures. The maximum allowable X-displacement for parallel injection in the initially focusing X-Z plane is larger than the maximum allowable Y-displacement for parallel injection in the initially defocusing Y-Z plane. A particle

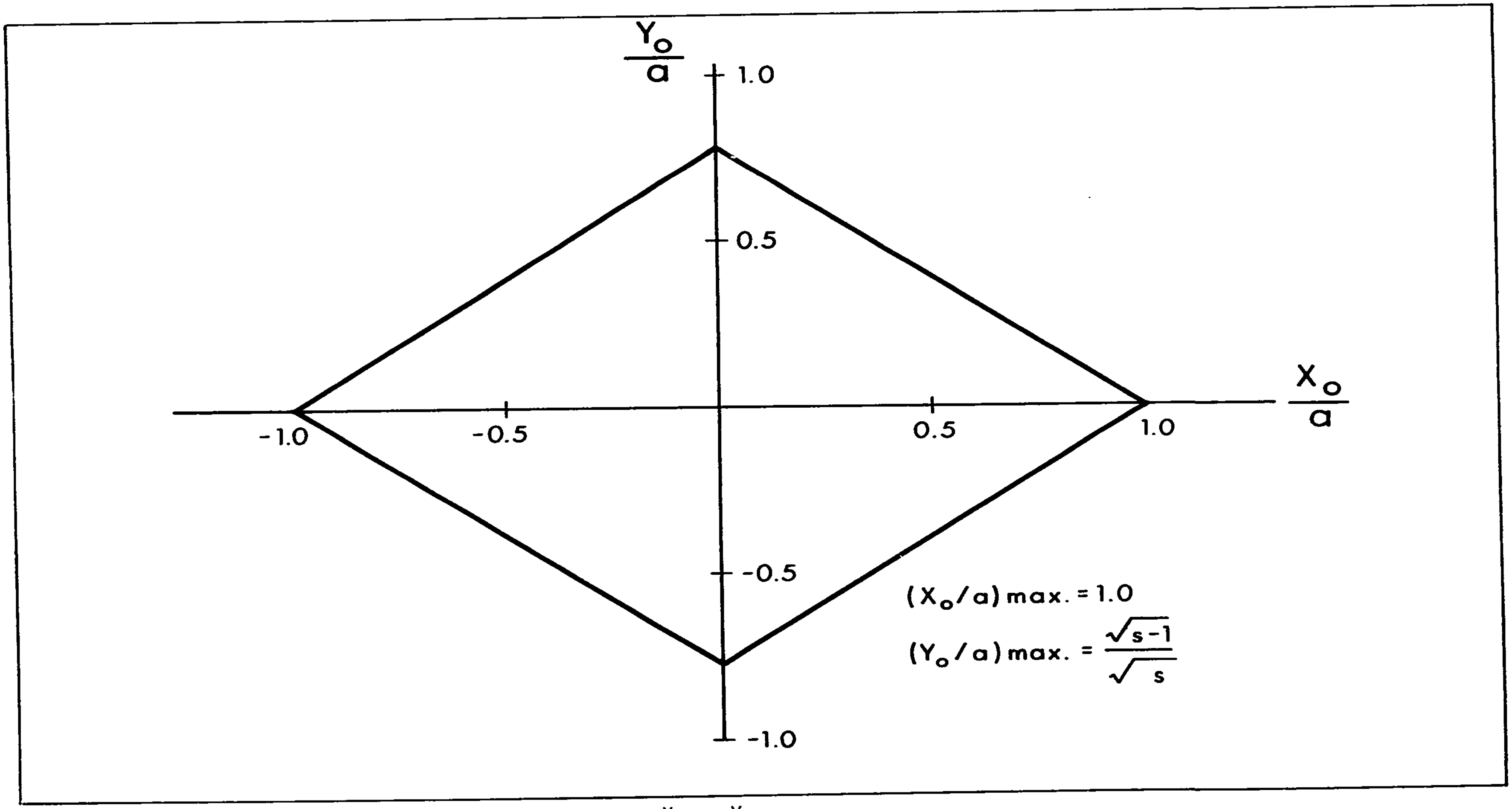
$\frac{Y_o}{a}$
1.0
0.5
-0.5
-1.0
$\frac{X_o}{a}$
-1.0
-0.5
0.5
1.0
$(X_o/a)\,\text{max.} = 1.0$
$(Y_o/a)\,\text{max.} = \frac{\sqrt{s-1}}{\sqrt{s}}$

Figure (3.1) Acceptance in the Normalized $\frac{X_o}{a}$ - $\frac{Y_o}{a}$ Transverse Coordinates Plane for Parallel Beam Injection.

may be injected in the X-Z plane with an initial displacement as large as the aperture radius. At first, the particle will be acted upon by large electric fields that deflect it towards the Z axis. As it progresses along the structure the forces acting on the particle will change and tend to deflect it away from the axis. This defocusing action will be followed by another focusing action as the forces change again and tend to deflect the particle back towards the axis. Thus, the particle will experience alternating focusing and defocusing forces as it passes along the structure. However, each time the forces are focusing the particle is farther away from the axis than it is during the time when it sees defocusing forces. Since the fields and hence the forces increase linearly with distance from the axis,the effect of those alternating forces will be a net focusing action on the particles.

On the other hand, particles cannot be injected in the Y-Z plane with Y_0 close to or equal to the aperture radius. A particle injected with Y_0 initially larger than the limit $\sqrt{\frac{s-1}{s}}\,a$ will encounter large defocusing forces that will deflect it away from the Z-axis so that its transverse displacement will exceed the aperture radius and it will be lost. For values of Y_0 equal to or less than $\sqrt{\frac{s-1}{s}}\,a$, the particle will be deflected away from the axis initially but the subsequent focusing action will be sufficient to turn the particle back towards the axis before it can be lost. As before the alternating focusing and defocusing forces will result in a net focusing action.

Unlike in classical quadrupole structures, the maximum acceptable value of X_0 for parallel injection along the twisted structure is dependent on the initial Y_0 displacement of the particle, as shown from equation

(3.12) and figure (3.1). This dependence is due to the coupling between the X and Y components of the particle motion along the twisted structure.

3.3.2 Point Source

For particles emerging from a point source at the input plane of the structure the initial transverse displacements, X_0 and Y_0, are zero at $Z = 0$ and the injection transverse momenta are given by P_{X_0} and P_{Y_0}. In this case the confinement criterion shows that P_{X_0} and P_{Y_0} are limited to values within the momenta space bounded by the curve

$$\begin{aligned}&\left|\left[s^2 P_{Y_0}{}^2 + s(s+1)P_{X_0}{}^2\right]^{1/2}\right| \\ &+\sqrt{\frac{s}{s-1}}\left|\left[s^2 P_{X_0}{}^2 + s(s-1)P_{Y_0}{}^2\right]^{1/2}\right| = |\beta\, a\, p_z| \qquad (3.13)\end{aligned}$$

where by equation (2.33) $p_z = P_{Z_0}$. Equation (3.13) is plotted (see Appendix D) for several values of s in figure (3.2). The axes have been normalized with respect to P_{Z_0} and the curves are plotted assuming $(\beta a)^2 = 0.1$. It is shown in Appendix D that the maximum allowable transverse momenta in the X and Y directions are:

$$|P_{X_0}|_{\max} = \frac{|\beta a\, P_{Z_0}|}{\sqrt{s}}\;\frac{1}{\sqrt{s+1} + s/\sqrt{s-1}} \text{ when } |P_{Y_0}| = 0 \qquad (3.14)$$

and

$$|P_{Y_0}|_{\max} = \frac{|\beta a\, P_{Z_0}|}{2s} \quad \text{when } |P_{X_0}| = 0 \qquad (3.15)$$

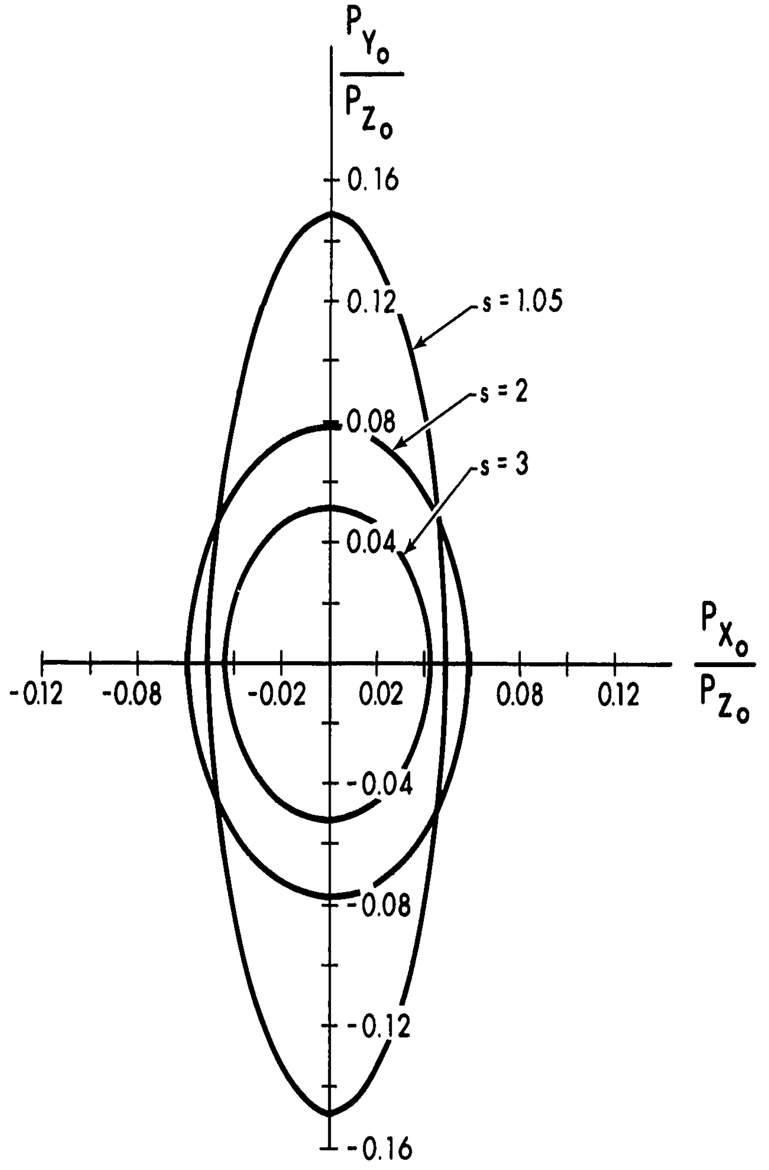

$$(\beta a)^2 = 0.1 \quad \frac{(P_{X_0})\,\mathrm{max}}{P_{Z_0}} = \frac{\beta a}{\sqrt{s}} \quad \frac{1}{\sqrt{s+1}+s/\sqrt{s-1}}$$

$$\frac{(P_{Y_0})\,\mathrm{max}}{P_{Z_0}} = \frac{\beta a}{2s}$$

Figure (3.2) Acceptance in the Normalized $\frac{P_{X_0}}{P_{Z_0}} - \frac{P_{Y_0}}{P_{Z_0}}$ Transverse Momenta Plane for Point Source Injection.

For values of s approaching unity, the value of $|P_{Y_o}|_{max}$ approaches $\frac{|\beta a\, P_{Z_o}|}{2}$ while $|P_{X_o}|_{max}$ approaches zero. As s increases the value of $|P_{Y_o}|_{max}$ decreases until it finally approaches zero as s approaches infinity. On the other hand as s increases the value of $|P_{X_o}|_{max}$ increases until $s = 1.3295$ is reached at which point $|P_{X_o}|_{max}$ reaches a maximum value of $0.226\ |\beta a\, P_{Z_o}|$. For values of s larger than 1.3295, $|P_{X_o}|_{max}$ decreases as s increases until $|P_{X_o}|_{max}$ approaches zero as s approaches infinity.

Similar to classical quadrupole structures the allowable values of $|P_{Y_o}|_{max}$ are always greater than the values of $|P_{X_o}|_{max}$ for all values of s. Comparing the alternating focusing and defocusing forces near the point of injection provides a qualitative explanation of this difference. A particle injected on the axis with Y-directed transverse momentum initially experiences a small defocusing force and is accelerated radially away from the Z-axis. By the time the forces on the particle change from defocusing to focusing, the particle will have been displaced a considerable distance from the Z-axis. Here, the focusing forces acting on the particle will be stronger than the defocusing forces previously encountered. Thus the net force in this initial region of the structure will be focusing. On the other hand, a particle injected with X-directed transverse momentum first experiences a small focusing force followed by a larger defocusing force as it moves away from the Z-axis. In this case the net force in the region near the point of injection is defocusing. In other words, a particle injected on the axis with X-directed momentum is initially defocused while a particle injected with Y-directed momentum is initially focused. Thus, it is to be expected that the allowable values of P_{Y_o} are larger than the allowable values of P_{X_o}.

A comparison of the allowable transverse momenta for point source injection in the case of the twisted and the classical quadrupole structures will be presented in Chapter 6.

Considering the cases of parallel injection and point source injection for the twisted structure, it is found that large values of s are desirable for parallel injection while they result in a reduction of the momentum acceptance for point source injection. A compromise value of s = 2 seems appropriate for both cases.

3.3.3 Injection on the X-Axis with X-Directed Momentum

A particle injected on the X-axis with X-directed transverse momentum has $Y_0 = P_{Y_0} = 0$. For such a particle $p_z = P_{Z_0}$, $|S| = (\beta a)^2 |\frac{V}{V_0}|$, and equation (3.10) gives the confinement criterion for this case as,

$$\left|\left[X_0^2 + \frac{s(s+1)}{\beta^2}\left(\frac{P_{X_0}}{P_{Z_0}}\right)^2\right]^{1/2}\right| + s\sqrt{\frac{s}{s-1}}\left|\frac{P_{X_0}}{\beta P_{Z_0}}\right| \le a$$

or

$$X_0^2 + s(s+1)\left(\frac{P_{X_0}}{\beta P_{Z_0}}\right)^2 \le a^2 - 2as\sqrt{\frac{s}{s-1}}\left|\frac{P_{X_0}}{\beta P_{Z_0}}\right| + \frac{s^3}{s-1}\left(\frac{P_{X_0}}{\beta P_{Z_0}}\right)^2$$

or

$$X_0^2 - \left[\frac{s}{s-1}\right]\left[\left(\frac{P_{X_0}}{\beta P_{Z_0}}\right)^2 - 2a\sqrt{s(s-1)}\left|\frac{P_{X_0}}{\beta P_{Z_0}}\right| + a^2 s(s-1)\right] \le a^2(1-s^2)$$

Taking into consideration that $|s| > 1.0$, the confinement criterion finally

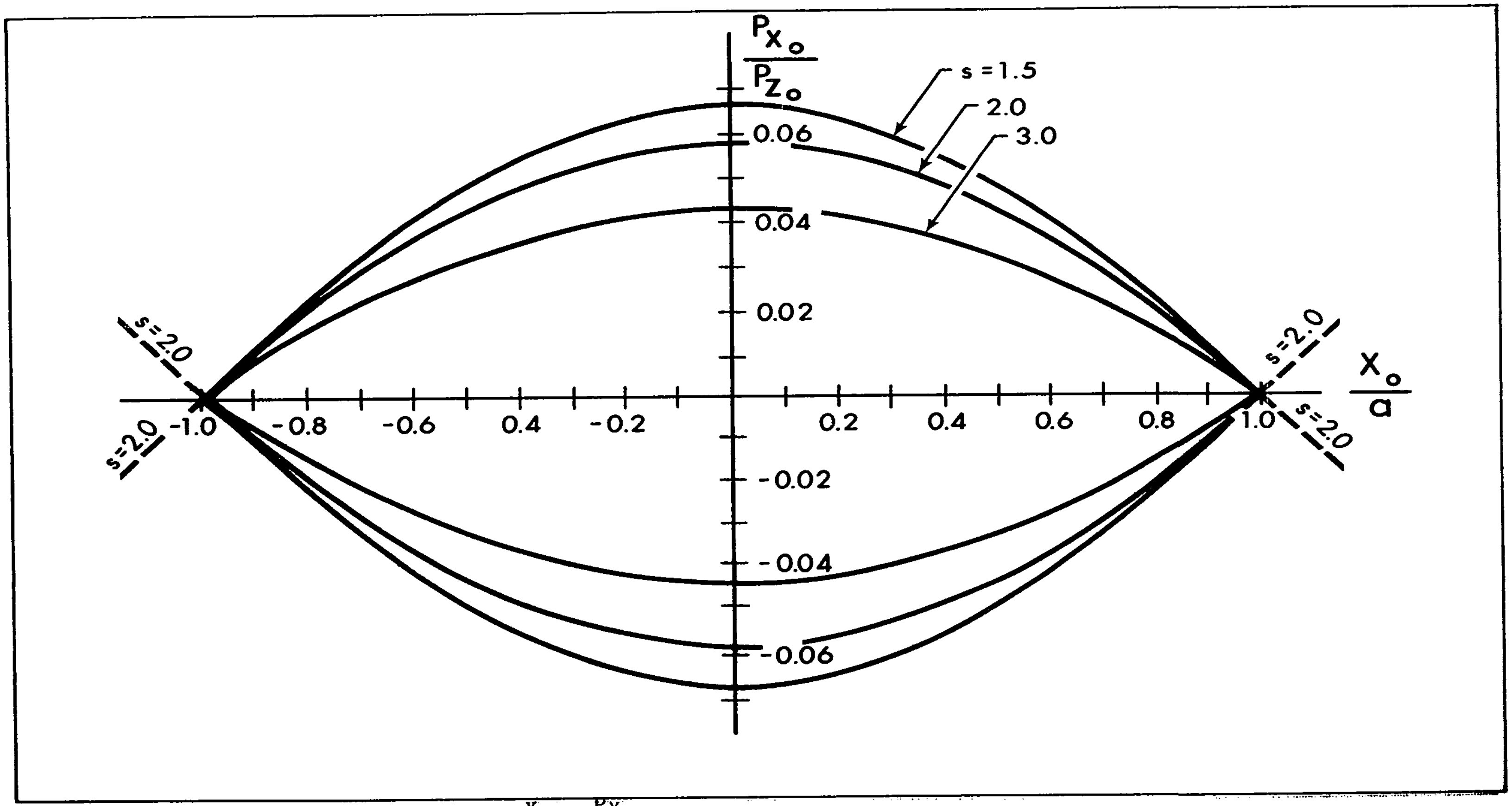

Figure (3.3) Acceptance in the $\frac{X_o}{a}$ - $\frac{P_{X_o}}{P_{Z_o}}$ Phase Plane for Injection on the X-Axis with X-Directed Transverse Momentum.

becomes:

$$\frac{\left\{\left|\frac{P_{X_0}}{\beta P_{Z_0}}\right| - a\sqrt{s^2 - s}\right\}^2}{\left\{a(s - 1)\sqrt{\frac{s + 1}{s}}\right\}^2} - \frac{X_0^{\,2}}{\left\{a\sqrt{s^2 - 1}\right\}^2} \le 1.0 \qquad (3.16)$$

Hence, for such a particle to be successfully guided by the structure, X_0 and $\frac{P_{X_0}}{P_{Z_0}}$ should be represented by a point within the area of intersection of the two hyperbolae represented by equation (3.16), as shown in figure (3.3). The axes in figure (3.3) have been normalized, X_0 with respect to a and P_{X_0} with respect to P_{Z_0}. Three cases were plotted in figure (3.3) for values of s = 1.5, 2.0 and 3.0. For all values of s the intersections of the hyperbolae occur on the $(\frac{X_0}{a})$ axis at $\frac{X_0}{a} = \pm 1.0$. This result is in agreement with the results obtained for the special case of parallel injection since figure (3.3) clearly shows that for $\frac{P_{X_0}}{P_{Z_0}} = 0$, together with $Y_0 = P_{Y_0} = 0$, the maximum allowable $|X_0|$ is equal to a. Figure (3.3) also shows that as s increases, the allowable transverse momentum decreases. Note that all values of s considered are larger than s = 1.3295 at which $|P_{X_0}|_{max}$ reaches its maximum value. The values shown in figure (3.3) for $\left|\frac{P_{X_0}}{P_{Z_0}}\right|_{max}$, at $X_0 = 0$, are the same as those predicted by equation (3.14) for the values of s considered.

3.3.4 Injection on the Y-Axis with Y-Directed Momentum

A particle injected right on the Y-axis with Y-directed transverse momentum has $X_0 = 0$ and $P_{X_0} = 0$. As was the case for the other special cases, $p_Z = P_{Z_0}$ and $s = (\beta a)^2 \left|\frac{V}{V_0}\right|$. The confinement criterion for this special case of injection, obtained by substituting in equation (3.10), is

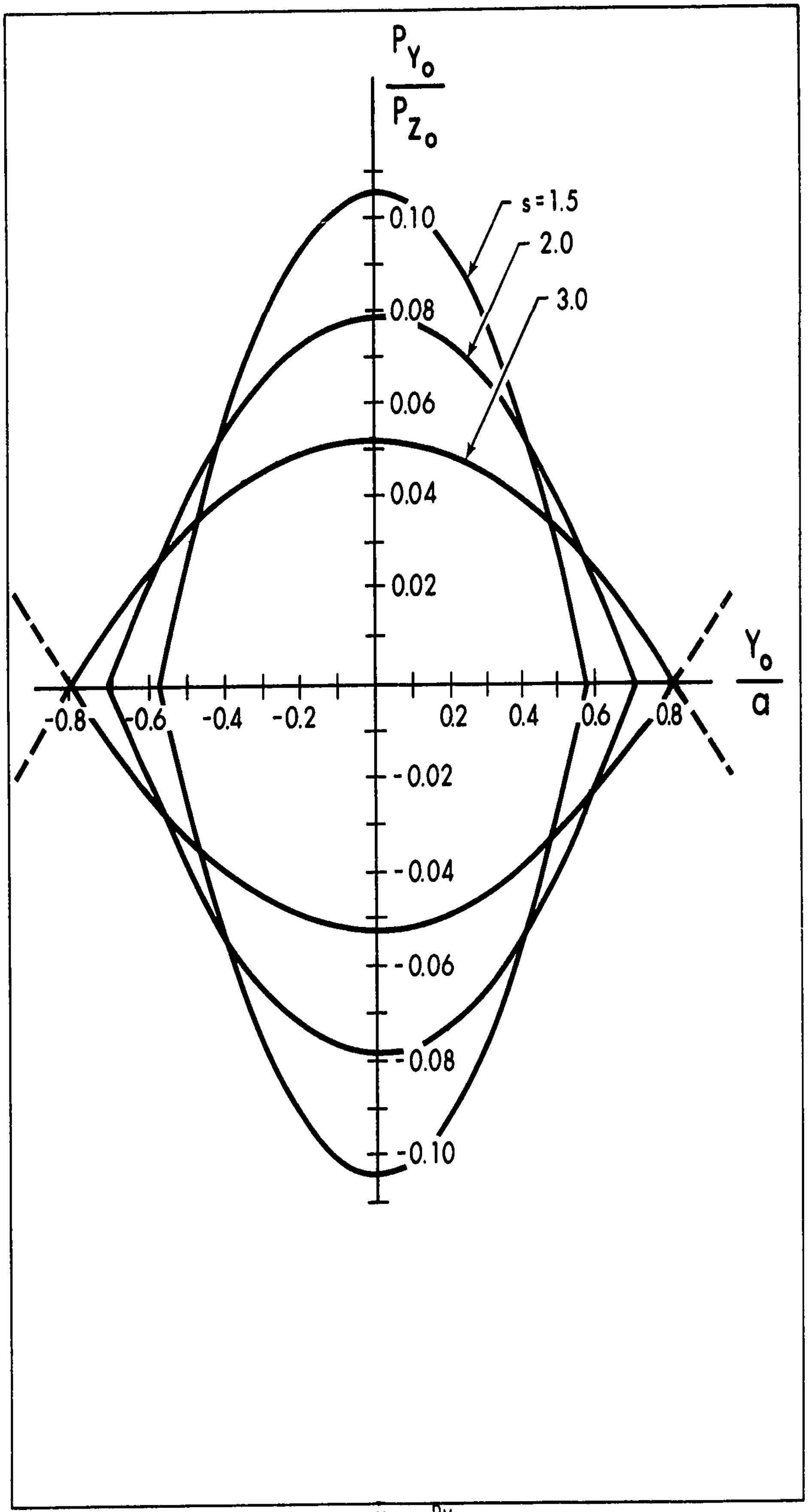

Figure (3.4) Acceptance in the $\frac{Y_o}{a}$ - $\frac{P_{Y_o}}{P_{Z_o}}$ Phase Plane for Injection on the Y-Axis with Y-Directed Transverse Momentum.

$$\left|\frac{s}{\beta}\frac{P_{Y_0}}{P_{Z_0}}\right| + \sqrt{\frac{s}{s-1}}\left|\left[Y_0^{\,2} + \frac{s(s-1)}{\beta^2}\left(\frac{P_{Y_0}}{P_{Z_0}}\right)^2\right]^{1/2}\right| \leq a$$

or

$$\frac{s}{s-1}Y_0^{\,2} + s^2\left(\frac{P_{Y_0}}{\beta P_{Z_0}}\right)^2 \leq a^2 - 2as\left|\frac{P_{Y_0}}{\beta P_{Z_0}}\right| + s^2\left(\frac{P_{Y_0}}{\beta P_{Z_0}}\right)^2$$

or

$$\frac{s}{s-1}\left(\frac{Y_0}{a}\right)^2 + 2\,\frac{s}{a}\left|\frac{P_{Y_0}}{\beta P_{Z_0}}\right| \leq 1 \qquad (3.17)$$

This equation shows that such a particle is successfully guided by the structure if Y_0 and $(\frac{P_{Y_0}}{P_{Z_0}})$ are represented by a point within the area of the intersection of the two parabolas represented by equation (3.17). Several such parabolas are plotted in figure (3.4). The axes in figure (3.4) have been normalized, Y_0 with respect to a and P_{Y_0} with respect to P_{Z_0}. Three cases were plotted in figure (3.4) for values of s = 1.5, 2.0 and 3.0. For the three values of s the intersection of the parabolas occurs on the $\frac{Y_0}{a}$ axis, but the point of intersection depends on the value of s. As expected from the special case of parallel injection, the maximum allowable values of Y_0 when $P_{Y_0} = 0$ are equal to $a\sqrt{\frac{s-1}{s}}$ and decrease as s decreases. Also as expected from the special case of point source injection, the acceptable values of P_{Y_0} for a particle injected at a point Y_0 with $X_0 = P_{X_0} = 0$ decrease as s increases.

3.3.5 Point Source at a Distance d From Input Plane

Consider a point source a distance d from the input plane of the twisted structure. A particle emerging from this source will have its transverse coordinates at the input plane, Z = 0, related to its momenta by

$$X_0 = \frac{P_{X_0}}{P_{Z_0}}.d \quad ,$$
$$Y_0 = \frac{P_{Y_0}}{P_{Z_0}}.d \quad . \qquad (3.18)$$

Thus $(X_0 P_{Y_0} - Y_0 P_{X_0}) = 0$ and $p_Z = P_{Z_0}$ for such particles. Substituting equations (3.18) into equation (3.10) gives the confinement criterion for this special case as

$$\left|\left\{\left[\frac{d}{a}\frac{P_{X_0}}{P_{Z_0}} - \frac{s}{\beta a}\frac{P_{Y_0}}{P_{Z_0}}\right]^2 + \frac{s(s+1)}{\beta^2 a^2}\frac{P_{X_0}^{\ 2}}{P_{Z_0}^{\ 2}}\right\}^{1/2}\right|$$
$$+\sqrt{\frac{s}{s-1}}\left|\left\{\left[\frac{d}{a}\frac{P_{Y_0}}{P_{Z_0}} - \frac{s}{\beta a}\frac{P_{X_0}}{P_{Z_0}}\right]^2 + \frac{s(s-1)}{\beta^2 a^2}\frac{P_{Y_0}^{\ 2}}{P_{Z_0}^{\ 2}}\right\}^{1/2}\right| \le 1.0 \qquad (3.19)$$

Equation (3.19) gives the values of the allowable divergence that a beam, emitted from the point source distant d from the input plane, can have so that all particles will be guided. The acceptance area in the transverse momentum $\frac{P_{X_0}}{P_{Z_0}} - \frac{P_{Y_0}}{P_{Z_0}}$ phase plane is bounded by an ellipsoidal curve which is tilted because of the cross terms $P_{X_0} P_{Y_0}$, $P_{X_0}^{\ 2} P_{Y_0}$, $P_{X_0} P_{y_0}^{\ 2}$ and $P_{X_0}^{\ 2} P_{Y_0}^{\ 2}$ that will appear in the expression of equation (3.19) if both sides of the inequality are squared. The degree of tilt of the acceptance curve is dependent on the value of $\frac{d}{a}$ considered as well as the structure parameters.

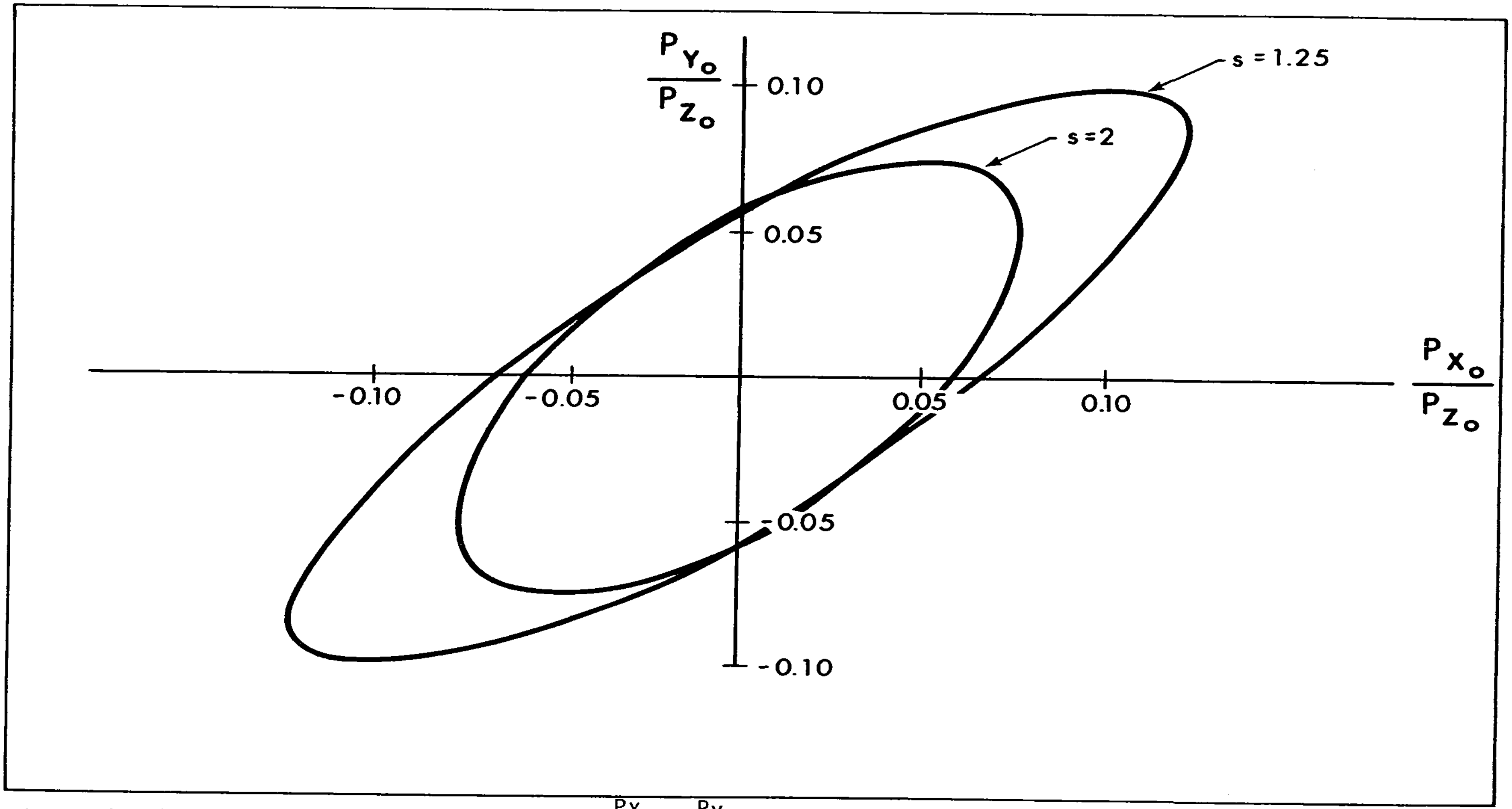

Figure (3.5) Acceptance in the Normalized ($\frac{P_{X_o}}{P_{Z_o}}$ - $\frac{P_{Y_o}}{P_{Z_o}}$) Transverse Momentum Plane for Injection from a Point Source at a Distance d from the Injection Plane.

For $\frac{d}{a} = 0.0$, equation (3.19) will reduce to equation (3.13) obtained for point source injection at the injection plane, $Z = 0.0$, and in this case the acceptance curve will not be tilted.

Figure (3.5) shows the acceptance limits in the transverse normalized momentum phase plane. The axes are normalized with respect to P_{Z_0}. The acceptance curves are for $s = 1.25$ and $s = 2.0$ for a counterclockwise twisted structure, β positive, having $(\beta a)^2 = 0.1$. The point source is at a distance $d = 5a$ from the injection plane.

CHAPTER 4

AN EVALUATION OF THE ANALYTIC SOLUTION

4.1 Introduction

The analytic solution developed in Chapter 2 is based on the assumptions that $(\beta a)^2 << 1$ and $(\frac{p_x}{p_z})^2$, $(\frac{p_y}{p_z})^2 << 1$. It was shown in Chapter 3 that these assumptions are justified for any particle whose maximum radial displacement from the structure axis is less than the aperture radius. Therefore, the approximate analytic solution is not restricted to small displacements from the Z axis. Further, it was proved in Chapter 3 that a particle will be successfully guided if its transverse coordinates and its momenta at injection satisfy the acceptance or confinement criterion given by equation (3.10). The first objective of this chapter is to establish the accuracy of the approximate analytic solution and in particular to test the validity of equation (3.10) in predicting the acceptance limits of the twisted structure. This objective is achieved through comparison of the trajectories computed using the analytic solution with the actual trajectories of the particles. The latter trajectories are computed through numerical integration of equations (2.6) which are the original equations of motion. These equations of motion as well as the approximate analytic solution are based on the approximate expression of the potential distribution given by equations

(2.1a) and (2.1b). The second objective of this chapter is to present a mode theory that is based on the general examination of the nature of the trajectories and which describes the projections of the particle trajectories on the fixed X-Z and Y-Z planes in terms of four spatial modes. This mode theory explains the apparent amplitude modulation in some of the particle trajectories as well as the presence of small ripple components superimposed on longer wavelength fundamental components. Using the expressions provided by this mode theory,for X and Y parametric in Z, it is possible to compute and plot average approximate particle trajectories instead of using the long expressions of equations (2.31) and (2.35).

A number of trajectories were computed and plotted using the analytic expressions of equations (2.31) and (2.35). The trajectories were plotted for a large number of injection coordinates and momenta satisfying equation (3.10). These trajectories will be referred to as the analytic trajectories. The first program listing in Appendix E shows the steps of computing these analytic trajectories. A second set of trajectories was then computed through the numerical integration of equations (2.6), the original non-linear coupled equations of motion, using the Runge-Kutta method of numerical integration(36). These trajectories were plotted for the same injection conditions considered for the analytic trajectories. The steps of the computations of these trajectories also are shown in the first program listing of Appendix E. They will be referred to as the Runge-Kutta trajectories and will be taken to represent the actual trajectories.

The numerical solution provided by the Runge-Kutta method is a step-by-step solution. The accuracy of such a step-by-step solution of differential equations is often difficult to determine(36). The Runge-Kutta method has no error checking equations. However, the truncation error is near the order of h^5 where h is the time interval used for computing X, Y, Z. Improvement on the accuracy may be achieved by using smaller time intervals. However, a decrease of the interval size, h, adds to the amount of computing time and increases the possible round-off-error. For choosing a suitable value of h so that both the truncation error and the round-off-error will be negligible, a set of Runge-Kutta trajectories were computed and their projections on the X-Z and the Y-Z planes were plotted using different values of h for the same particle. The value of h was varied from $\frac{L}{1000\, U_{Z_0}}$ up to $\frac{L}{50\, U_{Z_0}}$, where L is the periodic length of the twisted structure and U_{Z_0} is the initial axial velocity of the particle at injection. The computations were performed for a structure whose length is 24 meters, that is 800 L approximately. It was found that there is excellent agreement between the trajectories, computed and plotted for this long structure, corresponding to values of h from $\frac{L}{500\, U_{Z_0}}$ up to $\frac{L}{125\, U_{Z_0}}$. The consistency of the trajectories for this wide range of variation of h indicates that the value of h should be chosen between $\frac{L}{500\, U_{Z_0}}$ and $\frac{L}{125\, U_{Z_0}}$. It was decided to use a time interval h equal to $\frac{L}{250\, U_{Z_0}}$ in the computations of the Runge-Kutta trajectories. The same value of h is used in computing points of the analytic trajectories.

For the purpose of assessing the accuracy of the approximate analytic solution the analytic and Runge-Kutta trajectories are compared for a structure having an aperture radius, a = 1.5 cm and a periodic length L = 29.68 cm which corresponds to $(\beta a)^2 = (\frac{2\pi a}{L})^2 = 0.1$, hence satisfying equation (2.2). As shown in Chapter 3, a stability factor $s = 2.0$ will allow good use of the aperture for parallel injection and it also yields a relatively symmetric transverse momenta acceptance region for point source injection. It was also shown that for both parallel and point source injection $s = (\beta a)^2|\frac{V}{V_0}|$. Therefore, s can be set equal to 2.0, for parallel and point source injection, by setting the quadrupole voltage, V_0, equal to 1.5 KV for particles preaccelerated from rest through a potential V = 30 KV. It is evident that for particles with general injection conditions the value of s must be calculated for each particle using

$$s = (\beta a)^2|\frac{V}{V_0}|[1 + (\beta a)\{\frac{X_o}{a}\frac{P_{Y_o}}{P_{Z_o}} - \frac{Y_o}{a}\frac{P_{X_o}}{P_{Z_o}}\}]^2 \tag{4.1}$$

The discussion and the listing of the computer program used to compute and plot the analytic and Runge-Kutta trajectories are given in Appendix E.

Since only electrostatic fields are involved and all the particles are presumed to have been preaccelerated from rest through the same potential prior to injection, the trajectory of a particle along the structure is independent of the particle's charge to mass ratio. For computation of the trajectories the particles were assumed to have a charge to mass ratio equal to 30 coulomb/kilogram, which is typical of particles used in micrometeoroid simulation studies. In order to compute the analytic trajectories the values of the injection conditions X_o, Y_o, P_{X_o}, P_{Y_o} and P_{Z_o} were used to evaluate the constants of motion s, C_1, C_2, α_1, α_2 and p_z using equations (4.1), (2.33) and (2.37). Then by increasing the time t in steps, each equal to h seconds, and using equations (2.31), (2.34) and (2.35), the values of (x, y, p_x, p_y) and the corresponding values of the axial velocity $\dot{Z}$ and the axial distance Z were evaluated for each value of t. The analytic trajectories were then plotted in terms of the fixed (X, Y, Z) coordinates using equations (2.7). On the other hand, the Runge-Kutta trajectories computed using equations (2.6) are already in terms of the fixed, (X, Y, Z) coordinates.

The computations of both sets of trajectories were carried out using an IBM 360 digital computer and the projections of the trajectories on the X-Z plane, the Y-Z plane and the X-Y plane as well as $\dot{Z}$ versus Z were generated directly by the computer using a Calcomp Plotter model 770/663. The various trajectories are presented in figures (4.1) to (4.19).

4.2 Comparison of the Analytic and the Runge-Kutta Trajectories

The trajectories discussed below have been computed and plotted for a large number of injection conditions. Some of these injection conditions were general, that means particles having nonzero values of X_0, Y_0, P_{X_0} and P_{Y_0}. The restof the injection conditions considered were for the special cases of parallel and point source injection at Z = 0.

Figures (4.1) to (4.7) show the X-Z, Y-Z and X-Y projections of the trajectories for cases where the injection conditions are well within the limits set by equation (3.10). Figures (4.1) and (4.2) are for the general injection conditions (X_0 = 0.1 cm, Y_0 = 0.2 cm, $\frac{P_{X_0}}{P_{Z_0}} = 0.02$ and $\frac{P_{Y_0}}{P_{Z_0}} = 0.02$) and ($X_0$ = 0.3 cm, Y_0 = 0.2 cm, $\frac{P_{X_0}}{P_{Z_0}} = 0.01$ and $\frac{P_{Y_0}}{P_{Z_0}} = 0.01$)

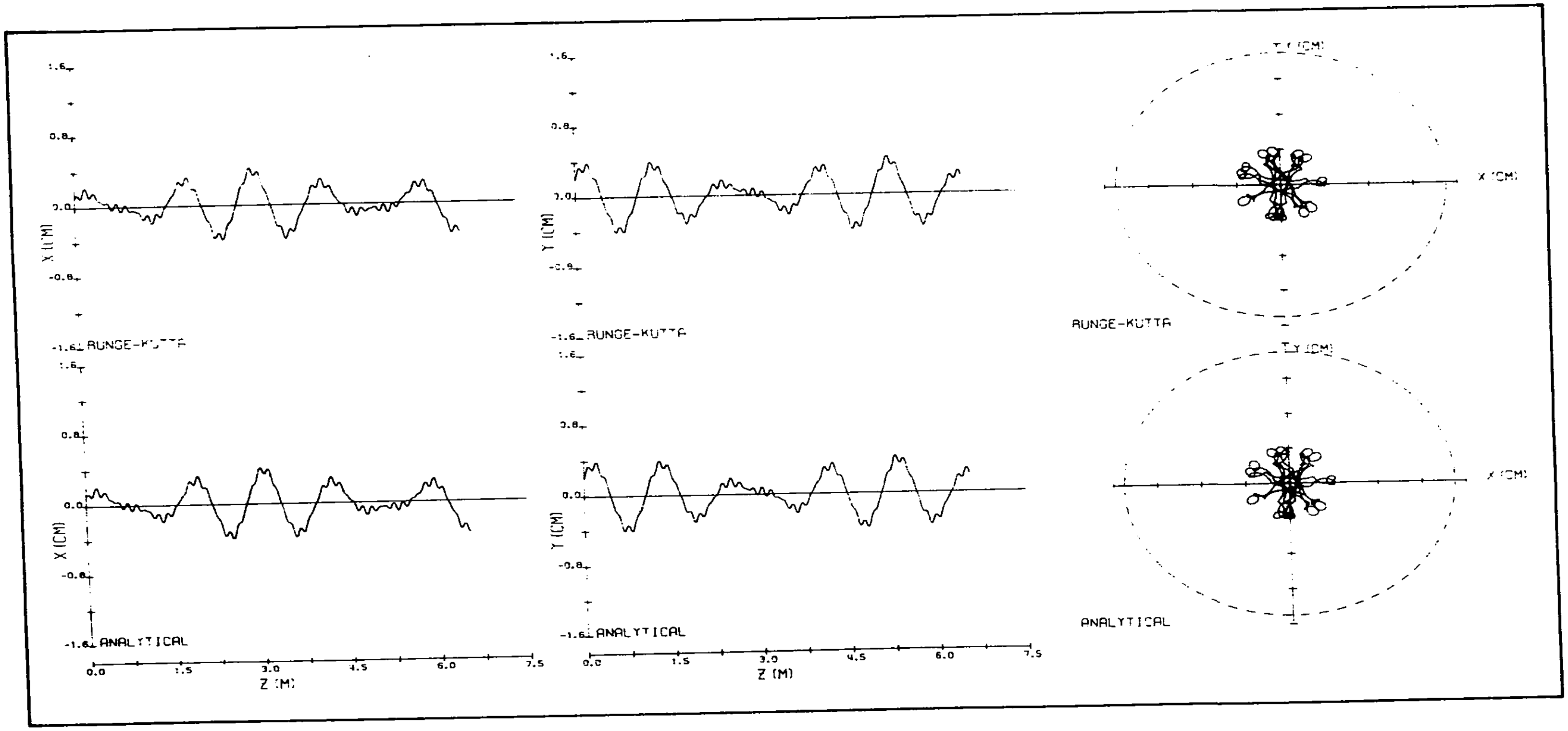

Figure (4.1) The X-Z, Y-Z and X-Y Projections of the Numerical (Runge-Kutta) and Analytical Trajectories, when (X_o = 0.1 cm, Y_o = 0.2 cm, $\frac{P_{X_o}}{P_{Z_o}}$ = 0.02, $\frac{P_{Y_o}}{P_{Z_o}}$ = 0.02).

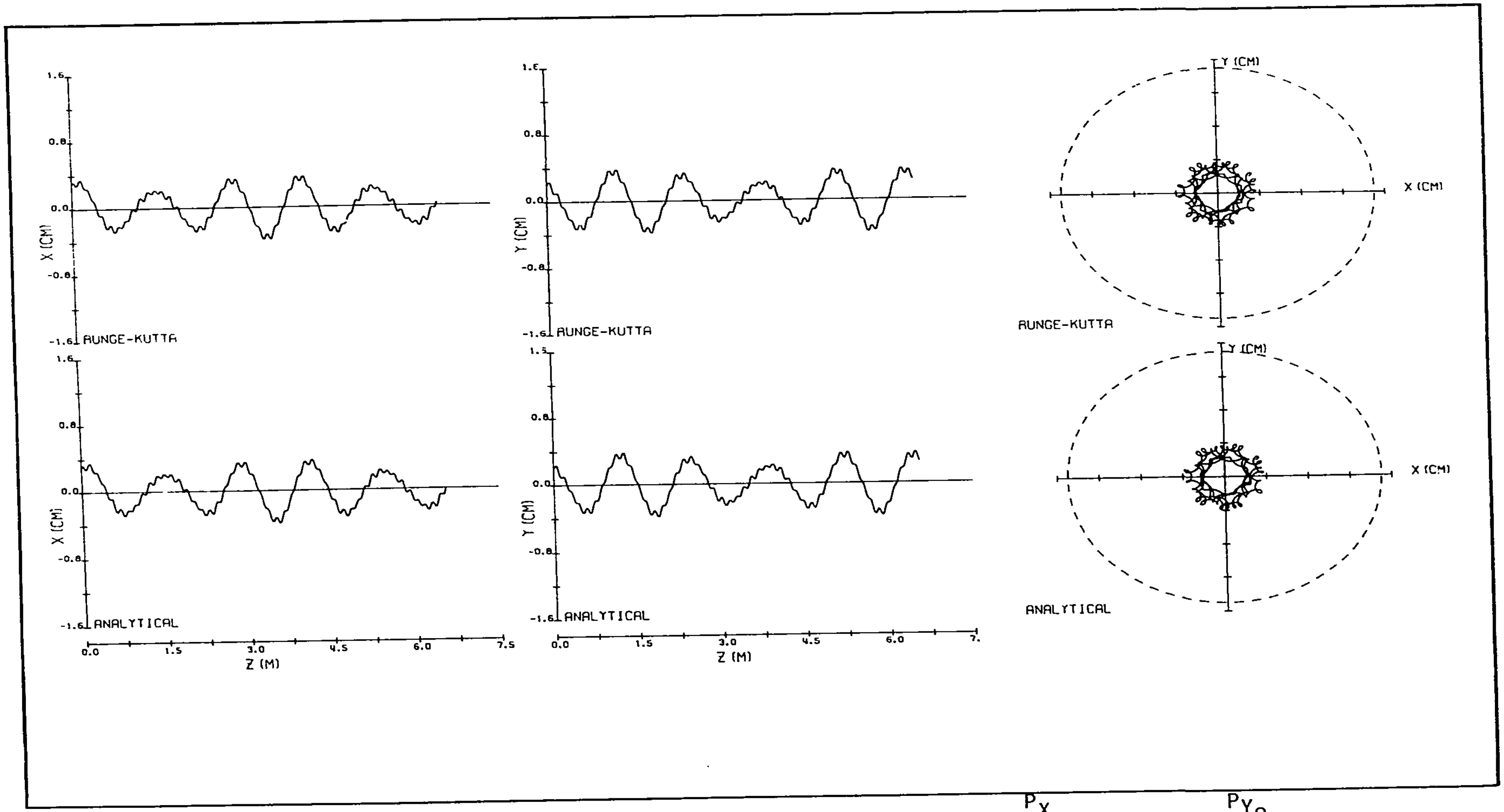

Figure (4.2) As in Figure (4.1) when (X_o = 0.3 cm, Y_o = 0.2 cm, $\frac{P_{X_o}}{P_{Z_o}}$ = 0.01 and $\frac{P_{Y_o}}{P_{Z_o}}$ = 0.01).

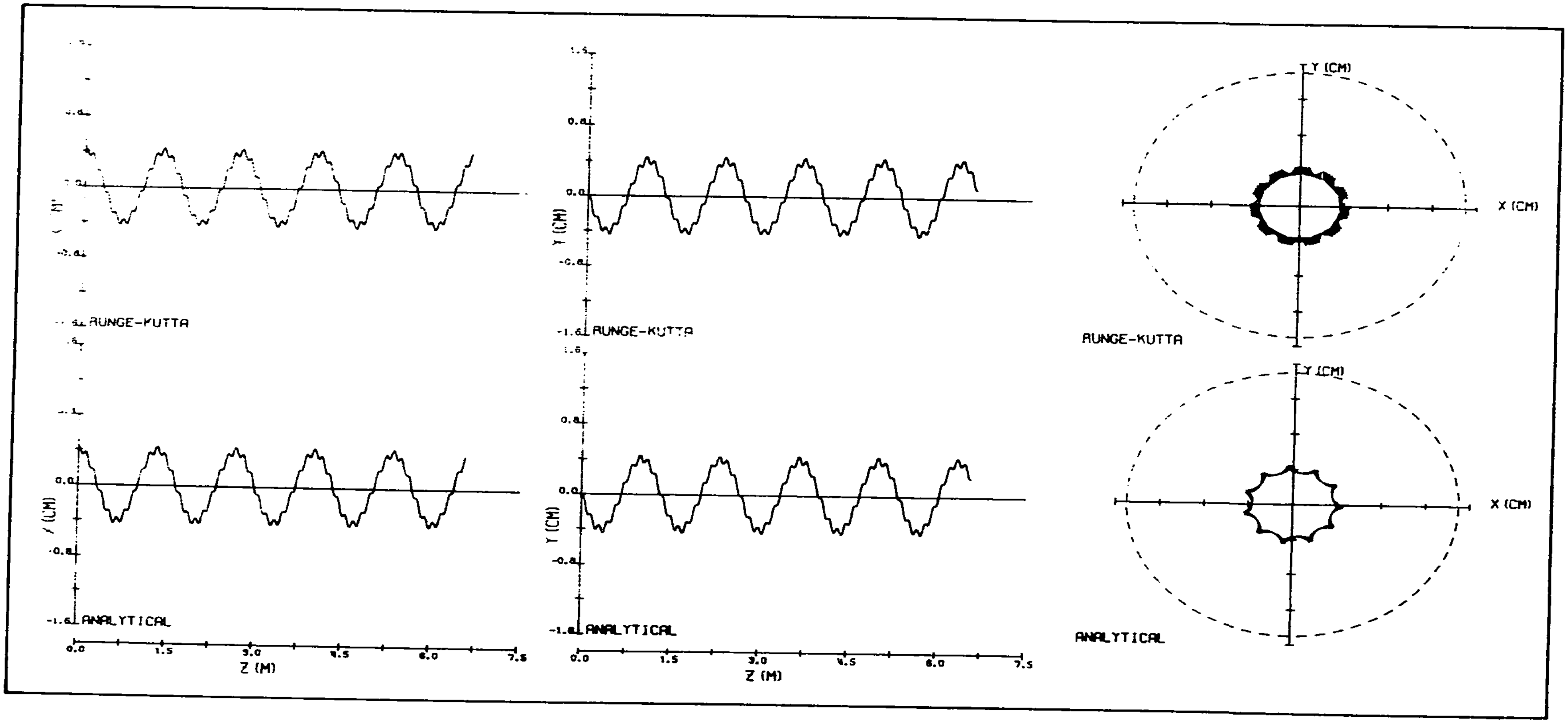

Figure (4.3) As in Figure (4.1) for Parallel Injection when (X_o = 0.45 cm, Y_o = 0).

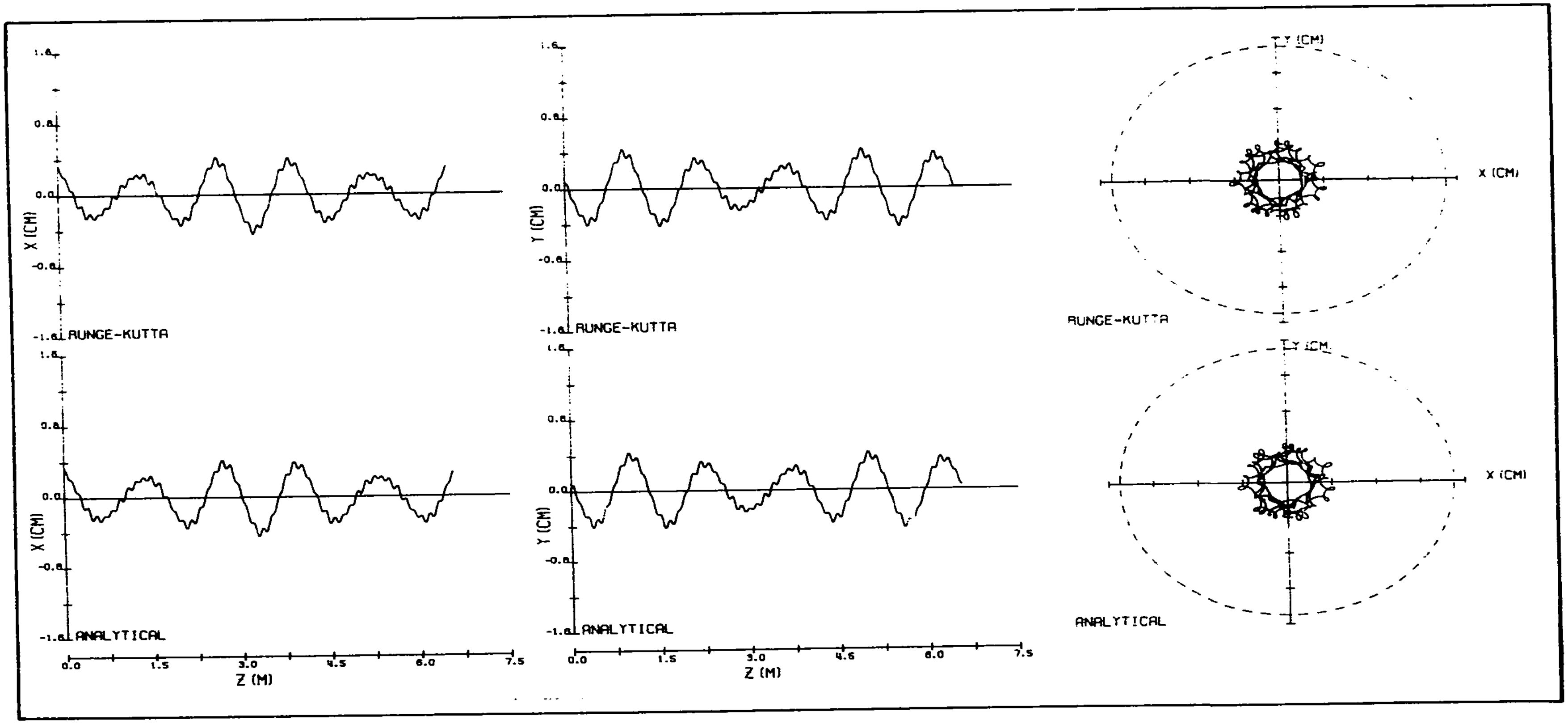

Figure (4.4) As in Figure (4.1) for Parallel Injection when (X_o = 0.337 cm, Y_o = 0.079 cm).

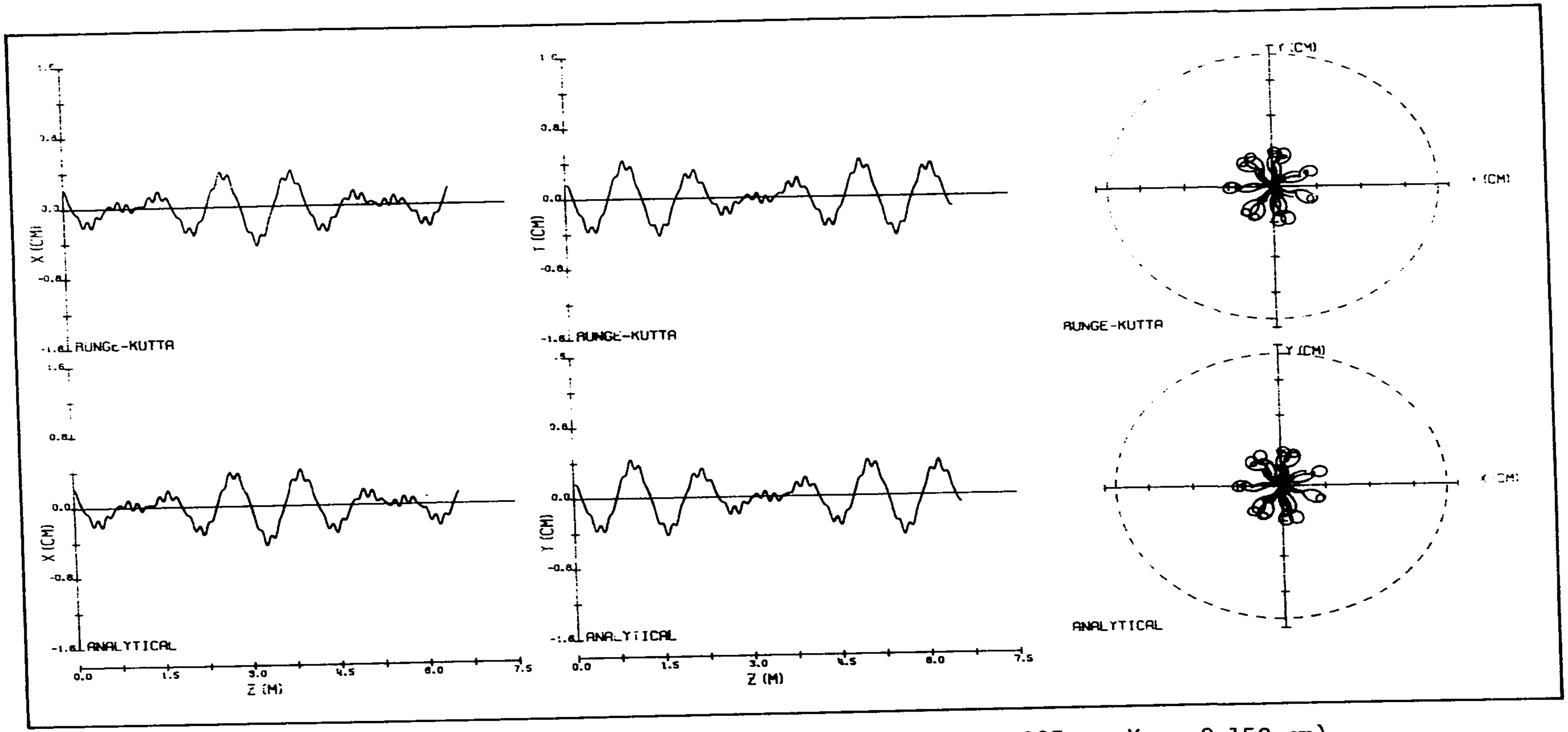

Figure (4.5) As in Figure (4.1) for Parallel Injection when (X_o = 0.225 cm, Y_o = 0.159 cm).

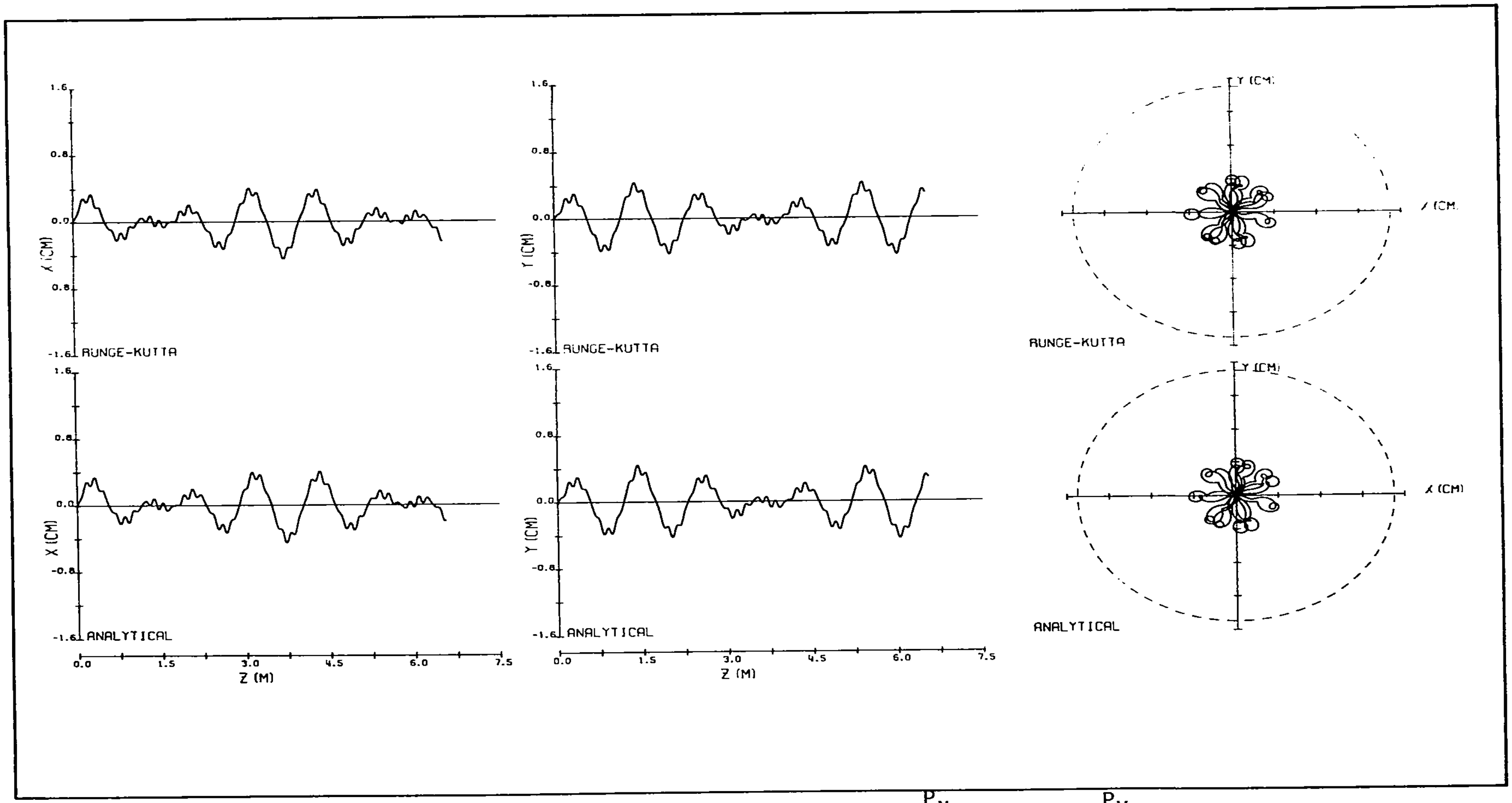

Figure (4.6) As in Figure (4.1) for Point Source Injection when $(\frac{P_{X_o}}{P_{Z_o}} = 0.016, \frac{P_{Y_o}}{P_{Z_o}} = 0.011)$.

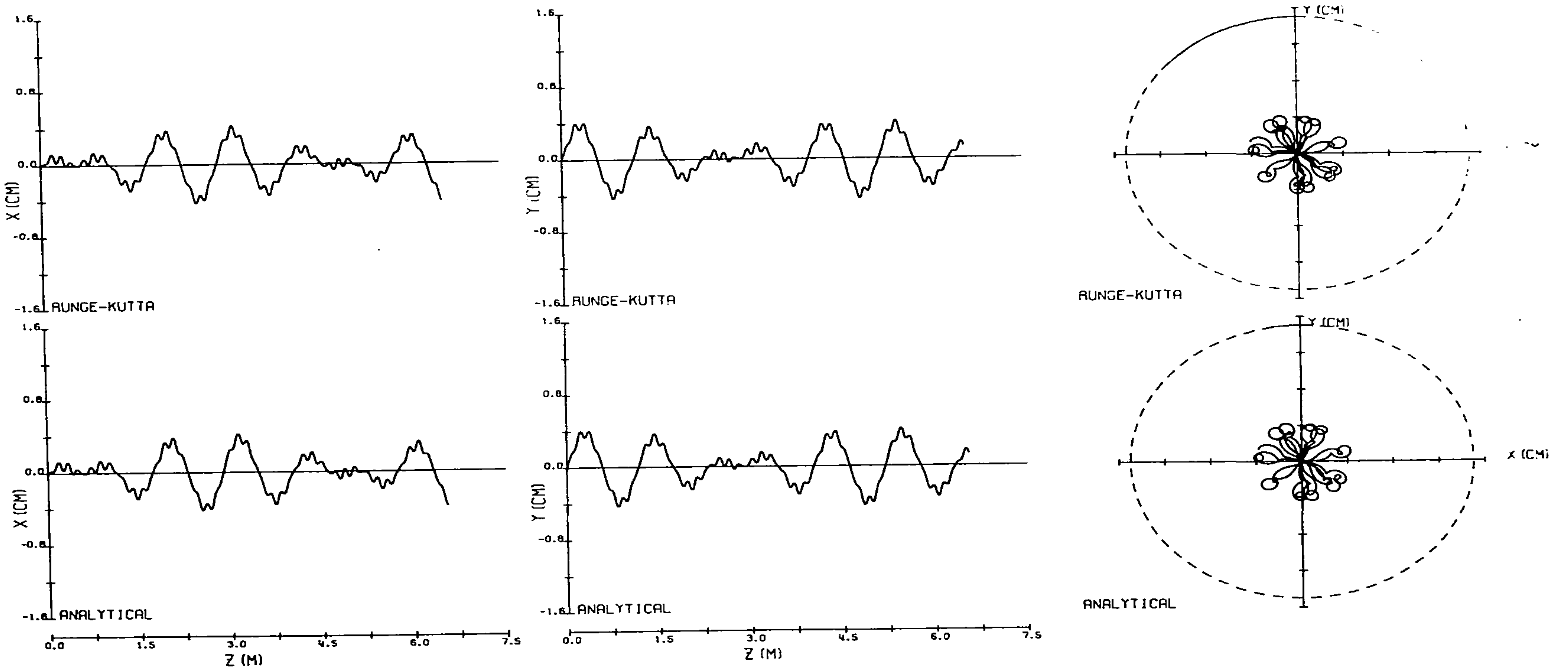

Figure (4.7) As in Figure (4.1) for Point Source Injection when ($\frac{P_{X_o}}{P_{Z_o}} = 0.007$, $\frac{P_{Y_o}}{P_{Z_o}} = 0.022$).

respectively. Figures (4.3), (4.4) and (4.5) are for parallel injection at the points (X_0 = 0.45 cm, Y_0 = 0), (X_0 = 0.337 cm, Y_0 = 0.079 cm) and (X_0 = 0.225 cm, Y_0 = 0.159 cm) respectively. For point source injection figures (4.6) and (4.7) show the trajectories for particles with injection transverse momenta ($\frac{P_{X_0}}{P_{Z_0}}$ = 0.016, $\frac{P_{Y_0}}{P_{Z_0}}$ = 0.011) and ($\frac{P_{X_0}}{P_{Z_0}}$ = 0.007, $\frac{P_{Y_0}}{P_{Z_0}}$ = 0.022) respectively. For each of the particles, there is nearly exact agreement between the analytic and the numerical trajectories. For all seven cases, figures (4.1) to (4.7) show that the X-Z and the Y-Z projections of the trajectories feature a dominant oscillation superimposed upon which there is a small ripple. The amplitudes and positions of the dominant oscillations and the ripples for each of these seven examples are found to be exactly the same in both the analytical and the Runge-Kutta trajectories. Moreover, the (X-Y) projections of the trajectories in figures (4.1) to (4.7) show that the maximum displacement is always less than the quadrupole aperture, a = 1.5 cm.

Figures (4.8) to (4.11) depict trajectories for particles with injection conditions chosen such that, as expected from studying equation (3.10), their maximum radial displacements are equal to or greater than half the aperture radius. Figures (4.8) and (4.9) are for parallel injection at (X_0 = 0.675 cm, Y_0 = 0.159 cm) and (X_0 = 0 , Y_0 = 0.53 cm) respectively. Figures (4.10) and (4.11) are for point source injection with transverse momenta ($\frac{P_{X_0}}{P_{Z_0}}$ = 0.017, $\frac{P_{Y_0}}{P_{Z_0}}$ = 0.051) and($\frac{P_{X_0}}{P_{Z_0}}$ = 0.047, $\frac{P_{Y_0}}{P_{Z_0}}$ = 0.012) respectively. All four cases show substantial agreement between the approximate analytic and the Runge-Kutta trajectories. The agreement is nearly exact up to a length equal to approximately 6L, or

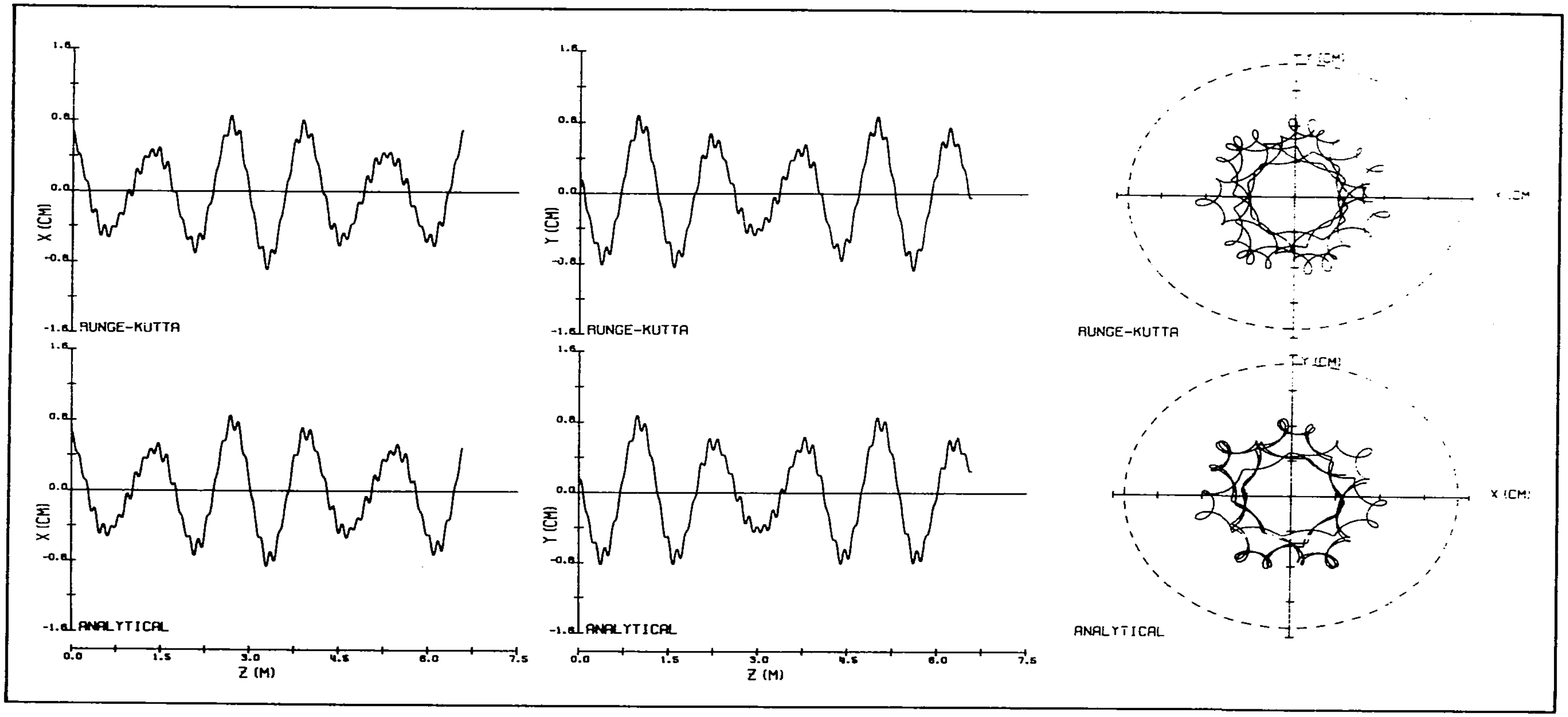

Figure (4.8) As in Figure (4.1) for Parallel Injection when (X_o = 0.675 cm, Y_o = 0.159 cm).

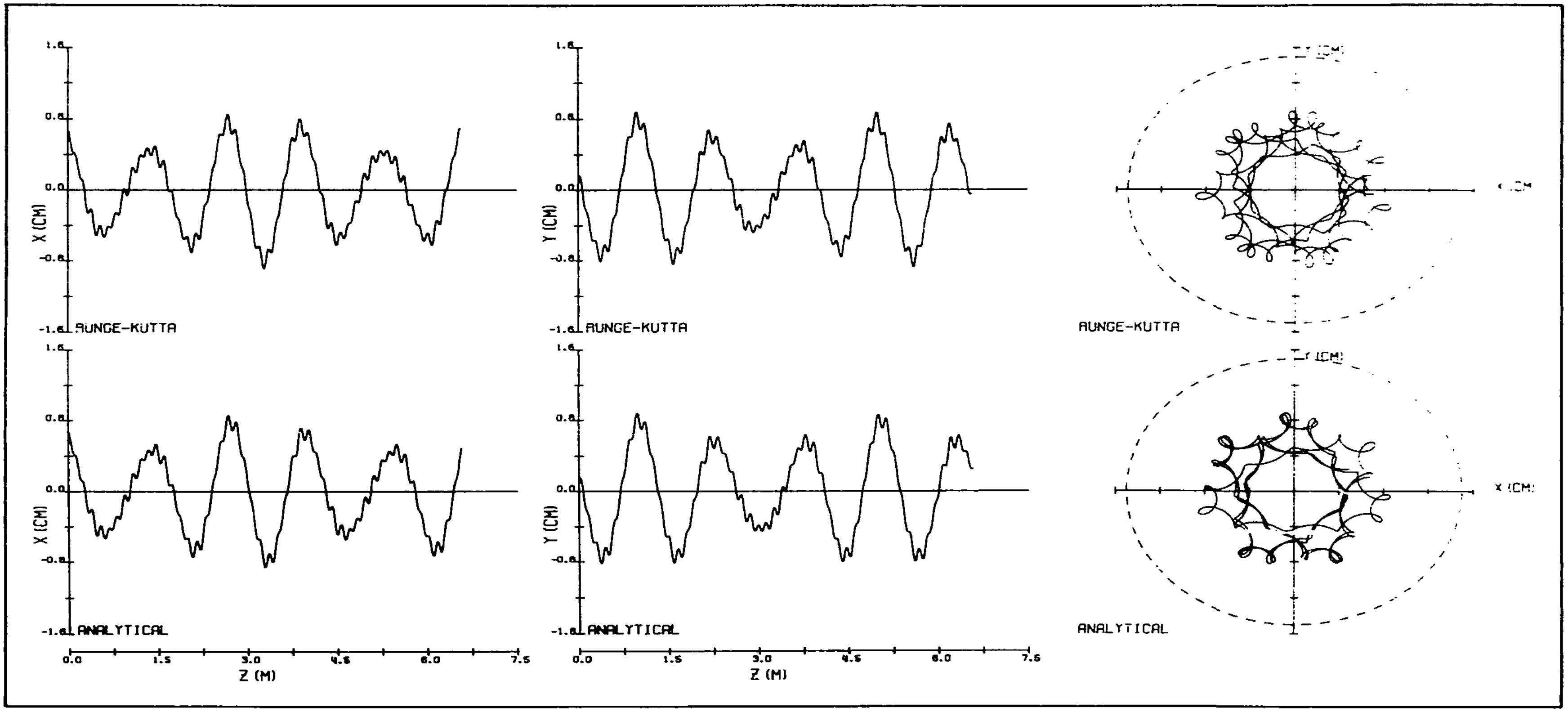

Figure (4.8) As in Figure (4.1) for Parallel Injection when (X_o = 0.675 cm, Y_o = 0.159 cm).

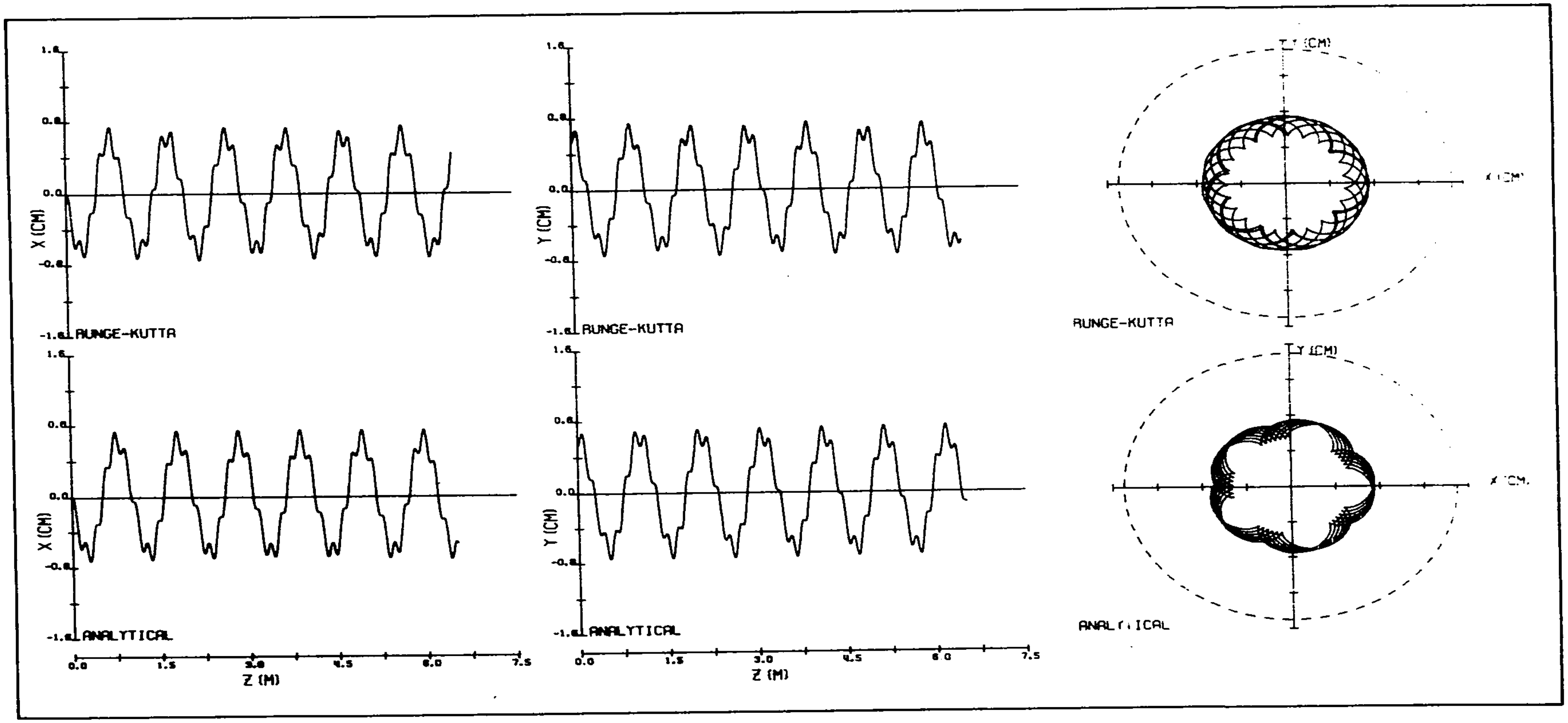

Figure (4.9) As in Figure (4.1) for Parallel Injection when ($X_o = 0$, $Y_o = 0.53$ cm).

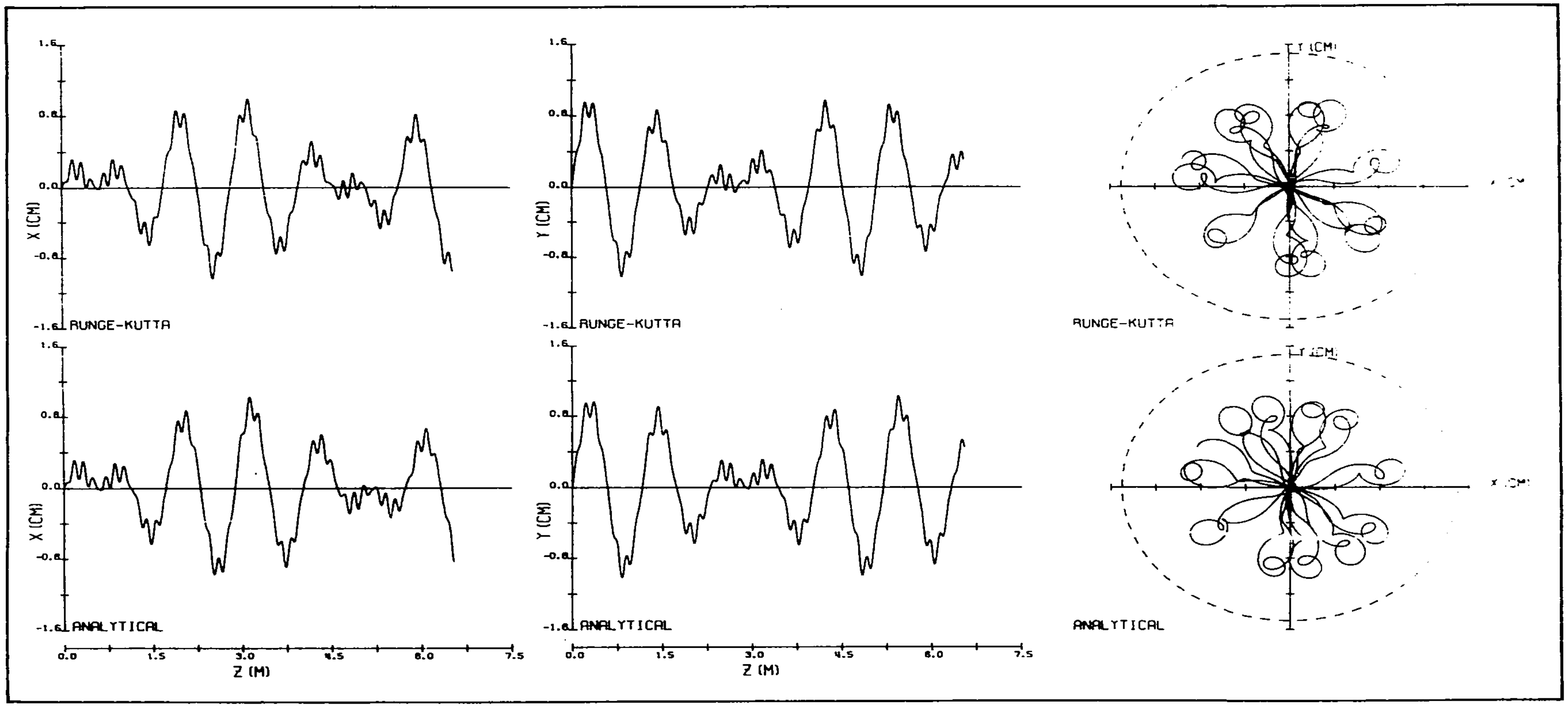

Figure (4.10) As in Figure (4.1) for Point Source Injection when ($\frac{P_{X_o}}{P_{Z_o}} = 0.017$, $\frac{P_{Y_o}}{P_{Z_o}} = 0.051$).

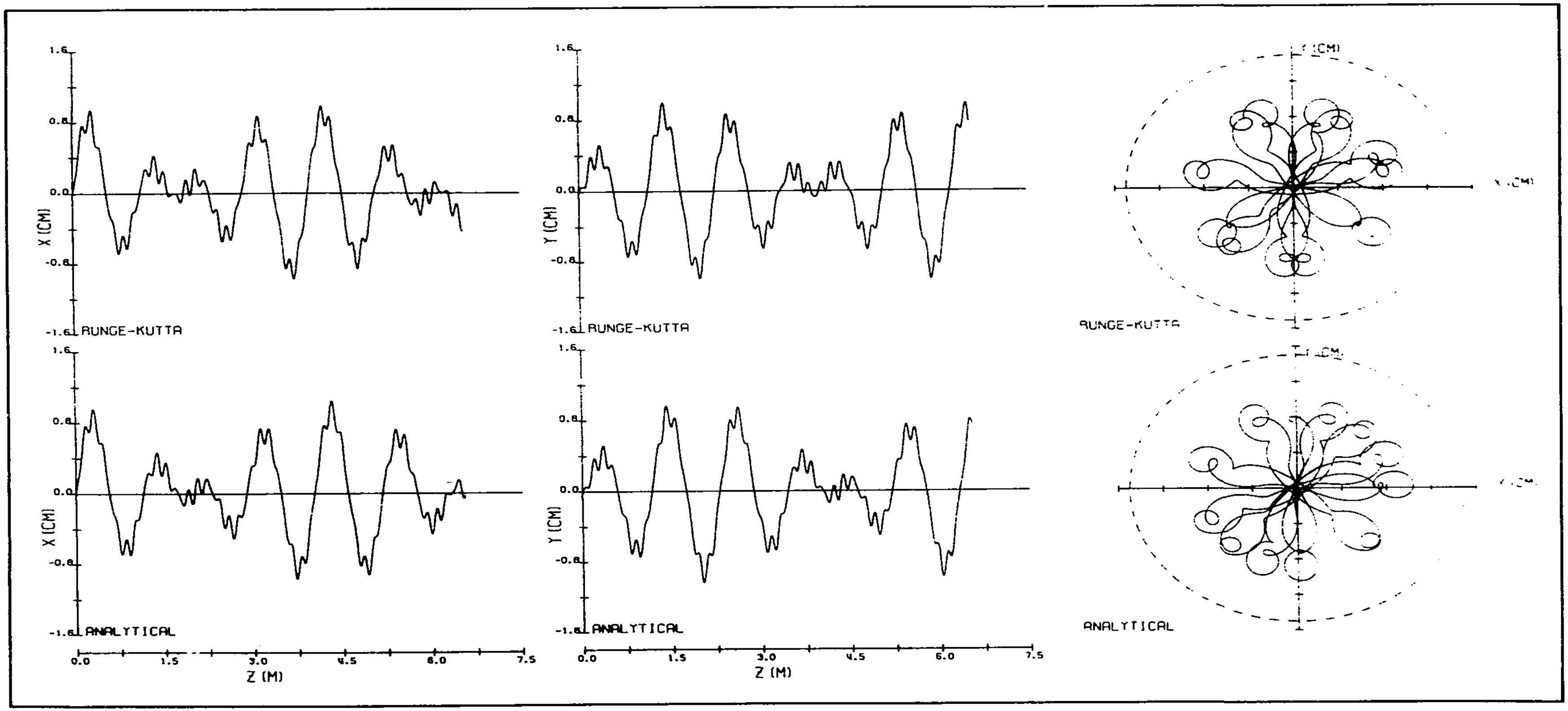

Figure (4.11) As in Figure (4.1) for Point Source Injection when $(\frac{P_{X_o}}{P_{Z_o}} = 0.047, \frac{P_{Y_o}}{P_{Z_o}} = 0.012)$.

about 1.8 meters. At this point a difference appears between the analytical and the Runge-Kutta trajectories in the form of an apparent phase shift between the trajectories. This small apparent phase shift arises because the numerical trajectories cross the Z axis before the corresponding analytic trajectories. A study of the previous four cases shows that the phase shift increases as the injection conditions approach the limiting values. This is especially evident in the positions of the ripple components. Note that the X-Y projections of the analytic and the Runge-Kutta trajectories, shown in figures (4.8) to (4.11) show that, as predicted by equation (3.10), the maximum radial displacements of the particles are less than the apterture radius.

Figures (4.12) and (4.17) represent particles for which the injection conditions are exactly equal to the limits set by equation (3.10). Figures (4.12), (4.13), and (4.14) show the trajectory projections for parallel injection at the limiting acceptance points ($X_0 = a = 1.5$ cm , $Y_0 = 0.0$), ($X_0 = 1.125$ cm, $Y_0 = 0.265$ cm) and ($X_0 = 0.187$ cm, $Y_0 = 0.928$ cm). Figures (4.15), (4.16) and (4.17) are for point source injection with the limiting transverse momenta ($\frac{P_{X_0}}{P_{Z_0}} = 0.0599$, $\frac{P_{Y_0}}{P_{Z_0}} = 0$), ($\frac{P_{X_0}}{P_{Z_0}} = 0.052$, $\frac{P_{Y_0}}{P_{Z_0}} = 0.038$) and ($\frac{P_{X_0}}{P_{Z_0}} = 0$, $\frac{P_{Y_0}}{P_{Z_0}} = 0.079$). Even in these limiting cases the essential features of the motions are quite accurately predicted by the analytic solution. However, examination of the trajectory projections again shows that the actual (Runge-Kutta) trajectory projections cross the Z axis somewhat before the corresponding analytic trajectory projections. In spite of the differences between the analytic and the actual trajectories for these limiting injection conditions, it should be noted that the X-Y

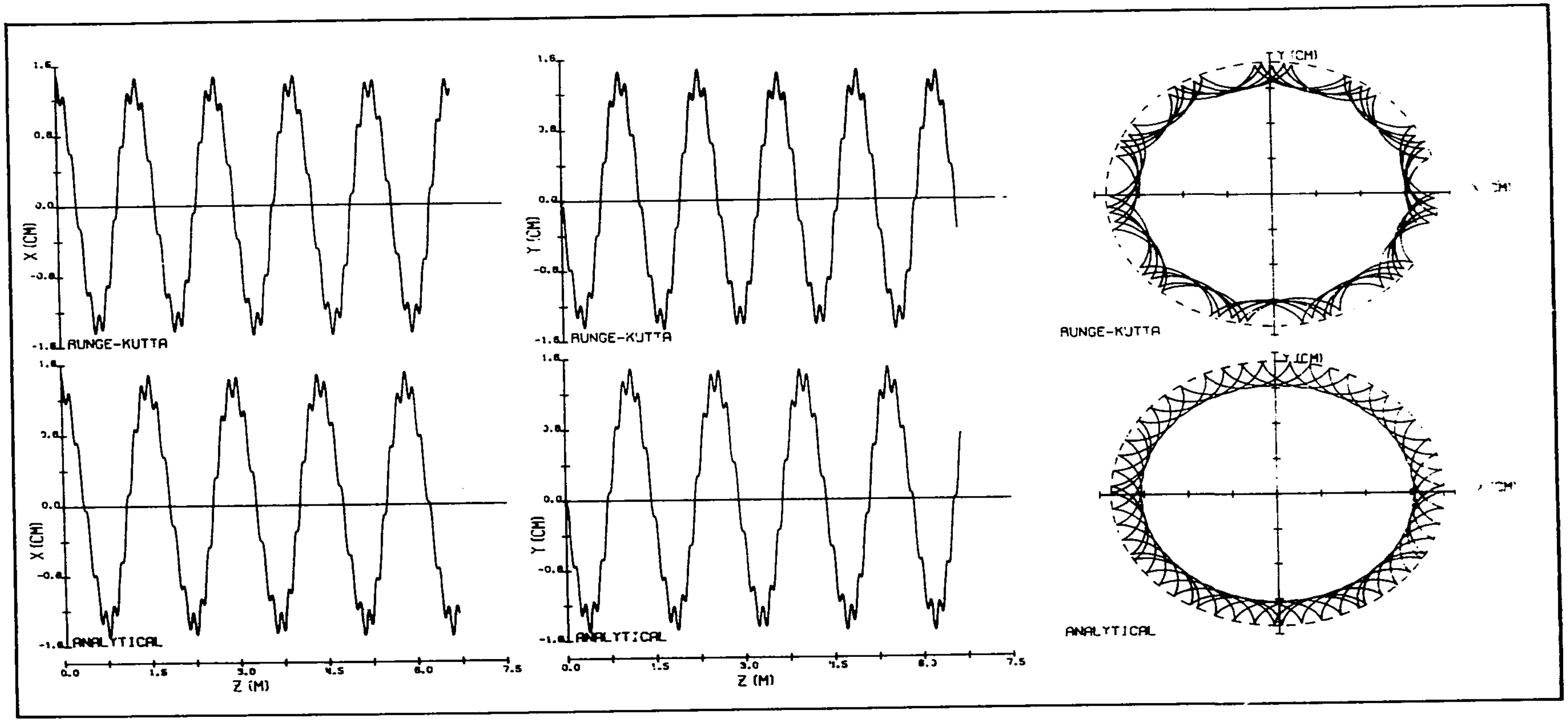

Figure (4.12) As in Figure (4.1) for Parallel Injection at the Limiting Acceptance Point (X_o = a = 1.5 cm, Y_o = 0.0).

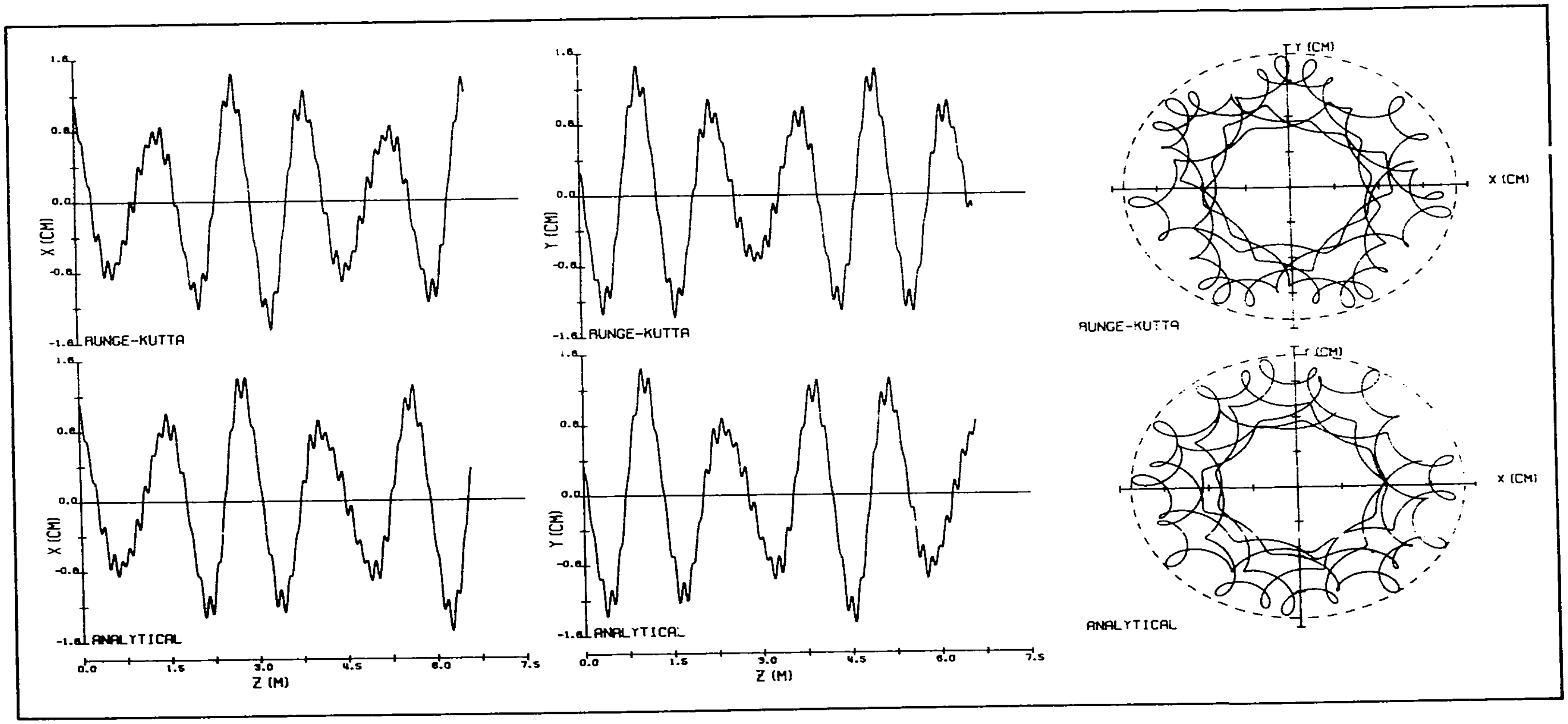

Figure (4.13) As in Figure (4.1) for Parallel Injection at the Limiting Acceptance Point (X_o = 1.125 cm, Y_o = 0.265 cm).

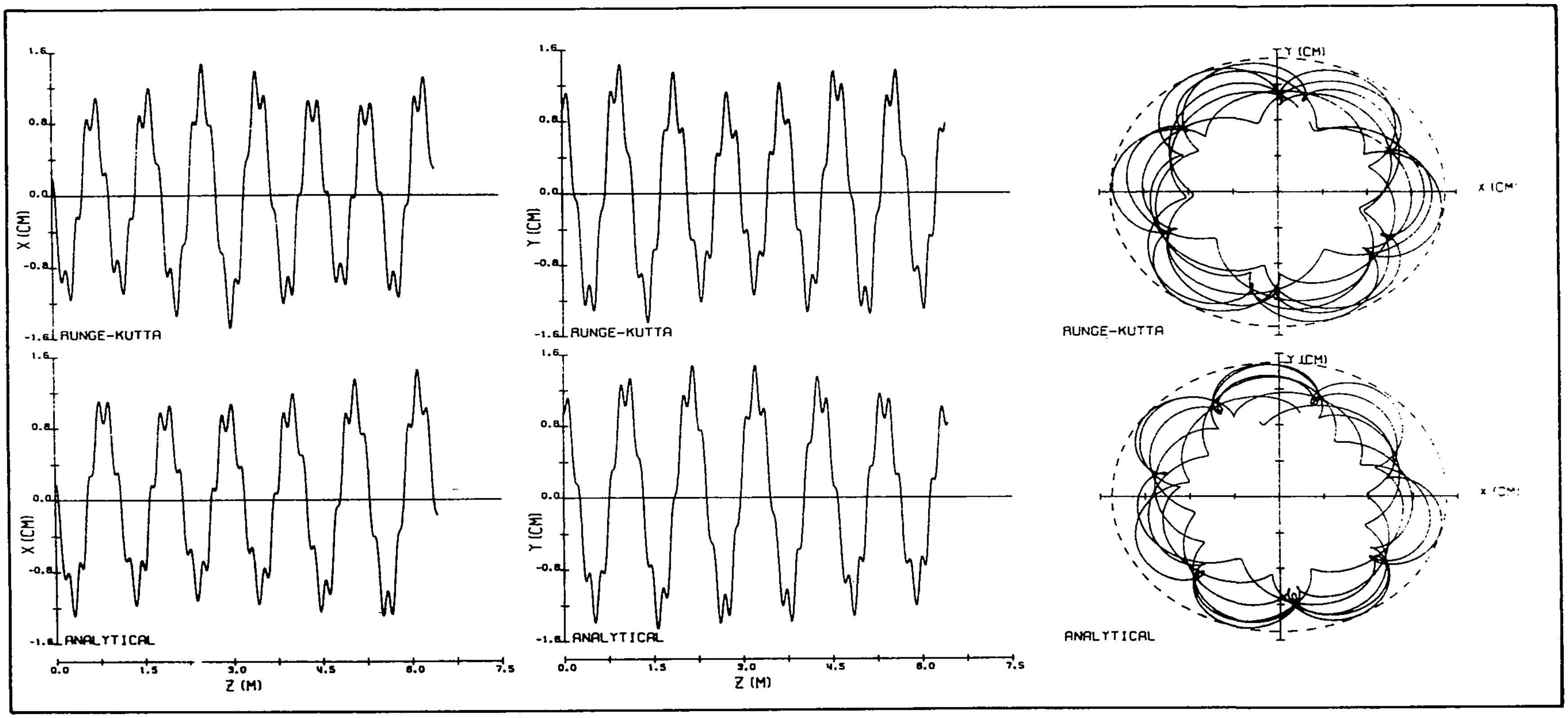

Figure (4.14) As in Figure (4.1) for Parallel Injection at the Limiting Acceptance Point (X_o = 0.187 cm, Y_o = 0.928 cm).

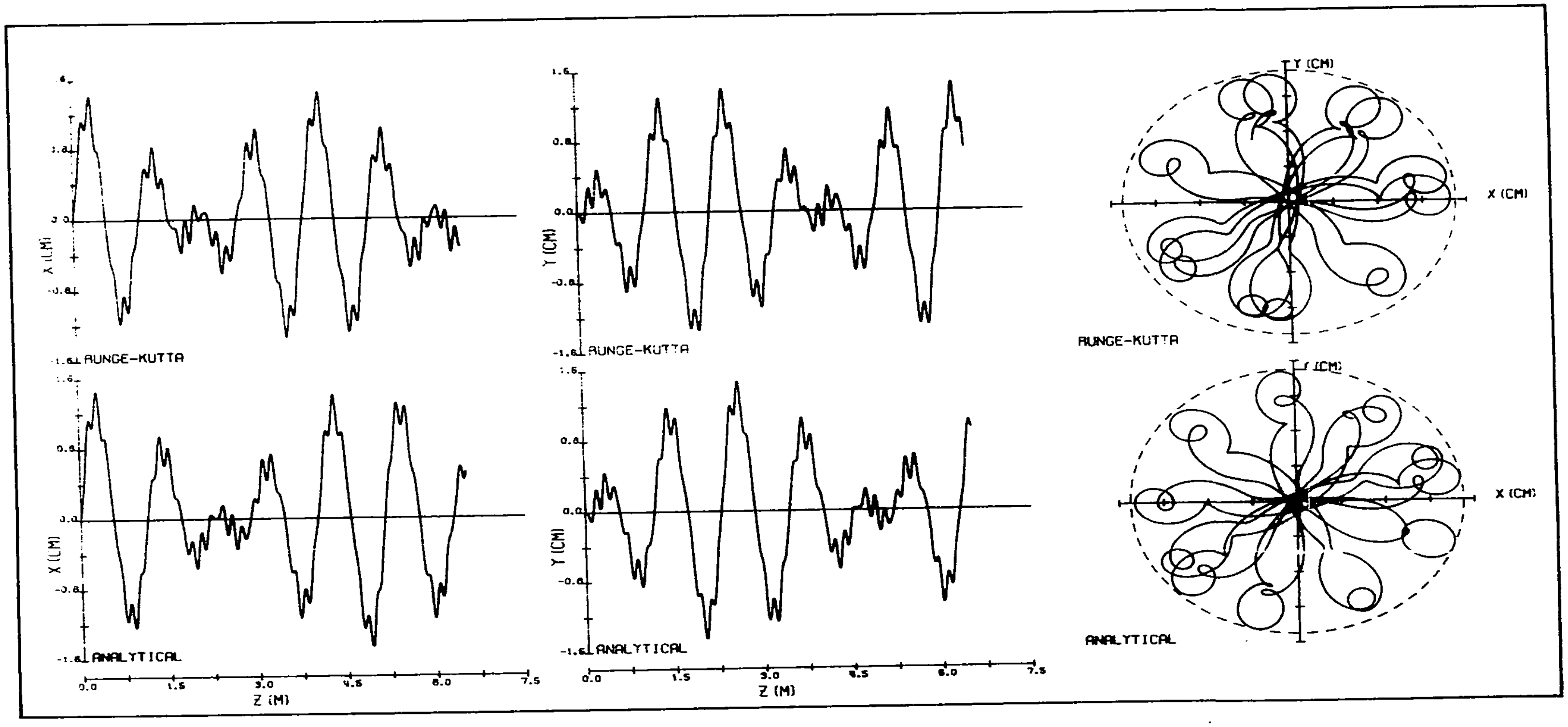

Figure (4.15) As in Figure (4.1) for Point Source Injection at the Limiting Acceptance Point $(\frac{P_{X_o}}{P_{Z_o}} = 0.0599, \frac{P_{Y_o}}{P_{Z_o}} = 0.0)$.

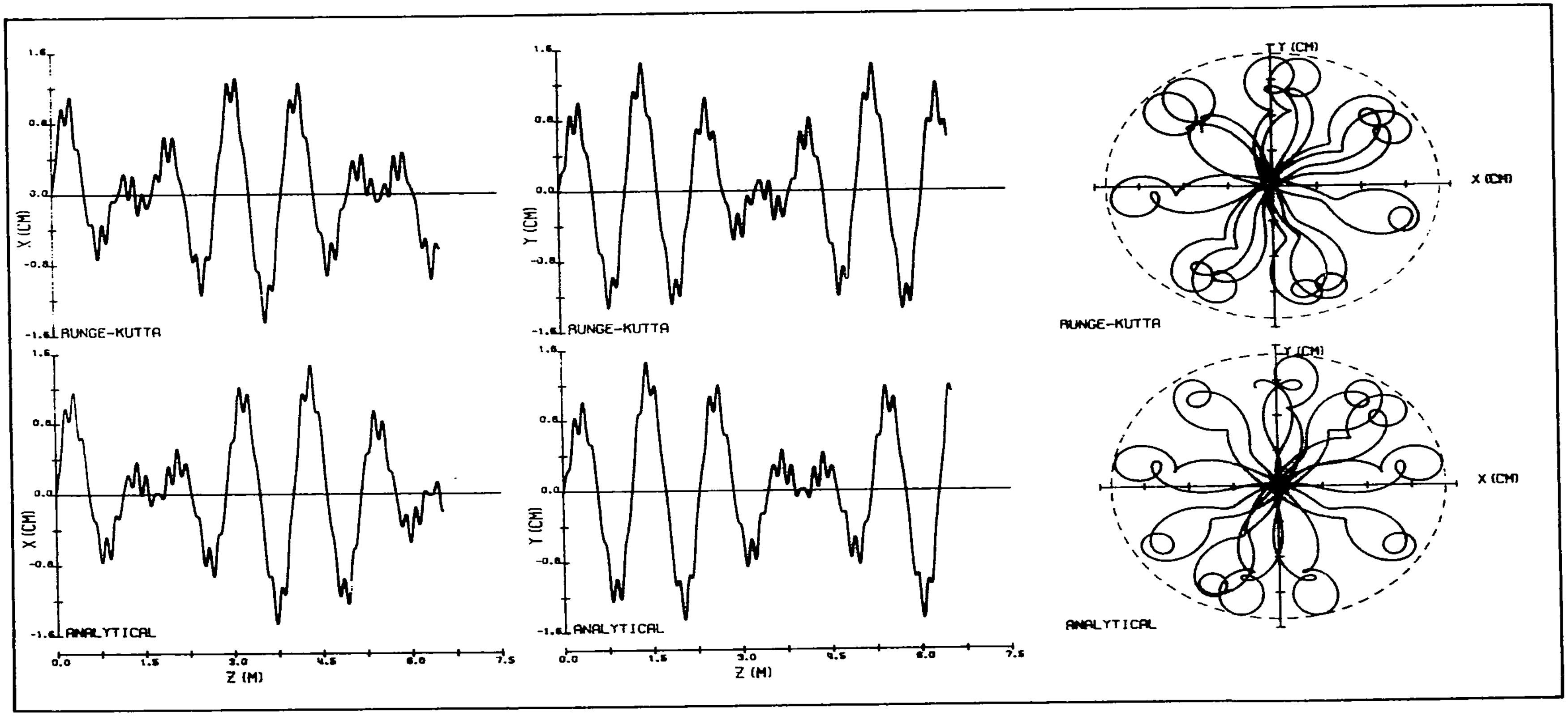

Figure (4.16) As in Figure (4.1) for Point Source Injection at the Limiting Acceptance Point $(\frac{P_{X_o}}{P_{Z_o}} = 0.052, \frac{P_{Y_o}}{P_{Z_o}} = 0.038)$.

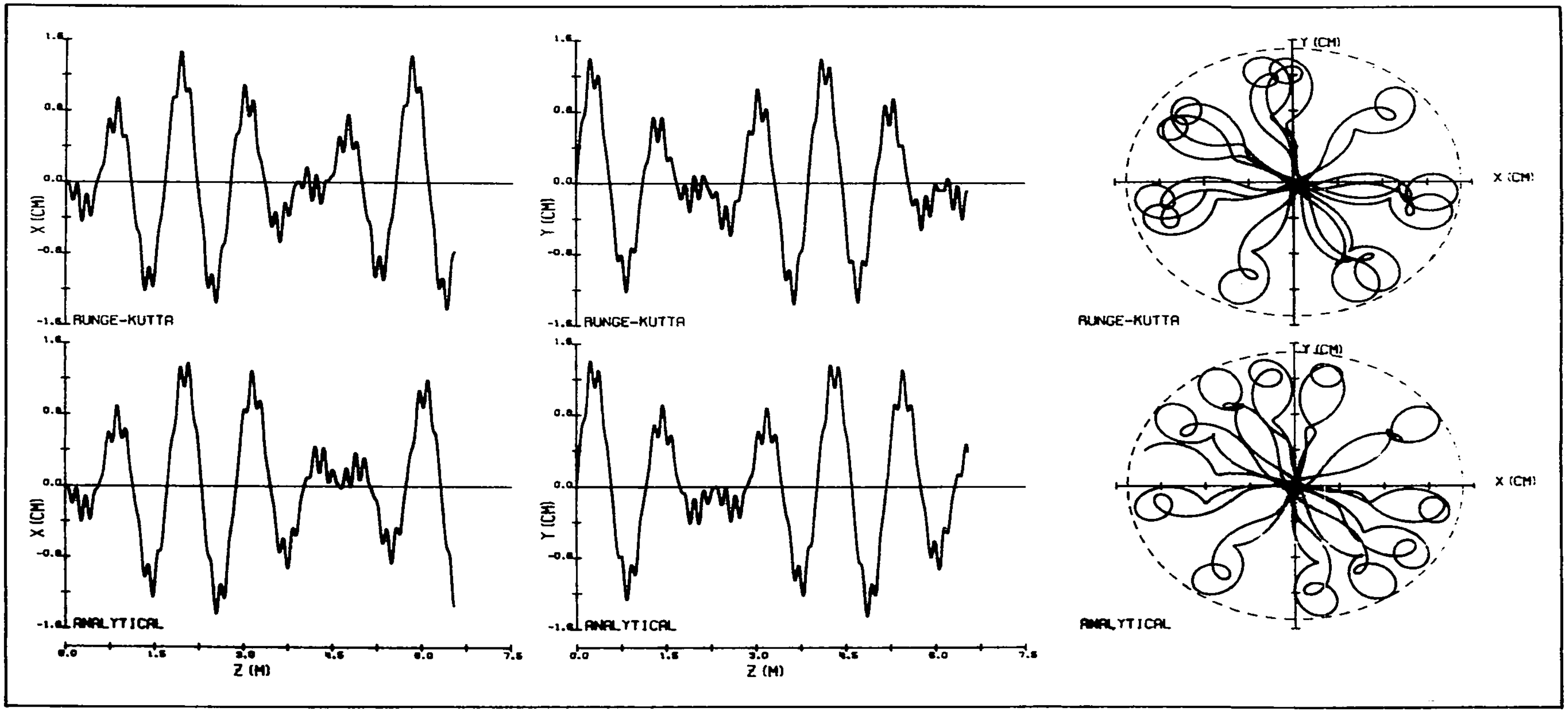

Figure (4.17) As in Figure (4.1) for Point Source Injection at the Limiting Acceptance Point ($\frac{P_{X_o}}{P_{Z_o}} = 0$, $\frac{P_{Y_o}}{P_{Z_o}} = 0.079$).

projections of the trajectories show that the maximum radial displacement is equal to or very slightly less than the aperture radius. In other words equation (3.10) has quite successfully predicted the acceptance limits of the twisted structure for these cases.

The study of all the above trajectories, both analytic and Runge-Kutta, shows that for all injection conditions accepted by the twisted structure the projections of the trajectories on the fixed X-Z plane and the fixed Y-Z plane feature a dominant oscillation superimposed upon which there is a shorter wavelength ripple. The study also shows that the relative amplitudes and positions of the ripple component with respect to the dominant oscillation depend on the particle's injection conditions.

For particles injected with small transverse coordinates (X_0, Y_0) and/or small transverse momenta (P_{X_0} , P_{Y_0}), that is for particles whose injection conditions are well within the limits set by equation (3.10), the comparison shows excellent agreement between the analytic and the Runge-Kutta trajectories. For such injection conditions, the amplitudes and positions of either the dominant oscillations or the ripples are the same in the analytic and the Runge-Kutta trajectories. Such excellent agreement indicates the degree of accuracy of the analytic solution and shows that the approximate assumptions of equation (2.15) are well justified for injection conditions well within the limits set by equation (3.10).

The comparison of the analytic and the Runge-Kutta trajectories for particles with injection conditions larger than those discussed above, but still within the limits set by equation (3.10), shows that there is still good agreement between the analytic and the Runge-Kutta trajectories.

Any differences between the two solutions are not evident for the first few periodic twists. Then a slight apparent phase shift starts to appear between the projections, on the X-Z and the Y-Z planes, of the analytic and the Runge-Kutta trajectories. The magnitude of this apparent phase shift increases as the injection conditions of the particle are increased towards the limiting values set by equation (3.10). This apparent phase shift arises because each time the Runge-Kutta trajectory projections cross the Z axis they do so earlier than the corresponding analytic trajectory projections. It would appear that in the actual structure the forces on the particle cause it to be returned towards the axis sooner than indicated by the analytic solution. In other words, the focusing action on the particles displaced from the Z-axis is actually somewhat stronger than is predicted by the analytic solution.

For injection conditions equal to the limits set by equation (3.10), there is still agreement in the general nature of the analytic and the Runge-Kutta trajectories. However, the apparent phase shift is larger than before indicating that the analytic solution fails to account fully for the strong focusing action of the actual structure.

It is important to note that examination of all the X-Y projections of the analytic and Runge-Kutta trajectories indicates that the maximum displacements of particles whose injection conditions satisfy equation (3.10) are equal to or less than the aperture radius, a. This result strongly supports the validity of using equation (3.10) in predicting the allowable injection conditions of the particles.

4.3 The Axial Velocity $\dot{Z}$

Equation (2.34) gives the axial velocity of the particle at any position along the twisted structure as a function of its axial velocity at injection, U_{Z_0}, its injection transverse coordinates and momenta, and the time, t, elapsed after injection. Equation (2.34) shows that $\dot{Z}$ varies about U_{Z_0} as the particle moves along the structure. It is also shown in Appendix B that, for particles whose maximum radial displacements from the Z axis are equal to or less than the aperture radius a, the maximum deviation of $\dot{Z}$ from U_{Z_0} is given by

$$U_{Z_0} \frac{[1 - \frac{(\beta a)^2}{s}]}{[1 + \frac{(\beta a)^2}{s}]} \leq \dot{Z} \leq U_{Z_0} \frac{[1 + \frac{(\beta a)^2}{s}]}{[1 - \frac{(\beta a)^2}{s}]}$$

$$\frac{0.95}{1.05} \leq \frac{\dot{Z}}{U_{Z_0}} \leq \frac{1.05}{0.95} \quad \text{for } s = 2 \text{ and } (\beta a)^2 = 0.1$$

which indicates that the axial velocity of any particle successfully guided by the structure is always approximately equal to the particle's axial velocity at injection, U_{Z_0}, at all points along the twisted structure.

For the large number of injection conditions considered in the comparison of the actual and analytical trajectories, the axial velocity $\dot{Z}$ was plotted versus the axial distance Z. In all cases the deviation between $\dot{Z}$ and U_{Z_0} was found to increase as the injection conditions of the particle approached the acceptance limits set by equation (3.10).

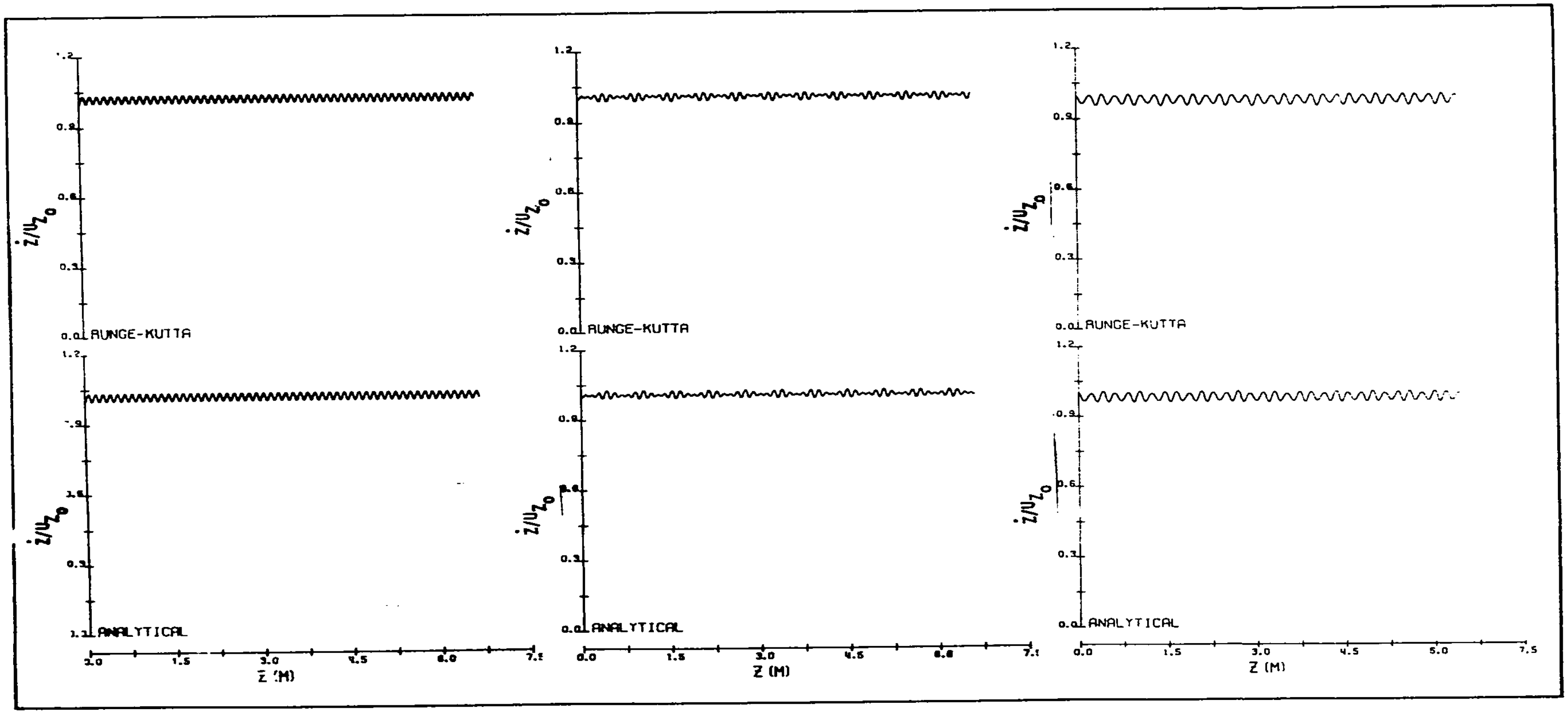

Figure (4.18) Plots of ($\dot{Z}/U_{Z_o}$) versus Z.

Plots show the degree of variation of $\dot{Z}$ about U_{Z_o}.

Cases a, b and c correspond to the limiting injection conditions considered in figures (4.12), (4.13) and (4.14) respectively.

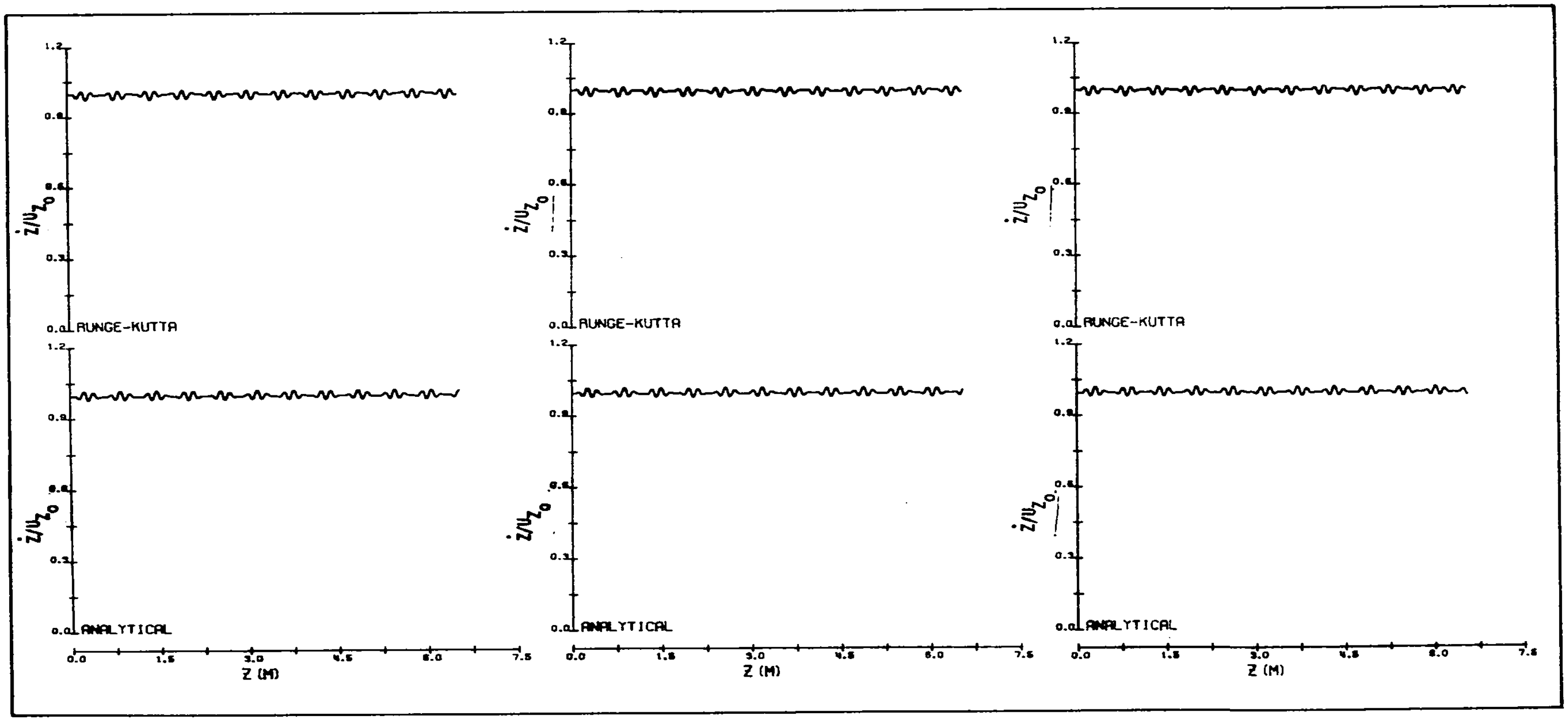

Cont. Figure (4.18) Cases d, e and f correspond to the limiting injection conditions considered in figures (4.15), (4.16) and (4.17) respectively.

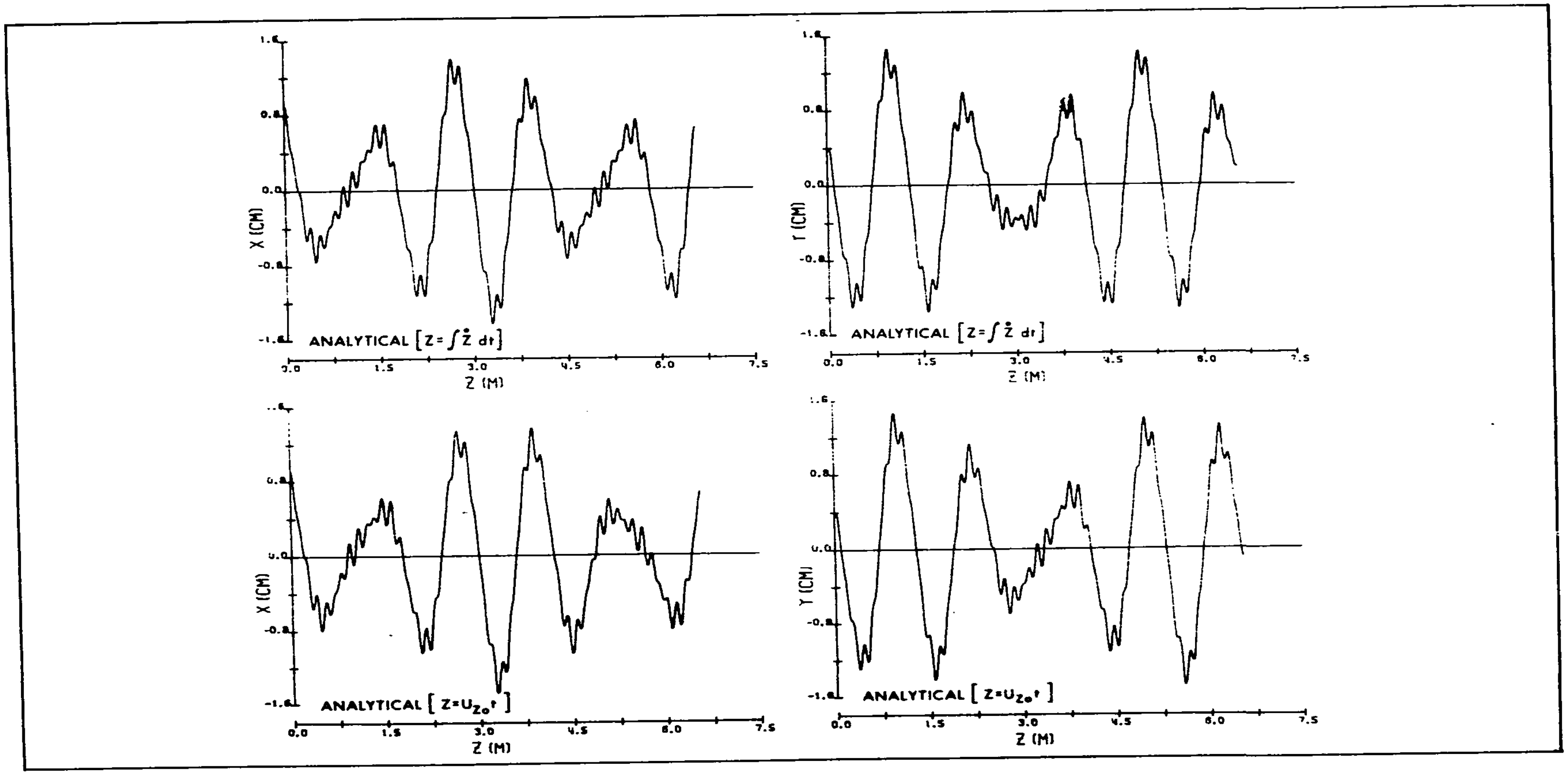

Figure (4.19) Analytical Trajectory Projections for a Particle when (X_o = 0.9 cm, Y_o = 0.4 cm, P_{X_o} = 0, P_{Y_o} = 0).

The top group was calculated using equation (2.33) and the bottom group was calculated using the approximation $\dot{Z} \cong U_{Z_o}$

It was also observed that for all actual numerical and analytic trajectories investigated the deviation was less than 3%, as shown in figures (4.18) a, b, c, d, e and f, for the particles with limiting injection conditions whose trajectories are shown in figures (4.12), (4.13), (4.14), (4.15), (4.16) and (4.17) respectively. Thus, without significantly affecting the accuracy of the solution, it may be assumed that, for particles confined by the twisted structure

$$\dot{Z} \cong U_{Z_0} \tag{4.2}$$

Figure (4.19) shows the trajectory projections for a particle with the injection conditions, $X_0 = 0.9$ cm, $Y_0 = 0.4$ cm and $P_{X_0} = P_{Y_0} = 0$. The (X-Z) and the (Y-Z) trajectory projections at the top of figure (4.19) were computed using equations (2.31) and the axial distance Z was computed as

$$Z = \int_0^t \dot{Z}\, dt \qquad \text{as given by equation (2.35).}$$

The X-Z and the Y-Z trajectory projections at the bottom of figure (4.19) were computed using equations (2.31) and the approximate value of the axial distance Z was computed as

$$Z \cong U_{Z_0} \cdot t$$

Comparison of the two trajectories verifies that the accuracy of the analytic solution is not significantly affected when using the above approximation for Z instead of the value given by equation (2.35).

4.4. Spatial Modes

The trajectories investigated exhibit three dominant features. Each consists of a long wavelength motion upon which is superimposed a small ripple of much shorter wavelength. Further, some of the trajectories display a slow amplitude modulation. All of these characteristics can be explained by expressing the trajectories in terms of cosine - like and sine - like modes of four fundamental spatial frequencies. It is shown in Appendix F that the trajectories given by equations (2.31) can be transformed to the fixed (X,Y,Z) coordinate frame by a simple rotation of coordinates, through an angle βZ, using equations (2.7). Thus, in terms of X, Y, Z and t the particle trajectories are given by:

$$\begin{aligned}
X = &+ \frac{1}{2} C_1\{1 + [\frac{s}{(s+1)}]^{1/2}\}\cos (f_1 t - \beta Z + \alpha_1) \\
&- \frac{1}{2} C_2\{1 + [\frac{s}{(s-1)}]^{1/2}\}\sin(-f_2 t + \beta Z - \alpha_2) \\
&+ \frac{1}{2} C_1\{1 - [\frac{s}{(s+1)}]^{1/2}\}\cos(f_1 t + \beta Z + \alpha_1) \\
&- \frac{1}{2} C_2\{1 - [\frac{s}{(s-1)}]^{1/2}\}\sin(f_2 t + \beta Z + \alpha_2),
\end{aligned}$$

$$\begin{aligned}
Y = &- \frac{1}{2} C_1\{1 + [\frac{s}{s+1}]^{1/2}\}\sin(f_1 t - \beta Z + \alpha_1) \\
&+ \frac{1}{2} C_2\{1 + [\frac{s}{s-1}]^{1/2}\}\cos(-f_2 t + \beta Z - \alpha_2)
\end{aligned}$$

$$+ \frac{1}{2} C_1\{1 - [\frac{s}{s+1}]^{1/2}\}\sin(f_1 t + \beta Z + \alpha_1)$$

$$+ \frac{1}{2} C_2\{1 - [\frac{s}{s-1}]^{1/2}\}\cos(f_2 t + \beta Z + \alpha_2) \cdot \qquad (4.3)$$

Using equation (4.2), the expressions for f_1t and f_2t for particles confined by the structure become:

$$f_1 t \cong f_1 \frac{1}{U_{Z_0}} Z = \sqrt{\frac{2qk}{M}}[s + 1]^{1/2} \frac{M}{P_{Z_0}} Z \cong \{\frac{s+1}{s}\}^{1/2} \beta Z \ ,$$

$$f_2 t \cong f_2 \frac{1}{U_{Z_0}} Z = \sqrt{\frac{2qk}{M}}[s - 1]^{1/2} \frac{M}{P_{Z_0}} Z \cong \{\frac{s-1}{s}\}^{1/2} \beta Z \cdot \qquad (4.4)$$

Substituting equations (4.4) into equations (4.3), the trajectories become linear combinations of modes at the following spatial frequencies:

$$\omega_1 = (f_1 t - \beta Z)/Z = \{[\frac{s+1}{s}]^{1/2} - 1\}\beta \quad ,$$

$$\omega_2 = (-f_2 t + \beta Z)/Z = \{1 - [\frac{s-1}{s}]^{1/2}\}\beta \quad ,$$

$$\omega_3 = (f_1 t + \beta Z)/Z = \{[\frac{s+1}{s}]^{1/2} + 1\}\beta \quad ,$$

$$\omega_4 = (f_2 t + \beta Z)/Z = \{1 + [\frac{s-1}{s}]^{1/2}\}\beta \quad . \qquad (4.5)$$

Consider the trajectory shown in figure (4.12). For this case $C_1 = a = 1.5$ cm, $C_2 = 0.0$, $\alpha_1 = 0.0$ and $\alpha_2 = 0.0$. Hence from equations (4.3), (4.4) and (4.5);

$$X = \frac{1}{2}\,a\{1 + [\frac{s}{s + 1}]^{1/2}\}\cos \omega_1 Z$$

$$+ \frac{1}{2}\,a\{1 - [\frac{s}{s + 1}]^{1/2}\}\cos \omega_3 Z \quad ,$$

$$Y = -\frac{1}{2}\,a\{1 + [\frac{s}{s + 1}]^{1/2}\}\sin \omega_1 Z$$

$$+ \frac{1}{2}\,a\{1 - [\frac{s}{s + 1}]^{1/2}\}\sin \omega_3 Z \quad . \qquad (4.6)$$

Clearly, $\omega_1 < \omega_3$ and the X-Z and Y-Z projections of the trajectory consist of a dominant oscillation at ω_1, with corresponding wavelength,

$$\lambda_1 = \{\frac{s^{1/2}}{[(s + 1)^{1/2} - s^{1/2}]}\}L \quad ,$$

upon which is superimposed a ripple at ω_3, with corresponding wavelength,

$$\lambda_3 = \{\frac{s^{1/2}}{[(s + 1)^{1/2} + s^{1/2}]}\}L \quad .$$

In figure (4.12), $s = 2$, thus $\lambda_1 = 4.45L$ and $\lambda_3 = 0.45L$. Similarly if injection conditions were such as to excite only the ω_2 and ω_4 modes, as in figure (4.9), the trajectory would consist of a dominant oscillation at ω_2 with $\lambda_2 = 3.42L$ ($s = 2$) and a ripple at ω_4 with $\lambda_4 = 0.586L$ ($s = 2$). In general, as in the other cases investigated in Section 4.2, all four modes are excited and the interpretation in terms of the spatial frequencies becomes more difficult. However, it is found that a general trajectory will feature a dominant oscillation with an apparent wavelength between λ_1 and λ_2 (approximately four times the periodic length of the twisted structure for s = 2). Superimposed upon this oscillation will appear a small ripple with an apparent wavelength between λ_3 and λ_4 (approximately equal to half the periodic length for s = 2).

When all modes are present a slow beat will be evident between the two large amplitude modes (ω_1, ω_2). As a result the dominant oscillation will appear to be amplitude modulated. An excellent example of this modulating effect is seen in figure (4.11). In this case equations (2.37) show that $C_1 = 0.561$ cm, $C_2 = 0.448$ cm, $\alpha_1 = 258°$ and $\alpha_2 = 169.6°$. Thus, from (4.3), (4.4) and (4.5) the expressions for X and Y become

$$X = 1.02\cos\left[\frac{(\omega_2 - \omega_1)}{2} Z + 11.185°\right]\sin\left[\frac{(\omega_2 + \omega_1)}{2} Z - 0.815°\right]$$

$$- 0.1026\sin\left[\frac{(\omega_4 - \omega_3)}{2} Z + 0.815°\right]\cos\left[\frac{(\omega_4 + \omega_3)}{2} Z - 11.185°\right]$$

$$+ 0.03\sin[\omega_2 Z + 10.37°] - 0.0415\sin[\omega_4 Z - 10.37°] \quad [\text{cm}]$$

$$Y = 1.02\sin\left[\left(\frac{\omega_2 - \omega_1}{2}\right)Z + 11.185°\right]\sin\left[\left(\frac{\omega_1 + \omega_2}{2}\right)Z - 0.815°\right]$$

$$- 0.1026\sin\left[\left(\frac{\omega_4 - \omega_3}{2}\right)Z + 0.815°\right]\sin\left[\left(\frac{\omega_4 + \omega_3}{2}\right)Z - 11.185°\right]$$

$$- 0.03\cos(\omega_2 Z + 10.37°) + 0.0415\cos(\omega_4 Z - 10.37°) \quad [\text{cm}].$$

The major portion of the motion consists of an oscillation at a frequency lying midway between ω_1 and ω_2 which is amplitude modulated at a rate equal to $\frac{1}{2}(\omega_2 - \omega_1)$. The corresponding modulating wavelength is given by:

$$\lambda_m = \{\frac{2s^{1/2}}{[2s^{1/2} - (s + 1)^{1/2} - (s - 1)^{1/2}}\}L$$

$$= 29.6L \quad \text{for} \quad s = 2$$

CHAPTER 5

EFFECT OF EARTH'S GRAVITY ON PARTICLE TRAJECTORIES

As mentioned previously the main objective of the analysis of the uniformly twisted electrostatic quadrupole is to provide a structure capable of guiding heavy charged particles, in particular charged micron-sized particles. Since the charge to mass ratios of such particles are very low, the earth's gravitational force could noticeably affect the motion of these particles along the twisted guiding channel. The objective of this chapter is to determine to what extent gravity modifies the particle trajectories and to find values of the focusing quadrupole potential, V_0, beyond which the gravitational effect can be neglected.

5.1 Particle Motion

Taking the horizontal axis of the twisted structure, the Z-axis, as the zero gravitational potential level, the gravitational potential, V_g, at any point is

$$V_g = MGY = MG(x \sin \beta z + y \sin \beta z) \tag{5.1}$$

where the (X,Y,Z) and the (x,y,z) coordinate systems are the same as defined in Chapter 2, where M is the mass of the particle and where G is the gravitational acceleration.

The earth's gravitational forces are accounted for by adding the potential V_g to the Hamiltonian of motion given by equation (2.16). The new Hamiltonian in terms of the rotating coordinates is,

$$H = \frac{1}{2M}[p_x{}^2 + p_y{}^2 + p_z{}^2 - 2\beta p_z(x\ p_y - y\ p_x)]$$

$$+ qk(x^2 - y^2) + MG[x \sin \beta z + y \cos \beta z] \qquad (5.2)$$

where p_x, p_y and p_z are as defined by equations (2.10) and it is still assumed that $(\frac{p_x}{p_z})^2$ and $(\frac{p_y}{p_z})^2 << 1$. The equations of motion generated from (5.2) are linear, inhomogeneous and coupled. By resorting to contact transformation using the generating function

$$F_G = x\ \bar{p}_x + y\ \bar{p}_y - \frac{\beta p}{2qMk}\ \bar{p}_x\ \bar{p}_y + z\ \bar{p}_z \qquad (5.3)$$

a new coordinate system $(\bar{x}, \bar{y}, \bar{z}, \bar{p}_x, \bar{p}_y, \bar{p}_z)$ is generated in which the equations of motion are uncoupled provided the constant p is selected properly. The new coordinates are related to the old ones as,

$$\bar{x} = \frac{\partial F_G}{\partial \bar{p}_x} = x - \frac{\beta p}{2qMk}\ \bar{p}_y \quad ,$$

$$\bar{y} = \frac{\partial F_G}{\partial \bar{p}_y} = y - \frac{\beta p}{2qMk}\ \bar{p}_x \quad ,$$

$$\bar{z} = \frac{\partial F_G}{\partial \bar{p}_z} = z, \quad ,$$

$$p_x = \frac{\partial F_G}{\partial x} = \bar{p}_x \quad ,$$

$$p_y = \frac{\partial F_G}{\partial y} = \bar{p}_y \quad ,$$

$$p_z = \frac{\partial F_G}{\partial z} = \bar{p}_z = P_Z + \beta(x\, p_y - y\, p_x) \quad . \tag{5.4}$$

The Hamiltonian in the new canonical coordinates is

$$\begin{aligned} H = \frac{1}{2M}[\bar{p}_x{}^2 + \bar{p}_y{}^2 + \bar{p}_z{}^2 - 2\beta\bar{p}_z[\{\bar{x} + \frac{\beta p}{2qMk}\,\bar{p}_y\}\bar{p}_y \\ - \{\bar{y} + \frac{\beta p}{2qMk}\,\bar{p}_x\}\bar{p}_x] + qk[\{\bar{x} + \frac{\beta p}{2qMk}\,\bar{p}_y\}^2 \\ - \{\bar{y} + \frac{\beta p}{2qMk}\,\bar{p}_x\}^2] + MG[\{\bar{x} + \frac{\beta p}{2qMk}\,\bar{p}_y\}\sin\beta\bar{z} \\ + \{\bar{y} + \frac{\beta p}{2qMk}\,\bar{p}_x\}\cos\beta\bar{z}] \end{aligned} \tag{5.5}$$

Rearranging these terms gives

$$\begin{aligned} H = \frac{\bar{p}_z{}^2}{2M} + \frac{1}{2M}[\bar{p}_x{}^2\{1 + \frac{2\beta^2 p\,\bar{p}_z}{2qMk} - \frac{\beta^2 p^2}{2qMk}\} + 2qMk\,\bar{x}^2] \\ + \frac{1}{2M}[\bar{p}_y{}^2\{1 - \frac{2\beta^2 p\,\bar{p}_z}{2qMk} + \frac{\beta^2 p^2}{2qMk}\} - 2qMk\,\bar{y}^2] \\ + MG[\bar{x}\sin\beta\bar{z} + \frac{\beta p}{2qMk}\,\bar{p}_x\cos\beta\bar{z}] \\ + MG[\bar{y}\cos\beta\bar{z} + \frac{\beta p}{2qMk}\,\bar{p}_y\sin\beta\bar{z}] \\ + \frac{1}{2M}[2\beta p - 2\beta\bar{p}_z][\bar{x}\,\bar{p}_y - \bar{y}\,\bar{p}_x] \end{aligned} \tag{5.6}$$

The following assumptions are now introduced:

1. It is assumed that $\bar{p}_z = P_Z$. This follows from (5.4) if the first order quantity, $\beta(x\ p_y - y\ p_x)$, is neglected.

2. It was shown in Chapter 4 that the axial velocity $\dot{Z} = \frac{P_Z}{M}$ is essentially constant and equal to its value at injection U_{Z_0}. It is within the same degree of approximation to assume that

$$\bar{p}_z \cong P_Z \cong P_{Z_0} = MU_{Z_0} \tag{5.7}$$

Taking (5.7) into consideration, equation (5.6) shows that the term $(\bar{x}\ \ \bar{p}_y - \bar{y}\ \bar{p}_x)$ is the only coupling term between the coordinates $\bar{x}$, $\bar{y}$, $\bar{p}_x$ and $\bar{p}_y$, and this term vanishes if p is selected as,

$$p = \bar{p}_z \cong P_{Z_0} \tag{5.8}$$

Substituting (5.7) and (5.8) into (5.6), the Hamiltonian reduces to,

$$\begin{aligned} H = {} & \frac{P_{Z_0}{}^2}{2M} + \frac{1}{2M}\left[\bar{p}_x{}^2\left\{\frac{\beta^2 P_{Z_0}{}^2}{2qMk} + 1\right\} + 2qMk\ \bar{x}^2\right] \\ & - \frac{1}{2M}\left[\bar{p}_y{}^2\left\{\frac{\beta^2 P_{Z_0}{}^2}{2qMk} - 1\right\} + 2qMk\ \bar{y}^2\right] \\ & + MG\left[\bar{x}\ \sin\beta\bar{z} + \frac{\beta P_{Z_0}}{2qMk}\,\bar{p}_x\ \cos\beta\bar{z}\right] \\ & + MG\left[\bar{y}\ \cos\beta\bar{z} + \frac{\beta P_{Z_0}}{2qMk}\,\bar{p}_y\ \sin\beta\bar{z}\right] \end{aligned} \tag{5.9}$$

From (5.9) the equations of motion are

$$\ddot{\bar{x}} + \frac{2qk}{M}(s_0 + 1)\bar{x} = -[2s_0 + 1]G \sin \beta U_{Z_0} t \quad ,$$

$$\ddot{\bar{y}} + \frac{2qk}{M}(s_0 - 1)\bar{y} = +[2s_0 - 1]G \cos \beta U_{Z_0} t \quad , \tag{5.10}$$

and two similar equations for $\bar{p}_x$ and $\bar{p}_y$ where s_0 is a stability factor. It is evident from equations (5.10) that the motion is stable if $|s_0| > 1$ where

$$s_0 = \frac{\beta^2 P_{Z_0}^{\ 2}}{2qMk} . \tag{5.11}$$

In equations (5.10) the approximation $\bar{z} = Z \cong U_{Z_0} t$ is introduced. It is evident from equations (5.4), (5.7) and the assumption that $\dot{Z}$ is essentially constant, that this approximation is justified.

The solutions of the inhomogeneous differential equations (5.10) consist of the homogeneous solutions, exactly analogous to the solutions given by equation (2.29) for the particle trajectories in the absence of gravitational forces, and the particular solutions given by

$$\bar{x}_G = -\frac{MG}{2qk}(2s_0 + 1)\sin \beta U_{Z_0} t \quad ,$$

$$\bar{y}_G = \frac{MG}{2qk}(2s_0 - 1)\cos \beta U_{Z_0} t \quad . \tag{5.12}$$

When transformed to the fixed (X,Y,Z) coordinate system, the particular solutions resulting from the gravitational forces are,

$$X_G = -\frac{MG}{2qk} \sin 2\beta Z$$

$$Y_G = \frac{MG}{2qk}[4s - \cos 2\beta Z] \tag{5.13}$$

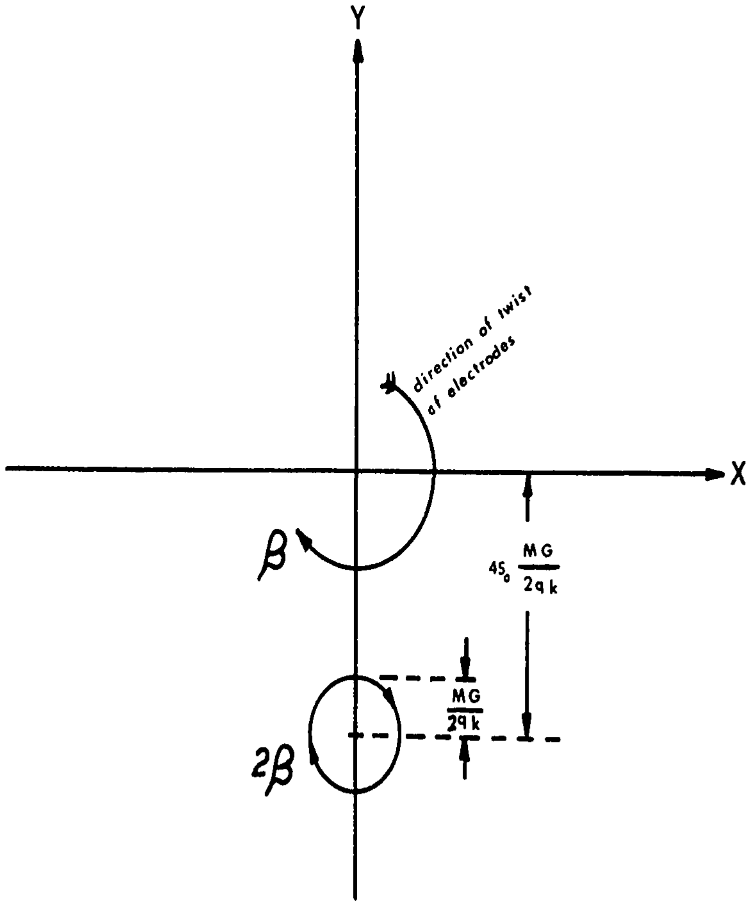

Figure (5.1) The Mean Orbit of Particle Motion when the Effect of Gravitational Forces is Taken into Consideration.

The projection of the particular solutions of equations (5.13) onto the fixed X-Y plane is plotted in figure (5.1). This figure indicates that the mean orbit of the particle trajectories, which was the horizontal Z axis when gravitational forces were neglected, has been modified to a helical orbit. The axis of this helical orbit is parallel to the Z axis at a distance $\frac{4MG}{2qk} s_0$ on the negative side of the Y-axis and the radius of this helical orbit is $\frac{MG}{2qk}$. As expected, equations (5.13) and figure (5.1) show that the effect of the gravitational forces becomes noticeable as $\frac{q}{M}$ decreases.

For the effect of gravitational forces to be neglected, the distance between the axis of the helical orbit and the Z axis should be much less than the aperture radius. This condition implies choosing the focusing potential to satisfy

$$4s_o \frac{MG}{2qk} << a \quad ,$$

that is

$$2 \frac{G\ a}{(\frac{q}{M})V_0} s_0 << 1 \quad . \tag{5.14}$$

As stated before the value of $\frac{q}{M}$ for micron sized charged particles may be as low as 0.01 coulomb/kilogram. For G = 9.81 m/sec^2 and a = 0.015 meter equation (5.14) becomes

$$V_0 >> \frac{.294 \frac{m^2}{sec^2} s_0}{\frac{q}{M}} \tag{5.15}$$

For $s_0 = 2.0$ the inequality (5.15) implies that

$$V_0 >> 58.8 \text{ volts for } \frac{q}{M} = 0.01 \text{ coulomb/kilogram.}$$

The parameters of the lens structure which is considered in Chapters 7 and 8 are

$s_0 = 1.25$
a = 0.015 meter
V_0 = 1200 volts .

Equation (5.14) shows that for these parameters gravity becomes negligible provided that the charge to mass ratios of the particles satisfy

$$\frac{q}{M} \gg 0.0003 \ \text{coulomb/kilogram} .$$

CHAPTER 6

A COMPARISON OF THE PROPERTIES OF THE UNIFORMLY TWISTED ELECTROSTATIC QUADRUPOLE STRUCTURE AND THE CLASSICAL ELECTROSTATIC QUADRUPOLE CHANNEL

6.1 Introduction

The theoretical and experimental investigations of the guiding properties of the uniformly twisted electrostatic quadrupole show that it can successfully guide charged particles provided that equations (3.3) and (3.10) are satisfied. It is of interest to compare the guiding properties of the twisted structure with those of a classical electrostatic quadrupole channel. The latter will be assumed to consist of symmetrical quadrupole triplets. Each triplet consists of a straight quadrupole section of length $\frac{\ell}{2}$ followed by a drift space of length d, then a second straight quadrupole section of length ℓ which is rotated 90° with respect to the first quadrupole section. The second quadrupole section is followed by another drift space of length d, and a third straight quadrupole section of length $\ell/2$ which is rotated a further 90° with respect to the second quadrupole section. The infinitely long classical channel constructed using such symmetrical triplets, will consist of a straight quadrupole section of length $\frac{\ell}{2}$ followed by a succession of drift spaces of length, d, and quadrupole sections of length, ℓ. The successive straight quadrupole sections will be rotated 90° with

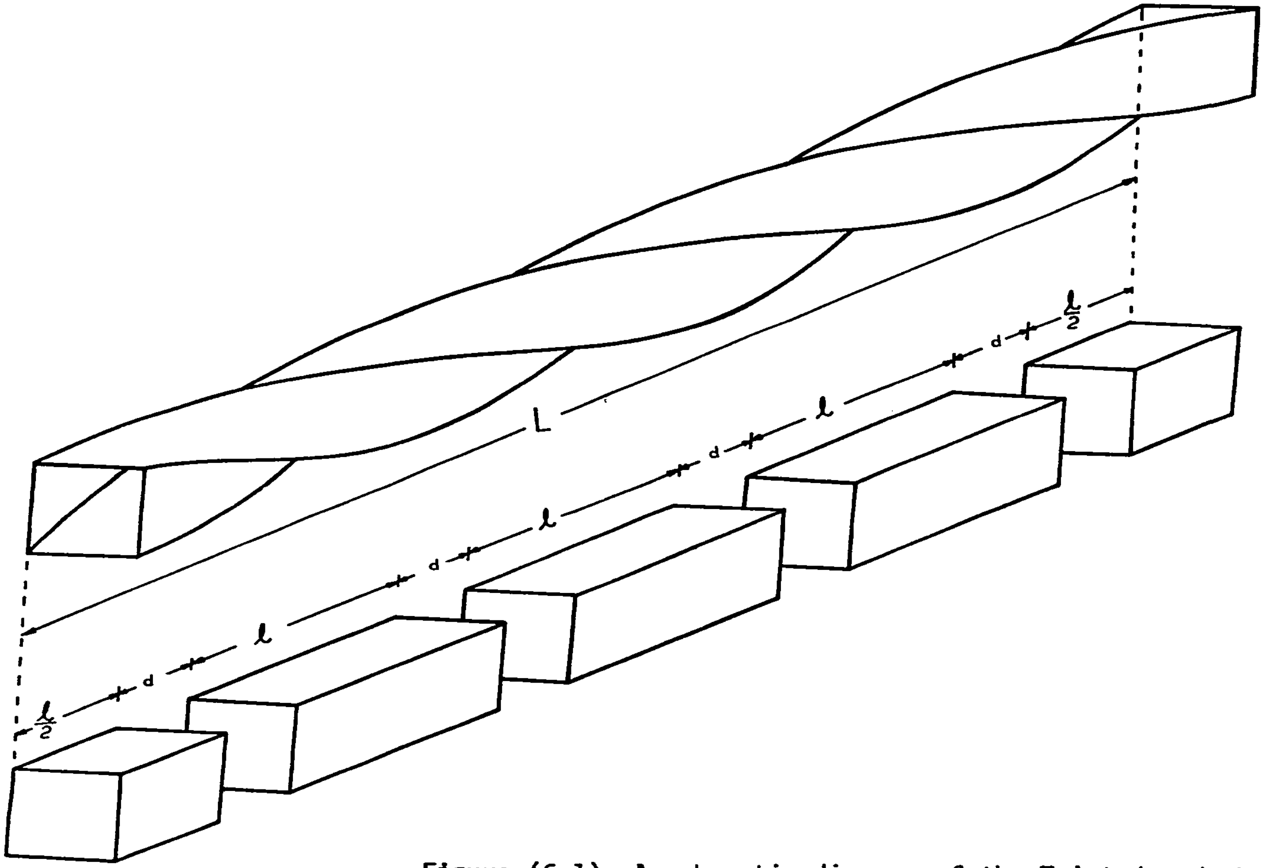
$\frac{\ell}{2}$
d
ℓ
d
ℓ
d
ℓ
d
$\frac{\ell}{2}$
L

Figure (6.1) A schematic diagram of the Twisted and the Classical Structures to be compared respect to each other.

Both the twisted and the classical structures to be compared will be assumed to have the same aperture radius, a, and the same electric field gradient. The classical channel has two symmetrical triplets in the same axial length as one complete twist of the twisted structure, as shown schematically in figure (6.1). Thus,

$$L = 4(\ell + d) \tag{6.1}$$

where, d = length of the drift space between the quadrupole sections of the classical channel.

ℓ = length of a complete quadrupole section of the classical channel.

L = periodic length of the twisted structure.

The fixed (X,Y,Z) coordinate system used in the previous chapters is used in the comparison. The classical and the twisted structures are oriented such that initially at Z = 0, the positive electrodes are aligned symmetrically about the X-axis. Thus the forces exerted on a positively charged particle at Z = 0, by either the classical or the twisted structures, are focusing forces in the X direction and defocusing forces in the Y direction. Therefore, the X-Z plane will be referred to as the initially focusing plane while the Y-Z plane will be referred to as the initially defocusing plane.

6.2 Acceptance Limits

6.2.1 The Classical Structure

If the axial momentum of a particle guided by the classical channel is assumed constant and equal to its value at injection, P_{Z_0}, the projections of the particle motion on the X-Z and the Y-Z planes are uncoupled. Therefore these projections can be independently analyzed. In the X-Z plane the analysis of the motion of a particle along the ith triplet gives the transverse coordinate X_i and the normalized transverse momentum X_i' of the particle at the exit plane of the triplet in terms of the transverse coordinate X_{io} and the normalized transverse momentum X_{io}' of the particle at the entry plane of the triplet as

$$\begin{bmatrix} X_i \\ \\ X_i' \end{bmatrix} = [T_2]\,[T_1] \begin{bmatrix} X_{io} \\ \\ X_{io}' \end{bmatrix} = [T] \begin{bmatrix} X_{io} \\ \\ X_{io}' \end{bmatrix} \tag{6.2}$$

where,

$$X' = \frac{dX}{dZ} = \frac{(dX/dt)}{(dZ/dt)} = \frac{P_X}{P_Z} \cong \frac{P_X}{P_{Z_0}}$$

$[T]$ = transformation matrix of the whole triplet in the X-Z plane,

$[T_1]$ = transformation matrix of the first half of the triplet in the X-Z plane$^{(37)}$

$$= \begin{bmatrix} \cosh \frac{\gamma\ell}{2} & \frac{1}{\gamma} \sinh \frac{\gamma\ell}{2} \\ \gamma \sinh \frac{\gamma\ell}{2} & \cosh \frac{\gamma\ell}{2} \end{bmatrix} \begin{bmatrix} 1 & d \\ 0 & 1 \end{bmatrix} \begin{bmatrix} \cos \frac{\gamma\ell}{2} & \frac{1}{\gamma} \sin \frac{\gamma\ell}{2} \\ -\gamma \sin \frac{\gamma\ell}{2} & \cos \frac{\gamma\ell}{2} \end{bmatrix} \tag{6.3a}$$

$[T_2]$ = transformation matrix of the second half of the triplet in the X-Z plane$^{(37)}$

$$= \begin{bmatrix} \cos\frac{\gamma\ell}{2} & \frac{1}{\gamma}\sin\frac{\gamma\ell}{2} \\ -\gamma\sin\frac{\gamma\ell}{2} & \cos\frac{\gamma\ell}{2} \end{bmatrix} \begin{bmatrix} 1 & d \\ 0 & 1 \end{bmatrix} \begin{bmatrix} \cosh\frac{\gamma\ell}{2} & \frac{1}{\gamma}\sinh\frac{\gamma\ell}{2} \\ \gamma\sinh\frac{\gamma\ell}{2} & \cosh\frac{\gamma\ell}{2} \end{bmatrix} \tag{6.3b}$$

The parameter γ is the quantity,

$$\gamma = \frac{1}{a}\sqrt{\frac{V_o}{V}} \tag{6.4}$$

where a, V and V_0 are the same as defined in Chapter 2.

It is readily shown by performing the indicated matrix multiplication that the transformation matrix [T] can be put in the form,

$$[T] = \begin{bmatrix} \cos\mu & \frac{1}{\gamma_X}\sin\mu \\ -\gamma_X\sin\mu & \cos\mu \end{bmatrix} ,$$

where,

$$\cos\mu = \cos\gamma\ell\cosh\gamma\ell + \gamma d\{\cos\gamma\ell\sinh\gamma\ell - \sin\gamma\ell\cosh\gamma\ell\}$$
$$- \frac{\gamma^2 d^2}{2}\sin\gamma\ell\sinh\gamma\ell ,$$

$$\gamma_X = \gamma \left[\frac{\{\sin \gamma\ell \cosh \gamma\ell - \sinh \gamma\ell\} + \gamma d\{\sin \gamma\ell \sinh \gamma\ell - (1 - \cos \gamma\ell)\cosh \gamma\ell\} -- }{\{\sin \gamma\ell \cosh \gamma\ell + \sinh \gamma\ell\} + \gamma d\{\sin \gamma\ell \sinh \gamma\ell + (1 + \cos \gamma\ell)\cosh \gamma\ell\}} \right.$$

$$---- \left. \frac{- \frac{\gamma^2 d^2}{2} (1 - \cos \gamma\ell)\sinh \gamma\ell}{+ \frac{\gamma^2 d^2}{2} (1 + \cos \gamma\ell)\sinh \gamma\ell} \right]^{1/2} \quad (6.5)$$

Then provided the stability condition

$$-1 < \cos \mu < +1$$

or

$$-1 < [\cos \gamma\ell \cosh \gamma\ell + \gamma d\{\cos \gamma\ell \sinh \gamma\ell - \sin \gamma\ell \cosh \gamma\ell\}$$

$$- \frac{\gamma^2 d^2}{2} \sin \gamma\ell \sinh \gamma\ell] < +1 \quad (6.6)$$

is satisfied it is apparent that in the X-Z plane the triplet exerts an overall focusing force on the particle. The projection of the particle's motion on the Y-Z or initially defocusing plane can be described in an analogous manner. Indeed, provided equation (6.6) is satisfied an overall focusing action also will result in the Y-Z plane.

A long chain of such triplets can be used to guide charged particles provided the components of the initial displacement and momentum along the X and Y axes are suitably restricted. In order that particles be confined within the structure it is necessary that the maximum displacements in the X and in the Y directions be less than, or at most equal to, the aperture radius of the structure. Thus, since the motion in the X-Z and Y-Z planes is uncoupled, $|X|_{max} \leq a$ and $|Y|_{max} \leq a$.

Smith,L. et al.(38) have shown that these conditions will be fulfilled when the following conditions are satisfied:

$$[\frac{X_o}{a}]^2 + [\frac{X'_o}{\gamma_X a}]^2 \leq 1 \qquad (6.7)$$

and

$$[\frac{\psi Y_o}{a}]^2 + [\frac{Y'_o}{\gamma_X \psi a}]^2 \leq 1 \qquad (6.8)$$

where,

X_o = initial X coordinate of the particle at injection,

$X'_o = \frac{P_{X_o}}{P_{Z_o}}$, P_{X_o} and P_{Z_o} are the injection X-directed transverse momentum and the injection axial momentum respectively,

Y_o = initial Y coordinate of the particle at injection,

$Y'_o = \frac{P_{Y_o}}{P_{Z_o}}$, P_{Y_o} is the injection Y directed transverse momentum,

$\psi^2 = \frac{a_{22}}{a_{11}}$.

The parameters a_{11} and a_{22} are the two diagonal elements of the transformation matrix $[T_1]$ of the first half of the triplet in the X-Z plane, that is

$$\begin{bmatrix} a_{11} & a_{12} \\ a_{21} & a_{22} \end{bmatrix} = \begin{bmatrix} \cosh \frac{\gamma \ell}{2} & \frac{1}{\gamma} \sinh \frac{\gamma \ell}{2} \\ \gamma \sinh \frac{\gamma \ell}{2} & \cosh \frac{\gamma \ell}{2} \end{bmatrix} \begin{bmatrix} 1 & d \\ 0 & 1 \end{bmatrix} \begin{bmatrix} \cos \frac{\gamma \ell}{2} & \frac{1}{\gamma} \sin \frac{\gamma \ell}{2} \\ -\gamma \sin \frac{\gamma \ell}{2} & \cos \frac{\gamma \ell}{2} \end{bmatrix}$$

Thus,

$$\psi^2 = \frac{\cos\frac{\gamma\ell}{2}\cosh\frac{\gamma\ell}{2} + \sin\frac{\gamma\ell}{2}\sinh\frac{\gamma\ell}{2} + \gamma d\cos\frac{\gamma\ell}{2}\sinh\frac{\gamma\ell}{2}}{\cos\frac{\gamma\ell}{2}\cosh\frac{\gamma\ell}{2} - \sin\frac{\gamma\ell}{2}\sinh\frac{\gamma\ell}{2} - \gamma d\sin\frac{\gamma\ell}{2}\cosh\frac{\gamma\ell}{2}} \tag{6.9}$$

In the limiting cases equations (6.7) and (6.8) describe the elliptic boundaries of the acceptance areas of the classical channel in the X - X' and the Y-Y' phase planes. For a particle to be successfully guided by the classical channel its injection conditions in both the X-X' and the Y-Y' phase planes should be within these elliptical boundaries. A particle with injection conditions outside these elliptical boundaries will have a maximum transverse displacement exceeding the aperture available and the particle will be lost. The areas bounded by the acceptance ellipses in the X-X' and the Y-Y' phase planes are equal and given by

$$A^C_{X-X'} = A^C_{Y-Y'} = \pi\, \gamma_X\, a^2 \tag{6.10}$$

For the special case of parallel injection along the classical structure, the maximum acceptable transverse injection conditions are independent of each other and their values are obtained from equations (6.7) and (6.8), by setting $X'_0 = 0$ and $Y'_0 = 0$, as

$$|X_0|_{max} = a \quad , \quad |Y_0|_{max} = \frac{a}{\psi} \quad . \tag{6.11}$$

Therefore, the acceptance area of the classical structures in the X-Y transverse coordinate plane is a rectangle whose area is

$$A^{C}_{X-Y} = \frac{a^2}{\psi} \quad \text{, where } \psi \text{ is given by equation (6.11).} \tag{6.12}$$

Similarly, for the special case of point source injection at $Z = 0$, the maximum acceptable values of the normalized injection transverse momenta are independent of each other and are obtained from equations (6.7) and (6.8), by setting $|X_0| = 0$ and $|Y_0| = 0$, as

$$|X'_0| = \gamma_X a \quad , \quad |Y'_0| = \psi\, \gamma_X a \tag{6.13}$$

Therefore, the acceptance area of the classical structure in the X'-Y' normalized transverse momenta plane is a rectangle whose area is

$$A^{C}_{X'-Y'} = \psi\, \gamma_X^2\, a^2 \tag{6.14}$$

6.2.2. The Twisted Structure

For the twisted structure values of X_{max} and Y_{max} cannot be specified separately as was the case for the classical quadrupole channel. In order that the particles be confined it was seen in Chapter 3 that the radial displacement must be at most equal to the aperture radius, a. Thus $r_{max} \leq a$. For particles confined within this circular aperture, equation (3.10) gives the acceptance limits of the twisted structure and shows how the maximum acceptable value of any of the injection conditions of a particle depends on the values of the other injection conditions of this particle. It is difficult to compute the acceptance limits for particles with general injection conditions and the comparison between the acceptance limits will be restricted to the special cases of parallel injection, point source injection, injection in the X-Z plane with X directed transverse momentum and injection in the Y-Z plane with Y directed transverse momentum. For these special cases the acceptance limits of the classical and the twisted structures in the X-Y transverse coordinate plane, in the X'-Y' transverse normalized momenta plane, in the X-X' phase plane and in the Y-Y' phase plane will be compared. The twisted structure will be assumed to have $(\beta a)^2 = 0.1$ in the computations which will follow.

The stability condition for the particle motion along the twisted structure, given by equation (3.3), can be written in terms of the normalized transverse momenta as,

$$|s| = \beta^2 a^2 \left|\frac{V}{V_0}\right| [1 + \beta(X_0 Y_0' - Y_0 X_0')]^2 > 1.0$$

For the special cases of injection to be considered in the comparison the term$(X_0 Y_0' - Y_0 X_0') = 0$. Also it was shown in Appendix B that for all particles successfully guided by the structure, $\beta(X_0 Y_0' - Y_0 X_0') \ll 1$. Therefore, for all acceptable injection conditions the stability condition can approximately be written as

$$|s| = 4\pi^2 \frac{a^2}{L^2} \left|\frac{V}{V_0}\right| = \frac{\pi^2}{4} \left[\frac{4a}{L} \sqrt{\frac{V}{V_0}}\right]^2 > 1.0$$

or in terms of γ as defined by equation (6.4),

$$|s| = \frac{\pi^2}{4}\left[\frac{4}{\gamma L}\right]^2 > 1 \qquad (6.15a)$$

From equation (6.15a) it is apparent that

$$0 < \frac{\gamma L}{4} < \frac{\pi}{2} \qquad (6.15b)$$

It is interesting to note that for particles guided by the classical channel equation (6.6) leads to the condition

$$0 < \frac{\gamma L}{4} < 1.873 \qquad (6.15c)$$

when there is no driftspace.

For particles injected in the X-Z plane with X directed transverse momentum, the acceptance limits are given by equation (3.14) which in terms of X_0 and X_0' becomes

$$\left\{\frac{|X_0'| - |\beta a|\sqrt{s}\,\sqrt{s - 1}}{|\beta a|\sqrt{\frac{s + 1}{s}}(s - 1)}\right\}^2 - \left\{\frac{X_0}{a\sqrt{s^2 - 1}}\right\}^2 \leq 1.0 \qquad (6.16)$$

Equation (6.16) represents the intersections of two hyperbolae and gives the maximum allowable values of $|X_0|$ and $|X_0'|$, for particles injected with $Y_0 = Y_0' = 0$, as

$$|X_0|_{max} = a \qquad \text{when} \qquad X_0' = 0$$

and

$$|X_0'|_{\max} = \frac{|\beta a|}{\sqrt{s}} \frac{1}{\sqrt{s+1} + s/\sqrt{s-1}} \quad \text{when} \quad X_0 = 0 \ .$$

The acceptance area bounded by the hyperbolae described by equation (6.16) is

$$A^T_{X-X'} = 4\int_0^a X_0' \, dX_0$$

$$= 4\beta a \int_0^a [\sqrt{s}\sqrt{s-1} - (s-1)\sqrt{\frac{s+1}{s}}\{1 + (\frac{X_0}{a\sqrt{s^2-1}})^2\}]^{1/2} dX$$

$$= \frac{4}{L}[\sqrt{s}\sqrt{s-1} - (s^2-1)\sqrt{\frac{s-1}{s}} \, \ell n\sqrt{\frac{s+1}{s-1}}]\pi a^2 , \qquad (6.17)$$

where ℓn denotes the natural logarithm.

For the special case of injection in the Y-Z plane with Y directed transverse momentum, the acceptance limits are given by equation (3.15) which in terms of Y_0 and Y_0' becomes

$$\frac{s}{s-1}[\frac{Y_0}{a}]^2 + 2\frac{s}{|\beta a|}|Y_0'| \le 1 \qquad (6.18)$$

representing the intersection of two parabolas. Equation (6.18) gives the maximum allowable values of $|Y_0|$ and $|Y_0'|$, for a particle injected with $X_0 = X_0' = 0$, as

$$|Y_0|_{\max} = \sqrt{\frac{s-1}{s}} \, a \quad , \qquad Y_0' = 0$$

and

$$|Y_0'|_{max} = \frac{|\beta a|}{2s} \quad , \quad Y_0 = 0$$

The acceptance area bounded by the parabolas described by equation (5.18) is,

$$A^T_{Y-Y'} = 4\int_0^{a\sqrt{\frac{s-1}{s}}} Y_0' \, d\, Y_0$$

$$= 4\int_0^{a\sqrt{\frac{s-1}{s}}} \frac{\beta a}{2s}\left[1 - \frac{s}{s-1}\,\frac{Y_0^{\,2}}{a}\right] d\, Y_0$$

$$= \frac{8}{3L}\sqrt{\frac{s-1}{s}}\;\frac{1}{s}\,\pi a^2 \tag{6.19}$$

For parallel injected particles the acceptable injection points (X_0, Y_0) should be within the parallelogram shaped area bounded by the straight lines, given by the limit of equation (3.12),

$$\left|\frac{X_0}{a}\right| + \sqrt{\frac{s}{s-1}}\,\left|\frac{Y_0}{a}\right| \leq 1 \tag{6.20}$$

and the acceptance area of the twisted structure in the X-Y transverse coordinate plane is

$$A^T_{X-Y} = 4\int_0^a Y_0 \, d\, X_0$$

$$= 4\int_0^a \sqrt{\frac{s-1}{s}}\,[a - X_0]\,d\,X_0$$

$$= 2\sqrt{\frac{s-1}{s}}\,a^2 \qquad (6.21)$$

For point source injection, equation (3.13) can be rewritten in terms of X_0' and Y_0' to give the acceptance limits of the twisted structure as

$$\left|[s^2\,Y_0'^2 + s(s+1)X_0'^2]^{1/2}\right| + \sqrt{\frac{s}{s-1}}\left|[s^2\,X_0'^2 + s(s-1)Y_0'^2]^{1/2}\right|$$

$$\leq |\beta a| \qquad (6.22)$$

and the acceptance area of the twisted structure in the X' - Y' phase plane is

$$A^T_{X'-Y'} = 4\int_0^{X'_{0_{max}}} Y_0'\,d\,X_0'\ ,$$ where X_0' and Y_0' are related by equation

(6.22) and $X'_{0_{max}} = \dfrac{|\beta a|}{\sqrt{s}}\,\dfrac{1}{\sqrt{s+1} + s/\sqrt{s-1}}$

$$= 4\int_0^{X'_{0_{max}}} \frac{1}{2\beta as}\left[\beta^4 a^4 - \beta^2 a^2\,\frac{4s^3 - 2s}{(s-1)}\,X_0'^2 + \frac{s^2}{(s-1)^2}\,X_0'^4\right]^{1/2} dX_0'$$

No analytical expression was obtained for $A^T_{X'-Y'}$ but its value can be calculated through numerical integration of equation (6.23).

6.3 Acceptance Comparison

The first objective of this section is to compare the acceptance limits of classical structures having $\frac{d}{\ell} = 0$, 0.125 and 0.25 with those of the twisted structure. Computation of the acceptance areas in the X - X' and the Y - Y' phase planes is performed over the stable range of V_0 and hence the stable range of $\frac{\gamma L}{4}$ for each of these four guiding structures. As mentioned before, the length of each of the symmetrical triplets constituting either one of the three classical channels is equal to half the periodic length of twist of the twisted structure. Thus for any value of $\frac{d}{\ell}$, $\gamma\ell$ and $\frac{\gamma L}{4}$ are related by

$$\frac{\gamma L}{4} = \gamma\ell(1 + \frac{d}{\ell}) \tag{6.24}$$

For the classical structure with no drift space, $\frac{d}{\ell} = 0$, $\gamma\ell = \frac{\gamma L}{4}$ and from equation (6.15c)

$$0 < \frac{\gamma L}{4} < 1.873 \tag{6.25}$$

For the classical structures with $\frac{d}{\ell} = 0.125$ and 0.25 the stable range of $\gamma\ell$ was computed using equation (6.6), then equation (6.24) was used to compute the corresponding range of $\frac{\gamma L}{4}$ as

$$0.0 < \frac{\gamma L}{4} < 1.89 \qquad \text{for } \frac{d}{\ell} = 0.125 \tag{6.26}$$

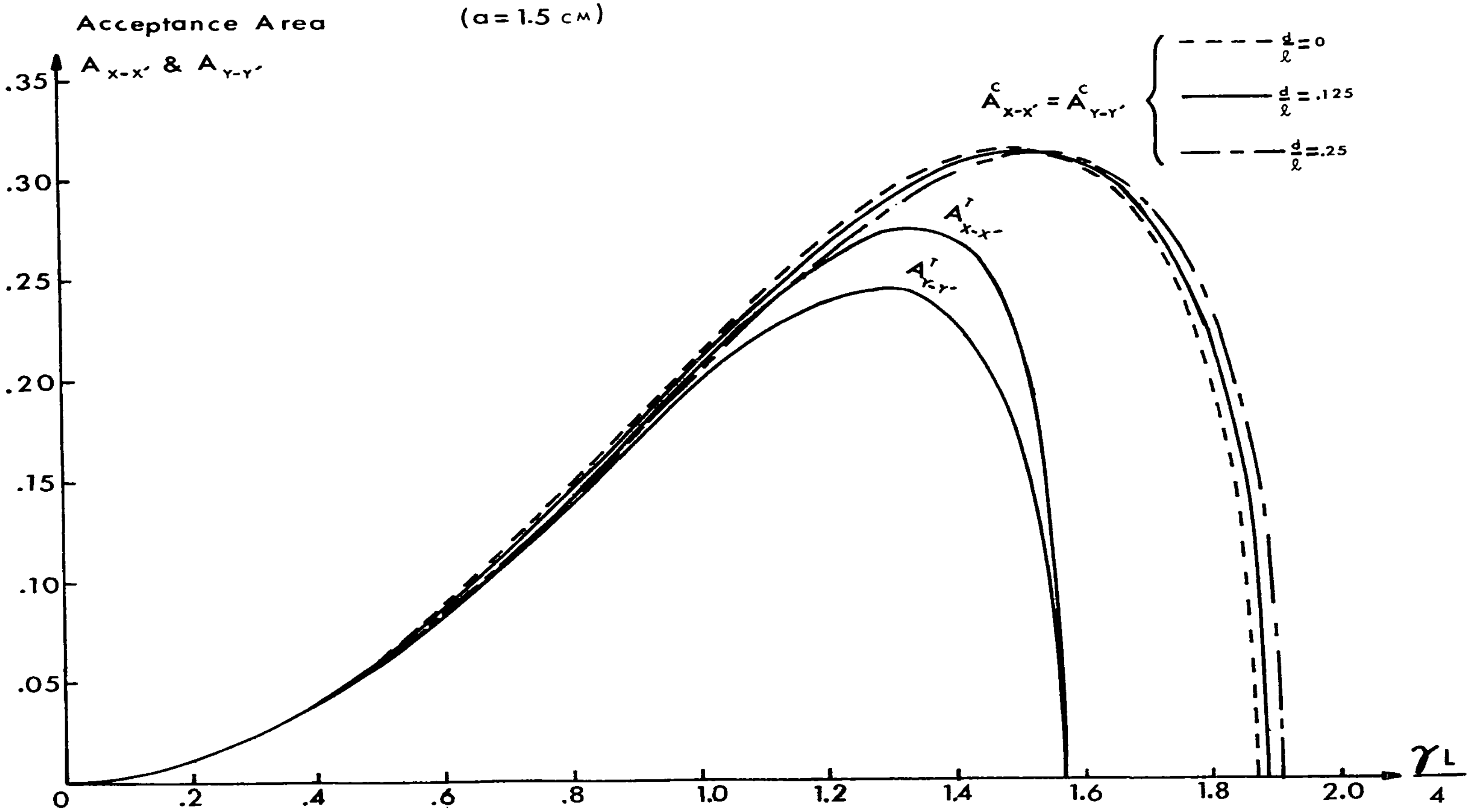

Figure (6.2) The Acceptance Areas in the X-X' and Y-Y' Phase Planes.

and

$$0 < \frac{\gamma L}{4} < 1.91 \qquad \text{for } \frac{d}{\ell} = 0.25 \tag{6.27}$$

The acceptance areas in the X - X' and the Y - Y' phase planes, $A^C_{X-X'}$, $A^C_{Y-Y'}$, $A^T_{X-X'}$ and $A^T_{Y-Y'}$, were computed using equations (6.10), (6.17) and (6.19). The computations were performed for the twisted structure and the classical structures having $\frac{d}{\ell} = 0$, 0.125 and 0.25, over the stable ranges of $\frac{\gamma L}{4}$ given by equations (6.15b), (6.25), (6.26) and (6.27) respectively. Figure (6.2) shows these acceptance areas drawn versus $\frac{\gamma L}{4}$. It is clear that the increase of $\frac{d}{\ell}$ from 0 to 0.25 decreases the acceptance areas $A^C_{X-X'}$ and $A^C_{Y-Y'}$ of the classical structures in the range $0 < \frac{\gamma L}{4} < 1.54$ radians while it increases them over the range of $\frac{\gamma L}{4}$ higher than 1.54 radians. It is also clear from figure (6.2) that for values of $\frac{\gamma L}{4}$ up to 1.0 the acceptance areas $A^T_{X-X'}$ and $A^T_{Y-Y'}$ of the twisted structure are nearly equal to those of the classical structures. For the range $1.0 < \frac{\gamma L}{4} < 1.3$, the acceptance areas of the classical structure having $\frac{d}{\ell} = 0$ are larger than the X - X' phase plane acceptance area of the twisted structure by less than 6% while they are larger than the Y - Y' acceptance areas of the twisted structure by less than 12%. For the range $\frac{\gamma L}{4} > 1.3$ the acceptance areas of the classical structure are much larger than those of the twisted structure since the latter drop rapidly for $\frac{\gamma L}{4} > 1.3$.

Equations (6.5), (6.7), (6.8), (6.9), (6.16) and (6.18) were used to compute the acceptance limits in the X - X' and the Y - Y' phase planes for the twisted structure and the classical structure having $\frac{d}{\ell} = 0$. These acceptance limits are shown in figures (6.3) and (6.4) for three different values of quadrupole voltage corresponding to s = 1.5, 2 and 3 or

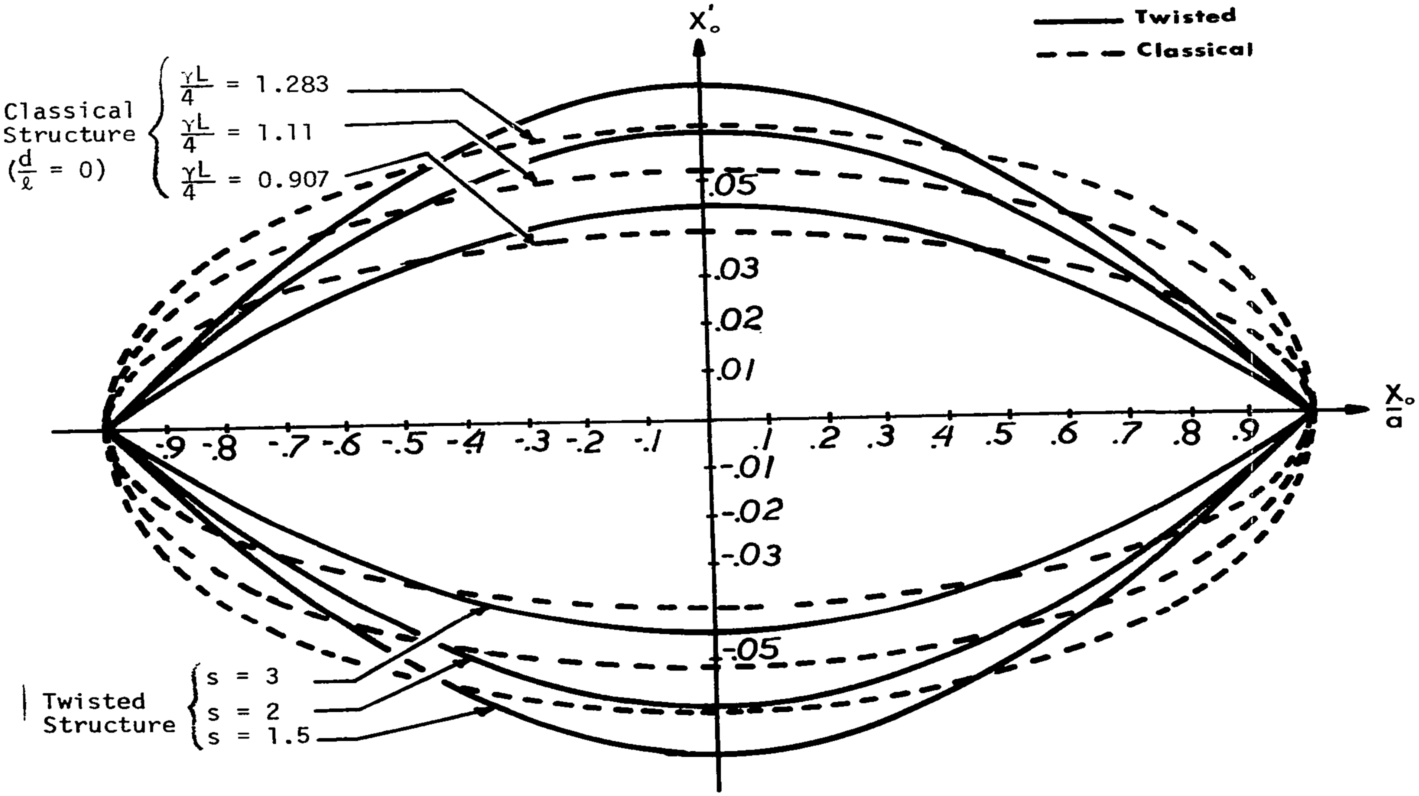

Figure (6.3) The Acceptance Limits in the X-X' Phase Plane.

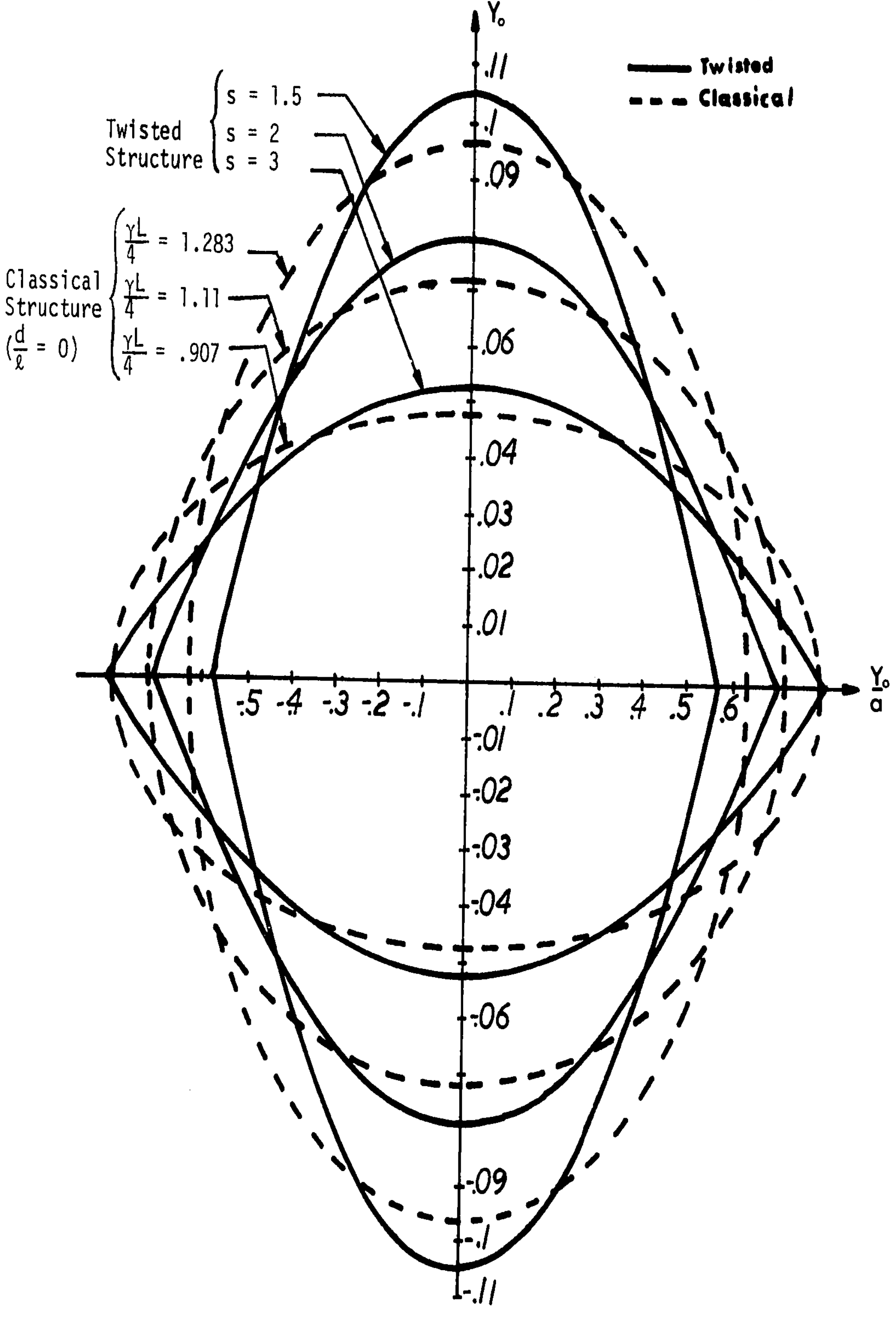

Figure (6.4) The Acceptance Limits in the Y-Y' Phase Plane.

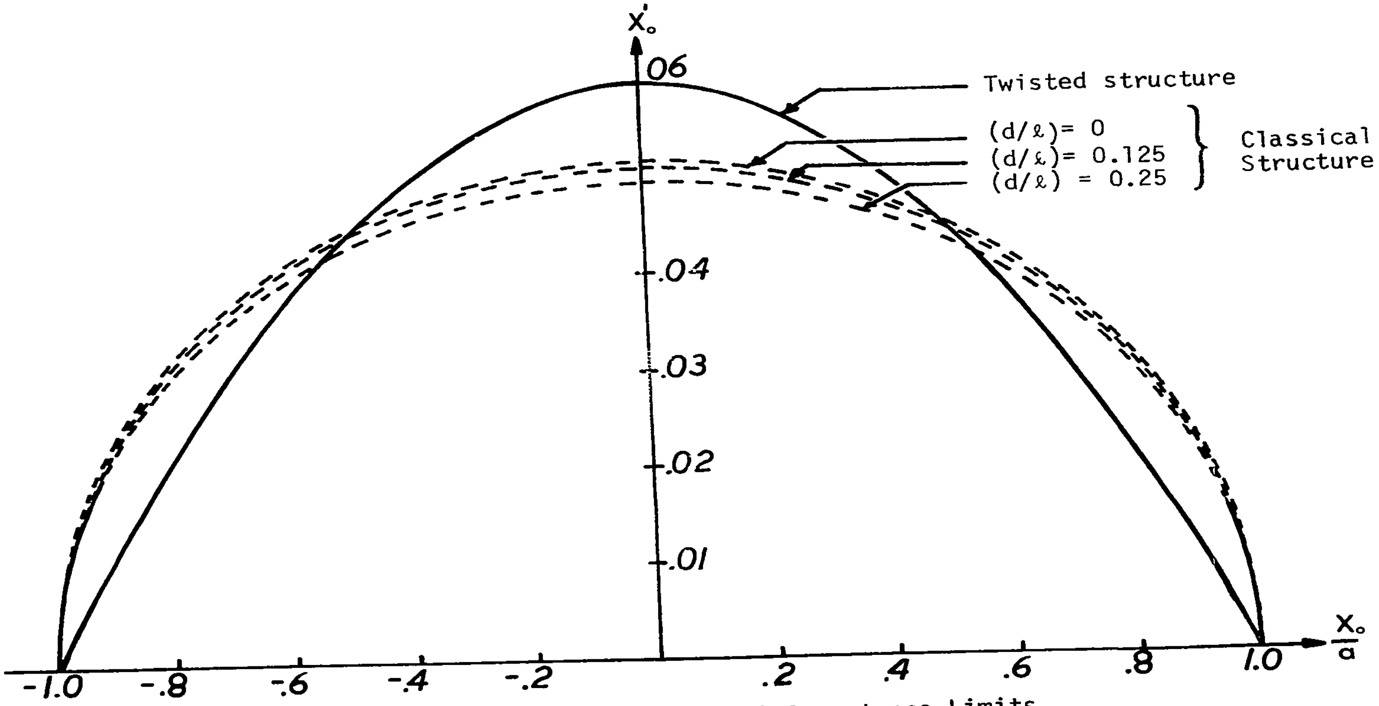

Figure (6.5) Effect of Drift Space on the X-X' Acceptance Limits of Classical Structures.

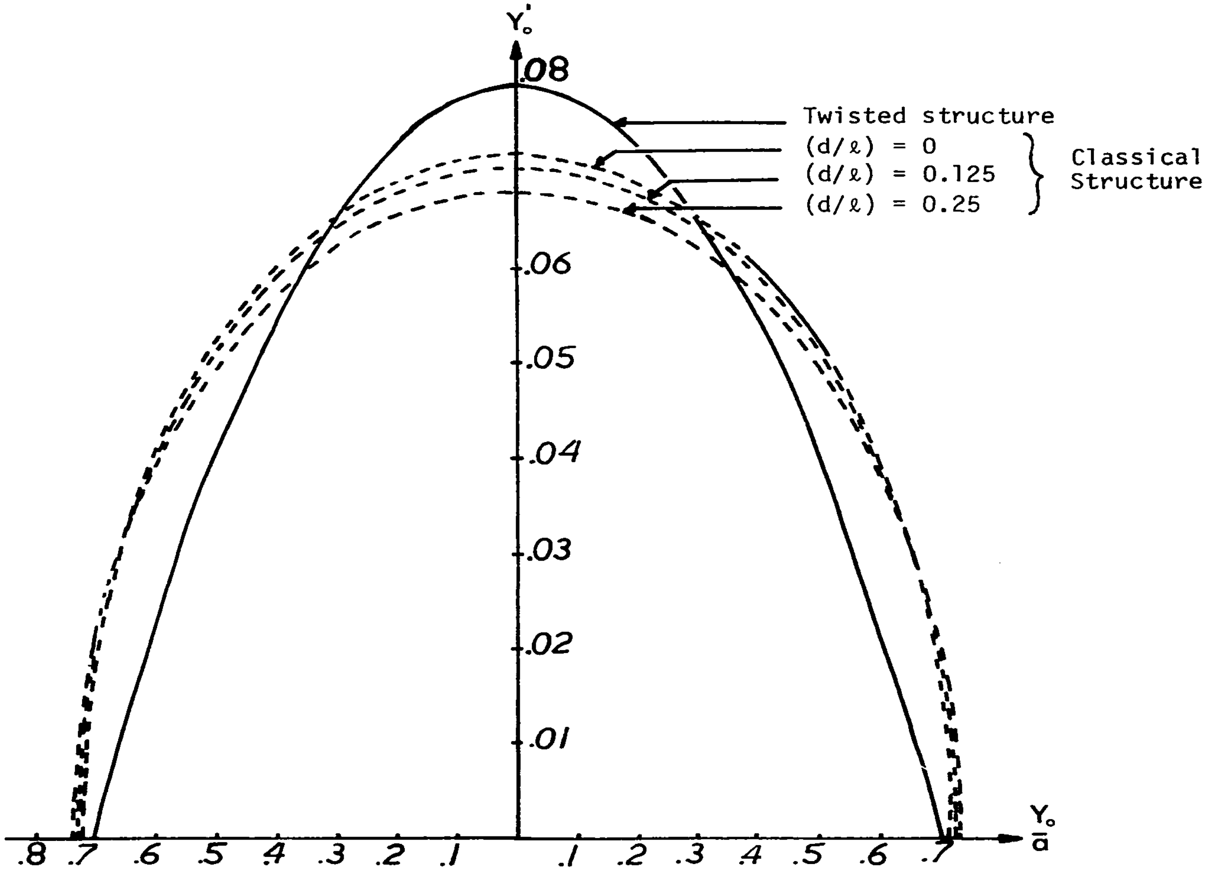

Figure (6.6) Effects of Drift Space on the Y-Y' Acceptance Limits of Classical Structures.

$\frac{\gamma L}{4}$ = 1.283, 1.11 and 0.907. These figures show clearly that even though $A^C_{X-X'}$ and $A^C_{Y-Y'}$ are slightly larger than $A^T_{X-X'}$ and $A^T_{Y-Y'}$ the acceptable maximum values of the normalized transverse momentum at injection, $|X'_o|_{max}$ and $|Y'_o|_{max}$, are considerably larger for the twisted structure than for the classical structure. Note also that for s = 3, $|Y_o|_{max}$ for the twisted structure is slightly larger than $|Y_o|_{max}$ for the classical channel. For s = 2 and s = 1.5 the values of $|Y_o|_{max}$ for the twisted structure become smaller than the corresponding values of $|Y_o|_{max}$ for the classical channel.

Equations (6.7), (6.8) and (6.9) were then used to compute the X - X' and the Y - Y' phase plane acceptance limits for the classical structures having $\frac{d}{\ell}$ = 0.125 and 0.25 for one value of $\frac{\gamma L}{4}$ = 1.11 which corresponds to s = 2. These acceptance limits, as well as those previously computed for the twisted structure and the classical structure having $\frac{d}{\ell}$ = 0 at s = 2 as $\frac{\gamma L}{4}$ = 1.11 radians, are shown in figures (6.5) and (6.6). It is clear from these figures that as $\frac{d}{\ell}$ increases the acceptable normalized transverse momenta, $|X'_o|_{max}$ and $|Y'_o|_{max}$, decrease for the classical structure. For $\frac{d}{\ell}$ = 0.25 and $\frac{\gamma L}{4}$ = 1.11 radians, the value of $|X'_o|_{max}$ acceptable by the classical structure is 0.0499 while that acceptable by the twisted structure is 0.0599. Also the value of $|Y'_o|_{max}$ acceptable by the classical structure having $\frac{d}{\ell}$ = 0.25, at $\frac{\gamma L}{4}$ = 1.11, is 0.0679 while that acceptable by the twisted structure is 0.079.

For the special case of parallel injection, equations (6.9), (6.11) and (6.20) were used to compute the acceptance limits in the X - Y transverse coordinate plane. The computations were performed for the twisted structure and for the classical structures having $\frac{d}{\ell}$ = 0, 0.125 and 0.25

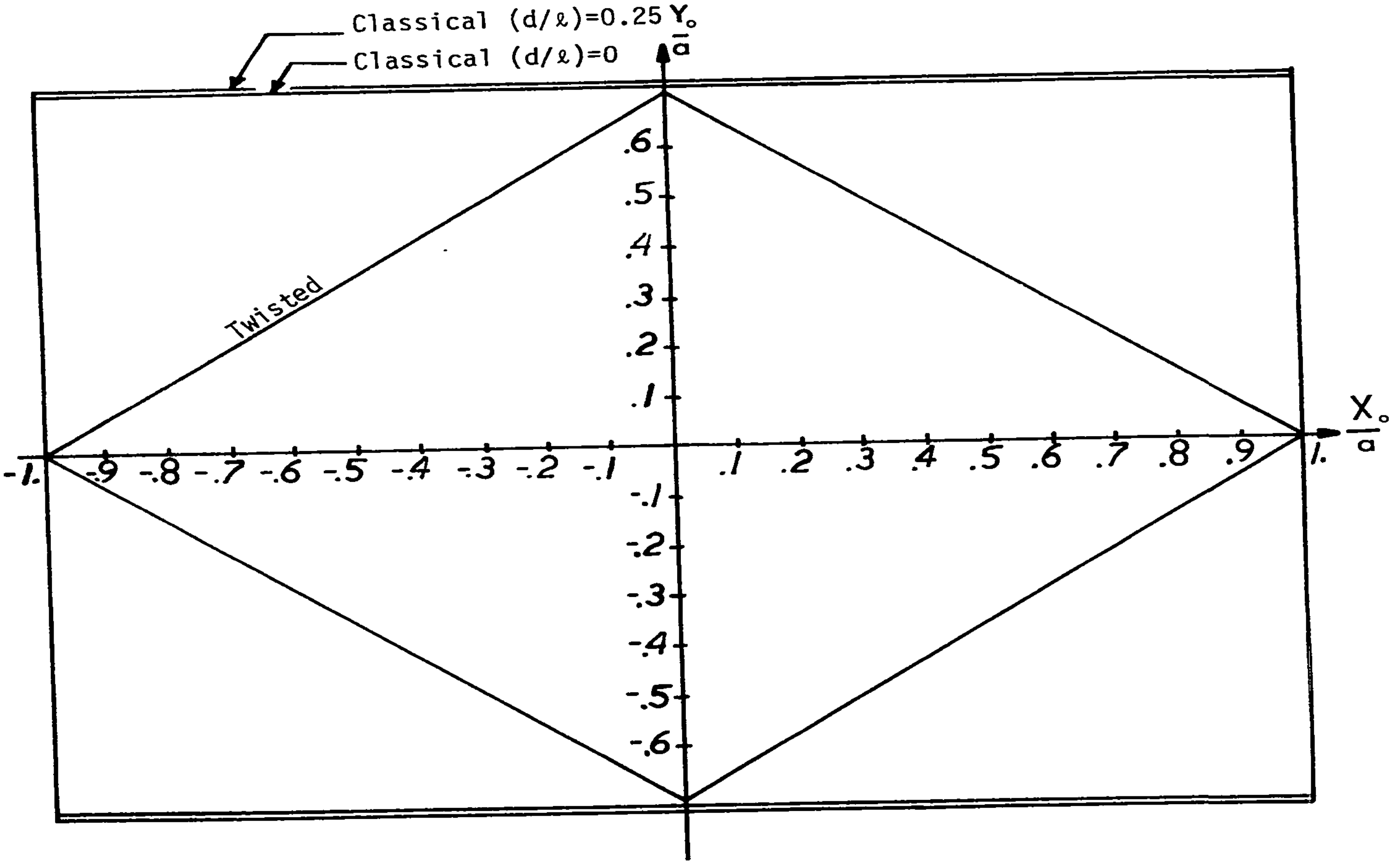

Figure (6.7) Effect of Drift Space on the $\frac{X}{a}$ - $\frac{Y}{a}$ Acceptance Limits of Classical Structures.

at s = 2 and the corresponding $\frac{\gamma L}{4} = 1.11$ radians. The computed acceptance limits are shown in figure (6.7) where the axes of the transverse coordinate plane are normalized with respect to the aperture radius. The areas in the X - Y plane available for parallel injection along the twisted structure and the classical structures considered were computed using equations (6.12) and (6.21) as

$$A^T_{X-Y} = 1.414\ a^2 \quad ,$$

$$A^C_{X-Y} = 2.8932\ a^2 \qquad \text{for } \frac{d}{\ell} = 0 \quad ,$$

$$A^C_{X-Y} = 2.906476\ a^2 \qquad \text{for } \frac{d}{\ell} = 0.125 \quad ,$$

$$A^C_{X-Y} = 2.93595\ a^2 \qquad \text{for } \frac{d}{\ell} = 0.25 \quad .$$

It is clear that the acceptance area in the X - Y transverse coordinates plane for the twisted structure is much less than the acceptance areas in the X - Y plane for classical structures with or without drift spaces. This situation is due to the coupling of the motion in the X - Z plane and the Y - Z plane of the twisted structure. Recall that in the case of the classical structure $|X|_{max} \leq a$ and $|Y|_{max} \leq a$ independently while for the twisted structure $(X^2 + Y^2)_{max} \leq a^2$. Of course the classical case is somewhat idealized since it completely ignores all fringing effects.

For the special case of point source injection at Z = 0, equations (6.9), (6.13) and (6.22) were used to compute the acceptance limits in the X' - Y' transverse normalized momentum plane. These acceptance limits are

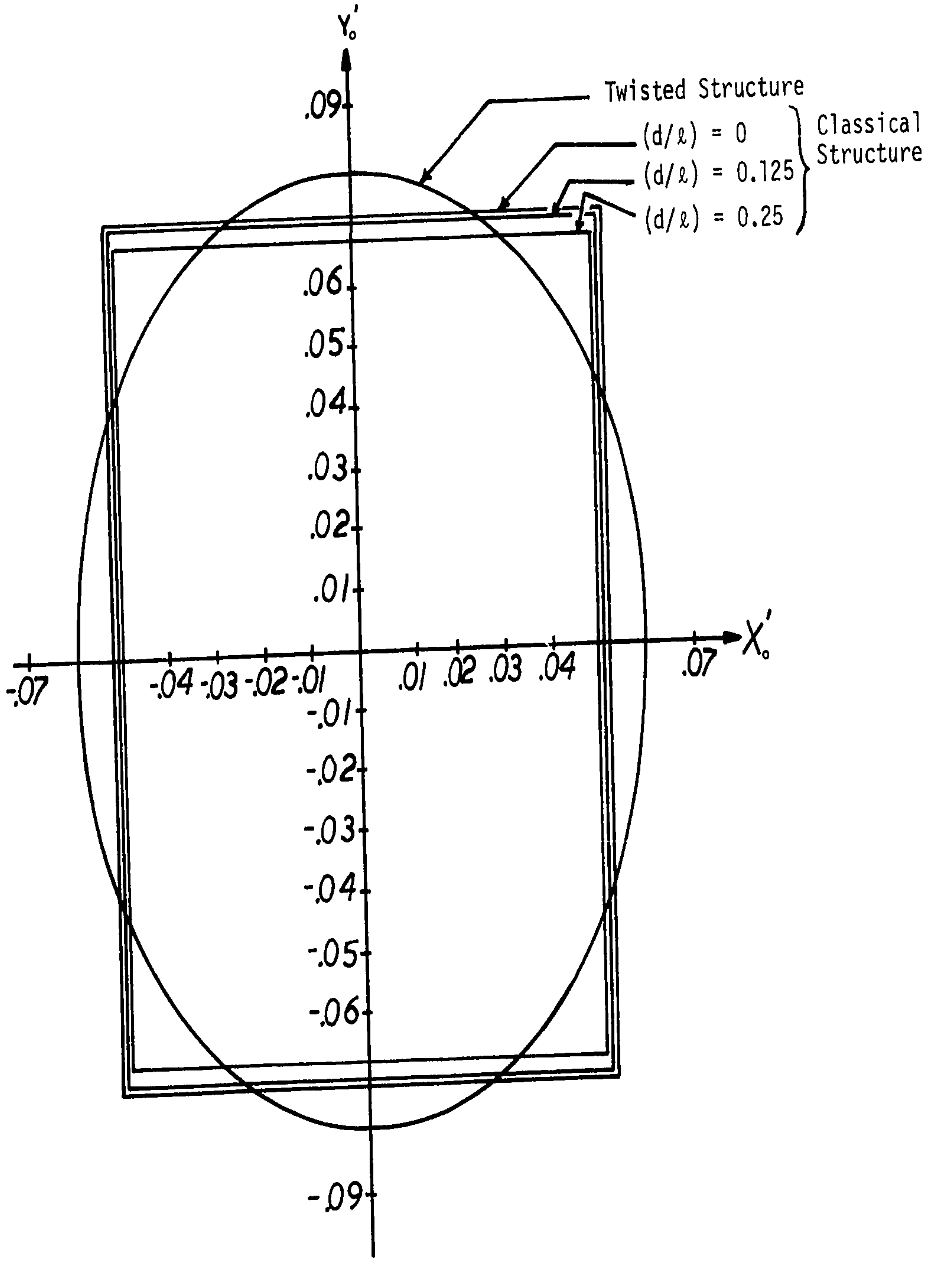

Figure (6.8) Effect of Drift Space on the X'-Y' Acceptance Limits of Classical Structures.

shown in figure (6.8) for the same quadrupole potential, s = 2 , and the same structures as considered in the case of parallel injection. The acceptance areas in the X' - Y' plane were computed using equation (6.14) and numerically integrating equation (6.23) using the approximate expression

$$A^T_{X'-Y'} = \sum_{j=0}^{100} \frac{|X'_o|_{max}}{100} [Y'_{o_{j+1}} - Y'_{o_j}]$$

where Y'_{o_j} is the value of Y'_o evaluated from equation (6.22) at $X'_o = j\frac{|X'_o|_{max}}{100}$. The acceptance areas in the X' - Y' plane were found to be:

$$A^T_{X'-Y'} = 0.0149$$

$$A^C_{X'-Y'} = 0.0149 \qquad \text{for } \frac{d}{\ell} = 0$$

$$A^C_{X'-Y'} = 0.0145 \qquad \text{for } \frac{d}{\ell} = 0.125$$

$$A^C_{X'-Y'} = 0.0136 \qquad \text{for } \frac{d}{\ell} = 0.25$$

Based on the degree of accuracy of the numerical integration the areas $A^T_{X'-Y'}$ and $A^C_{X'-Y'}$ are essentially equal for $\frac{d}{\ell} = 0$ while for the practical values of $\frac{d}{\ell} = 0.125$ and 0.25 $A^T_{X'-Y'}$ is larger than $A^C_{X'-Y'}$. Figure (6.8) also shows, as was pointed out earlier, that $|X'_o|_{max}$ and $|Y'_o|_{max}$ are significantly larger for the twisted structure than for the classical structures having $\frac{d}{\ell} = 0 \rightarrow 0.25$.

The above comparison shows that the X-Y acceptance of the twisted structure is smaller than that of the classical structure with or without drift spaces. However, the comparison shows that the twisted structure allows more divergence of the beam than that allowed by the classical structures, especially those with drift spaces. This larger acceptance area of the twisted structure in the X' - Y' phase plane makes it very suitable for guiding beams emerging from point sources.

6.4 The Focusing Strength

The focusing strengths of the twisted structure and the classical structure having $\frac{d}{\ell} = 0$ can be compared by tracing particle trajectories along both structures. The projections of these trajectories on the X-Z and the Y-Z planes were computed and plotted for each particle traced. On the X-Z or the Y-Z planes, the projection of a particle trajectory along the structure which has a higher focusing strength in the respective plane should intersect the Z axis before the intersection of the projection of the trajectory of the same particle along the other structure.

Equations (2.31), (2.35) and the transformation equations (2.7) were used to compute the X-Z and the Y-Z projections of the trajectories along the twisted structure. For the trajectories along the classical structure, the X-Z plane projections were computed using the matrix representation of equation (6.2) along each of the symmetrical triplets. The Y-Z projections along each of the triplets were computed using the matrix representation(39)

$$\begin{bmatrix} Y_i \\ \\ Y_i' \end{bmatrix} = [T_1] \quad [T_2] \begin{bmatrix} Y_{io} \\ \\ Y_{io}' \end{bmatrix} \text{, for the } \underline{ith} \text{ triplet.}$$

where $[T_1]$ and $[T_2]$ are as defined by equations (6.3a) and (6.3b).

Particles with various injection conditions were considered in the comparison of the focusing strengths of the twisted and the classical structure. Some of these conditions were within the acceptance limits of one structure only. For all cases considered, it was found that the twisted structure has a higher focusing strength in either the X-Z plane or in the Y-Z planes than has the classical structure.

Figure (6.9) shows the Y-Z projections of the trajectories of a particle injected at $Z = 0$ with $X_0 = Y_0 = X_0' = 0.0$ and $Y_0' = 0.07$. These injection conditions are within the acceptance limits of both structures. It is clear that the twisted structure has a higher focusing strength in the Y-Z plane than has the classical structure.

For a parallel beam injected at $X_0 = \frac{a}{2}$ and $Y_0 = 0$, figure (6.10) shows the X-Z projections of the trajectories along the twisted and the classical structures. Note that the trajectory along the classical structure returns to $X = 0$ just after the return of the trajectory along the twisted structure to $X = 0$. Again, the twisted structure has a slightly higher focusing strength in the X-Z plane than has the classical structure.

It is clear from the above examples that the twisted structure is more strongly focusing than is the classical structure with no drift space. Moreover, because of the absence of drift spaces, the classical channel is itself stronger focusing than any practically realizable

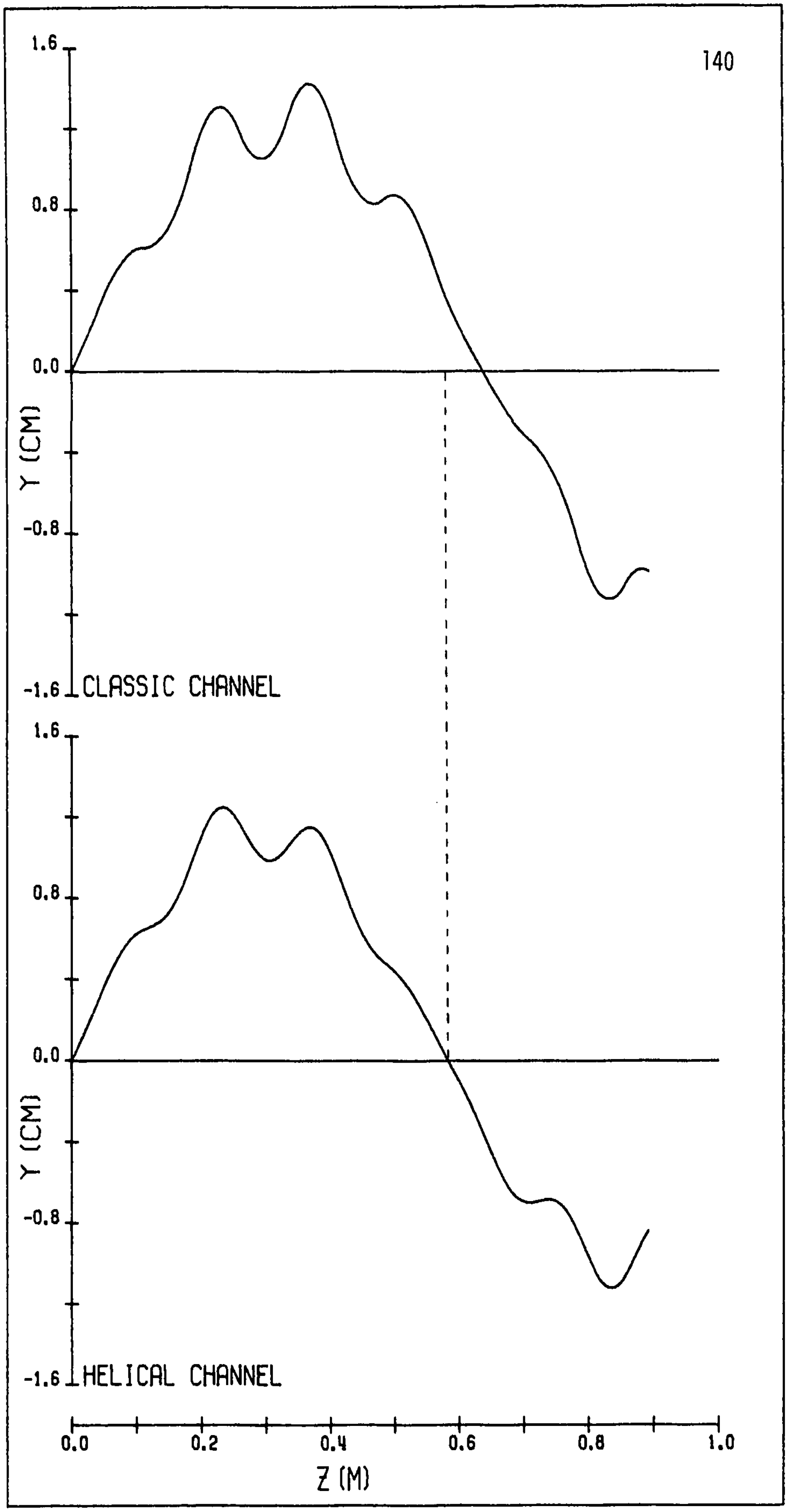

Figure (6.9) The Y-Z Projections of the Trajectory of a Particle Along the Twisted Structure and Along the Classical Structure with $\frac{d}{\ell} = 0$, when ($X_0 = 0$, $Y_0 = 0$).

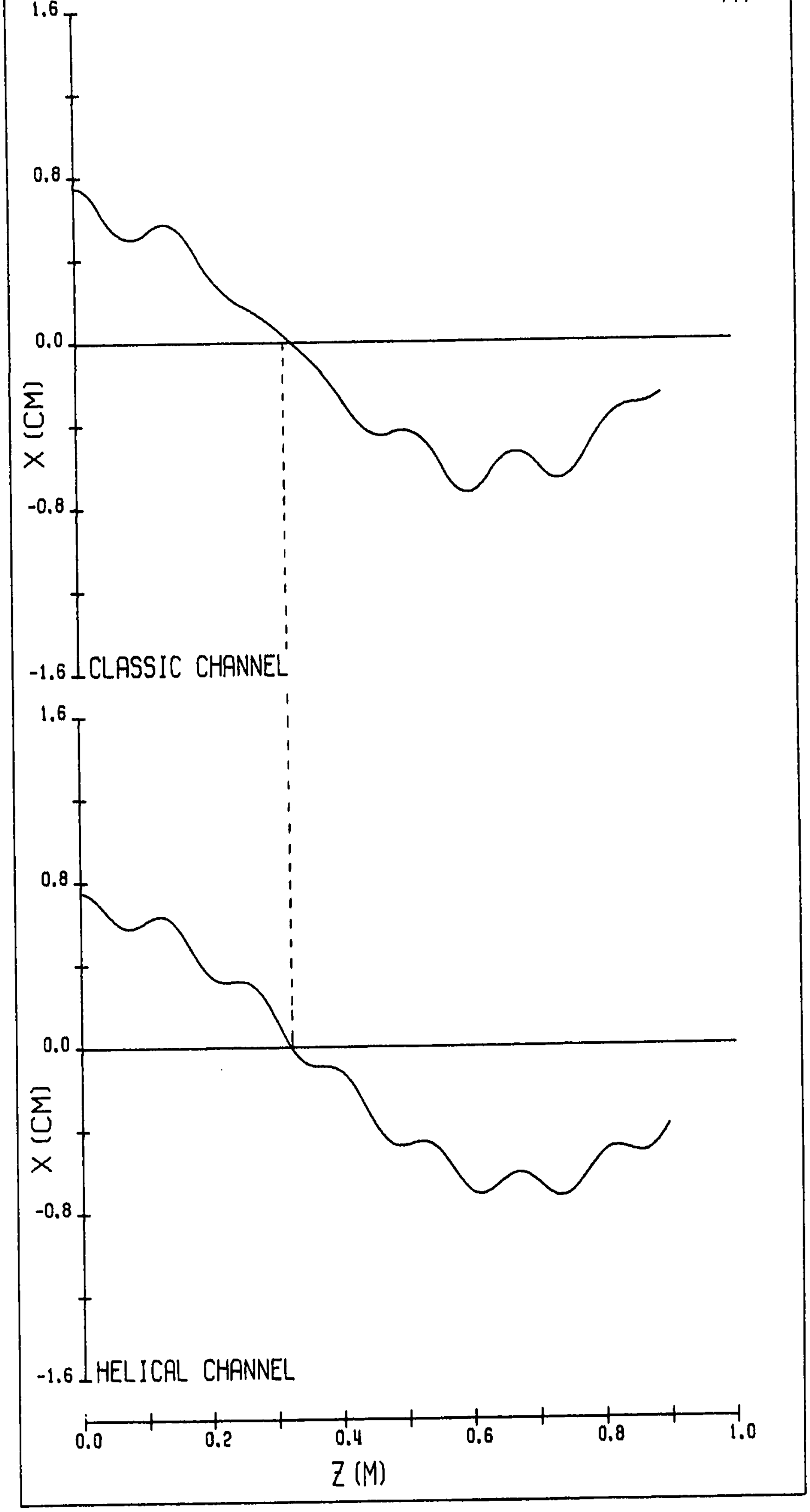

Figure (6.10) The X-Z Projections of the Trajectory of a Particle Along the Twisted Structure and Along the Classical Structure with $\frac{d}{\ell} = 0$, when ($X_0 = \frac{a}{2} = 0.75$ cm, $Y_0 = 0$, $X_0' = 0$, $Y_0' = 0$).

classical channel. This stronger focusing action of the twisted channel indicates the possibility of shorter focusing structures than are realizable with a classical structure.

CHAPTER 7

THE ELECTROSTATIC TWISTED QUADRUPOLE AS A NOVEL IDENTICAL IMAGING LENS

7.1 Introduction

The analytic solution for charged particle trajectories along the uniformly twisted electrostatic quadrupole was developed in Chapter 2 using two approaches. These were the contact transformation approach and the linear algebra approach. The two different forms of the solution were then shown to be equivalent in Appendix C. The first solution, shown in equations (2.31) and (2.35) was successfully used for studying the guiding properties of a long uniformly twisted electrostatic quadrupole channel. The second solution, shown in equations (2.49) and (2.50) and describing the particle trajectories in a matrix form in terms of the injection conditions is in suitable form to show that a finite length of the twisted structure can serve as an imaging device.

Examination of the matrix Q(t) of equation (2.50) shows that all elements are dependent on f_1t, f_2t as well as s, βp_z and 2qMk. Through proper choice of the structure parameters the values of f_1 and f_2 can be adjusted so that at a certain time t_1 all nondiagonal terms of the matrix will vanish while the four diagonal terms will all be + 1.0 or all be - 1.0. Hence,at this time t_1,and at the corresponding length of the structure,the transformation matrix $Q(t_1)$ will be either +I or -I, where I is the 4x4 identity matrix.

It will be shown in detail that the twisted lens structure with the properly chosen parameters will provide identical imaging of the injection conditions at $Z = 0$, the lens injection plane, into a target plane at $Z = \ell$, the lens exit plane. Identical imaging means that the exit coordinates and momenta in the target plane are equal, with or without inversion, to the coordinates and momenta at injection. The target plane has its axes rotated an angle $\beta\ell$ with respect to the fixed (X,Y) axes that coincide with the electrodes axes at $Z = 0$ as defined in Chapter 2.

The study of the imaging of a single particle by the twisted lens is followed by a discussion and a numerical study of the aberration that takes place when a beam of particles is considered. It is shown that the degree of aberration is small and that it can be further reduced by following the twisted lens structure by an equal but oppositely twisted lens structure.

This chapter then presents a numerical study of the effect, on the imaging properties of the lens, of detuning the quadrupole voltage, about the exact imaging value. The study also discusses the characteristics of the exit beam cross-section for various values of drift space beyond the end of the lens. This last part of Chapter 7 forms the basis for the experimental investigations of the lens properties described in Chapter 8.

7.2 Particle Imaging

The matrix representation of the motion of a charged particle along the twisted structure is given by equation (2.49) as,

$$\begin{bmatrix} x(t) \\ y(t) \\ p_x(t) \\ p_y(t) \end{bmatrix} = [Q(t)] \begin{bmatrix} x_0 \\ y_0 \\ p_{x_0} \\ p_{y_0} \end{bmatrix} \tag{7.1}$$

where x_0, y_0, p_{x_0} and p_{y_0} are the initial transverse displacements and their initial conjugate momenta at $t = 0$, $Z = 0$ with respect to the rotating coordinate system (x,y,z). $x(t)$, $y(t)$, $p_x(t)$ and $p_y(t)$ are the transverse displacements and their conjugate momenta at time t, also with respect to the rotating coordinate system. For the convenience of the reader the matrix Q(t) is reproduced on the following page and renamed equation (7.2).

It is now clear that a particle's coordinates and momenta will be imaged in the rotating coordinate system at some distance along the structure, if at some time, $t = t_1$,

$$Q(t_1) = \pm I \tag{7.3}$$

where I is the 4x4 unit matrix. If $Q(t_1) = - I$ the particle's coordinates and momenta will be imaged in an inverted form. In other words $x(t_1) = -x_0$, $y(t_1) = -y_0$, $p_x(t_1) = -p_{x_0}$ and $p_y(t_1) = -p_{y_0}$. The conditions which must be

$$
Q(t) = \left[\begin{array}{c|c|c|c}
\cos f_1 t & \frac{\beta p_z}{\sqrt{2Mqk}} \frac{\sin f_2 t}{\sqrt{s-1}} & \frac{\sqrt{s+1}}{\sqrt{2Mqk}} \sin f_1 t - \frac{s}{\sqrt{2Mqk}} \frac{\sin f_2 t}{\sqrt{s-1}} & \frac{\beta p_z}{2Mqk} (\cos f_2 t - \cos f_1 t) \\
\hline
- \frac{\beta p_z}{\sqrt{2Mqk}} \frac{\sin f_1 t}{\sqrt{s+1}} & \cos f_2 t & \frac{\beta p_z}{2Mqk} (\cos f_1 t - \cos f_2 t) & \frac{s}{\sqrt{2Mqk}} \frac{\sin f_1 t}{\sqrt{s+1}} - \frac{\sqrt{s-1}}{\sqrt{2Mqk}} \sin f_2 t \\
\hline
- \frac{\sqrt{2Mqk}}{\sqrt{s+1}} \sin f_1 t & 0 & \cos f_1 t & \frac{\beta p_z}{\sqrt{2Mqk}} \frac{\sin f_1 t}{\sqrt{s+1}} \\
\hline
0 & \frac{\sqrt{2Mqk}}{\sqrt{s-1}} \sin f_2 t & - \frac{\beta p_z}{\sqrt{2Mqk}} \frac{\sin f_2 t}{\sqrt{s-1}} & \cos f_2 t
\end{array}\right] \qquad (7.2)
$$

imposed on the elements of the matrix so that it becomes either +I or -I are:

$$\cos f_1t_1 = \cos f_2t_1 = \pm 1 \quad ,$$

$$\sin f_1t_1 = \sin f_2t_1 = 0 \quad .$$

or

$$f_1t_1 = m\pi \quad ,$$

$$f_2t_1 = n\pi \quad . \tag{7.4}$$

where m and n are integers, both odd or both even so that the term $\frac{\beta p_z}{2qMk}\{\cos f_2t_1 - \cos f_1t_1\} = 0$. Substituting for f_1 and f_2 in terms of the stability factor s, equations (7.4) become,

$$\sqrt{\frac{2qk}{M}}\sqrt{s+1}\, t_1 = m\pi \quad ,$$

$$\sqrt{\frac{2qk}{M}}\sqrt{s-1}\, t_1 = n\pi \quad .$$

It follows that for imaging to occur at $t = t_1$, the stability factor s must have the value

$$s = \frac{m^2 + n^2}{m^2 - n^2} \tag{7.5}$$

and m > n. Also, since the magnitude of s must be greater than unity, neither m nor n can be zero.

Thus, when the parameters of the twisted quadrupole structure are chosen so that s assumes one of the values indicated by equation (7.5), the particle will be identically imaged in the rotating coordinate system at a time

$$t_1 = \frac{m\pi}{f_1} = \frac{n\pi}{f_2} = \pi\sqrt{\frac{M}{2qk}}\sqrt{\frac{m^2 - n^2}{2}} \tag{7.6}$$

The image occurs at a distance along the structure given by

$$\ell = \int_0^{t_1} \dot{Z}\, dt \tag{7.7}$$

Appendix B shows that the axial velocity $\dot{Z}$ during the traversal of the twisted structure differs only slightly from the axial velocity at injection, U_{Z_0}, and that the approximation $\dot{Z} \cong U_{Z_0}$ is within the same degree of approximation used in deriving the analytic solution of the particle trajectories. In fact, during extensive computer calculation of particle trajectories over a wide range of injection conditions no case was found where $\dot{Z}$ differed from U_{Z_0} by more than 3%. Taking these results into consideration, $\dot{Z}$ is assumed to be constant and equal to the axial velocity at injection, U_{Z_0}. Thus, the value of ℓ may be approximated by replacing $\dot{Z}$ with U_{Z_0} in equation (7.7). Thus,

$$\ell \cong U_{Z_0} t_1$$

$$= \pi \frac{P_{Z_0}}{M}\sqrt{\frac{M}{2qk}}\sqrt{\frac{m^2 - n^2}{2}}$$

$$= \frac{2\pi}{L} \, \frac{p_z}{\sqrt{2qkM}} \, \frac{P_{Z_o}}{p_z} \, \frac{L}{2}\sqrt{\frac{m^2 - n^2}{2}}$$

$$= \frac{\beta p_z}{\sqrt{2qkM}} \, \frac{L}{2} \, \frac{P_{Z_o}}{p_z}\sqrt{\frac{m^2 - n^2}{2}}$$

giving,

$$\ell \cong \frac{L}{2}\sqrt{s} \, \frac{P_{Z_o}}{p_z}\sqrt{\frac{m^2 - n^2}{2}}$$

Substituting for s from equation (7.5) gives the length of the imaging lens as

$$\ell \cong \frac{L}{2}\sqrt{\frac{m^2 + n^2}{2}} \qquad \frac{P_{Z_o}}{p_z} \tag{7.8}$$

At this point it has been shown only that it is possible to image a particle in the rotating coordinate frame, where $p_x(t)$ and $p_y(t)$ are not true mechanical momenta. Now consider a fixed coordinate system (X_t, Y_t, Z) whose axes X_t, Y_t are rotated an angle $\beta Z(t)$ with respect to the fixed coordinate system (X,Y,Z), $Z(t)$ being the distance along the structure given by

$$Z(t) = \int_0^t \dot{Z}(t)\, dt \tag{7.9}$$

The axes X_t, Y_t of such a coordinate system coincide with the rotating coordinate axes, $x(t)$ and $y(t)$, at the distance given by equation (7.9).

The transformation equations relating the two fixed coordinate systems (X_t, Y_t, Z) and (X,Y,Z) are

$$X = X_t \cos \beta Z(t) - Y_t \sin \beta Z(t) \quad ,$$

$$Y = X_t \sin \beta Z(t) + Y_t \cos \beta Z(t) \quad ,$$

$$P_X = P_{X_t} \cos \beta Z(t) - P_{Y_t} \sin \beta Z(t) \quad ,$$

$$P_Y = P_{Y_t} \sin \beta Z(t) + P_{Y_t} \cos \beta Z(t) \quad , \qquad (7.10)$$

where P_{X_t} and P_{Y_t} are the transverse mechanical momenta conjugate to X_t and Y_t. Comparison of equations (7.10) with equations (2.7) and (2.13) shows that $x(t)$, $y(t)$, $p_x(t)$ and $p_y(t)$ correspond identically to X_t, Y_t, P_{X_t}, P_{Y_t}, the latter being coordinates and momenta in the fixed coordinate frame that coincides with the twisting axes at an axial distance given by equation (7.9).

Thus from equations (2.7) and (2.13), it is apparent that at $Z = 0$ x_0, y_0, p_{x_0} and p_{y_0} are identical to X_0, Y_0, P_{X_0} and P_{Y_0}. Similarly equations (2.7), (2.13) and (7.10) show that in a fixed coordinate frame (X_T, Y_T, Z), which coincides with the twisting coordinates at the end of the lens, $x(t_1) = X_T$, $y(t_1) = Y_T$, $p_x(t_1) = P_{X_T}$ and $p_y(t_1) = P_{Y_T}$. Thus, for a structure whose parameters are chosen properly to satisfy equation (7.5), it follows from equation (7.1) that,

$$\begin{bmatrix} X_T \\ Y_T \\ P_{X_T} \\ P_{Y_T} \end{bmatrix} = \pm I \begin{bmatrix} X_0 \\ Y_0 \\ P_{X_0} \\ P_{Y_0} \end{bmatrix} \qquad (7.11)$$

It is evident from equations (2.32) and (2.33) that the axial momentum at $Z = \ell$ is then exactly equal to P_{Z_0}, the axial momentum at injection. In other words the initial transverse displacements and the initial momenta of the particle are reproduced in the fixed target coordinate frame (X_T, Y_T, Z). The fixed X_T, Y_T axes coincide with the x, y axes at $Z = \ell$. Thus, the target reference frame axes are rotated an angle $\beta\ell$ with respect to the X, Y axes which coincide with the rotating axes at $Z = 0$.

It is now clear that the twisted electrostatic quadrupole lens can image a single particle. The usefulness of any lens, however, lies in its ability to image a whole system of particles. In this respect the twisted quadrupole will generally suffer from aberrations. For instance, s is given by equation (4.1) as

$$s = (\beta a)^2 \left|\frac{V}{V_0}\right| \left[1 + (\beta a)\left\{\frac{X_0}{a}\frac{P_{Y_0}}{P_{Z_0}} - \frac{Y_0}{a}\frac{P_{X_0}}{P_{Z_0}}\right\}\right]^2 \qquad (7.12)$$

When a system of particles enters the quadrupole structure as either a point source or a parallel beam, then

$$X_0 P_{Y_0} - Y_0 P_{X_0} = 0 \quad , \qquad (7.13)$$

and s has the same value for all particles. The value of s can then be adjusted, for example by varying the quadrupole voltage V_0, to satisfy equation (7.5) for these particles. However, when particles are injected under general conditions of transverse displacements and momenta,s may be different for the various particles in the beam. Condition (7.5) may not be satisfied for every particle. Then,the nondiagonal terms of Q(t) do not completely vanish for every particle and aberration will result. From equation (7.12) it is evident that this aberration will be minimal for particles injected close to the axis with small transverse momenta.

Even though a system of particles may have a single value of s and hence may not exhibit the aberration described above, a different type of aberration may still be present. The latter appears because each particle, according to its injection conditions, may have its own variation of $\dot{Z}$ about U_{Z_0}, as described by equation (2.34). Thus, the required length of the lens as given by equation (7.7) will differ slightly for each particle. This in turn means that for each particle a different error is incurred when computing the length of the lens from equation (7.8). As a consequence the degree by which the nondiagonal terms of the matrix $Q(t_1)$ will differ from zero varies for each particle according to its injection conditions, thus giving rise to aberration.

Computer evaluation of many trajectories has shown this latter type of aberration to be negligible when compared with the aberration resulting from changes in the stability factor. This phenomenon will be illustrated by examples of the trajectories shown in the following section.

7.3 Results

Using the analytic solution and the transformation equations (7.10), sets of particles with a variety of initial conditions were traced through the twisted quadrupole to graphically demonstrate the latter's imaging properties. In each case the numerical computations were performed with the aid of an IBM 360 computer. A listing as well as the discussion of the program used are given in Appendix E. The trajectories were plotted directly by a Calcomp Plotter in the (X,Y,Z) fixed coordinate system. Although trajectories of charged particles through such an electrostatic lens are independent of the charge to mass ratios of the particles, for the purpose of computation,particles with a charge to mass ratio of 30 coulomb per kilogram were considered.

The lens was chosen to have $a = 1.5\text{cm}$ and $(\beta a)^2 = 0.1$. Since the parameters m and n have to be integers, both odd or both even and $m > n > 0$, the lens was chosen to have $m = 3$ and $n = 1$. These values of m and n correspond to the shortest possible length of the imaging lens. Thus at time t_1,

$$\cos f_1 t_1 = \cos f_2 t_1 = -1 \qquad ,$$

and

$$\sin f_1 t_1 = \sin f_2 t_1 = 0 \qquad ,$$

and $Q(t_1) = -I$ for these particles which have

$$s = \frac{m^2 + n^2}{m^2 - n^2} = \frac{9 + 1}{9 - 1} = 1.25$$

The calculations were carried out assuming that every particle entering the lens structure had been accelerated through the same potential, V, and that the angle of divergence of the injected beam was very small, such that each particle had an axial injection momentum, $P_{Z_0} \cong (2qMV)^{1/2}$. The quadrupole potential, V_0, was adjusted so that the stability factor was 1.25 for particles injected from a point source or a parallel beam where equation (7.13) was satisfied. In this case, from equation (7.12)

$$s = (\beta a)^2 \frac{P_{Z_0}^{\ 2}}{2qMV_0} = (\beta a)^2 \left|\frac{V}{V_0}\right| \quad .$$

The accelerating voltage was assumed to be 30 KV which for $(\beta a)^2 = 0.1$ required a quadrupole potential of 2.4 KV.

The required length ℓ of the lens was calculated from equation (7.8) to be approximately 33.3 cm, assuming either point source or parallel beam injection. Hence, imaging should occur in a target frame whose axes (X_T, Y_T) are rotated with respect to the (X,Y) axes by the angle $\beta\ell = 403° = 360° + 43°$.

Figure (7.1a) shows the trajectories of a set of particles which were injected from a point source at $Z = 0.0$. Each particle was injected with the same value of P_{X_0} but a different value of P_{Y_0}. It is evident from figure (7.1a) that the point source is reproduced at $Z = \ell$. Figure (7.1b) shows a projection of the trajectories in momentum space onto the fixed $(\frac{P_{X_0}}{P_{Z_0}}, \frac{P_{Y_0}}{P_{Z_0}})$ normalized transverse momentum plane. For sake of clarity those trajectories for which $P_{Y_0} < 0$ have been omitted. Notice that the particles are imaged in inverted form in the target reference frame.

Figure (7.2a) shows the trajectories of a beam which was parallel at injection. Each particle was injected with the same value of X_0 but with different values of Y_0. Notice that the emerging particles are again travelling parallel to the Z axis at $Z = \ell$. Figure (7.2b) shows a projection of the trajectories in coordinate space onto the fixed (X,Y) transverse coordinate plane. Again it may be seen that the injection coordinates are imaged in inverted form in the target reference frame.

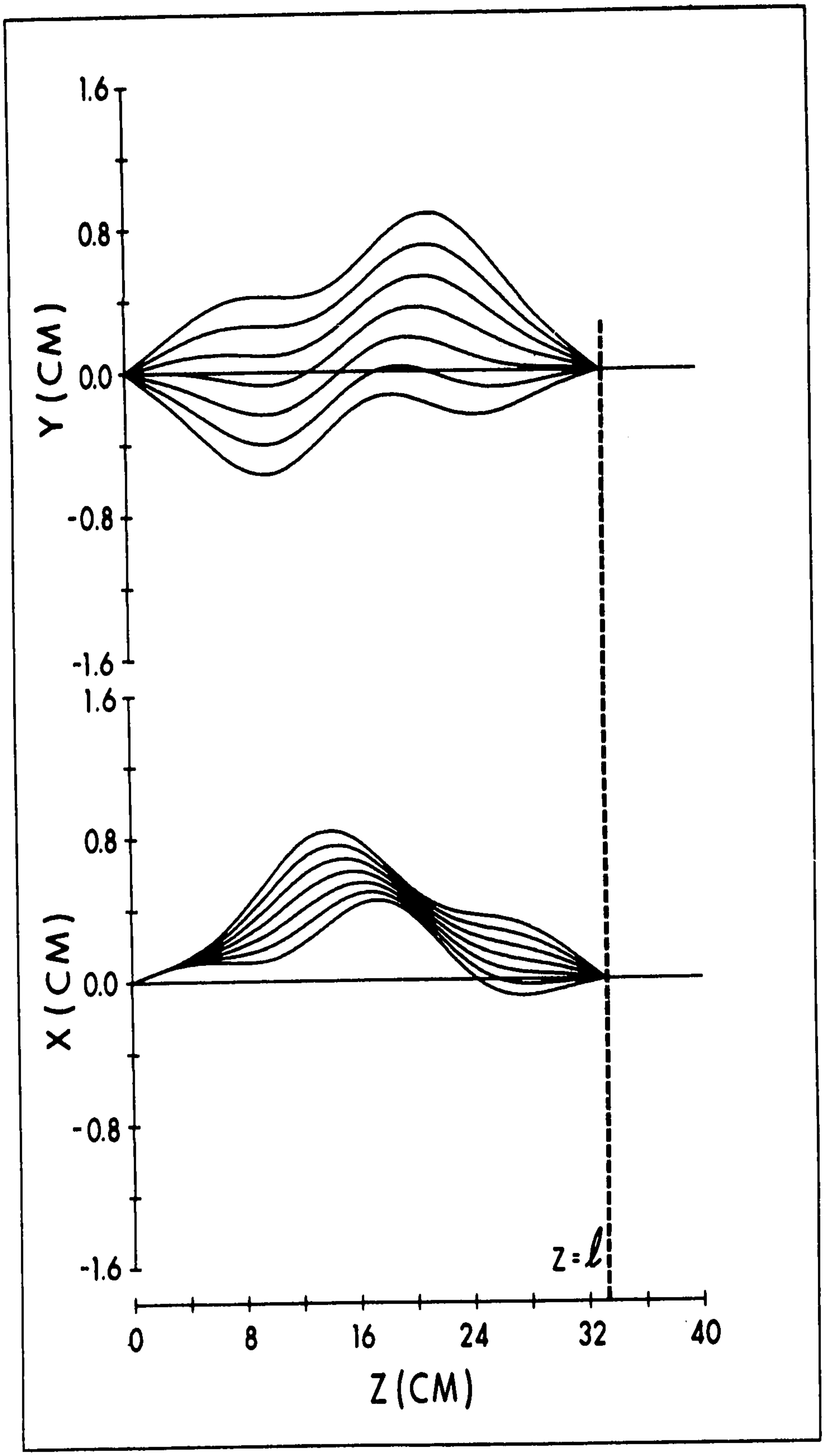

Figure (7.1a) X and Y versus Z for Point Source Injection.

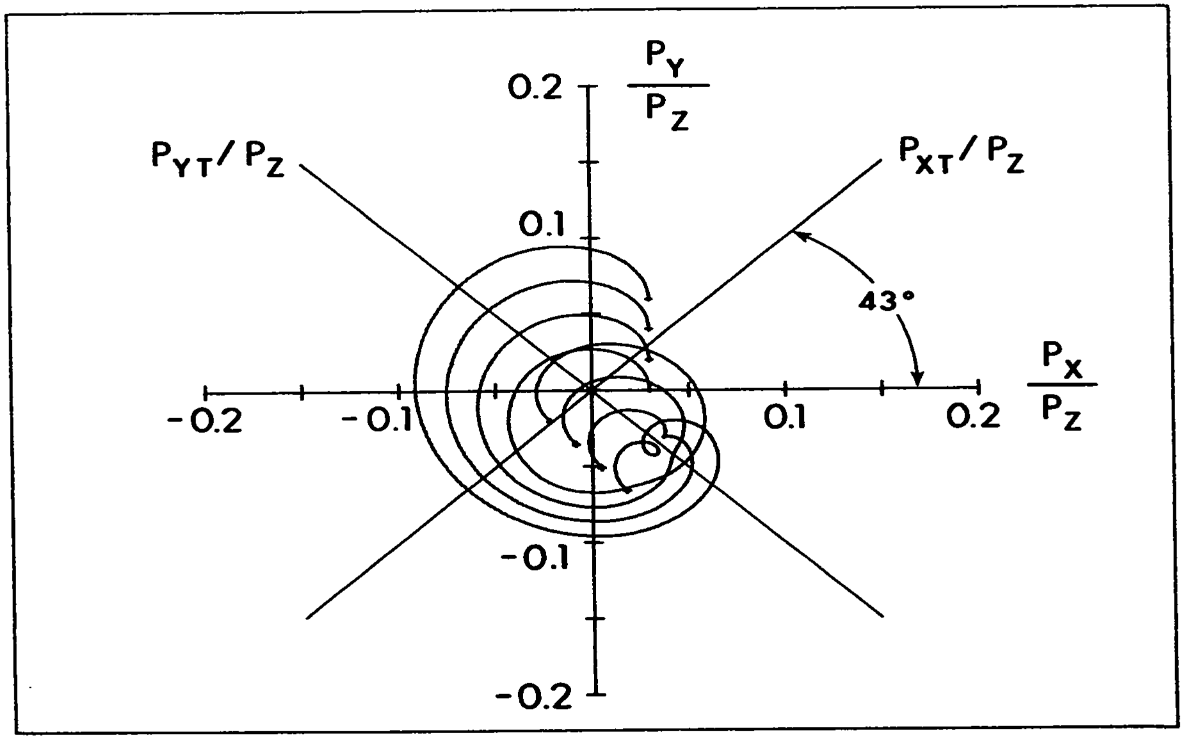

Figure (7.1b) Injection and Exit Momenta for Point Source Injection.

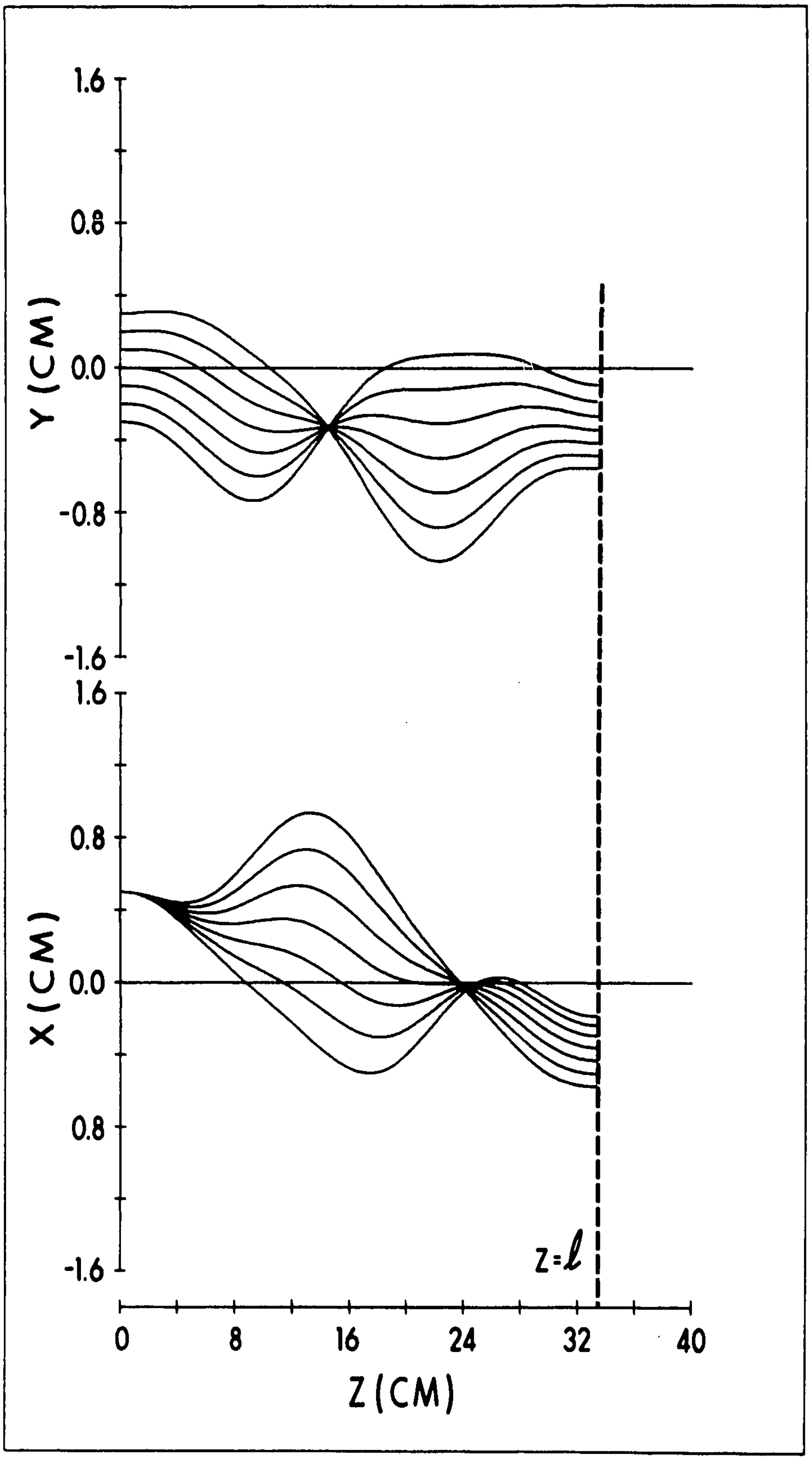

Figure (7.2a) X and Y Versus Z for Parallel Beam Injection.

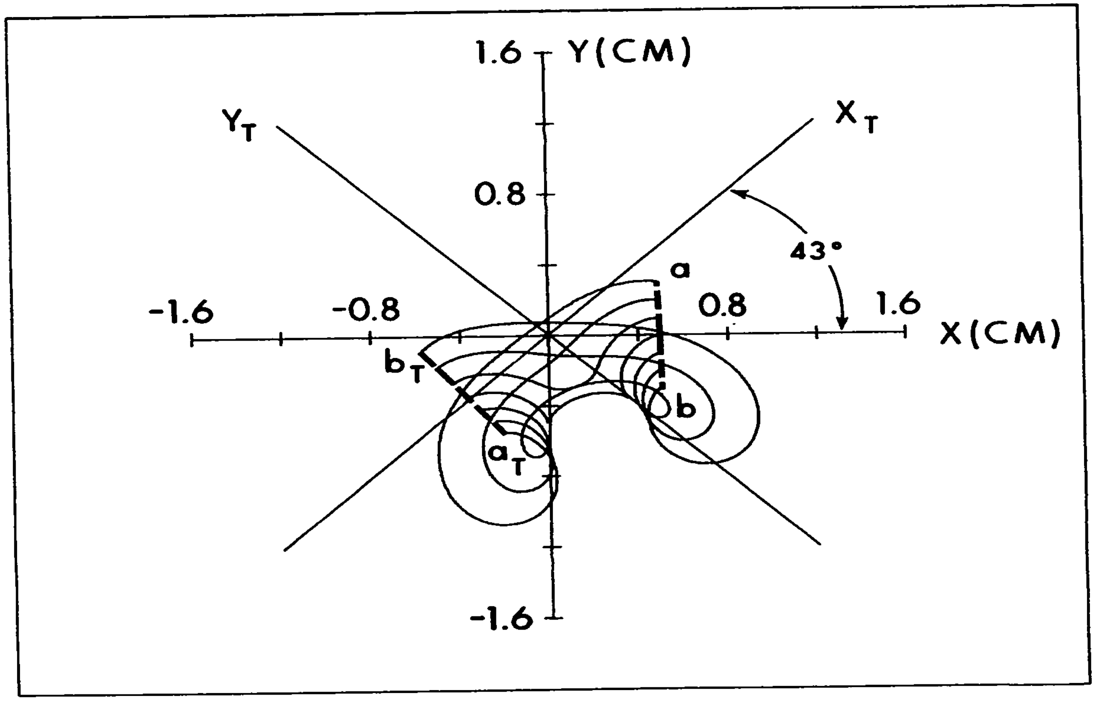

Figure (7.2b) Injection and Exit Coordinates for Parallel Beam Injection.

It should be noted that neither of the two foregoing examples indicates the presence of aberration. Since the two examples respectively illustrate point source and parallel beam injection, the only source of any possible undetected aberration would be a variation in $\dot{Z}$ which, by equation (7.7), would mean that the length of the lens is not correct for all particles.

Figure (7.3a) represents the injection and exit coordinates of 28 sets of particles. The injection coordinates lie along the periphery of the rectangle whose sides are parallel to the X,Y fixed axes. Each cross (+) represents five individual particles with the same value of X_0 and Y_0 but with different transverse injection momenta at Z = 0. These transverse momenta are shown in figure (7.3b). They are represented respectively by five (+) marks at the center and the four corners of the square whose sides are parallel to the $\frac{P_X}{P_Z}$ and $\frac{P_Y}{P_Z}$ axes. Figure (7.3b) also shows the exit transverse momenta. In general these particles do not have $s = 1.25$ and therefore cannot be imaged without aberration. Figures (7.3a) and (7.3b) clearly show the presence of this aberration which is due to the variations in both s and $\dot{Z}$.

Figures (7.4a) and (7.4b), which feature the same injection conditions as figures (7.3a) and (7.3b), show the effect of joining to the first section of twisted quadrupole a second equal but oppositely twisted section. For this composite structure the transformation matrix Q(t) in equation (7.1) is $(-I)^2$ or $+I$. Therefore, the injection conditions are now reproduced in a target plane without inversion or rotation.

The computation of the trajectories along the composite structure was started by computing the trajectories along the first section, using

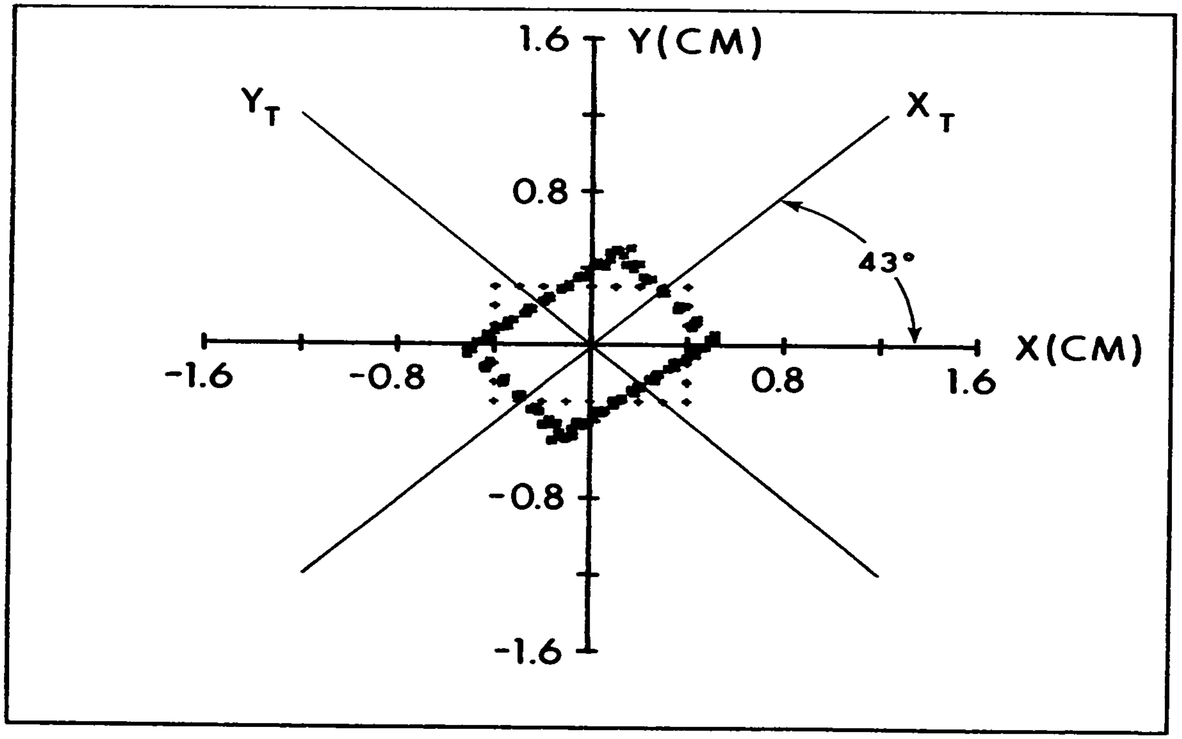

Figure (7.3a) Injection and Exit Coordinates for a Single Twisted Lens.

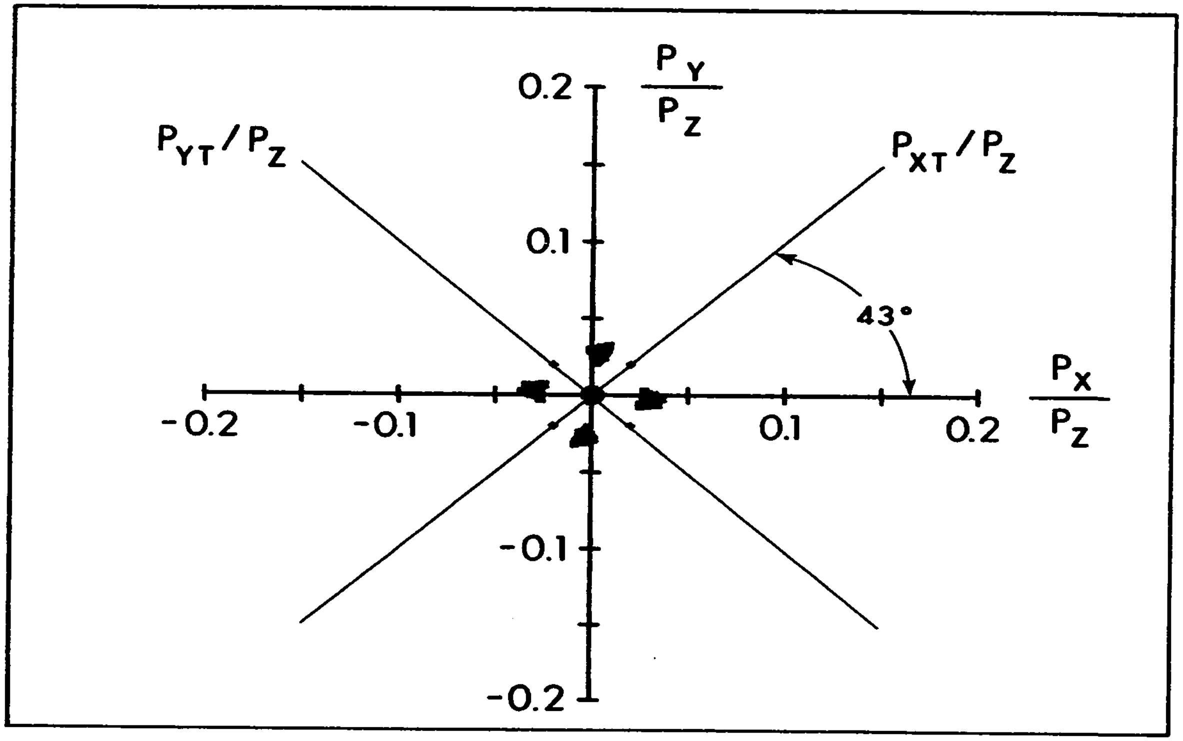

Figure (7.3b) Injection and Exit Momenta Corresponding to the Coordinates of Figure (7.3a) for a Single Twisted Lens.

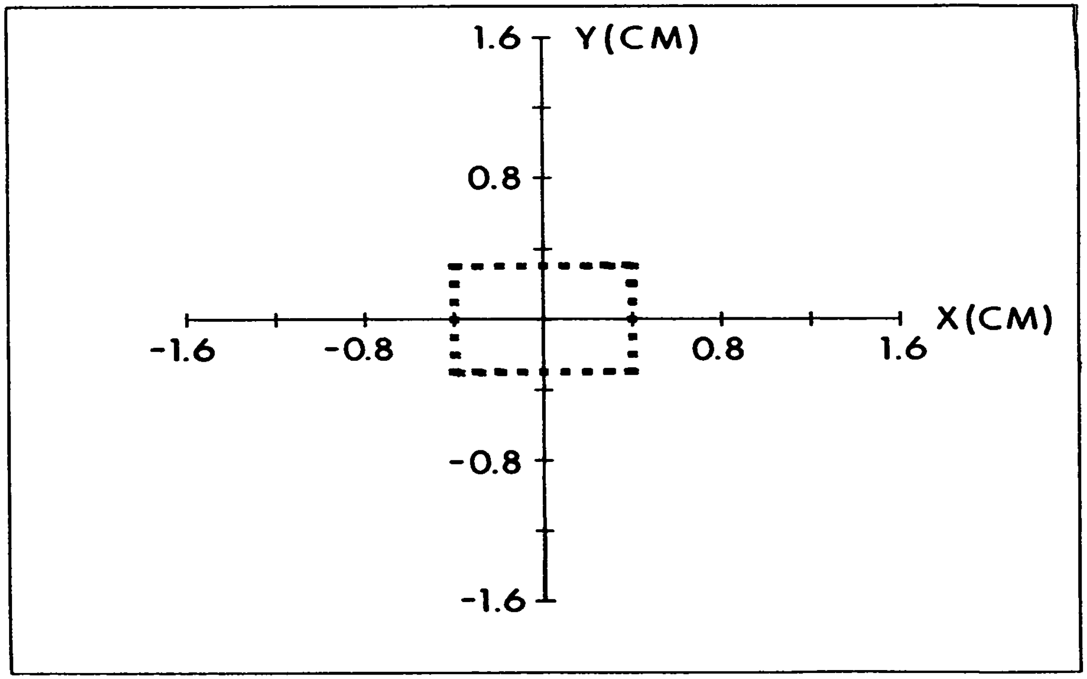

Figure (7.4a) Injection and Exit Momenta for Two Adjoining Lens Sections of Equal Length but Opposite Twist.

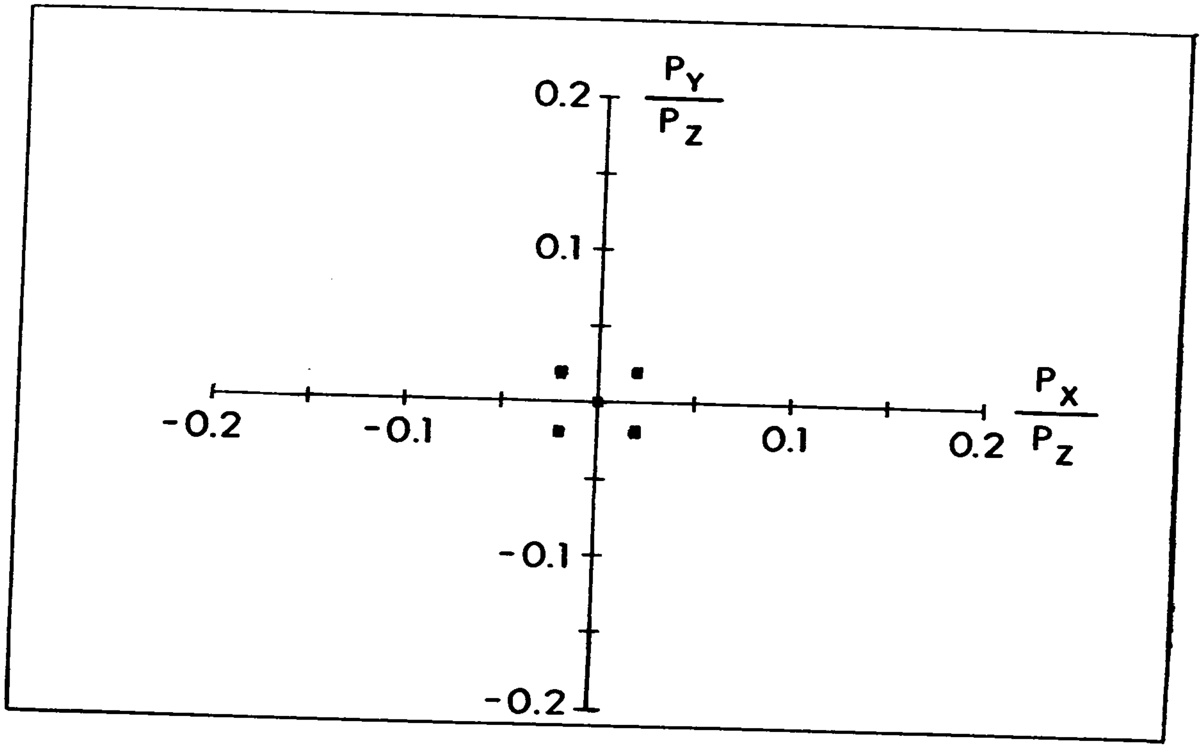

Figure (7.4b) Injection and Exit Momenta Corresponding to the Coordinates of Figure (7.4a) for Two Adjoining Lens Sections of Equal Length but Opposite Twist.

equations (7.12) then equations (2.31) and (2.35). Then, for each individual particle the axial momentum, $P_Z = M\dot{Z}$ at $Z = \ell$, was calculated using equation (2.34). The fixed target plane of the first section coincides with the fixed injection plane of the second section. Therefore, the coordinates and momenta at the exit of the first section, in the fixed target plane which is rotated 403° with respect to the (X,Y) axes, are the injection coordinates and momenta to the second twisted section. For each individual particle, its input transverse coordinates and momenta as well as its input axial momentum to the second section were used to calculate the value for the motion of this particle through the second section, using equation (7.2). Equations (2.31) and (2.35) were then used to calculate the trajectory of the particle through the second section.

Figures (7.4a) and (7.4b) show that the injection coordinates and momenta are now reproduced without inversion in a target plane that coincides with the fixed (X, Y) plane. It is evident that some aberration is still present. However, this aberration is greatly reduced when compared to the results obtained with the single twisted quadrupole and shown in figures (7.3a) and (7.3b).

7.4 Effect of Detuning s About Its Imaging Value

Equation (7.12) gives the stability factor s in terms of the parameters V, V_0 and $(\beta a)^2$ and the injection conditions of the particle X_0, Y_0, P_{X_0}, P_{Y_0} and P_{Z_0} as

$$|s| = (\beta a)^2 \left|\frac{V}{V_0}\right| \left[1 + (\beta a)\left\{\frac{X_0}{a}\frac{P_{Y_0}}{P_{Z_0}} - \frac{Y_0}{a}\frac{P_{X_0}}{P_{Z_0}}\right\}\right]^2 \qquad (7.12)$$

The twisted structure acts as an imaging lens if the structure parameters and the particle's injection conditions are chosen to give a value of s equal to

$$s = s_0 = \frac{m^2 + n^2}{m^2 - n^2} \quad \text{where m and n are as defined by equation (7.5)}$$

Any deviation of V, V_0, (βa) or $\{\frac{X_0}{a}\frac{P_{Y_0}}{P_{Z_0}} - \frac{Y_0}{a}\frac{P_{X_0}}{P_{Z_0}}\}$ from the proper values corresponding to $s = s_0$, will lead to aberration. In practice, an error in the length of the imaging lens, an error in the value of the aperture radius or any deviation of the fields from those derived from the focusing potential of equations (2.1a) and (2.1b) may require adjusting the structure parameters to values other than those corresponding to $s = s_0$ so that imaging will occur. Any deviation from this new setting of the parameters again will lead to aberration.

In the present section the length, aperture radius and fields are assumed to be exact and the effects of the variation of s, about s_0, on the imaging properties of the lens are investigated. A study is also made of how the emerging beam parameters are affected, for values of s equal to and not equal to s_0, by introducing a drift space beyond the exit plane of the lens.

A sketch of the arrangement for performing the foregoing studies is shown in figure (7.5a). A beam of particles is assumed to originate from a point source at a distance ℓ_i from the injection plane of the lens used in the numerical investigations of section (7.3). Before injection the beam cross-section is shaped by using a rectangular aperture E centered at $X_0 = Y_0 = 0$ and having its sides parallel to the fixed X, Y

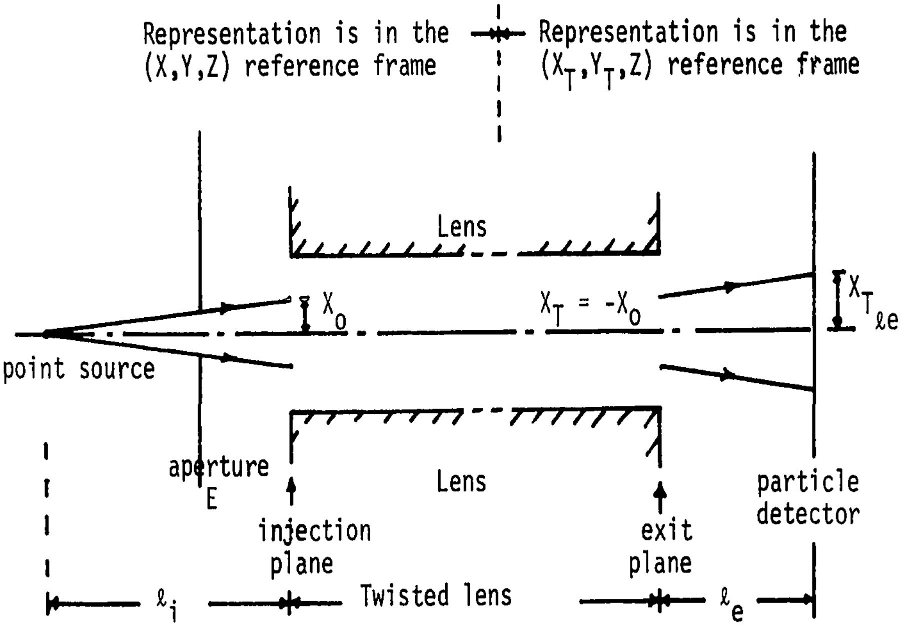
Representation is in the (X,Y,Z) reference frame
Representation is in the (X_T,Y_T,Z) reference frame
Lens
X_o
$X_T = -X_o$
$X_{T_{\ell e}}$
point source
aperture E
Lens
injection plane
exit plane
particle detector
ℓ_i
Twisted lens
ℓ_e

Figure (7.5a) Schematic of the Arrangement Used for Studying the Effect of Detuning s.

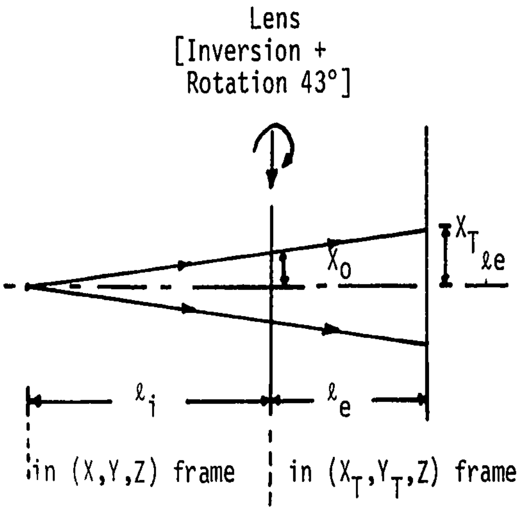
Lens
[Inversion +
Rotation 43°]
X_o
$X_{T_{\ell e}}$
ℓ_i
ℓ_e
in (X,Y,Z) frame
in (X_T,Y_T,Z) frame

Figure (7.5b) Lens Equivalent at Imaging Values of s.

At s = 1.25 (V_o = 1200 volts) the effect of the lens is inversion and rotation of the coordinates and momenta.

axes, with the longer side parallel to the X-axis. The dimensions of the aperture E are chosen so that the dimensions of the injected beam rectangular cross-section are 1 mm x 2 mm With this aperture the angle of divergence of the injected beam will be less than 0.038 radians for $\ell_i = 6$ cm, and the injection axial momentum of all particles will be approximately given by $P_{Z_0} \cong \sqrt{2qMV}$. Also, with this small aperture, the injection conditions of the particles will be within the limits set by the confinement criterion of equation (3.10).

Figure (7.5a) shows that the coordinates and momenta of the particles at the injection plane are related by

$$X_0 = \ell_i \frac{P_{X_0}}{P_{Z_0}} \quad ,$$

$$Y_0 = \ell_i \frac{P_{Y_0}}{P_{Z_0}} \quad . \tag{7.14}$$

Thus, for all injected particles

$$[X_0 P_{Y_0} - Y_0 P_{X_0}] = 0 \quad ,$$

which together with the approximation $P_{Z_0} \cong \sqrt{2qMV}$ will give s as

$$|s| = (\beta a)^2 \left|\frac{V}{V_0}\right|$$

Thus, for the arrangement of figure (7.5a) and for the lens structure considered in Section 7.3 for which $s_0 = 1.25$, the exact imaging quadrupole voltage is V_0 = 1200 volts when the accelerating potential is 15 KV.

In the numerical investigation, presented at the end of this section only particles on the circumference of the rectangular injected beam are considered. The coordinates and momenta of these particles at the exit plane of the lens are computed using the transformation matrix Q(t) given by equation (7.2). The time t_1 in which the particle traverses the lens structure is approximated by

$$t_1 \cong \frac{\ell}{U_{Z_0}} \cong \frac{\ell}{\sqrt{2\frac{q}{M}V}}$$

With this approximation $f_1 t_1 = \frac{\sqrt{s+1}\,\ell}{\sqrt{V}}$ and $f_2 t_1 = \frac{\sqrt{s-1}\,\ell}{\sqrt{V}}$ where ℓ = 33.3 cm as computed in Section 7.3.

At the exact imaging voltage V_0 = 1200 volts, corresponding to $s = s_0 = 1.25$, the exit coordinates of the particles at the exit plane of the lens will be related to the coordinates at the injection plane by

$$X_{T_{exit}} = -X_0 \qquad \text{and } Y_{T_{exit}} = -Y_0 \tag{7.15}$$

Therefore, with no drift space beyond the lens exit plane, the exit coordinates of the particles will lie on the circumference of a rectangle having the same dimensions as the injection rectangle and having its sides rotated 43° with respect to the X and Y axes, that is parallel to the X_T and Y_T axes of figure (7.2b). Moreover, the exit momenta will be

$$P_{X_{T_{exit}}} = -P_{X_0} = -X_0 \frac{P_{Z_0}}{\ell_i} = X_{T_{exit}} \frac{P_{Z_0}}{\ell_i}$$

$$P_{Y_{T_{exit}}} = - P_{Y_o} = - Y_o \frac{P_{Z_o}}{\ell_i} = Y_{T_{exit}} \frac{P_{Z_o}}{\ell_i} \qquad (7.16)$$

and thus $[X_{T_{exit}} P_{Y_{T_{exit}}} - Y_{T_{exit}} P_{X_{T_{exit}}}] = 0$. Equation (2.32) gives the axial exit momentum for such particles as

$$P_{Z_{exit}} = P_{Z_o} . \qquad (7.17)$$

Equations (7.16) and (7.17) give the relations between the exit coordinates and the exit momenta of a particle, when there is no drift space beyond the lens exit plane, in terms of the (X_T, Y_T, Z) coordinate system as

$$P_{X_{T_{exit}}} = X_{T_{exit}} \frac{P_{Z_{exit}}}{\ell_i} ,$$

$$P_{Y_{T_{exit}}} = Y_{T_{exit}} \frac{P_{Z_{exit}}}{\ell_i} . \qquad (7.18)$$

Equations (7.15) and (7.18) show that the coordinates of a particle at a distance ℓ_e beyond the exit of the lens, as shown in figure (7.5a), are

$$X_{T_{\ell_e}} = X_{T_{exit}} + \frac{P_{X_{T_{exit}}}}{P_{Z_{exit}}} \ell_e = X_T(1 + \frac{\ell_e}{\ell_i})$$

$$= - X_o(1 + \frac{\ell_e}{\ell_i}) ,$$

similarly $Y_{T_{\ell_e}} = -Y_o(1 + \frac{\ell_e}{\ell_i})$,

$$P_{X_{T_{\ell_e}}} = P_{Z_0} \frac{X_{T_{\ell_e}}}{\ell_e + \ell_i} ,$$

$$P_{Y_{T_{\ell_e}}} = P_{Z_0} \frac{Y_{T_{\ell_e}}}{\ell_e + \ell_i} ,$$

$$P_{Z_{\ell_e}} = P_{Z_0} . \tag{7.19}$$

Thus, at $s = s_0 = 1.25$, the introduction of a drift space ℓ_e beyond the exit of the lens will not change the geometrical shape of the beam from that at the exit. The length of the sides, however, is increased by the ratio $(1 + \frac{\ell_e}{\ell_i})$. Thus at $s = s_0 = 1.25$, the action of the lens itself can be represented by the introduction of a rotation through $2\pi + 43°$ and inversion of the coordinates and transverse momenta as presented schematically in figure (7.5b).

Having considered the properties of the image produced by the experimental arrangement of figure (7.5a) at $s = s_0 = 1.25$ without and with a drift space ℓ_e beyond the lens exit, a study was made to determine the effect of varying s by considering values of V_0 other than 1200 volts. It should be noted that for particles whose coordinates and momenta are related by equations (7.14), the relations between these coordinates and momenta and those at the exit of the lens are linear for all values of V_0. For values of V_0 different from 1200 volts the matrix Q(t) at $Z = \ell$ will be different from -I but the transformation described by equations (2.49) and (2.50) will still be linear and can be written, using equations (2.49) and (7.14), as

$$\begin{bmatrix} X_T \\ Y_T \\ P_{X_T} \\ P_{Y_T} \end{bmatrix} = [Q(\ell)] \begin{bmatrix} X_o \\ Y_o \\ P_{X_o} \\ P_{Y_o} \end{bmatrix} = [Q(\ell)] \begin{bmatrix} X_o \\ Y_o \\ \frac{P_{Z_o}}{\ell_i} X_o \\ \frac{P_{Z_o}}{\ell_i} Y_o \end{bmatrix}$$

Substituting for the elements of $[Q(\ell)]$ as Q_{ij}, $i = 1,2,3,4$, $j = 1,2,3,4$, the above matrix relation can be put in the form

$$\begin{bmatrix} X_T \\ Y_T \\ P_{X_T} \\ P_{Y_T} \end{bmatrix} = \begin{bmatrix} Q_{11} + \frac{P_{Z_o}}{\ell_i} Q_{13} & Q_{12} + \frac{P_{Z_o}}{\ell_i} Q_{14} \\ Q_{21} + \frac{P_{Z_o}}{\ell_i} Q_{23} & Q_{22} + \frac{P_{Z_o}}{\ell_i} Q_{24} \\ Q_{31} + \frac{P_{Z_o}}{\ell_i} Q_{33} & Q_{32} + \frac{P_{Z_o}}{\ell_i} Q_{34} \\ Q_{41} + \frac{P_{Z_o}}{\ell_i} Q_{43} & Q_{42} + \frac{P_{Z_o}}{\ell_i} Q_{44} \end{bmatrix} \begin{bmatrix} X_o \\ Y_o \end{bmatrix} \tag{7.20}$$

where the elements Q_{ij}'s are evaluated from (2.50) at the value of V_o considered. Equation (7.20) shows X_T, Y_T, P_{X_T} and P_{Y_T} to be linear combinations of X_o and Y_o. The coordinates of such particles, whose coordinates and momenta at the lens exit are given by equation (7.20), at distance ℓ_e from the exit plane of the lens are,

$$X_{T_{\ell_e}} = X_T + P_{X_T} \frac{\ell_e}{P_{Z_{exit}}} \quad ,$$

$$Y_{T_{\ell_e}} = Y_T + P_{Y_T} \frac{\ell_e}{P_{Z_{exit}}} \qquad (7.21)$$

Substituting equations (7.20) into equations (7.21) gives

$$\begin{aligned} X_{T_{\ell_e}} &= [(Q_{11} + \frac{P_{Z_o}}{\ell_i} Q_{13}) + \frac{\ell_e}{P_{Z_{exit}}} (Q_{31} + \frac{P_{Z_o}}{\ell_i} Q_{33})]X_o \\ &\quad + [(Q_{12} + \frac{P_{Z_o}}{\ell_i} Q_{14}) + \frac{\ell_e}{P_{Z_{exit}}} (Q_{32} + \frac{P_{Z_o}}{\ell_i} Q_{34})]Y_o \quad , \\ Y_{T_{\ell_e}} &= [(Q_{21} + \frac{P_{Z_o}}{\ell_i} Q_{23}) + \frac{\ell_e}{P_{Z_{exit}}} (Q_{41} + \frac{P_{Z_o}}{\ell_i} Q_{43})]X_o \\ &\quad + [(Q_{22} + \frac{P_{Z_o}}{\ell_i} Q_{24}) + \frac{\ell_e}{P_{Z_{exit}}} (Q_{42} + \frac{P_{Z_o}}{\ell_i} Q_{44})]Y_o \quad . \end{aligned}$$

or

$$X_{T_{\ell_e}} = A_1 X_o + A_2 Y_o \quad ,$$

$$Y_{T_{\ell_e}} = A_3 X_o + A_4 Y_o \quad , \qquad (7.22)$$

where A_1, A_2, A_3 and A_4 are functions of ℓ_i, ℓ_e and the structure parameters at the value of V_o considered.

Now, consider particles whose coordinates X_o, Y_o at $Z = 0$ lie on a straight line such that X_0, Y_0 are related by

$$Y_0 = b_1 X_0 + b_2, \text{ where } b_1 \text{ and } b_2 \text{ are constants.} \tag{7.23}$$

Equations (7.22) and (7.23) give the relation between $X_{T_{\ell_e}}$ and $Y_{T_{\ell_e}}$, at a distance ℓ_e from the exit plane, for a particle whose injection coordinates are related by equation (7.23) as,

$$Y_{T_{\ell_e}} = \frac{A_3 + b_1 A_4}{A_1 + b_1 A_2} X_{T_{\ell_e}} + b_2 \frac{A_1 A_4 - A_2 A_3}{A_1 + \beta_1 A_2} \tag{7.24}$$

Equations (7.23) and (7.24) show that particles injected with their coordinates lying on a straight line will have their coordinates at any value of drift space from the lens exit plane lying on a straight line defined by equation (7.24). The slope and intercept of the line defined by equation (7.24) is clearly dependent on the original orientation of the line defined by equation (7.23), as well as on ℓ_i, ℓ_e and the structure parameters.

Exit coordinates and momenta of the particles on the circumference of the injection rectangle were computed for different values of s by considering values of V_0 equal to 1150, 1180, 1200, 1210, 1220, 1250, and 1300 volts. The computations were repeated for values of ℓ_e equal to 0.0, 1.0, 2.0 and 3.0 cm while ℓ_i was equal to 6 cm. The computed exit coordinates in the target reference frame (X_T, Y_T, Z) are shown in figures (7.6), (7.7), (7.8) and (7.9) for ℓ_e = 0.0, 1.0, 2.0 and 3.0 cm respectively.

Figure (7.6) shows the exit coordinates corresponding to

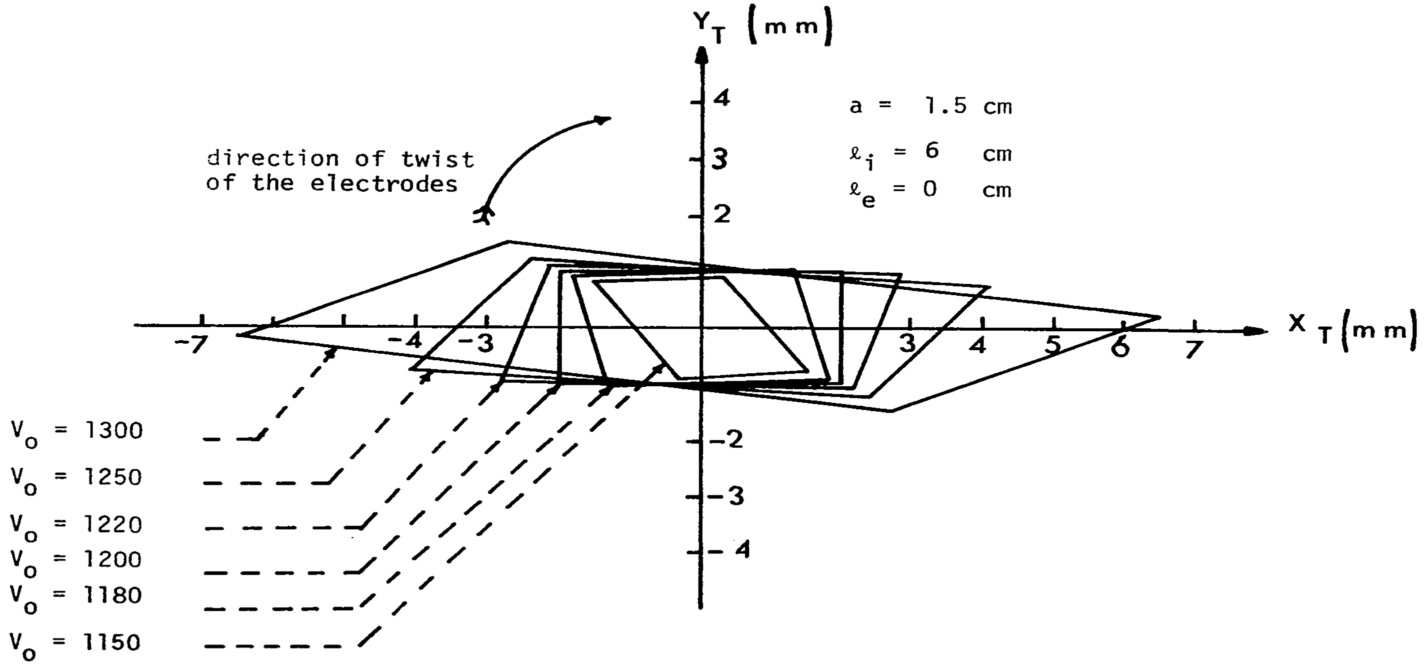

Figure (7.6) Exit Coordinates of Particles at the Lens Exit Plane (ℓ_e = 0).

The injection coordinates of the particles considered are on the circumference of a 4 mm x 2 mm rectangle whose sides are parallel to the X and Y axes at the injection plane, the longer side in the X direction. The exit rectangles are shown at values of V_o corresponding to values of s larger, equal and smaller than 1.25.

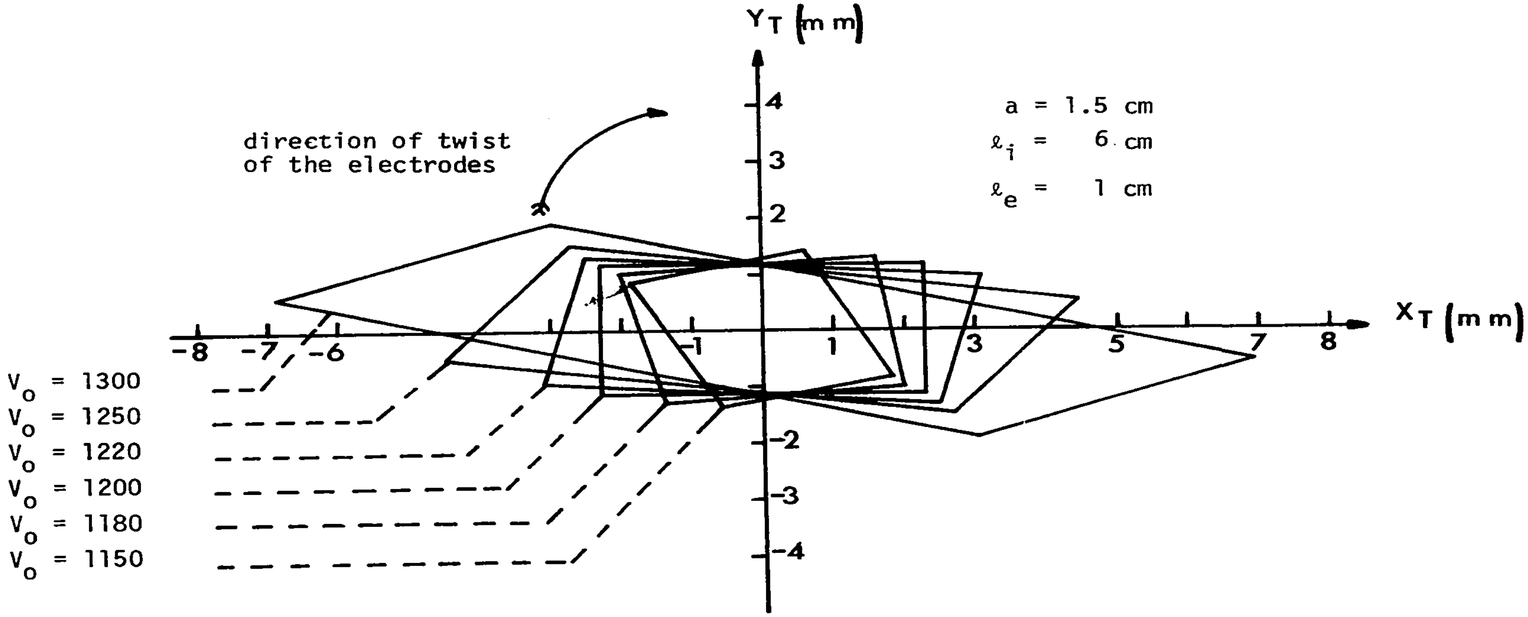

Figure (7.7) The Exit Coordinates of Particles at a Distance, ℓ_e = 1cm, Beyond the Lens Exit Plane.

The injected particles are the same particles considered in figure (7.6).

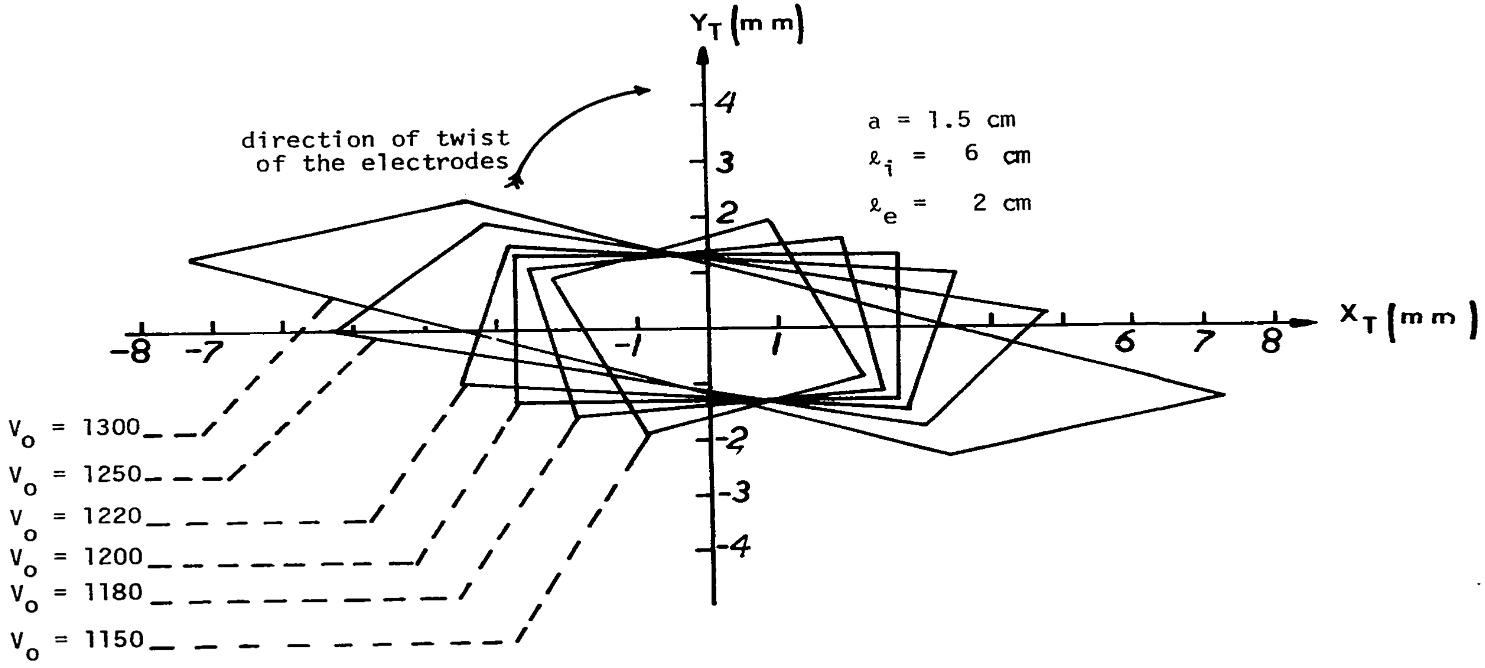

Figure (7.8) As in Figure (7.7) Except at a Distance ℓ_e = 2 cm Beyond the Lens Exit.

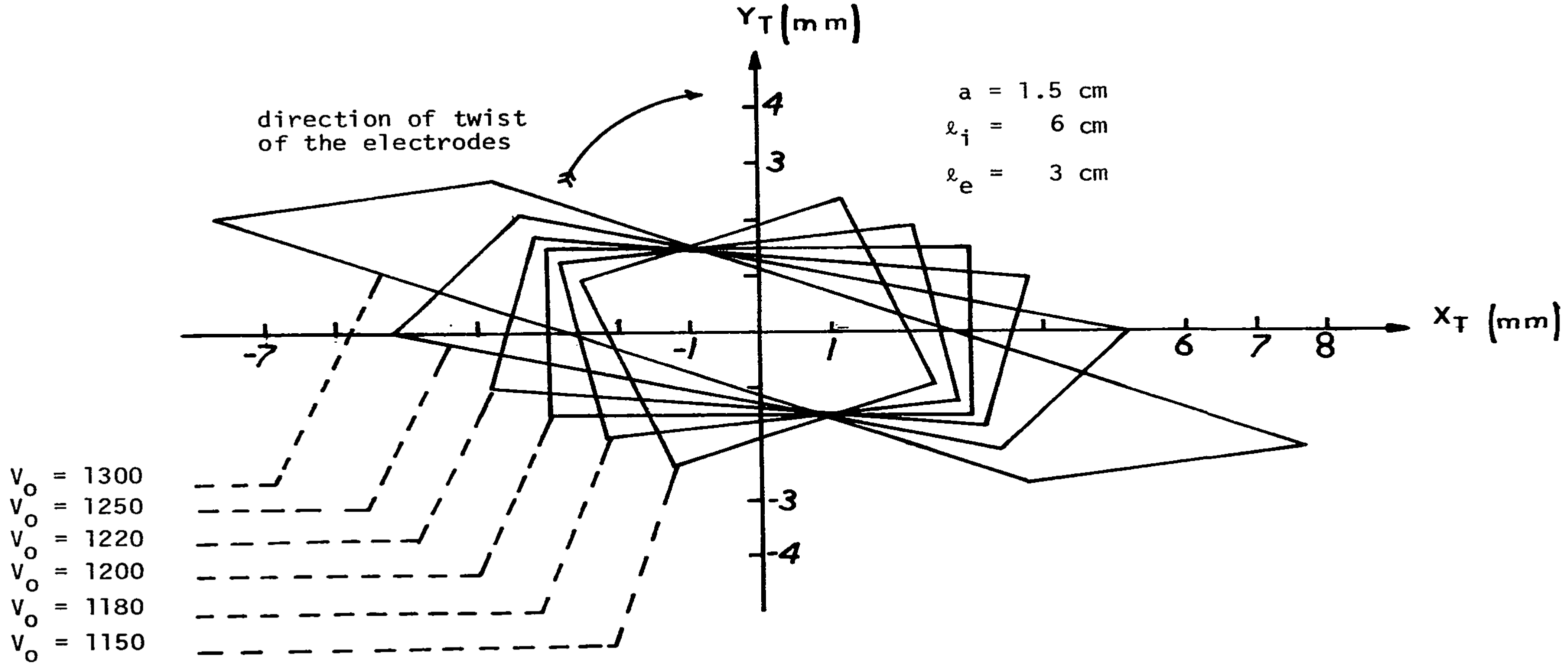

Figure (7.9) As in Figure (7.7) Except at a Distance ℓ_e = 3 cm Beyond the Lens Exit.

V_0 = 1200 volts, that is $s = s_0 = 1.25$, to be exactly on the circumference of a rectangle whose sides are equal to those of the rectangular cross-section of the beam at the input plane and are exactly parallel to the X_T and Y_T axes. As V_0 is decreased below 1200 volts, corresponding to s increasing to values larger than 1.25, the dimensions of the sides that should be parallel to the X_T axes decrease at a rate much higher than the rate of decrease of the other sides that should be parallel to the Y_T axis. At the same time the exit rectangle is deformed into a parallelogram that is rotated in a direction opposite to that of twist of the quadrupole electrodes. The angle of rotation of the parallelogram increases and its dimensions decrease as V_0 decreases.

On the other hand, as V_0 is increased above 1200 volts the exit rectangle deforms into a parallelogram that is rotated in the same direction as the twist of the lens electrodes. At the same time the lengths of the sides increase and the sides that should be parallel to the X_T axis increase in length at a rate higher than the rate of increase of the other two sides.

Figures (7.7) to (7.9) show the exit coordinates of the particles injected at Z = 0 on the circumference of the injection rectangle, at values of drift spaces ℓ_e beyond the lens exit plane, of 1 , 2 and 3 cm.The value of ℓ_i, shown in figure (7.5a), is 6 cm as it was for the case $\ell_e = 0$ of figure (7.6). Figures (7.7) to (7.9) show that the sizes of the exit parallelograms, at all values of V_0 increase as ℓ_e is increased. The exit coordinates at V_0 = 1200 form a rectangle with its sides parallel to the X_T and Y_T axes for all values of ℓ_e considered, as expected from equations (7.18). The exit coordinates for values of V_0 less than 1200 volts are parallelograms, as for $\ell_e = 0$, rotated in a direction opposite to the direction of twist of the lens electrodes. It is observed that the rotation of these parallelograms increases as V_0 is decreased and/or the value of ℓ_e is increased. For values of V_0 larger than 1200 volts the exit parallelograms are still rotated in the same direction of twist as that of the electrodes for all values of the drift space ℓ_e beyond the lens exit. It is also found that the degree of rotation increases as the length of the drift space ℓ_e is increased and/or the value of V_0 is increased.

The investigations of this section are of great importance since they are the basis for some of the experiments of Chapter 8. The experimental arrangement used for investigating the imaging properties of the twisted lens is exactly that of figure (7.6a), and the results of the present section are used to check the experimental results of section (8.4).

CHAPTER 8

EXPERIMENTAL INVESTIGATIONS OF THE IMAGING PROPERTIES OF THE TWISTED ELECTROSTATIC LENS

The theoretical analysis for the motion of charged particles along the uniformly twisted electrostatic quadrupole structure shows that the trajectories and hence the guiding, focusing and imaging properties of the structure are independent of the charge-to-mass ratios of the particles. Therefore, either electron beams, ion beams or any other charged particle beams can be used in the experimental investigations of the structure properties. However, since the present work was aimed at providing a successful guiding structure for microparticle beams, a charged microparticle beam was used in the experimental investigations. The microparticle beam was generated through contact charging in a microparticle charger specially designed to meet the requirements of the experiments.

8.1 High Vacuum System

The vacuum system that was used in all experiments is a CHA High Vacuum Pumping Station type SS-600-RAM. It consists of a 7 3/4 inch, 4-stage water cooled oil diffusion pump with liquid nitrogen trap. Pressure measurements were made by means of two DV-6M thermocouple gauge tubes and one Bayard-Albert hot wire IG-100-N ionization gauge tube. The experimental chamber consisted of two pyrex glass crosses, one having

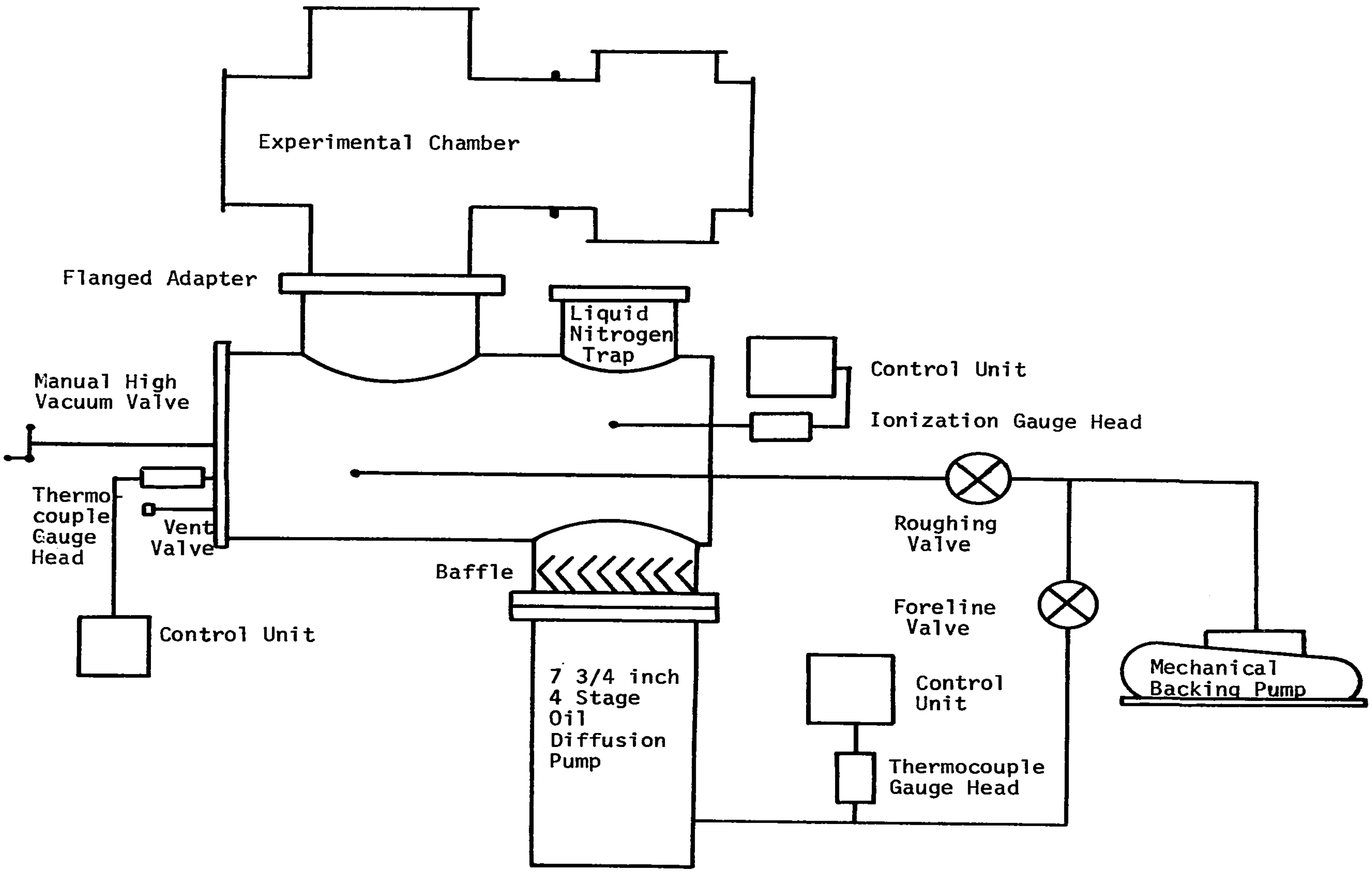
Experimental Chamber
Flanged Adapter
Liquid Nitrogen Trap
Control Unit
Ionization Gauge Head
Manual High Vacuum Valve
Thermocouple Gauge Head
Vent Valve
Control Unit
Baffle
Roughing Valve
Foreline Valve
Mechanical Backing Pump
7 3/4 inch 4 Stage Oil Diffusion Pump
Control Unit
Thermocouple Gauge Head

Figure (8.1) High Vacuum System.

symmetrical arms both with inside diameters of six inches, the other having arms with inside diameters of four inches and six inches. A combination of aluminum and perspex end plates together with rubber O-rings was used for sealing the system. The usual operating pressure ranged from 1 x 10^{-7} torr to 5 x 10^{-7} torr. A schematic diagram of the high vacuum system is shown in figure 8.1.

8.2 The Microparticle Charger

The charger was based on the technique of contact charging of the micron-sized particles(40). Electric fields are then used to accelerate these heavy charged particles. Several microparticle contact chargers have been designed by other workers(40 - 41) to produce single particles with the highest possible charge-to-mass ratios. The charging electrode in each of these chargers is usually a very small sphere, of radius less than 100 microns, supported by a thin tapered needle. The small size of the sphere, for a given sphere potential, assures a very high surface electric field and consequently results in high charge-to-mass ratios for the particles. On the other hand, the small size of the sphere also means that charged particles are emitted at a very low rate. Such chargers are best suited for providing single highly charged microparticles for studying hypervelocity impacts(41) or for evaluating microparticle detectors(42).

In the present experimental investigations high charge-to-mass ratios are not the main objective. As long as gravity effects are negligible and provided all particles have been preaccelerated through the same potential, particle motion in the structure is independent of charge-to-mass ratio. However, since the microparticle beam cross-section is detected visually by intercepting the particles on a greased glass plate, the charger should provide a large flux of microparticles for long periods of time, irrespective of charge-to-mass ratio.

The present microparticle charger has a conical charging electrode with a rounded tip. The large radius of curvature of the tip increases the probability of emission of charged particles. Thus, a high density microparticle beam is generated although the particles have charge-to-mass ratios much lower than in the case of small spherical charging electrodes. The charger has a microparticle reservoir from which particles are fed mechanically into the charging chamber. The reservoir system permits continuous operation of the charger for more than 12 hours.

The charger is shown schematically in figure 8.2. The charging chamber consists of two brass circular walls, A and B, separated by the insulating perspex wall, C. The stainless steel cylindrical charging electrode with its conical charging tip, having a head angle of 60°, is screwed into the central threaded hole of wall A. Two nuts are used to set the distance that the charging electrode protrudes into the charging chamber. Vertically above the charging electrode is a hole R in wall A. P is the microparticle powder reservoir. It consists of a brass body to which a vertical glass tube is fixed. P is vertically mounted on the brass cylinder T and a vertical hole in T connects the interior of P to the hollow interior of T. A threaded auger O passes through the horizontal cylindrical hole inside T and protrudes into hole R. The auger is mechanically coupled to a teflon insulating shaft which in turn is fixed to a thin stainless steel shaft. The latter passes through a rotary vacuum feed-through on the left hand side aluminum end plate of

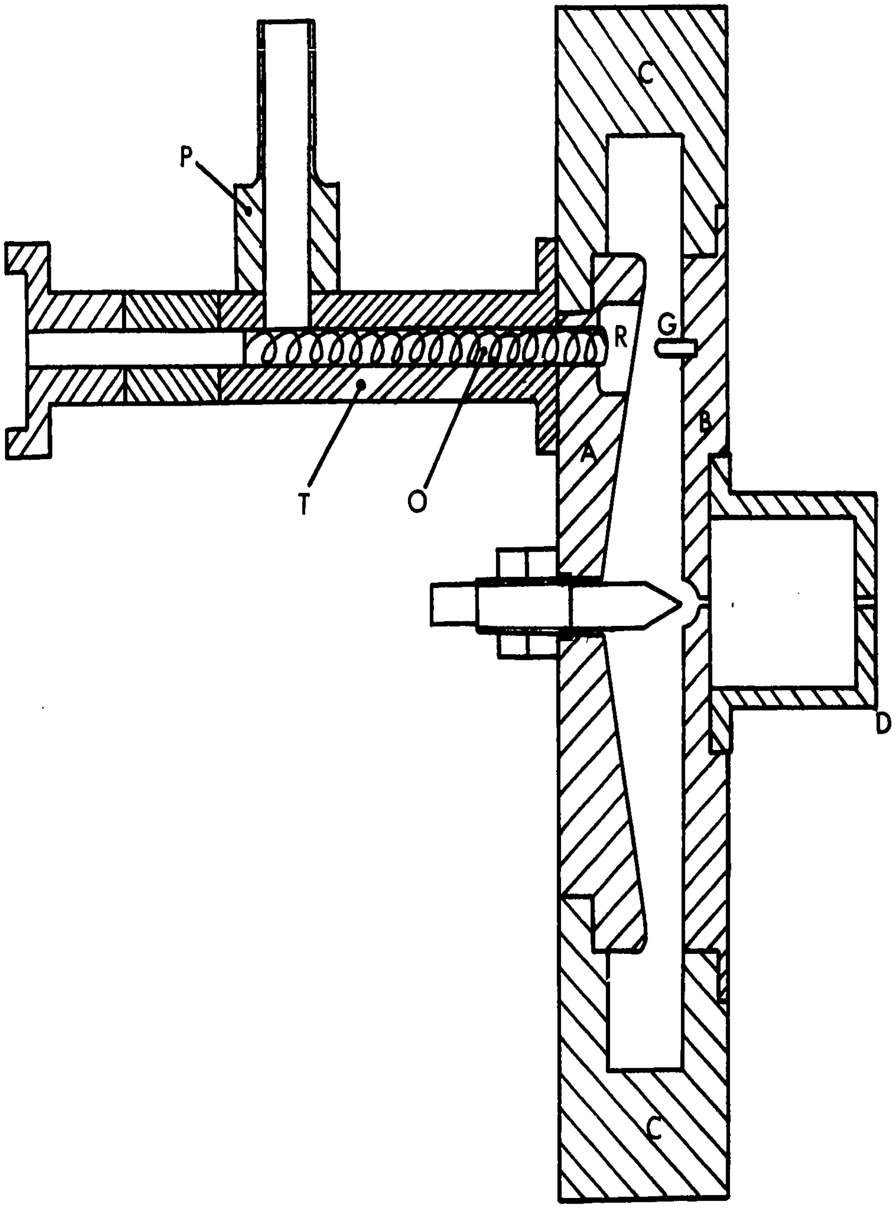
C
P
R
G
B
A
T
O
D
C

Figure (8.2) The Microparticle Charger.

the 6-inch pyrex glass cross. The shaft is rotated by a synchronous motor at a speed of 10 R.P.M. The charging electrode, wall A, and the conducting parts of the feeding mechanism are at a potential of 15 KV with respect to a common ground point to which wall B is connected.

The microparticles in P drop onto the auger O through the vertical hole in T. As the auger is rotated it transports the particles toward the charging chamber between walls A and B. The electric fields that exist between the grounded brass peg G, which acts as a field intensifier, and wall A induce charges on the particles that have fallen into R. The charged particles in R are accelerated towards wall B. Striking either the peg G or wall B, these particles exchange charge and are repelled towards wall A. This process repeats itself many times and aids in the deagglomeration of the microparticles entering the charger. The tapering of the interior side of wall A causes the electric fields between A and B to have components that force the charged particles, undergoing alternate collisions between A and B, towards the center of the charging chamber. This action enhances the flux of particles in the vicinity of the charging electrode and, as described below, helps to increase the rate of emission of charged particles.

Some of the particles at the center of the charging chamber will enter the region of high electric field between the conical tip of the charging electrode and the hemispherical depression in wall B. As the particles contact the tip of the charging electrode, each particle gains a high positive charge and is accelerated toward wall B. Some of these particles pass through the aperture while others continue to alternately collide with wall B and the charging electrode. The latter particles

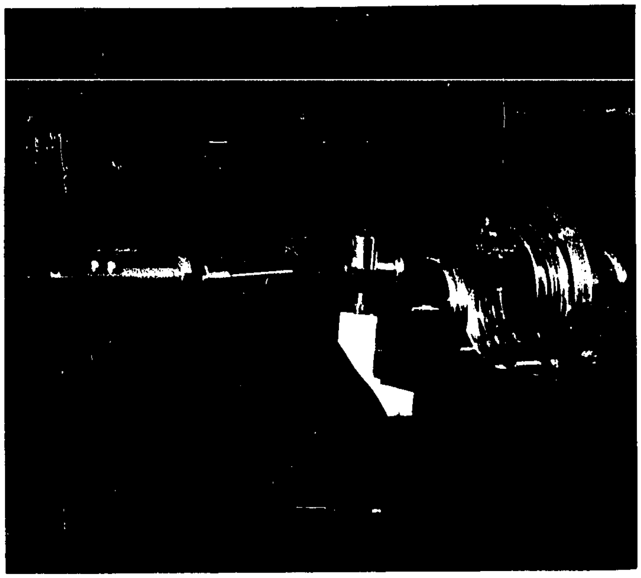

Figure (8.3) Exploded Front View of the Charging Mechanism.

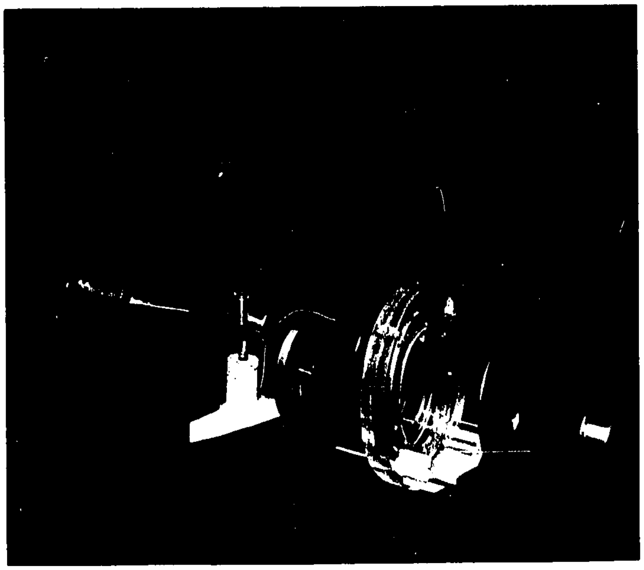

Figure (8.4) Exploded Rear View of the Charging Mechanism.

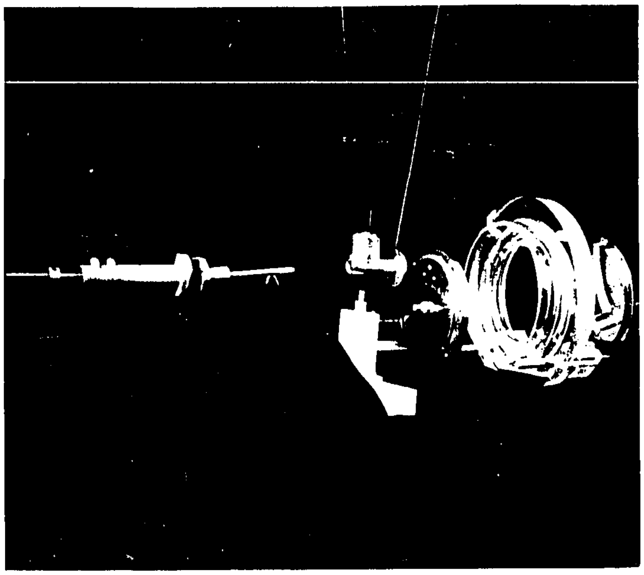

Figure (8.3) Exploded Front View of the Charging Mechanism.

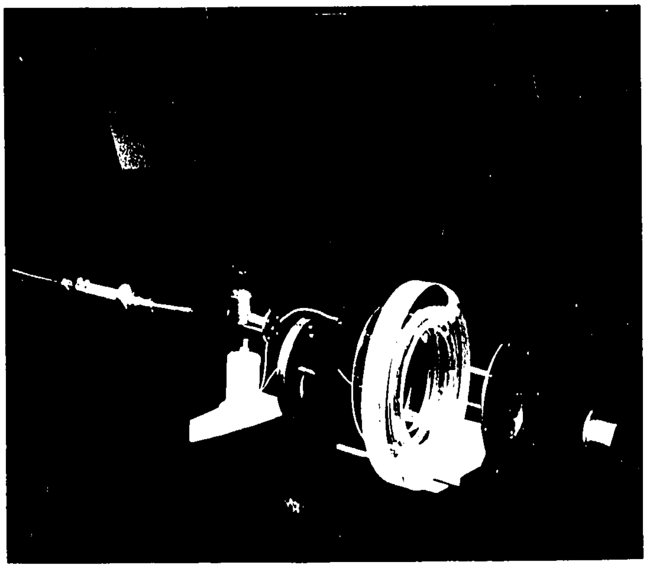

Figure (8.4) Exploded Rear View of the Charging Mechanism.

may pass through the aperture subsequently or they leave the region of high electric field and settle on the interior of the insulating perspex cylinder, C.

Since the emitted charged particles leave the tip of the charging electrode at various angles, it was found necessary to place a second aperture in the path of the particles. This second aperture, D, limits the divergence of the emitted microparticle beam and helps to avoid contamination of the vacuum system. Exploded views showing the components of the microparticle charger are shown in figures (8.3) and (8.4).

8.2.1 Testing of the Charger

The charger was tested to determine the breakdown voltage between the charging electrode and wall B. With no particles inside the charging chamber, a potential of 30 KV was reached without breakdown. During the experimental investigations the microparticle reservoir was filled with 3 micron carbonyl iron microparticles. When these particles were fed into the chamber, breakdown occured at lower voltages. During these experiments the value of the breakdown voltage was dependent on the distance between the charging electrode tip and the hemispherical depression on wall B and also on the rate of feeding of the particles. Through trial and error it was decided to use an operating voltage equal to 15 KV in all experiments.

It was then observed that after a period of operation, the auger ceased to feed the particles into the charging chamber although the particle reservoir P was still full. This failure was attributed to the small sizes of the particles that cause them to stick together and to the

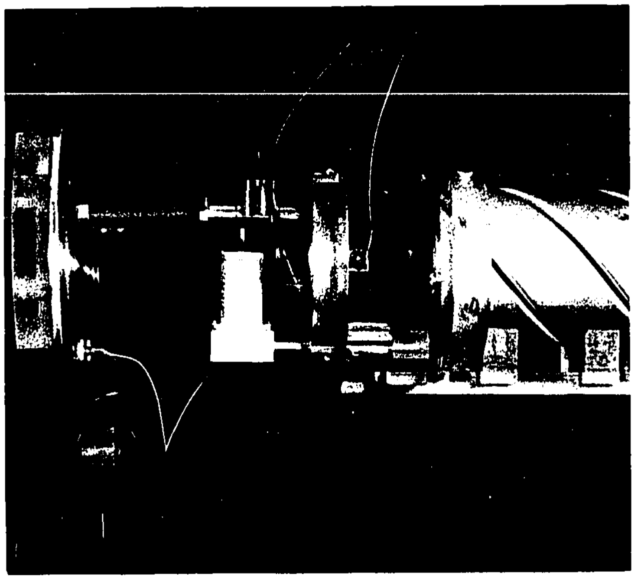

Figure (8.5) Microparticle Charger and Tapping Mechanism.

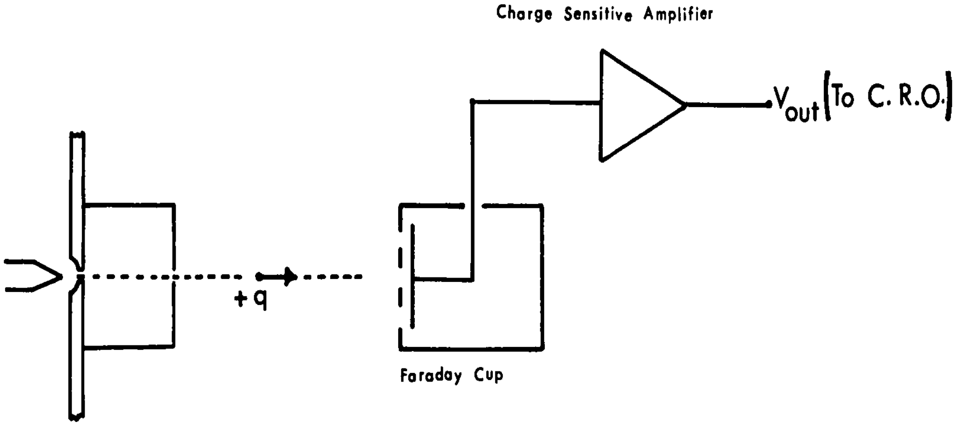
Charge Sensitive Amplifier
V_{out} (To C.R.O.)
+q
Faraday Cup

Figure (8.6) Sketch of the Charge Detection Arrangement.

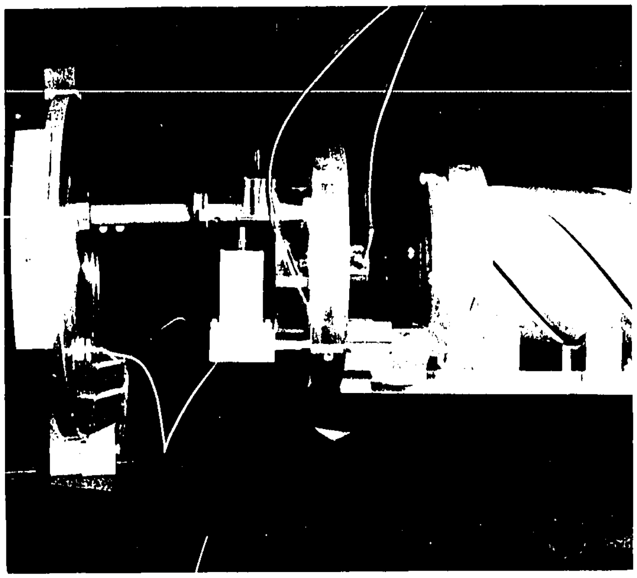

Figure (8.5) Microparticle Charger and Tapping Mechanism.

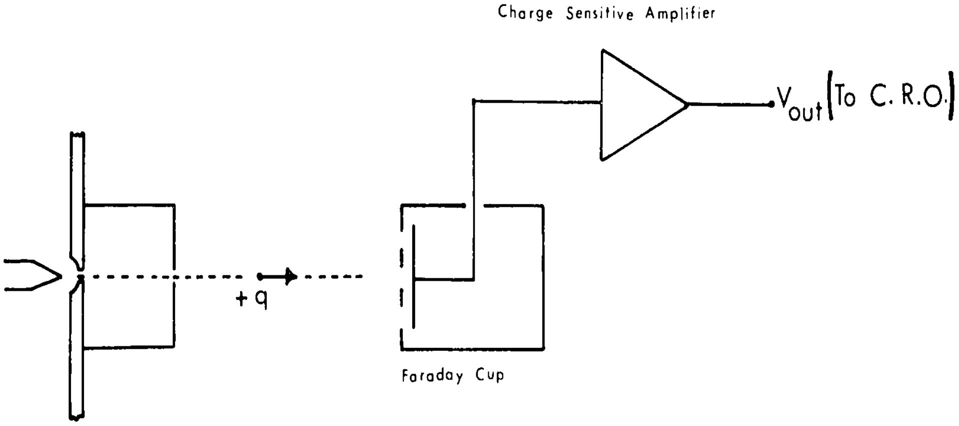
Charge Sensitive Amplifier
V_{out} (To C.R.O.)
+q
Faraday Cup

Figure (8.6) Sketch of the Charge Detection Arrangement.

walls of the reservoir. By tapping on the auger cylinder, T, it was found that the feeding action could be restarted. During the experiments the tapping was provided by a teflon-iron plunger actuated by an electrical solenoid. Figure (8.5) shows the assembled microparticle charger with the tapping mechanism mounted below the auger cylinder, T. The circuit used to actuate the solenoid consists of a silicon controlled rectifier which is triggered by pulses from a pulse generator. The repetition frequency of the pulses was 10 cycles/sec and the width of the pulse was 8.33 msec. When triggered, the SCR connects the terminals of the solenoid to the secondary of a step-down transformer, whose primary is connected to the mains via a manual switch. The latter also turns on the motor that drives the auger mechanism.

8.2.2 Charge Detection

The objective of this experiment was to ensure that charged particles were emitted from the charger. The position of the charging electrode tip with respect to wall B, the rate of particle feeding, the rate of actuating the tapping plunger, and pitch of the auger thread, were all adjusted through trial and error until a reasonable rate of emission was obtained without breakdown.

Since particles are not emitted from the charger as single particles but rather as a continuous stream it was not readily possible to carry out conventional time of flight experiments(43) to determine the charge-to-mass ratios of the particles. However, it was possible to detect the charges of the particles by using a Faraday cup that intercepted the particles emitted from the aperture D. The Faraday cup was followed by a charge sensitive amplifier whose output was fed to a Cathode Ray Oscillograph as shown schematically in figure (8.6).

Figure (8.7) depicts the typical output of the charge sensitive amplifier and shows the wide range of the charges on the microparticles. This wide variation is due in part to the size distribution of the particles. Also, since the charge induced on each particle depends on the particle shape, any irregularly shaped particle will accumulate a charge different from that on a spherical particle of similar size. Even if all particles have the same size and the same spherical shape, two or more of these particles may agglomerate to form a larger irregularly shaped particle. The latter, when charged, will have a charge on it different from those on the single spherical particles. Another factor that may cause similar particles to have different charges is the dynamic nature of the contact charging process. Little is known about the latter, but it is possible that the time constant of this process is much larger than the time of contact between the microparticle and the charging electrode. Therefore, the microparticle could leave the charging electrode before the charging is complete.

A typical value of the charge on the carbonyl iron particle, as calculated from the detected output voltage of the charge sensitive amplifier is

$$q = .56 \times 10^{-14} \text{ coulomb}$$

Assuming spherical particles of carbonyl iron with a diameter of 3 microns which equals the average size specified by the manufacturer, the mass of

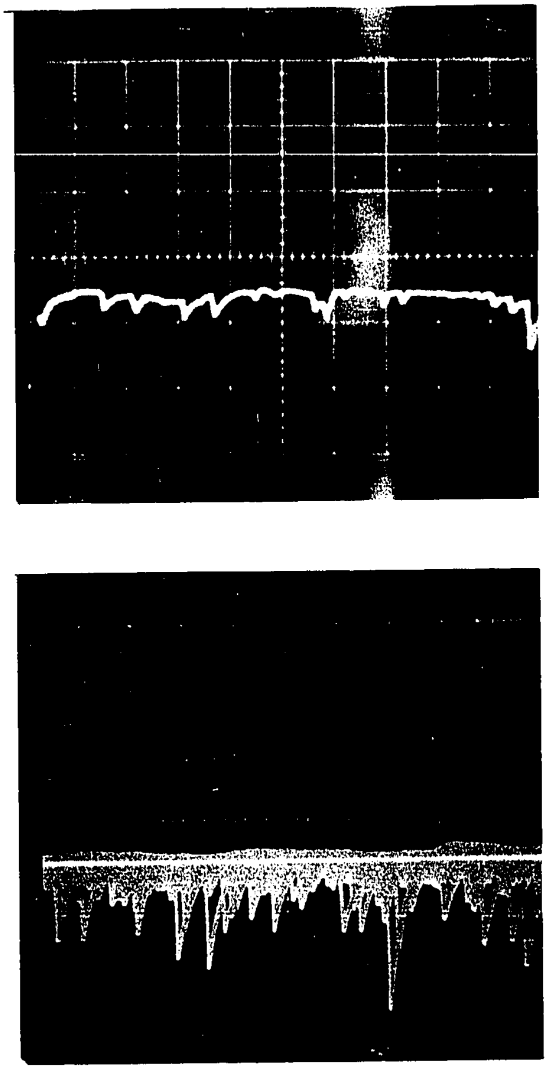

Figure (8.7) Photographs of Oscilloscope Trace of the Typical Output from the Charge-Sensitive Amplifier.

(a) Output recorded during a single sweep on the C.R.O.

(b) Output stored during several sweeps on the C.R.O.

Sensitivity: 5 mV/cm, 1 ms/cm.

Typically, $q = 0.56.10^{-14}$ coulomb, $M = 1.13.10^{-13}$ kilogram and $\frac{q}{M} = 0.05$ coulomb/kilogram.

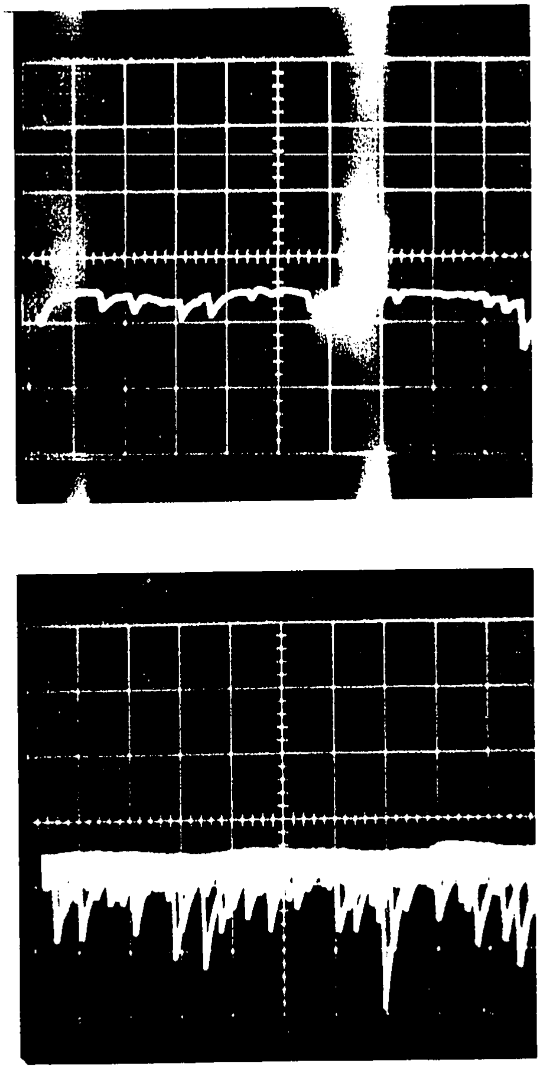

Figure (8.7) Photographs of Oscilloscope Trace of the Typical Output from the Charge-Sensitive Amplifier.

(a) Output recorded during a single sweep on the C.R.O.

(b) Output stored during several sweeps on the C.R.O.

Sensitivity: 5 mV/cm, 1 ms/cm.

Typically, $q = 0.56.10^{-14}$ coulomb, $M = 1.13.10^{-13}$ kilogram and $\frac{q}{M} = 0.05$ coulomb/kilogram.

a single particle is

$$M = \frac{4}{3}\pi\rho\ r^3$$

$$= \frac{4}{3}\pi \times 8000 \times (1.5 \times 10^{-6})^3$$

$$= 1.13 \times 10^{-13} \text{ Kilogram}$$

Thus the typical value for the charge-to-mass ratio of the particle produced by the charger is

$$\frac{q}{M} \cong 0.05 \text{ coulomb/kilogram}$$

It is evident that for $V_0 = 1200$ volts the effect of gravity on these particles will be negligible.

8.3 The Uniformly Twisted Quadrupole Structure

8.3.1 The Electrode Shapes

To provide the desired quadrupole field as given by equations (2.1a) and (2.1b), the electrodes must be shaped to coincide with a set of hyperbolic equipotential surfaces extending to infinity. If electrodes of finite size are used the field will be distorted. However, in designing the poles or electrodes for straight classical quadrupole sections it has been found that even circular(44) or semi-circular(44) electrodes can give acceptable quadrupole fields provided their dimensions are suitably chosen(44).

The electrodes for the uniformly twisted electrostatic structure are most easily manufactured by producing a cylindrical mould with the required electrode shape. As it is no more difficult to machine a mould of hyperbolic cross-section than to machine a mould of circular cross-section, it was decided to use moulds of hyperbolic cross-section. In order to reduce the amount of truncation distortion of the fields within the quadrupole structure aperture, the outer surface diameters of the electrodes were made greater than 3 times the aperture diameter.

8.3.2 Structure Parameters

The aperture radius and the periodic length of the twisted structure must satisfy the condition $(\beta a)^2 << 1$. Choosing $(\beta a)^2 = 0.1$ and the aperture radius $a = 1.5$ cm, the periodic length of twist is $L = 29.68$ cm. To test the imaging properties of the twisted electrostatic lens, the parameters of the structure were chosen to correspond to the minimum possible length of the lens. It was shown in Chapter 7 that this minimum length corresponds to $m = 3$ and $n = 1$. These values in turn correspond to $s = 1.25$ and give the length of the lens as $\ell = \frac{\sqrt{5}}{2} L = 33.3$ cm. Equation (7.12) shows that for these values of s and $(\beta a)^2$ and an accelerating potential of 15 KV, which is provided by the microparticle charger, the magnitude of the quadrupole focusing voltage must be $V_0 = 1.2$ KV.

8.3.3 Fabrication of the Twisted Structure

A mould is used to fabricate each of the twisted electrodes of the structure. The mould, shown in figure (8.8), consists of a cylindrical aluminum split sleeve which encases a machined aluminum cylinder. The

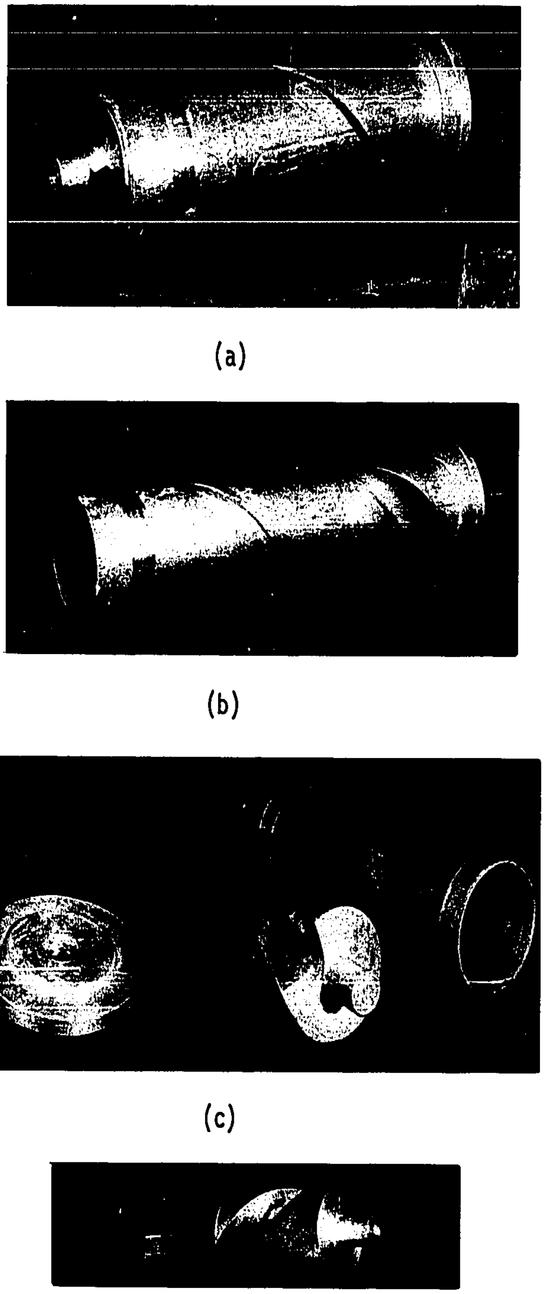

(a)

(b)

(c)

(d)

Figure (8.8) The Mould that was Used to Fabricate the Twisted Electrodes.

Photographs (a), (b), (c) show the mould for the clockwise twisted lens at different stages of assembly. The electrode is still inside the mould. Photograph (d) shows the mould for the counter-clockwise twisted electrodes.

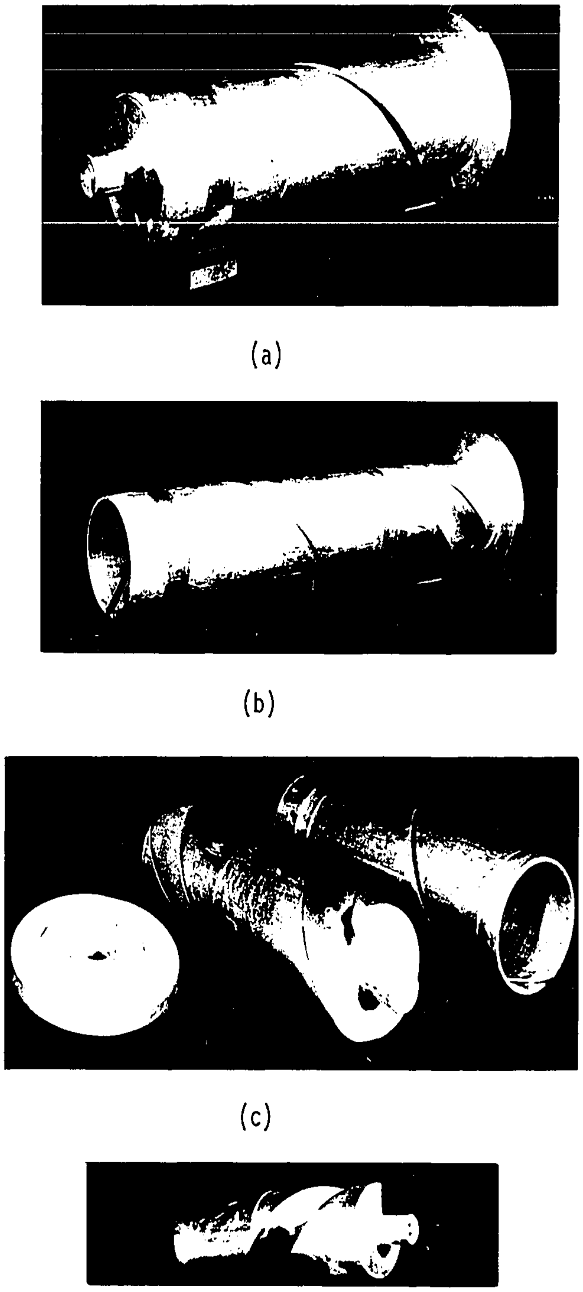

(a)

(b)

(c)

(d)

Figure (8.8) The Mould that was Used to Fabricate the Twisted Electrodes.

Photographs (a), (b), (c) show the mould for the clockwise twisted lens at different stages of assembly. The electrode is still inside the mould. Photograph (d) shows the mould for the counter-clockwise twisted electrodes.

latter is manufactured by first mounting the aluminum cylinder on a milling machine with its axis parallel to the horizontal bed of the machine. Then, while the cylinder, through an appropriate gearing mechanism, is slowly turning about its axis and while the milling machine bed is moving horizontally, a vertical cutting tool mills an initial small groove. The vertical position of the cutting tool and the initial angular position of the cylinder are then precisely adjusted for the milling of a second groove. The process is repeated many times until a mould with the desired hyperbolic cross-section is completed. The direction of twist of the final electrodes is determined by the direction in which the aluminum cylinder is turning during the milling process. The outer surface diameter of the machined aluminum cylinder is 9.3 cm, greater than 3 times the aperture diameter. The length of the cylinder is approximately 2 cm longer than the required length of the imaging lens in order to allow for the shrinkage of the moulding resin as it solidifies and in order that the ends of the electrode can be finally machined to the exact required length with the end faces exactly perpendicular to the axis of the cylinder.

Once the mould is machined, the fabrication of the electrodes is started by spraying the mould with a standard release agent. The sleeve is then placed around the mould. The two liquid components of a general purpose rigid low temperature potting resin are then mixed together. The mould is filled with the resin and it is left to cure under vacuum. Once cured the solid electrode is withdrawn from the mould, the release agent is cleaned off and the electrode's ends are cut to the prescribed length. The surface of the insulating electrode, shown in figure (8.9a), is then sprayed with a conductive silver paint. Four silver painted electrodes

Figure (8.9a) A Clockwise Twisted Electrode Before Painting.

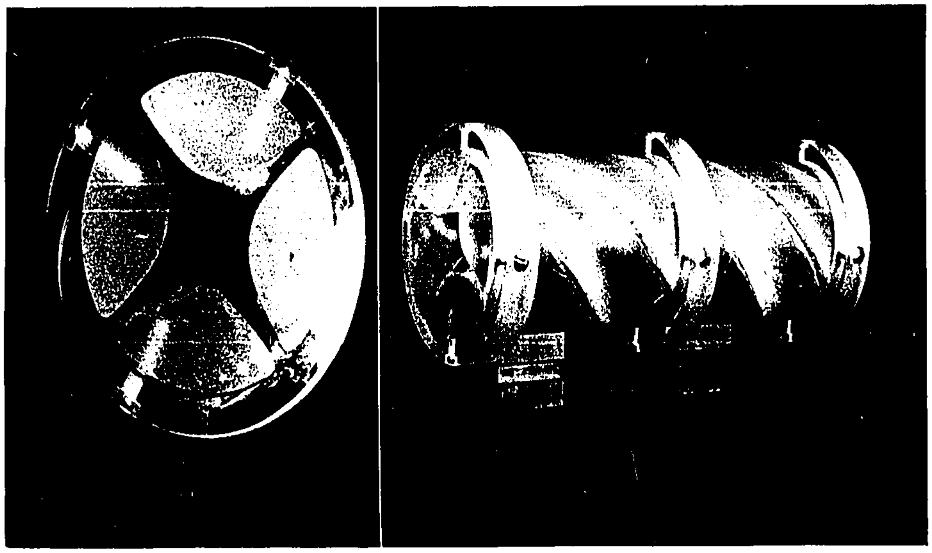

Figure (8.9b) Front and Side Views of the Clockwise, β - ve, Twisted Lens Before Painting.

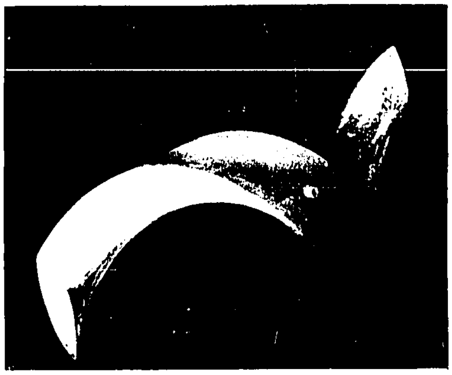

Figure (8.9a) A Clockwise Twisted Electrode Before Painting.

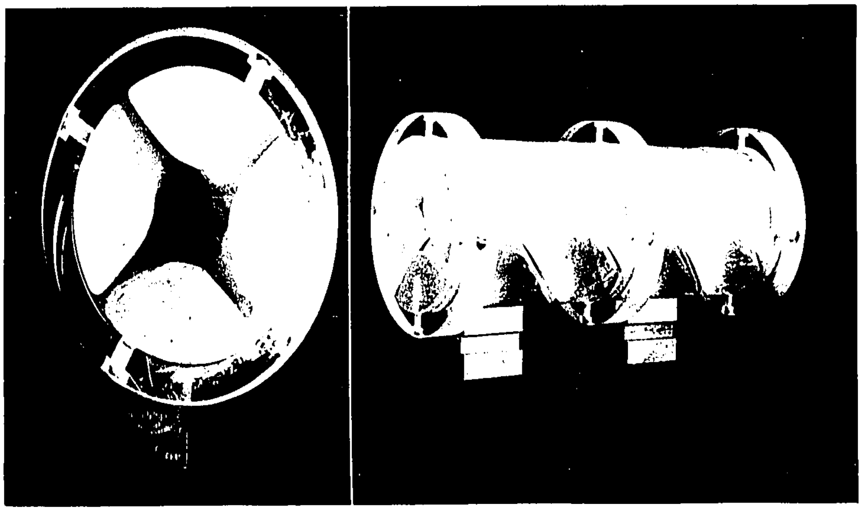

Figure (8.9b) Front and Side Views of the Clockwise, β - ve, Twisted Lens Before Painting.

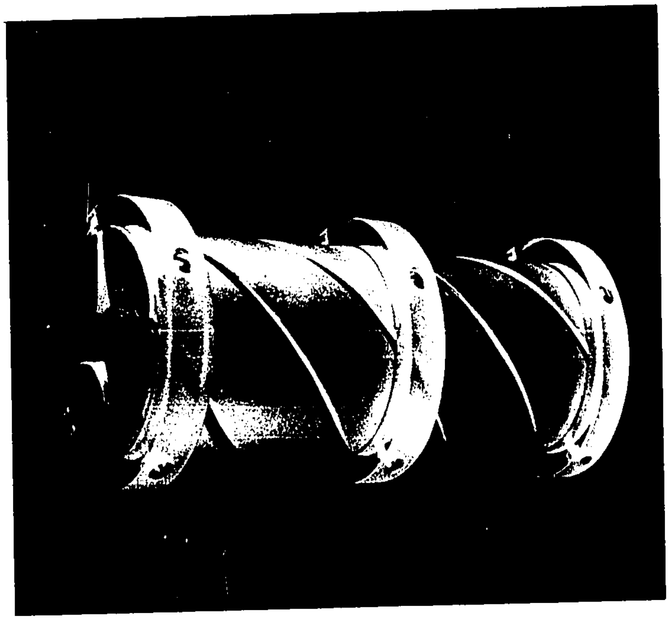

Figure (8.9c) The Uniformly, Clockwise, Twisted Lens After Silver Painting.

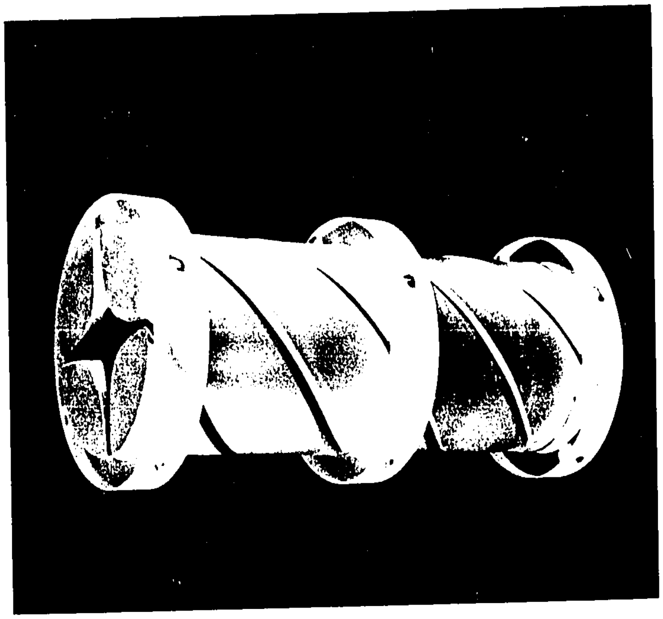

Figure (8.9c) The Uniformly, Clockwise, Twisted Lens After Silver Painting.

are then assembled to form the twisted lens. The electrodes are held in place by using perspex supporting sleeves. Figures (8.9b) and (8.9c) show the assembled lens before and after silver painting.

Two moulds were machined, one for the counter-clockwise twisted electrodes, β positive, and the other for the clockwise twisted electrodes, β negative. For each of the twisted lenses opposite electrodes are connected by a high voltage cable. Two other high voltage cables supply the focusing voltages $+ V_0$ and $- V_0$ to two adjacent electrodes. The focusing voltages $+ V_0$ and $- V_0$ are supplied by a high voltage supply built for this purpose. A circuit diagram of this supply is shown in Figure (8.10).

A breakdown test of the twisted lens was performed with one opposite pair of electrodes grounded and the other pair at high potential. Breakdown between adjacent electrodes occured at a potential of 3.5 KV. There was no breakdown at the required operating potential difference of $2V_0 = 2.4$ KV.

8.4 Experiments

The schematic diagram of figure (8.11) shows the arrangement used to investigate the imaging properties of the twisted lens. The microparticle charger and the twisted lens are mounted on a horizontal insulating slab inside the vacuum system. The horizontal axes of the charger and the lens are carefully aligned to avoid aberration caused by misalignment. The twisted structure is oriented such that the electrode axes at the injection plane, $Z = 0$, that is the fixed X and Y axes of the theoretical analysis, are in the horizontal and vertical directions.

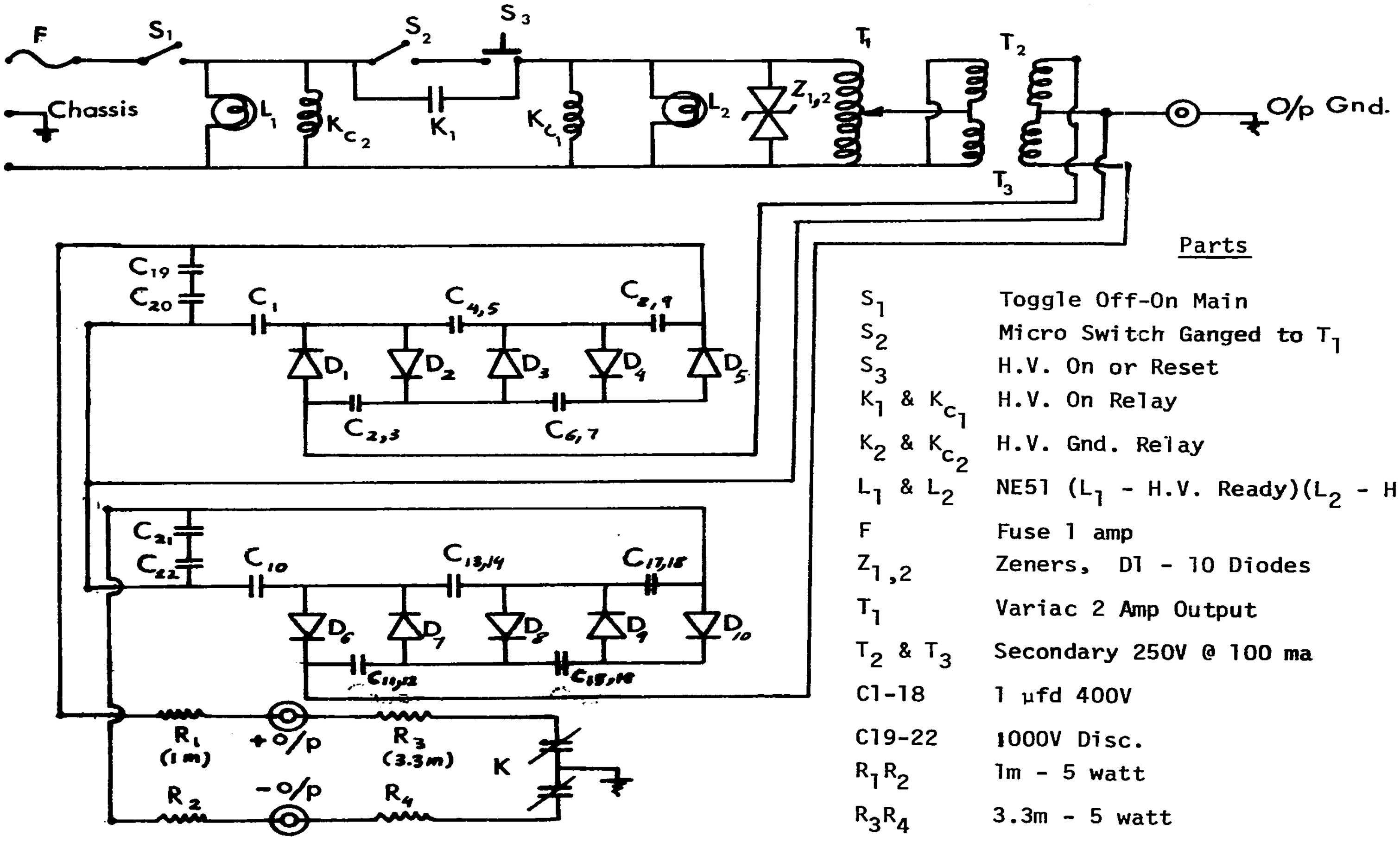
F
S1
S2
S3
Chassis
L1
Kc2
K1
Kc1
L2
Z1,2
T1
T2
T3
O/p Gnd.
C19
C20
C1
C4,5
C8,9
D1
D2
D3
D4
D5
C2,3
C6,7
C21
C22
C10
C13,14
C17,18
D6
D7
D8
D9
D10
C11,12
C15,16
R1 (1m)
+o/p
R3 (3.3m)
K
R2
-o/p
R4

Parts

S_1	Toggle Off-On Main
S_2	Micro Switch Ganged to T_1
S_3	H.V. On or Reset
K_1 & K_{C_1}	H.V. On Relay
K_2 & K_{C_2}	H.V. Gnd. Relay
L_1 & L_2	NE51 (L_1 - H.V. Ready)(L_2 - H.V. On)
F	Fuse 1 amp
$Z_{1,2}$	Zeners, D1 - 10 Diodes
T_1	Variac 2 Amp Output
T_2 & T_3	Secondary 250V @ 100 ma
C1-18	1 μfd 400V
C19-22	1000V Disc.
R_1R_2	1m - 5 watt
R_3R_4	3.3m - 5 watt

Figure (8.10) Circuit Diagram of the Quadrupole Focusing Voltage Supply.

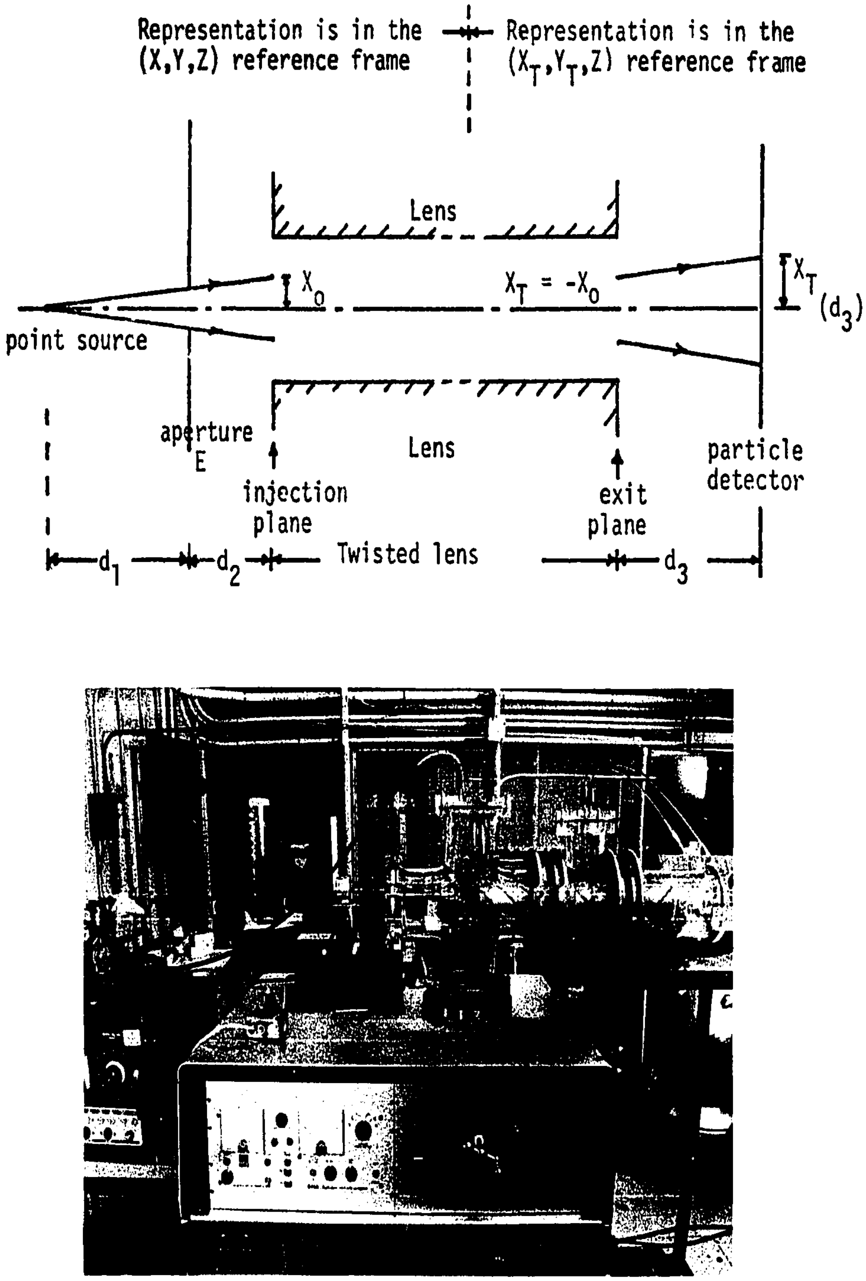
Representation is in the (X,Y,Z) reference frame
Representation is in the (X_T,Y_T,Z) reference frame
Lens
X_0
$X_T = -X_0$
$X_T(d_3)$
point source
aperture
E
Lens
injection plane
exit plane
particle detector
d_1
d_2
Twisted lens
d_3

Figure (8.11) Sketch and Photograph of the Experimental Arrangement Used to Test the Imaging Properties of the Twisted Lens Structures.

The imaging properties of the twisted lens are examined by shaping the cross-section of the injected microparticle beam and then studying the beam cross-section as the particles emerge from the lens. At first two crossed thin wires were used to shape the injected beam cross-section. It was found that these wires caused scattering of some of the particles which gave these particles a large transverse momentum, which in turn caused the injection conditions of these particles to lie outside the acceptance limits of the structure. It was then decided to use a rectangular aperture to give the injected beam a rectangular cross-section, similar to that discussed in Section (7.4). The detected exit beam cross-section can then be compared with the results obtained in Section 7.4.

The circular disc E, shown in figure (8.11), has a rectangular aperture whose sides, equal to $\eta_1 = 1.56$ mm and $\eta_2 = 0.85$ mm, are parallel to the fixed X, Y axes. In order to detect the degree of rotation of the emerging beam without ambiguity, the sides of the aperture are chosen non-equal. The ratio between their lengths is approximately 11 : 6, the longer side being in the fixed X-direction, as shown in figure (8.12).

To ensure that the tip of the charging electrode can be considered as a point source and hence to make sure that the cross-section of the injected beam at the input plane, Z = 0, is a rectangle; the following experiments were performed.

The first experiment was to examine the microparticle distribution at the plane of the aperture E to ensure full coverage of this rectangular aperture. The experimental arrangement shown in figure (8.13a) was used. The rectangular aperture was replaced by a greased glass slide. The

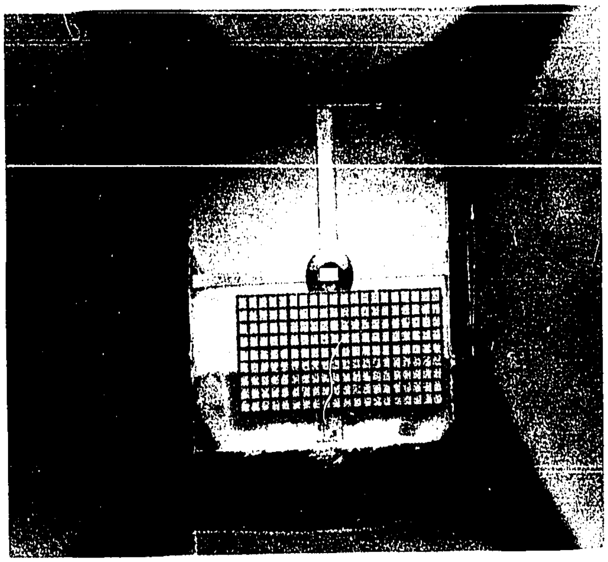

Figure (8.12) The Injected Beam Shaping Aperture.

The rectangular aperture E is mounted in front of the lens injection plane to shape the injected beam cross-section.

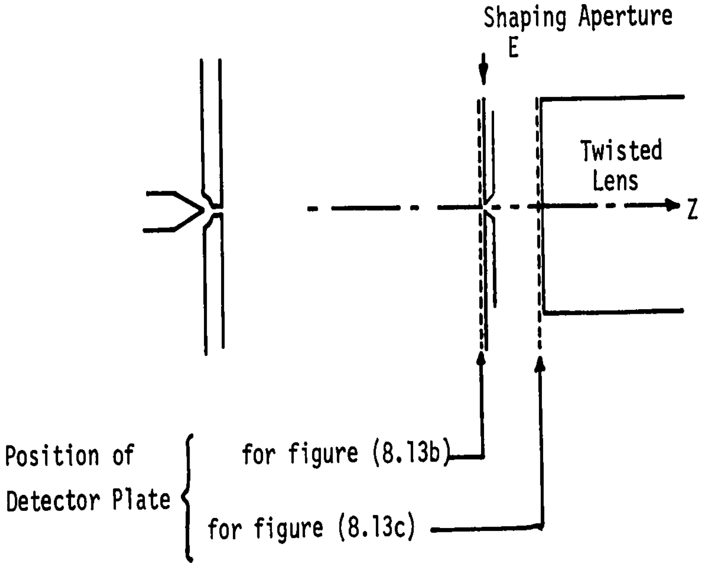
Shaping Aperture
E
Twisted
Lens
Z
Position of
Detector Plate
for figure (8.13b)
for figure (8.13c)

Figure (8.13a) Sketch of the Experimental Arrangement Used to Test the Injected Beam Cross-Section.

The greased detector plate is first placed at the plane of the aperture E and then at the injection plane of the lens beyond the aperture E.

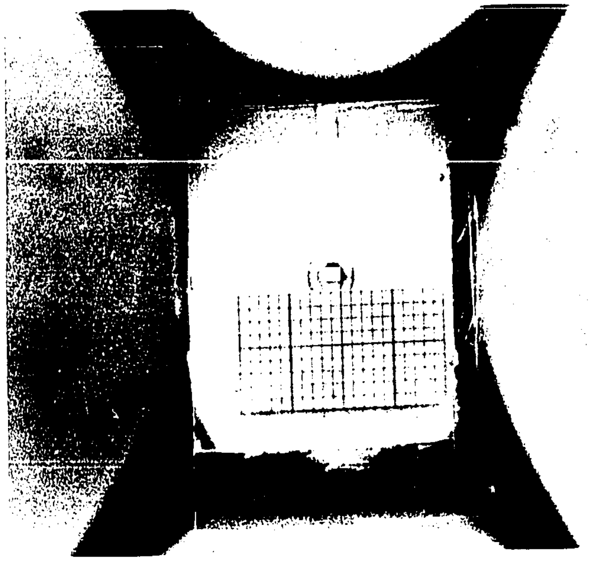

Figure (8.12) The Injected Beam Shaping Aperture.

The rectangular aperture E is mounted in front of the lens injection plane to shape the injected beam cross-section.

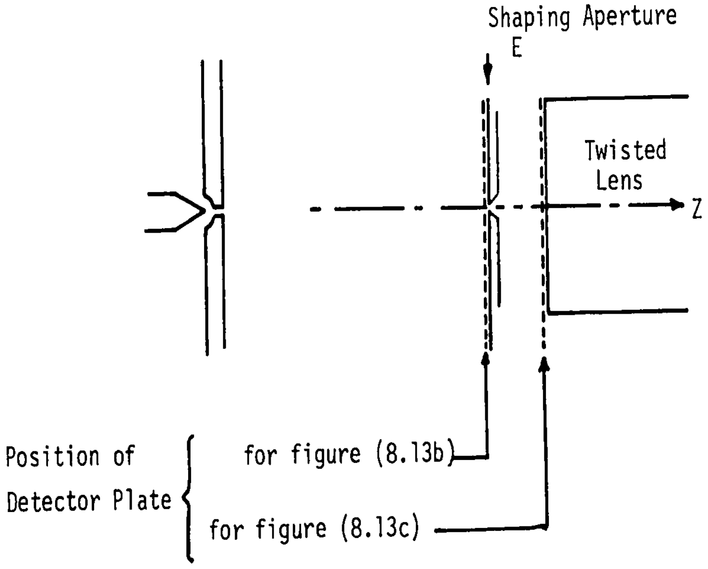
Shaping Aperture
E
Twisted
Lens
Z
Position of
Detector Plate
for figure (8.13b)
for figure (8.13c)

Figure (8.13a) Sketch of the Experimental Arrangement Used to Test the Injected Beam Cross-Section.

The greased detector plate is first placed at the plane of the aperture E and then at the injection plane of the lens beyond the aperture E.

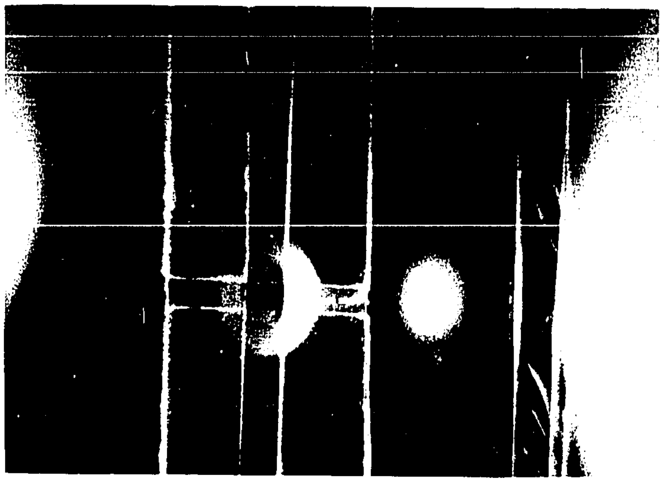

Figure (8.13b) Photograph of Injected Microparticle Beam Cross-Section at the Plane of the Shaping Aperture E.

The detector slide was moved horizontally to photograph the detected beam cross-section and the aperture E simultaneously. The illuminated circular area behind the rectangular aperture is the reflection of light from the tapered hole in perspex plate supporting the aperture E.

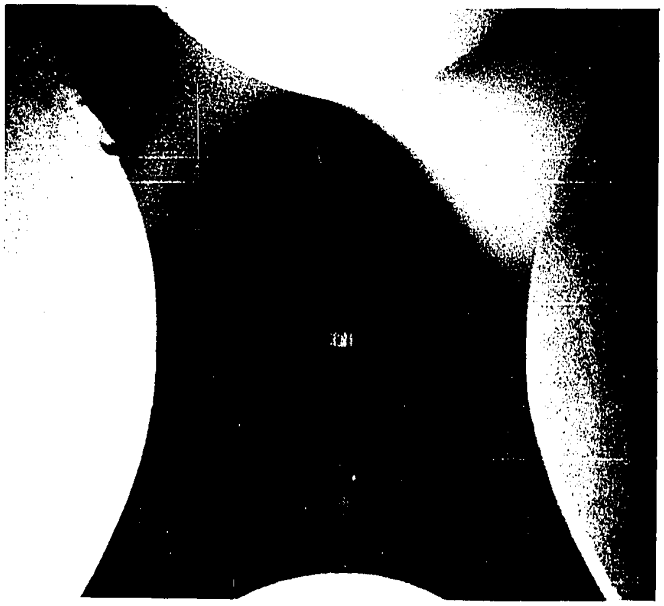

Figure (8.13c) Photograph of the Injected Beam Cross-Section at the Lens Injection Plane.

The detector slide is still mounted at the lens injection plane.

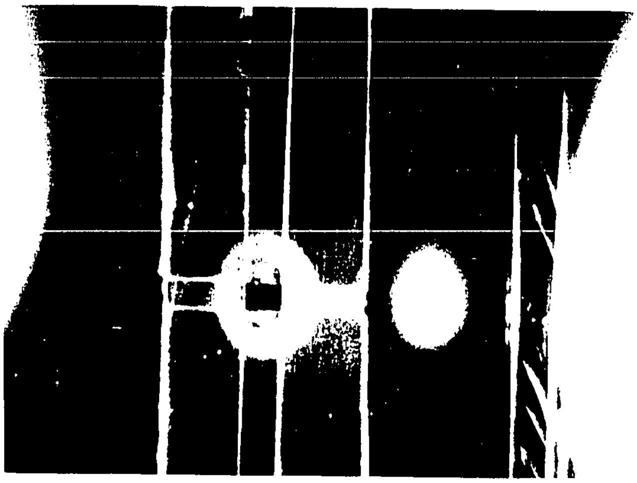

Figure (8.13b) Photograph of Injected Microparticle Beam Cross-Section at the Plane of the Shaping Aperture E.

The detector slide was moved horizontally to photograph the detected beam cross-section and the aperture E simultaneously. The illuminated circular area behind the rectangular aperture is the reflection of light from the tapered hole in perspex plate supporting the aperture E.

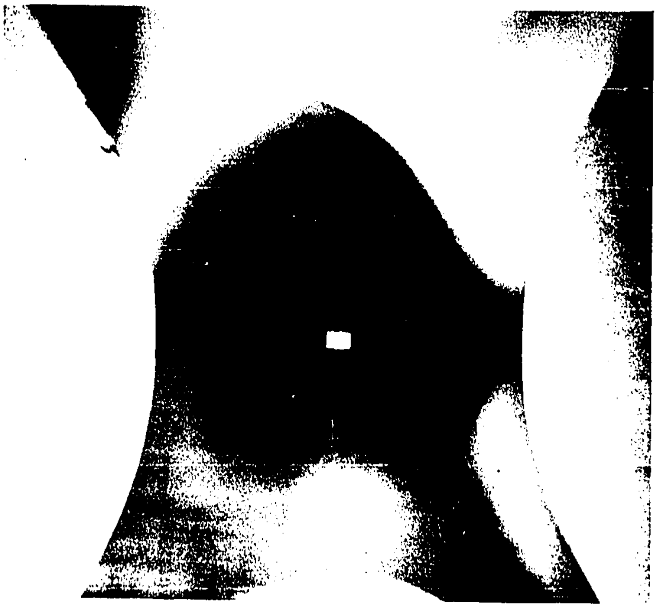

Figure (8.13c) Photograph of the Injected Beam Cross-Section at the Lens Injection Plane.

The detector slide is still mounted at the lens injection plane.

greased detector slide was mounted on the disc of the aperture E. Figure (8.13b) shows the detected beam cross-section. The detector slide was moved horizontally to be able to photograph the detected cross-section. Figure (8.13b) also shows the rectangular aperture E and shows that the detected beam cross-section is reasonably uniform. The diameter of the circular aperture D was 1 mm and the distance between it and the tip of the charging electrode was 28 mm. The distance between the tip of the charging electrode and the surface of the greased glass slide, the position of the aperture E, was 67.5 mm. The diameter of the detected beam cross-section was equal to 2.4 mm which is equal to 1 mm. $\frac{67.5}{28}$. This result indicates that the tip of the charging electrode can be considered as a point source. Also the detected beam cross-section at the position of the rectangular aperture ensures full coverage of this rectangular aperture by the microparticle beam.

A second experiment was performed to insure that the microparticle beam cross-section, at $Z = 0$, in the presence of the aperture E between the charger and the lens as shown in figure (8.11), is a rectangle. A greased glass slide was placed at the input plane, $Z = 0$. With no quadrupole voltage and using a charger voltage equal to 15 KV, the detected beam cross-section was, as shown in figure (8.13c) in which the detector plate is still mounted on the entry of the lens, a rectangle. This rectangle had its sides parallel to the electrode axes at $Z = 0$, that is parallel to the sides of the aperture E. The microparticle distribution over the detected rectangular cross-section was more or less uniform. The sides of the rectangle were equal to 1.73 mm and 0.95 mm, the longer side being in the fixed X- direction.

The last two experiments show that the tip of the charging electrode can be considered as a point source at a distance $(d_1 + d_2)$ from the lens input plane. Therefore the experimental arrangement of figure (8.11) is exactly that of figure (7.5a). The injected beam at $Z = 0$ has a rectangular cross-section centered at the center of the quadrupole lens aperture. The sides of the injection rectangle are parallel to the fixed X and Y axes and are equal to

$$\eta_1 \frac{d_1 + d_2}{d_1} = 1.73 \text{ mm} \quad ,$$

$$\eta_2 \frac{d_1 + d_2}{d_1} = 0.95 \text{ mm} \quad . \tag{8.1}$$

where η_1 and η_2 are the dimensions of the aperture E and (d_1, d_2) are as shown in figure (8.11).

Also by considering the tip of the charging electrode as a point source, the transverse momenta of each particle at $Z = 0$ are related to the coordinates of the particle at $Z = 0$ as,

$$P_{X_0} = \frac{P_{Z_0}}{d_1 + d_2} X_0 \quad ,$$

$$P_{Y_0} = \frac{P_{Z_0}}{d_1 + d_2} Y_0 \quad . \tag{8.2}$$

where P_{Z_0} is the axial momentum of the particle at injection. The dimensions and the position of the aperture E during the experiments were chosen such that the angle of divergence of the injected beam is small. Thus, the axial momentum of each particle at injection can be assumed equal to its total injection momentum P_0. Hence

$$P_{Z_0} \cong P_0 = (2qMV)^{1/2}, \text{ where V is the charger high voltage = 15 KV.} \tag{8.3}$$

The analysis of Section 7.4 shows that for an injected beam having the rectangular cross-section provided by the aperture E and whose particles have their coordinates and momenta related by equations (8.2) and (8.3), the exit beam cross-section at the exact imaging values of the lens parameters should be a rectangle. This exit rectangle should be at the center of the quadrupole aperture and its sides should be parallel to the electrodes axes at the exit, the (X_T,Y_T) axes. The beam cross-section should be rotated $2\pi + 43°$ with respect to the fixed X, Y axes in case of the counter-clockwise twisted lens. The exit rectangular cross-section should have the same dimensions as the cross-section of the rectangular injected beam at $Z = 0$. Moreover, the mechanical momenta of any of the exit particles in the fixed target plane should be

$$P_{X_T} = \frac{P_{Z_0}}{d_1 + d_2} X_T,$$

$$P_{Y_T} = \frac{P_{Z_0}}{d_1 + d_2} Y_T,$$

$$P_{Z_{exit}} = P_{Z_0} \quad , \tag{8.4}$$

where X_T and Y_T are the exit coordinates of the emerging particle with respect to the (X_T, Y_T, Z) fixed target coordinate frame.

According to the relations of (8.4), if a drift space d_3 is introduced beyond the lens exit, the particles should cover an expanded rectangular area whose sides are still rotated 43° with respect to the X, Y axes. The ratio between the lengths of these sides should be that between the sides of the rectangular aperture E, that is $n_1:n_2 \cong 11:6$.

In the experiments, the microparticle beam cross-section was detected on a greased glass slide as the beam emerged from the lens. Arrangements were made so that the distance between the lens exit plane and the greased face of the glass slide could be adjusted. Also a ratchet and vacuum feed-through mechanism were used to move the greased glass slide in the horizontal direction parallel to the exit plane so that more than one experiment could be conducted without opening the experimental vacuum chamber to air.

8.4.1 Experimental Results

(a) Single Twisted Electrostatic Quadrupole Lens

The experiment which is described below comprises two separate experiments, one for the counter-clockwise twisted lens, the other for the clockwise twisted lens. For all experiments the greased detector slide was mounted exactly at the end of each of the single twisted lenses and the charger high voltage was constant at 15 KV. For the initial part of the experiment the quadrupole focusing voltage was adjusted to the exact theoretical imaging value of 1200 volts. The detected exit beam cross-section at this focusing voltage closely approximated a rectangle but the ratio between its sides was less than 11:6; the longer sides were smaller than expected from equation (8.1). The angle of rotation of the sides of this cross-section with respect to the fixed (X,Y) axes (the horizontal and vertical axes) was slightly smaller than $2\pi + 43°$. The theoretical study, already described in Section 7.4 was then carried out and it became apparent that the twisted lens was in effect slightly detuned from its actual imaging value.

The previously mentioned ratchet mechanism was then introduced to allow movement of the detector plate in the horizontal direction so that several experiments could be carried out without letting the system up to air. A series of experiments was then carried out while the focusing voltage was varied in steps from 1150 volts up to 1250 volts. It was found that a potential of 1210 volts produced the best image for both the counter-clockwise and the clockwise twisted lenses. At this value of V_0, the detected beam cross-section is a rectangle whose sides are parallel to the electrode axes at the exit (X_T, Y_T), that is rotated $2\pi + 43°$ with respect to the fixed (X, Y) axes. The dimensions of the rectangle are equal to 1.73 mm and 0.95 mm, exactly equal to those of the injected beam at $Z = 0$. Photos of the detected exit beam cross-section at $V_0 = 1210$ volts, with the detector plate mounted at the exit of the lens, are shown in figure (8.14) for the counter-clockwise twisted lens and in figure (8.15) for the clockwise twisted lens.

The detected exit beam cross-sections with no drift space beyond the exit of the lens and at values of the focusing voltage less than,

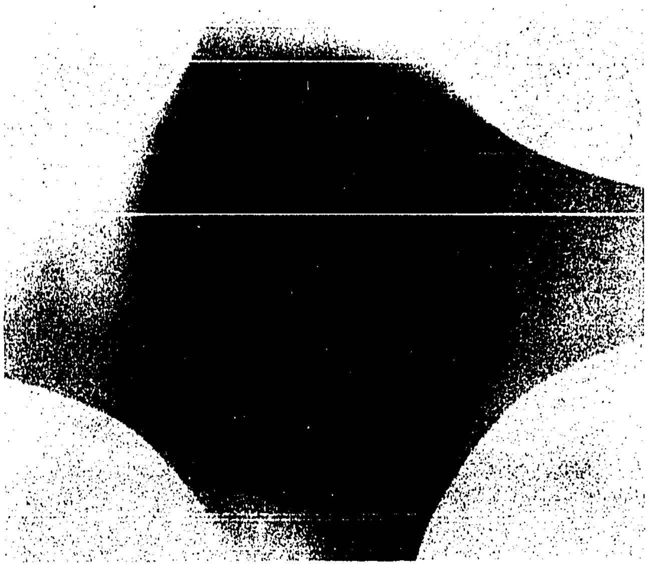

Figure (8.14) Beam Cross-Section at the Exit Plane of the Counter-Clockwise, β + ve, Twisted Lens at V_0 = 1210 volts.

This is a rear view with the detector slide still mounted at the exit plane of the lens.

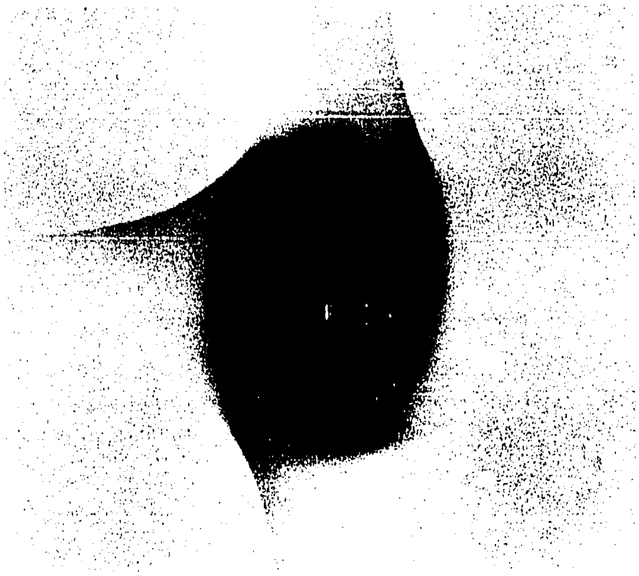

Figure (8.15) As in Figure (8.14) for the Clockwise, β - ve, Twisted Lens.

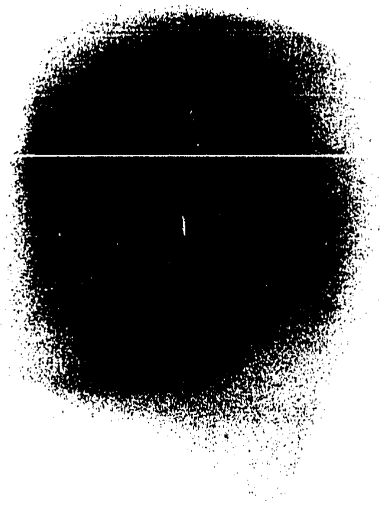

Figure (8.14) Beam Cross-Section at the Exit Plane of the Counter-Clockwise, β + ve, Twisted Lens at V_0 = 1210 volts.

This is a rear view with the detector slide still mounted at the exit plane of the lens.

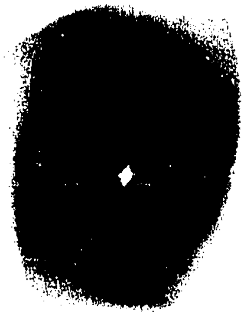

Figure (8.15) As in Figure (8.14) for the Clockwise, β - ve, Twisted Lens.

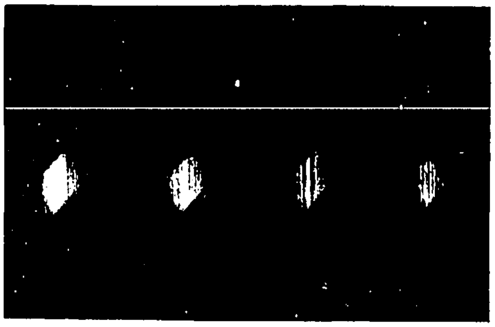

Figure (8.16) Beam Cross-Sections at the Exit Plane of the Counter-Clockwise Twisted Lens for Different Values of V_0.

The values of V_0 are (from left to right) 1190, 1200, 1210 and 1220 volts. The cross-sections are photographed in the direction of incidence of the beam on the detector.

Scale of reproduction: 1 cm on photograph → .21cm.

Figure (8.17) Beam Cross-Sections at the Exit Plane of the Clockwise Twisted Lens for Different Values of V_0.

The values of V_0 are (from left to right) 1180, 1190, 1200, 1210 and 1220 volts. The cross-sections are photographed in the direction of incidence of the beam on the detector.

Scale of reproduction: 1 cm on photograph → .22 cm.

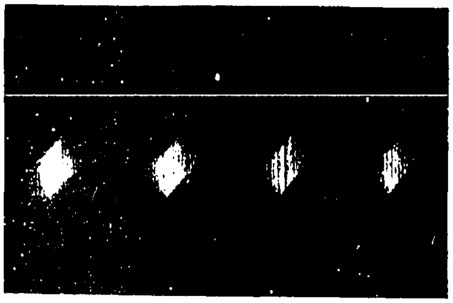

Figure (8.16) Beam Cross-Sections at the Exit Plane of the Counter-Clockwise Twisted Lens for Different Values of V_0.

The values of V_0 are (from left to right) 1190, 1200, 1210 and 1220 volts. The cross-sections are photographed in the direction of incidence of the beam on the detector.

Scale of reproduction: 1 cm on photograph → .21cm.

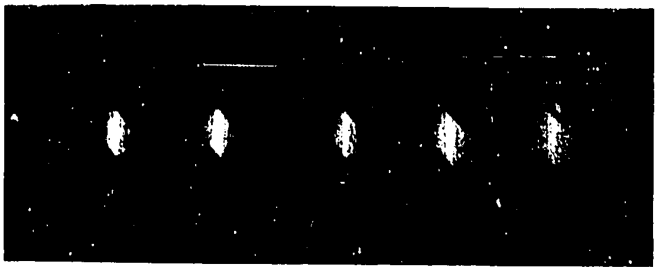

Figure (8.17) Beam Cross-Sections at the Exit Plane of the Clockwise Twisted Lens for Different Values of V_0.

The values of V_0 are (from left to right) 1180, 1190, 1200, 1210 and 1220 volts. The cross-sections are photographed in the direction of incidence of the beam on the detector.

Scale of reproduction: 1 cm on photograph → .22 cm.

equal to and greater than 1210 volts are shown in figure (8.16) for the counter-clockwise twisted lens and in figure (8.17) for the clockwise twisted lens. For values of V_0 greater than 1210 volts, the detected beam cross-sections are nearly rectangular parallelograms whose sides are rotated with respect to the X, Y axes through an angle slightly larger than $2\pi + 43°$. The angle of rotation as well as the dimensions of the parallelograms increase as the value of the focusing voltage increases. Also the lengths of the sides that should be parallel to the X_T axis at $V_0 = 1210$ volts, are observed to increase at a higher rate than that of the increase of the other two sides.

As the focusing voltage is decreased to values less than 1210 volts, the detected beam cross-sections are nearly rectangular parallelograms rotated with respect to the X and Y axes through an angle less than $2\pi + 43°$. The angle of rotation decreases as the focusing voltage is decreased. The parallelograms detected at values of V_0 less than 1210 volts have smaller areas than the rectangular cross-section detected at 1210 volts and it is found that the exit beam cross-section decreases as V_0 is decreased. It is also observed that the lengths of the sides that should be parallel to the X_T axis at 1210 volts decrease at a rate higher than that of the decrease of the other two sides. The experimentally observed phenomena are in good agreement with the theoretical results of Section 7.4. However, it is clear from figures (8.16) and (8.17) that the density of the particles is higher in the middle of the exit beam cross-section than on the boundaries. This exit beam density distribution is different from the more or less even microparticle distribution over the rectangular

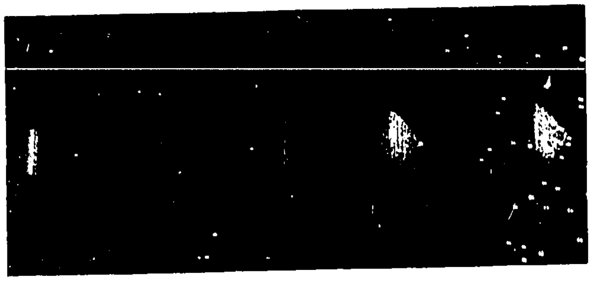

Figure (8.18) Beam Cross-Sections at a Distance d_3 = 7 mm Beyond the Exit Plane of the Clockwise Twisted Lens for Different Values of V_0.

The values of V_0 are (from left to right) 1150, 1180, 1200, 1210 and 1220 volts. Direction of photography the same as figure (8.17). The bubbles in the background are due to some moisture trapped under the grease and heated during photography.

Scale of reproduction: 1 cm on photograph → .25 cm.

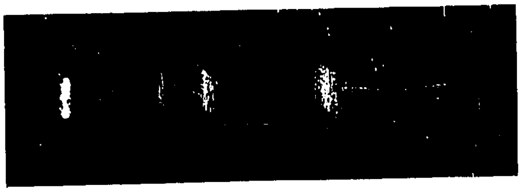

Figure (8.19) Beam Cross-Sections at a Distance d_3 = 17.5 mm Beyond the Exit Plane of the Clockwise Twisted Lens for Different Values of V_0.

The values of V_0 (from left to right) 1150, 1180, 1200 and 1210 volts. Direction of photography the same as figure (8.17). The overlapping of the second and third exit beam cross-sections was due to insufficient movement of the ratchet mechanism. The effect of trapped moisture is more pronounced in this case.

Scale of Reproduction: 1 cm on photograph → .27 cm.

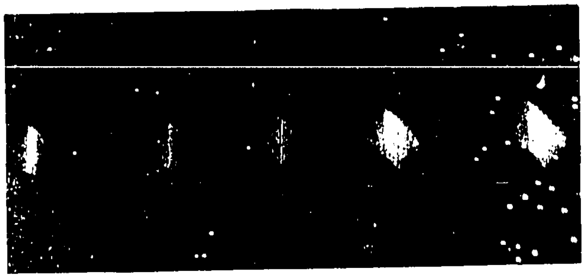

Figure (8.18) Beam Cross-Sections at a Distance d_3 = 7 mm Beyond the Exit Plane of the Clockwise Twisted Lens for Different Values of V_0.

The values of V_0 are (from left to right) 1150, 1180, 1200, 1210 and 1220 volts. Direction of photography the same as figure (8.17). The bubbles in the background are due to some moisture trapped under the grease and heated during photography.

Scale of reproduction: 1 cm on photograph → .25 cm.

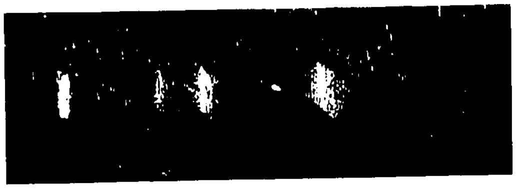

Figure (8.19) Beam Cross-Sections at a Distance d_3 = 17.5 mm Beyond the Exit Plane of the Clockwise Twisted Lens for Different Values of V_0.

The values of V_0 (from left to right) 1150, 1180, 1200 and 1210 volts. Direction of photography the same as figure (8.17). The overlapping of the second and third exit beam cross-sections was due to insufficient movement of the ratchet mechanism. The effect of trapped moisture is more pronounced in this case.

Scale of Reproduction: 1 cm on photograph → .27 cm.

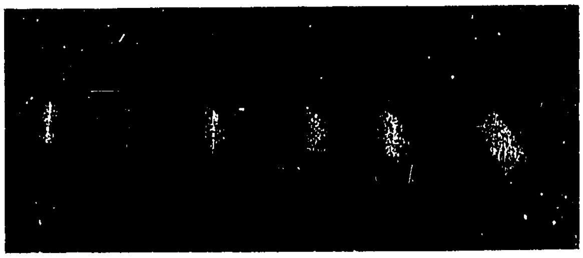

Figure (8.20) Beam Cross-Sections at a Distance d_3 = 33 mm Beyond the Exit Plane of the Clockwise Twisted Lens for Different Values of V_0.

The values of V_0 are (from left to right) 1150, 1180, 1200, 1210, 1220 and 1230 volts. Direction of photography the same as figure (8.17).

Scale of Reproduction: 1 cm on photograph → .31 cm.

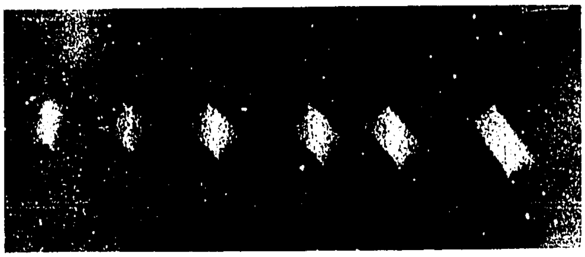

Figure (8.20) Beam Cross-Sections at a Distance d_3 = 33 mm Beyond the Exit Plane of the Clockwise Twisted Lens for Different Values of V_0.

The values of V_0 are (from left to right) 1150, 1180, 1200, 1210, 1220 and 1230 volts. Direction of photography the same as figure (8.17).

Scale of Reproduction: 1 cm on photograph → .31 cm.

beam cross-section at the injection plane. A discussion of this form of aberration will follow the presentation of the remaining experimental results.

While the foregoing series of experiments examined the imaging of the particle coordinates, the series of experiments which is described below examines the imaging of the particle momenta. Since the two lens sections used in the previous series of experiments are identical except for the direction of twist of the electrodes, it was decided to carry out these experiments for the counter-clockwise twisted lens only. The experiments were performed by using different values of drift space d_3, as shown in figure (8.11), between the exit plane of the lens and the greased detector slide.

Figures (8.18), (8.19) and (8.20) show the exit beam cross-sections at drift spaces equal to 7 mm, 17.5 mm and 33.6 mm respectively. At V_0 = 1210 volts, it is clear that the exit beam retains its rectangular shaped cross-section and the ratio between the lengths of the rectangle's sides is still 11:6. Also the directions of the sides are still parallel to the X_T and Y_T axes and the dimensions of the rectangular cross-sections at V_0 = 1210 volts in all three cases are exactly as theoretically predicted in Section 7.4. In interpreting figures (8.18), (8.19) and (8.20) it must be noted that their scales of reproduction are not the same.

(b) Two Oppositely Twisted Equal Sections

The oppositely twisted sections that were investigated separately were mounted and electrically connected so as to have no drift space between then, as shown in figure (8.21). The rectangular aperture E

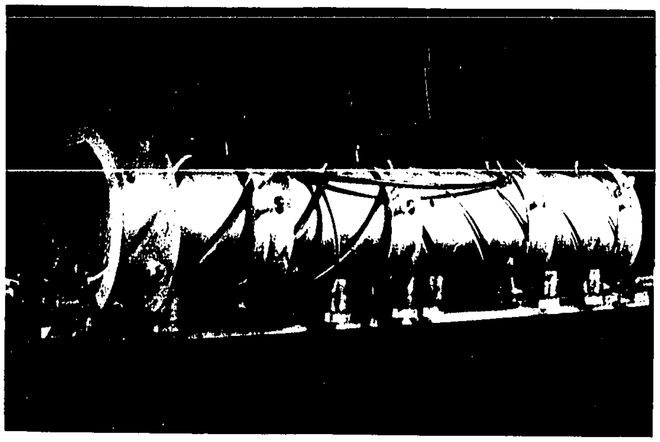

Figure (8.21) Photograph of a Lens Structure that Consists of Two Adjoining Sections of Equal Length but Opposite Twist.

Photograph shows the mounting base plate and the focusing voltage calbes.

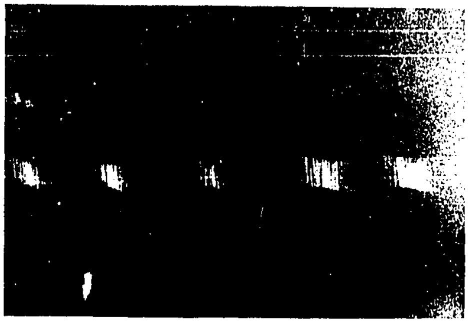

Figure (8.22) Beam Cross-Sections at the Exit Plane of the Lens Shown in Figure (8.21) for Different Values of V_0.

The values of V_0 are (from left to right) 1190, 1200, 1210, 1220 and 1230 volts. Direction of photography the same as figure (8.17).

Scale of Reproduction: 1 cm on photograph → .21 cm.

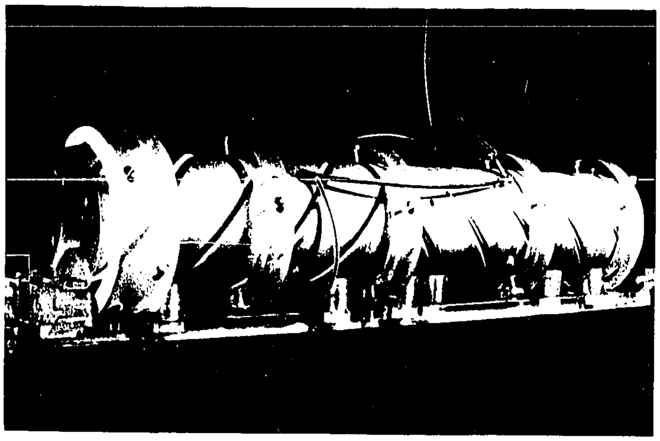

Figure (8.21) Photograph of a Lens Structure that Consists of Two Adjoining Sections of Equal Length but Opposite Twist.

Photograph shows the mounting base plate and the focusing voltage calbes.

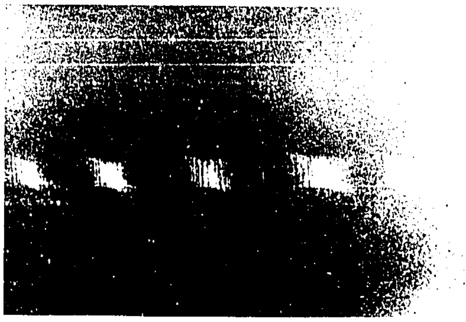

Figure (8.22) Beam Cross-Sections at the Exit Plane of the Lens Shown in Figure (8.21) for Different Values of V_0.

The values of V_0 are (from left to right) 1190, 1200, 1210, 1220 and 1230 volts. Direction of photography the same as figure (8.17).

Scale of Reproduction: 1 cm on photograph → .21 cm.

previously used was again employed in these experiments. As before the sides of the rectangular aperture were kept parallel to the axes of the electrodes of the first twisted lens at $Z = 0$, that is the sides were parallel to the horizontal and the vertical directions. According to the theoretical analysis of section (7.3), the exit beam cross-section at the exact imaging voltage should be a rectangle with its sides in the horizontal and vertical directions. The dimensions of this rectangle should be equal to those of the injected beam rectangular cross-section at $Z = 0$, that is 1.73 mm in the horizontal direction and 0.95 mm in the vertical direction. The two section lens structure was tested at different values of V_0 and the corresponding beam cross-sections, detected right at the end of the structure, are shown in figure (8.22). This experiment verified that exact imaging with no rotation with respect to the fixed X, Y axes occurs at V_0=1210 volts. The beam cross-sections at values of V_0 greater than 1210 volts are slightly expanded but their shapes are still nearly rectangular parallelograms. These parallelograms are slightly rotated with respect to the X, Y axes.

The results of the experimental investigations of either the single twisted lens or the structure consisting of two oppositely twisted sections show that these lenses are capable of identically imaging the injection conditions of the particles of the microparticle beam at $V_0 = 1210$ volts. Also the results shown in figures (8.16) to (8.20) and in figure (8.22) are in good agreement with the theoretical analysis of Chapter 7. However, these figures show that there is some aberration that results in a higher microparticle's density at the middle of the exit beam cross-section than on the boundaries and in some slight curvature of these boundaries.

This aberration is undoubtedly due to several factors, the most important of which is the misalignment of the axes of the microparticle injector and the lens structure. In some preliminary experiments the microparticle charger and the lens structure were separately mounted and aligned optically. The exit beam cross-sections were so distorted as to be almost unrecognizable. Subsequently the charger and the lens were mechanically mounted to one rigid base plate and then aligned optically. With this arrangement it was immediately possible to obtain exit beam cross-sections that clearly demonstrated the imaging properties of the lens. The effect of misalignment was found to be most pronounced in the case where the structure consisted of two oppositely twisted sections. In this case proper alignment was most difficult to achieve. This sensitivity to misalignment is common to all quadrupole structures(45).

During the experiments the quadrupole focusing voltage was kept constant within a few volts by regulating the mains feeding the quadrupole voltage supply. However, the mains feeding the charger high voltage source was not regulated and some of the observed aberration may be due to drift in the value of V during the experiments.

In Chapter 5 it was found that for V_0 = 1200 volts, the effect of gravitational forces is negligible if $\frac{q}{M} >> 0.0003$ coulomb/kilogram. During the charge detection experiments described in Section 8.2.2 it was observed that the values of the charge-to-mass ratios of the particles fluctuate over a wide range. Some of the particles emitted from the charger may well have charge-to-mass ratios low enough that their motion will be noticeably affected by the gravitational forces. Such particles will not be properly imaged and hence contribute to the observed aberration.

Further, fringing fields at the entry and exit planes of the lens structure as well as any tolerances in the length, radius, mounting and cutting of the electrodes may be responsible for some of the aforementioned aberration.

The aberrations discussed above are significant only in that they affect the identical imaging properties of a lens section. They are unimportant in terms of simply guiding and transporting a beam of particles. The experimental results clearly indicate that in all cases the injected particles are confined within the aperture of the structure, inspite of any aberration. In the experiments described above,particles have been successfully guided over a maximum distance of approximately 67 cm. It is important to note that without the twisted structure these same particles would be spread over an aperture approximately 19.5 mm in diameter as opposed to the 1.73 mm x 0.95 mm rectangle produced by the lens at V_0 = 1210 volts.

CHAPTER 9

THE CIRCULAR UNIFORMLY TWISTED ELECTROSTATIC QUADRUPOLE

9.1 Introduction

As a beam transport system is often required to bend the beam to direct it to a certain experimental area, it is of interest to analyze the effect on the particle motion caused by gradually bending the twisted quadrupole structure. Such effect is studied in this chapter by analyzing the motion of a charged particle which travels along a circular uniformly twisted electrostatic quadrupole structure. Beside being of importance for beam bending devices, the above analysis is also relevant to the design of storage rings for heavy charged particles.

Figure (9.1) illustrates the coordinate systems used in the analysis that follows. The (X,Y,Z) coordinate system is a fixed coordinate system whose origin coincides with the circular axis of the bent structure, which has a radius R_0, at $\phi = 0$. The coordinates (X', Y', ϕ) are related to the (X,Y,Z) coordinates as follows,

$$\begin{aligned} X &= X' \cos \phi + R_0(1 - \cos \phi) \\ Y &= Y' \\ Z &= (R_0 - X')\sin \phi \qquad (9.1) \end{aligned}$$

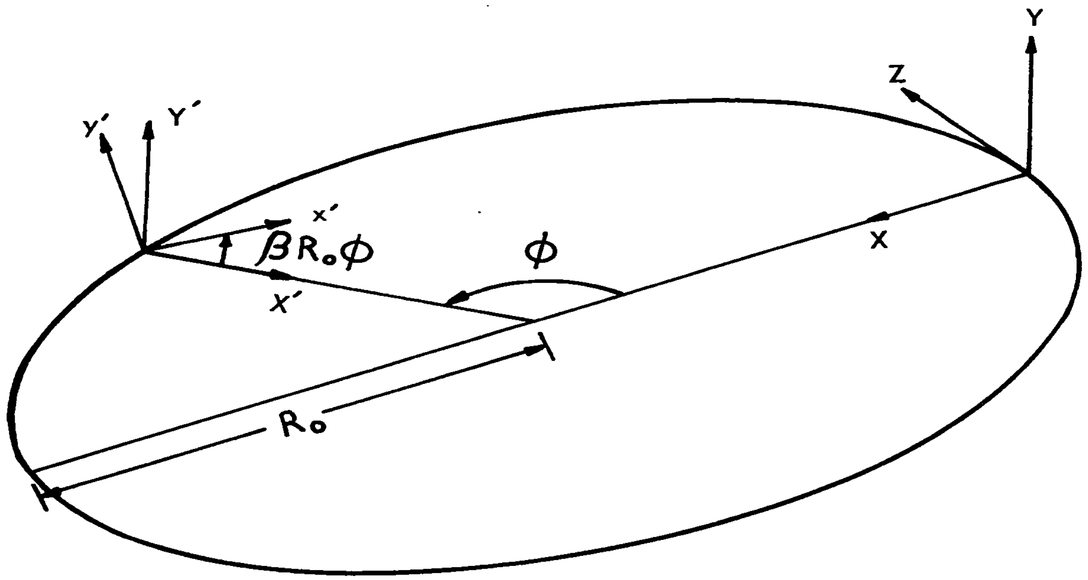
Y
Z
X
Y'
Y'
x'
$\beta R_o \phi$
x'
ϕ
R_o

Figure (9.1) Coordinate System for the Circular Uniformly Twisted Quadrupole Structure.

9.2 The Hamiltonian of the Motion

The kinetic energy of a particle of mass M in terms of the (X', Y', ϕ) coordinate system is

$$T = \frac{M}{2}\left[\dot{X}^2 + \dot{Y}^2 + \dot{Z}^2\right]$$

$$= \frac{M}{2}\left[\dot{X}'^2 + \dot{Y}'^2 + (R_0 - X')^2\dot{\phi}^2\right] \tag{9.2}$$

If the radius of curvature of the circular axis of the structure, R_0, is much larger than the aperture radius, a, and if $(\beta a)^2 << 1$, then the potential at any point within the aperture in terms of the coordinates X', Y' and ϕ is

$$V(X',Y',\phi) \cong k[\{X'^2 - Y'^2\}\cos 2\beta R_0\phi + \{2X'Y'\}\sin 2\beta R_0\phi].$$

Since $V(X',Y',\phi)$ is velocity independent, the momenta conjugate to the (X', Y', ϕ) coordinates are(34)

$$P_{X'} = \frac{\partial T}{\partial \dot{X}'} = M\dot{X}'$$

$$P_{Y'} = \frac{\partial T}{\partial \dot{Y}'} = M\dot{Y}'$$

$$P_{\phi} = \frac{\partial T}{\partial \dot{\phi}} = M\dot{\phi}(R_0 - X')^2 \tag{9.3}$$

and the Hamiltonian of motion in the (X', Y', ϕ) coordinate system is

$$H = \frac{1}{2M}[P_{X'}{}^2 + P_{Y'}^2 + \frac{P_\phi{}^2}{(R_0 - X')^2}] + qV(X',Y',\phi) \tag{9.4}$$

Equation (9.4) can be used to derive the equations of motion in the (X', Y', ϕ) coordinate system. However, the equations of motion thus derived are found to be nonlinear and coupled. At this stage the problem can be simplified by referring the motion to the rotating coordinate system (x', y', ϕ) where coordinates (x',y') are related to X', Y' by

$$X' = x' \cos \beta R_0\phi - y' \sin \beta R_0\phi$$

$$Y' = x' \sin \beta R_0\phi + y' \cos \beta R_0\phi \tag{9.5}$$

Differentiating equations (9.5) and substituting into equation (9.2), the kinetic energy of the particle in terms of the coordinate system (x', y' ϕ) is

$$T = \frac{M}{2} [\dot{x}'^2 + \dot{y}'^2 + \dot{\phi}^2(R_0 - X')^2$$

$$+ 2\beta R_0\dot{\phi}(\dot{y}'\, x' - \dot{x}'\, y') + \beta^2 R_0^2\, \dot{\phi}^2(x'^2 + y'^2)] \tag{9.6}$$

and the momenta conjugate to x', y', ϕ are

$$p_{x'} = \frac{\partial T}{\partial \dot{x}'} = M\, \dot{x}' - M\, \beta R_0\dot{\phi}y' \quad ,$$

$$p_{y'} = \frac{\partial T}{\partial \dot{y}'} = M\, \dot{y}' + M\, \beta R_0\dot{\phi}x' \quad ,$$

$$p_\phi = \frac{\partial T}{\partial \dot{\phi}} = M\,\dot{\phi}(R_0 - X')^2 + M\,\beta R_0(x'\,\dot{y}' - \dot{x}'\,y')$$

$$+ M\,\beta^2 R_0^2\,\dot{\phi}(x'^2 + y'^2)$$

$$= P_\phi + \beta R_0(x'\,p_{y'} - y'\,p_{x'}) \qquad (9.7)$$

Using equations (9.3), (9.4), (9.5) and (9.7) it now follows that the Hamiltonian in the (x', y', ϕ) coordinate system is

$$H = \frac{1}{2M}\left[p_{x'}^2 + p_{y'}^2 + \frac{[p_\phi - \beta R_0(x'\,p_{y'} - y'\,p_{x'})]^2}{(R_0 - X')^2}\right]$$

$$+ qV(x', y', \phi) \qquad (9.8)$$

If (9.8) is expanded and if all of

$$\left(\frac{p_{x'}}{p_\phi/R_0}\right)^2,\ \left(\frac{p_{y'}}{p_\phi/R_0}\right)^2,\ (\beta x')^2,\ (\beta y')^2 \text{ and } \left(\frac{X'}{R_0}\right)^2 \ll 1 \qquad (9.9)$$

then to first order the above Hamiltonian becomes

$$H = \frac{1}{2M}\left[p_{x'}^2 + p_{y'}^2 + \left(\frac{p_\phi}{R_0}\right)^2 - 2\beta(x'\,p_{y'} - y'\,p_{x'})\,\frac{p_\phi}{R_0}\right.$$

$$\left. + \frac{2\,p_\phi^2}{R_0^3}(x'\cos\beta R_0\phi - y'\sin\beta R_0\phi)\right] + qk(x'^2 - y'^2)$$

$$(9.10)$$

The Hamiltonian of equation (9.10) leads to coupled equations of motion and a new coordinate system must be generated in which the motion is uncoupled. It is found that the generating function

$$G_R = x'\,\overline{p_{x'}} + y'\,\overline{p_{y'}} - \frac{\beta\bar{p}}{2qMk}\,\overline{p_{x'}}\,\overline{p_{y'}} + \bar{\phi}\,\overline{p_\phi} \qquad (9.11)$$

generates through contact transformation the coordinate system ($\bar{x}'$, $\bar{y}'$, $\bar{\phi}$, $\overline{p_{x'}}$, $\overline{p_{y'}}$, $\overline{p_\phi}$) in which the equations of motion are uncoupled, provided that the constant $\bar{p}$ is chosen properly. The new coordinates are related to the old coordinates by[34]

$$\begin{aligned}
\bar{x}' &= \frac{\partial G_R}{\partial \overline{p_{x'}}} = x' - \frac{\beta\bar{p}}{2qMk}\,\overline{p_{y'}} \quad , \\
\bar{y}' &= \frac{\partial G_R}{\partial \overline{p_{y'}}} = y' - \frac{\beta\bar{p}}{2qMk}\,\overline{p_{x'}} \quad , \\
\bar{\phi} &= \frac{\partial G_R}{\partial \overline{p_\phi}} = \phi \quad , \\
p_{x'} &= \frac{\partial G_R}{\partial \bar{x}'} = \overline{p_{x'}} \quad , \\
p_{y'} &= \frac{\partial G_R}{\partial \bar{y}'} = \overline{p_{y'}} \quad , \\
p_\phi &= \frac{\partial G_R}{\partial \bar{\phi}} = \overline{p_\phi} \quad .
\end{aligned} \qquad (9.12)$$

Upon substitution of (9.12) into (9.10), the final Hamiltonian is obtained as

$$H = \frac{1}{2M}\,[\overline{p_{x'}}^{\,2}(1 + \frac{\beta^2\bar{p}}{qMk}\frac{\overline{p_\phi}}{R_0} - \frac{\beta^2\bar{p}^2}{2qMk})$$

$$+ \overline{p_{y'}}^{2}\left(1 - \frac{\beta^{2}\bar{p}\,\overline{p_{\phi}}}{qMk\ R_{0}} + \frac{\beta^{2}\bar{p}^{2}}{2qMk}\right) + \frac{\overline{p_{\phi}}^{2}}{R_{0}^{2}}$$

$$+ \frac{2\overline{p_{\phi}}^{2}}{R_{0}^{3}} (\cos \beta R_{0}\bar{\phi})\left(\bar{x}' + \frac{\beta\bar{p}\ \overline{p_{y'}}}{2qMk}\right)$$

$$- \frac{2\overline{p_{\phi}}^{2}}{R_{0}^{3}} (\sin \beta R_{0}\bar{\phi})\left(\bar{y}' + \frac{\beta\bar{p}\ \overline{p_{x'}}}{2qMk}\right) + 2qMk(\bar{x}'^{2} - \bar{y}'^{2})$$

$$- 2B\bar{x}'\ \overline{p_{y'}}\ \left(\frac{\overline{p_{\phi}}}{R_{0}} - \bar{p}\right) + 2\beta\bar{y}'\overline{p_{x'}}\left(\frac{\overline{p_{\phi}}}{R_{0}} - \bar{p}\right)] \quad . \tag{9.13}$$

9.3 The Equations of Motion

The following approximations are now introduced:

1. It is assumed that $\overline{p_{\phi}} = P_{\phi}$. This follows from equations (9.7) and (9.12) if first order quantities are neglected. Then from equations (9.3), to the same degree of accuracy

$$\overline{p_{\phi}} = M\ R_{0}^{2}\ \dot{\phi} \tag{9.14}$$

2. Based on the results for the straight uniformly twisted electrostatic quadrupole, where by neglecting first order quantities it was shown that the axial velocity $\dot{Z}$ is essentially constant, it is now assumed that the circumferential velocity, $R_{0}\dot{\phi}$, is also constant. Thus from equation (9.14)

$$\overline{p_{\phi}} = M\ R_{0}\ U_{0} \tag{9.15}$$

where U_{0} is the initial circumferential velocity.

The value of the constant $\bar{p}$ which appears in the generating function G is now selected as

$$\bar{p} = M\,U_0 = p_0 \tag{9.16}$$

Finally at this stage, the equations of motion are derived from equation (9.13). These equations are coupled. However, upon introducing equations (9.15) and (9.16), the equations of motion become uncoupled and appear as follows:

$$\begin{aligned}
\dot{\bar{x}}' &= \frac{\overline{p_{x'}}}{M}(1 + s_0) - \frac{p_0^3\beta}{2M^2R_0qk}\sin\beta R_0\bar{\phi} \\
\dot{\bar{y}}' &= \frac{\overline{p_{y'}}}{M}(1 - s_0) + \frac{p_0^3\beta}{2M^2R_0qk}\cos\beta R_0\bar{\phi} \\
\dot{\overline{p_{x'}}} &= -2qk\,\bar{x}' - \frac{p_0^2}{MR_0}\cos\beta R_0\bar{\phi} \\
\dot{\overline{p_{y'}}} &= 2qk\,\bar{y}' + \frac{p_0^2}{MR_0}\sin\beta R_0\bar{\phi}
\end{aligned} \tag{9.17}$$

where the stability factor s_0 is given by

$$s_0 = \frac{\beta^2p_0^2}{2Mqk} \tag{9.18}$$

It now follows immediately from equations (9.17) that

$$\ddot{\bar{x}}' + \frac{2qk}{M}(s_0 + 1)\bar{x}' = -(1 + 2s_0)\frac{p_0^2}{M^2R_0}\cos\beta U_0t$$

$$\ddot{y}' + \frac{2qk}{M}(s_0 - 1)\bar{y}' = (1 - 2s_0)\frac{p_0^2}{M^2 R_0}\sin \beta U_0 t \tag{9.19}$$

since, from equations (9.12), (9.14) and (9.15) $\bar{\phi} = (U_0/R_0)t$.

One recognizes immediately that the homogeneous solutions of equations (9.19) are exactly analogous to the solutions obtained in Chapter 2 for $\bar{x}$ and $\bar{y}$. The complete solutions of equations (9.19) are the sum of these homogeneous solutions and the particular solutions, where the latter are

$$\bar{x}' = -\frac{p_0^2(1 + 2s_0)}{2Mqk\ R_0}\cos \beta U_0 t \quad ,$$

$$\bar{y}' = -\frac{p_0^2(1 - 2s_0)}{2Mqk\ R_0}\sin \beta U_0 t \quad .$$

When these particular solutions are transformed back to the X', Y', ϕ coordinate system, X' and Y' of these solutions are

$$X' = -\frac{s_0}{\beta^2 R_0}(4s_0 + \cos 2\beta R_0\phi) \quad ,$$

$$Y' = -\frac{s_0}{\beta^2 R_0}(\sin 2\beta R_0\phi) \quad . \tag{9.20}$$

The projection of the particular solutions of equations (9.20) onto the transverse plane X'-Y' is plotted in figure (9.2). This figure indicates that the particle trajectories in the circular twisted structure are in fact essentially the same as the trajectories in the linear structure, except that the mean orbit of particles no longer lies on the structure axis.

Instead, the mean orbit is now a helical orbit whose axis is displaced radially outward in the X-direction by an amount $\frac{4s_0^2}{\beta^2 R_0}$. The radius of this helical orbit is equal to $\frac{s_0}{\beta^2 R_0}$.

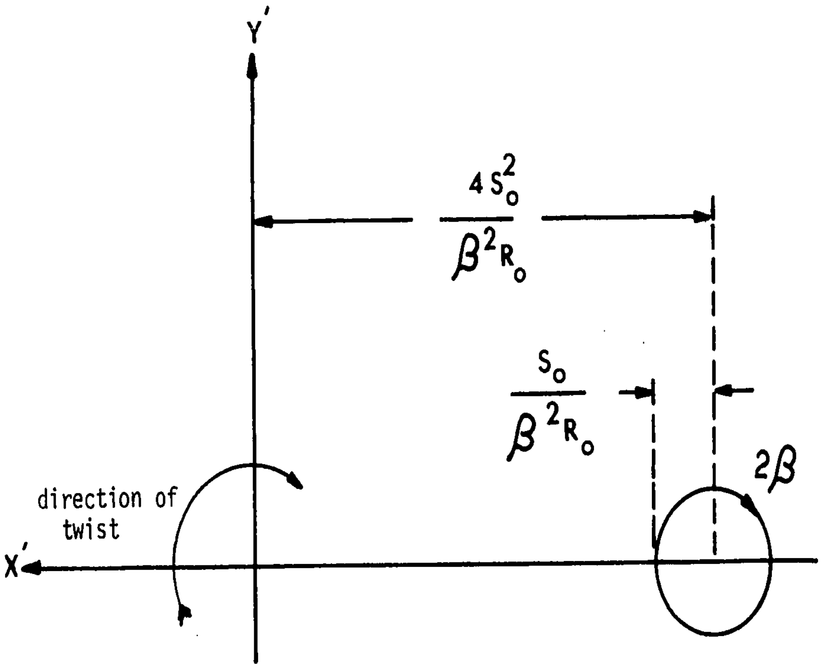

Figure (9.2) The Mean Orbit of Particles Along the Circular Twisted Structure.

Because of the displaced mean orbit the acceptance conditions for the circular structure are difficult to compute and no expression for the confinement criterion is obtained. However, it is of interest to study at least one specific example to illustrate what order of magnitude the radius of curvature R_0 must have relative to the aperture radius a.

Example: Consider a particle which is injected with initial conditions

$$X_0' = -\frac{s_0}{\beta^2 R_0}(1 + 4s_0) \quad , \quad Y_0' = 0$$

$$\dot{X}_0' = 0 \qquad , \quad \dot{Y}' = -\frac{2s_0 U_0}{\beta R_0} \qquad (9.21)$$

As mentioned above the complete solutions of equations (9.19) are the sum of the homogeneous solutions, analogous to those given by equations (2.31) and the particular solutions. It can be shown that the trajectory of the particle whose injection conditions are given by equations (9.21) is just that of the particular solutions of equations (9.20) and the homogeneous solutions for these particles are zero.

If the maximum radial displacement of this particle is now chosen as a, then

$$a = \frac{s_0}{\beta^2 R_0}(1 + 4s_0) \qquad (9.25)$$

Further, if one sets

$$s_0 = 2 \quad \text{and} \quad (\beta a)^2 = 0.1$$

it then follows from (9.25) that $R_0 = 180a$ and that the circular twisted quadrupole must execute a total of 57 twists in going once around the circular structure.

CONCLUSION

During the past few years special attention has been focused on the charging and acceleration of heavy ions as well as heavy micron-sized solid and liquid particles. The capability of the uniformly twisted electrostatic quadrupole structure to guide beams of heavy microparticles has been investigated in detail. A first order analytic solution for particle trajectories has been developed. This analytic solution shows that stable trajectories exist for particles with arbitrary charge-to-mass ratios provided that the structure parameters are properly chosen. It was shown that it is possible to confine particles stably provided their injection conditions are within the acceptance limits set by an analytically derived confinement criterion. This criterion was used to study the acceptance limits of the twisted structure for some special cases of injection. Comparison of the analytically computed trajectories with those computed through numerical integration of the exact equations of motion showed that the analytic solution is accurate over the entire quadrupole aperture. Furthermore the comparison showed that the confinement criterion successfully predicts the acceptance limits of the twisted structure. The effect of gravitational forces on the motion of heavy particles along the twisted structure also has been studied. It was found that the influence of gravity is negligible provided the charge-to-mass ratio of the particle is higher than a value that depends on the structure parameters.

The guiding properties of the twisted structure were compared with those of the classical electrostatic quadrupole channel. It was found that the twisted structure has a stronger focusing action and hence is especially suitable for guiding beams emerging from point sources.

The investigation of the analytic solution showed that for suitably chosen parameters a finite length of the twisted structure can be operated as a novel type of lens. By using this imaging lens, the initial injection coordinates and momenta of a system of particles were found to be identically reproduced in a coordinate plane located at the exit of the lens. The imaging takes place with a small amount of aberration. Numerical investigations showed that this aberration can be eliminated almost entirely by constructing the lens of two equal but oppositely twisted sections.

The identical imaging property of the twisted quadrupole has been experimentally tested. The lens structures have been fabricated by moulding. A microparticle contact charger was designed to provide the high density microparticle beam that was used in the experiments. The results of the experiments were in good agreement with the theoretical analysis inspite of the presence of some aberration. It is expected that this aberration can be reduced if more accurate methods of alignment and machining are used.

Also, particle motion has been studied along a twisted structure whose axis is bent in a circle. The results of this study are important to the design of beam bending devices and to the design of storage rings for heavy microparticles. The analysis showed that for proper choice of the structure parameters stable trajectories exist and that the mean particle orbits are displaced from the structure axis.

The twisted electrostatic quadrupole structures can be used as beam transport elements in conjunction with very heavy ion accelerators, or with accelerators for simulation of micrometeoroids. A further use could be the guiding of electrostatically sprayed liquids, such as the exhaust streams of colloidal propulsion devices. Another application could be as a confinement device for clouds of positively and negatively charged microparticles for the study of microparticle plasmas.

REFERENCES

1. BOLOTIN, L.J. et al. A Linear Accelerator of Multi-Charged Ions. International Conference of High Energy Accelerators, CERN 1959, p. 643.

2. HUBBARD, E.L. et al. Heavy Ion-Linear Accelerator. Rev. Sci. Instr. Vol. 32, 1961, p. 621.

3. BIETH, C. et al. A One MeV/Nucleon Heavy Ion Linear Accelerator. Proc. 1966 Linear Accelerator Conference, Los Alamos, LA 3609, p. 508.

4. MAIN, R.M. Proposed Modifications of the Berkeley Hilac. IEEE Trans. Nucl. Sci. NS-16, No. 3, 1969, p. 791.

5. SCHMELZER, C.H. Special Problems in Heavy Ion Acceleration. "Linear Accelerators" (Edited by Lapostolle, P.M. and Septier, A.L.), North Holland Publishing Company, Amsterdam, 1970, pp. 1029-1045.

6. KAMPHOEFNER, F.J. Ink Jet Printing. IEEE Trans. Elect. Devices. ED-19, No. 4, 1972, p. 584.

7. CHUTE, F.S. et al. Electric Propulsion in Space. Canadian Aeronautics and Space Journal, Vol. 15, No. 9, 1970, p. 381.

8. HARRISON, E.R. The Problem of Producing Energetic Macrons (Macroscopic Particles). Plasma Physics, Vol. 9, 1967, p. 183.

9. DINGMAN, E.H. and TOPEY, W. Theory and Operation of Microparticle Accelerators. Research Report R-64-10, Martin-Marietta Corporation, 1964.

10. BÖHNE, D. and SCHMELZER, C.H. Existing and Proposed Heavy Ion Linear Accelerators, "Linear Accelerators" (Edited by Lapostolle, P.M. and Septier, A.L.), North Holland Publishing Company, Amsterdam, 1970, pp. 1047-1071.

11. BOUSSARD, D. Radiofrequency Focusing in Heavy Ion Linear Accelerators. "Linear Accelerators" (Edited by Lapostolle, P.M. and Septier, A.L.), North Holland Publishing Company, Amsterdam, 1970, pp. 1073-1087.

12. CHO, A.Y.H. Contact Charging of Micron-Sized Particles in Intense Electric Fields. J. of Appl. Phys., Vol. 35, No. 9, 1964, p. 2561.

13. PEREL, J. et al. Research and Development of a Charged-Particle Bipolar Thrustor. AIAA Journal, Vol. 7, No. 3, 1969, p. 507.

14. ANDRIANOV, A.M. et al. Production of 3-MOe Pulsed Magnetic Fields by Discharging a Capacitor Bank. JETP Lett., Vol. 11, 1970, p. 402.

15. Loc. cit. (11).

16. PANOFSKY, W.K.H. Linear Accelerator Beam Dynamics. UCRL 1216, Univ. of Calif. Radiation Lab., Berkeley, California, 1951.

17. SMITH, L. and GLUCKSTERN, R.L. Focusing in Linear Ion Accelerators. Rev. Sci. Instr., Vol. 26, No. 2, 1955, p. 220.

18. LAPOSTOLLE, P. Dispositif de Focalisation Pour Accélérateurs Linéaires à Ions Lourds, MSC-62-4 CERN, Geneva, Switzerland, 1962.

19. Loc. cit. (11) pp. 1080-1082.

20. BEITH, C. et al. Heavy Ion Injection for Stripping in the Central Region of the Cevil. IEEE Trans. Nucl. Sci. NS-13, No. 4, 1966 , p. 182.

21. BOUSSARD, D. Self Focusing in Heavy Ion Linacs. Proc. 1966 Linear Accelerator Conference, Los Alamos, LA 3609, 1966, p. 96.

22. EL-KAREH, A.B. and EL-KAREH, J.C.J. "Electron Beams, Lenses and Optics". Vol.1, Academic Press Book Co., New York and London, 1970 , pp. 54-65.

23. HUGUENIN, J. and VOSICKI, B. Pre-Injectors. "Linear Accelerators" (Edited by Lapostolle, P.M. and Septier, A.L.), North Holland Publishing Company, Amsterdam, 1970, p. 852.

24. COURANT, E.D. et al. The Strong Focusing Synchrotron - A New High Energy Accelerator. Phys. Rev., Vol. 88, 1952, pp. 1190.

25. SEPTIER, A.L. Strong-Focusing Lenses. Advances in Electronics and Electron Physics, Vol. 14, 1961, pp. 85-205.

26. BANFORD, A.P. The Transport of Charged Particle Beams. E. & F.N. Spon Limited, London, 1966, pp. 100-119.

27. Loc. cit. (25). p. 124.

28. TRAN, D.T. Focusing of an Alvarez Linac by Use of Magnetic Quadrupoles Oriented at 45°, 1964 Linear Accelerator Conf. Proc., MURA, 1964, p. 309.

29. FUNSTEN, H.O. Properties of an Infinite Focusing Channel with Successive Quadrupole Rotations not equal to 90°. Nucl. Instr. and Meth., Vol. 44, 1966, p. 301.

30. COUTEUR, J.L. Particle Guiding by Helical Multipole Fields, Plasma Phys., Vol. 9, 1967, p. 457.

31. SALARDI, G. et al. A Quadrupolar Hellicoidal Pulsed Device for Particle Focusing. Nucl. Instr. and Meth., Vol. 59, 1968, p. 152.

32. SITTE, K. Micrometeoroid Simulation and Calibration Experiments. Max-Planck-Institut-Für-Kernphysik, Heidelberg, 1967.

33. GOLDSTEIN, H. "Classical Mechanics". Addison-Wesley Publishing Company Inc., 1950, p. 54.

34. Loc. cit. (33) pp. 237-247.

35. OGATA, K. "State Space Analysis of Control Systems". Prentice Hall, 1967, p. 108.

36. NIELSEN, K.L. "Methods in Numerical Analysis". The Macmillan Company, New York, 1964, pp. 236-247.

37. REGENSTREIF, E. Focusing with Quadrupoles, Doublets, and Triplets. "Focusing of Charged Particles". (Edited by Septier, A.L.), Academic Press, New York and London, 1967, pp. 353-410.

38. Loc. cit. (17).

39. Loc. cit. (37).

40. FRIICHTENICHT, J.F. Two-Million-Volt Electrostatic Accelerator for Hypervelocity Research. Rev. Sci. Instr., Vol. 33, 1962, p. 209.

41. SHELTON, H. et al. Electrostatic Acceleration of Microparticles to Hypervelocities. J. Appl. Phys., Vol. 31, No. 7, 1960, p. 1243.

42. VERMEULEN, F. Electrical Charging and Detection of Microparticles for the Simulation of Micrometeoroids. Ph.D. Thesis, Univ. of Alberta, 1966.

43. DINGMAN, E.H. A Hypervelocity Microparticle Linear Accelerator for Use in Micrometeoric Simulation. IEEE Trans. Nuc. Sci., Vol. 12, No.3, 1965, p. 544.

44. GRIVET,P. and SEPTIER, A. Les Lentilles Quadrupolaires Magnetiques (I). Nucl. Inst. and Meth., Vol. 6, 1960, p. 126.

45. HAWKES, P.W. "Quadrupoles in Electron Lens Design". Advances in Electronics and Electron Physics, Supplement 7, 1970.

APPENDIX A

POTENTIAL DISTRIBUTION IN THE UNIFORMLY TWISTED ELECTROSTATIC QUADRUPOLE.

The potential at any point in a charge free region should satisfy Laplace's equation, which in polar coordinates is

$$\frac{\partial^2 V}{\partial r^2} + \frac{1}{r}\frac{\partial V}{\partial r} + \frac{1}{r^2}\frac{\partial^2 V}{\partial \theta^2} + \frac{\partial^2 V}{\partial Z^2} = 0$$

For an infinitely long, uniformly twisted structure, the potential at a point (r, θ, Z) is exactly that at the points $(r, \theta + \beta\ell, Z + \ell)$ where ℓ can be any distance. Therefore the potential should be in the form

$$V(r, \theta - \beta Z) = \sum_{n=0}^{\infty} R_n(r) f_n(\theta - \beta Z)$$

Substitution of this potential in Laplace's equation, and separation of the variables gives

$$f_n''(\theta - \beta Z) + n^2 f_n(\theta - \beta Z) = 0$$

and

$$R_n''(r) + \frac{1}{r} R_n'(r) + [- \frac{n^2}{r^2} - n^2\beta^2] R_n(r) = 0$$

The solutions of these two differential equations give

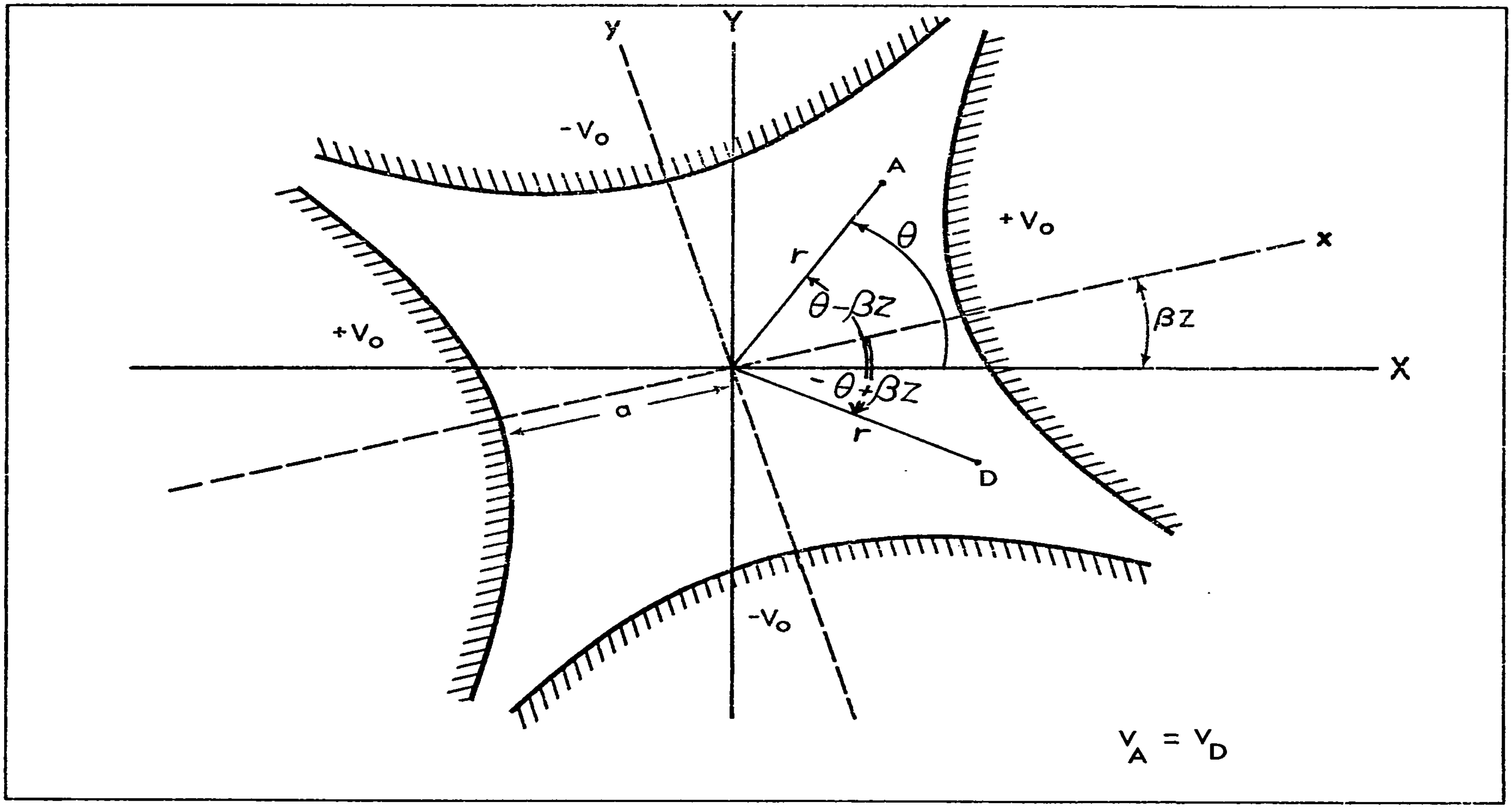
y
Y
$-V_o$
A
$+V_o$
x
θ
r
$\theta-\beta Z$
βZ
$+V_o$
X
$-\theta+\beta Z$
a
r
D
$-V_o$
$V_A = V_D$

Figure (A.1) Symmetry Properties of the Twisted Structure.

$$V(r, \theta - \beta Z) = \sum_{n=0}^{\infty} I_n(n\beta r)[\alpha_n \cos n(\theta - \beta Z) + \beta_n \sin n(\theta - \beta Z)]$$

where $I_n(n\beta r)$ is the modified Bessel function of the first kind and order n.

For a symmetrical twisted quadrupole structure the following conditions must be satisfied (see figure (A.1))

$$V(r, \theta - \beta Z) = V(r, -\theta + \beta Z)$$

$$V(r, \theta - \beta Z) = V(r, \theta - \beta Z + \pi)$$

$$V(r, \theta - \beta Z) = -V(r, \theta - \beta Z + \frac{\pi}{2}) .$$

These conditions imply that $V(r, \theta - \beta Z)$ should be

$$V(r, \theta - \beta Z) = \sum_{m=1,3,5}^{\infty} \alpha_m I_{2m}(2m\beta r)\cos 2m(\theta - \beta Z) \qquad (A.1)$$

Equation (A.1) gives the potential produced by a twisted structure whose electrodes can be of any shape and twisted at any rate. The coefficients, α_m, must be numerically evaluated by matching the potential at points on the electrode surfaces with $V(r, \theta - \beta Z)$ of equation (A.1). This matching produces a set of independent algebraic equations whose number is equal to that of the points considered.

For the special case of slowly twisted structures the Bessel functions of equation (A.1) can be approximated as follows:

$$I_{2m}(2m\beta r) = \sum_{\ell=0}^{\infty} \frac{1}{\ell!(\ell+2m)!} \left(\frac{2m\beta r}{2}\right)^{2\ell+2m}$$

$$= \frac{(m\beta)^{2m}}{(2m)!} r^{2m}\left[1 + \frac{m^2\beta^2 r^2}{(2m+1)} + \ldots.\right]$$

$$\cong \frac{(m\beta)^{2m}}{(2m)!} r^{2m} \qquad \text{for } \beta r << 1$$

For guiding and focusing structures the only values of r which are of interest are those within the aperture, $r \leq a$. Thus, the potential at points within the aperture of a slowly twisted quadrupole structure, with any electrode shape, is

$$V \cong k_1 r^2 \cos 2(\theta - \beta Z) + k_2 r^6 \cos 6(\theta - \beta Z)$$

$$+ k_3 r^{10} \cos 10(\theta - \beta Z) + \ldots \qquad \text{(A.2)}$$

provided only that $(\beta a)^2 << 1$. The coefficients k_m can be evaluated by potential matching at points on the electrode surfaces. For the special case of hyperbolic shaped electrodes, the surfaces of the electrodes are described by

(a) Positive electrodes, $V = V_0$

$$r^2 \cos 2(\theta - \beta Z) = a^2 \text{ for } -\frac{\pi}{4} < \theta - \beta Z < \frac{\pi}{4}, \frac{3\pi}{4} < \theta - \beta Z < \frac{5\pi}{4}$$

(b) Negative electrodes, $V = -V_0$

$$r^2 \cos 2(\theta - \beta Z - \frac{\pi}{2}) = a^2 \text{ for } \frac{\pi}{4} < \theta - \beta Z < \frac{3\pi}{4}, \frac{5\pi}{4} < \theta - \beta Z < \frac{7\pi}{4}$$

Therefore, for the slowly twisted structure with hyperbolic electrodes, the coefficients of equation (A.2) are

$$K_1 = \frac{V_o}{a^2}, \quad k_m = 0 \text{ for } m > 1.$$

The potential at points within the aperture when $(\beta a)^2 \ll 1$ is thus given approximately by

$$V = K\, r^2 \cos 2(\theta - \beta Z) \quad \text{where } k = \frac{V_o}{a^2} \tag{A.3}$$

Since

$$r^2 = X^2 + Y^2$$

and $$\theta = \tan^{-1} \frac{Y}{X}$$

equation (A.3) may be rewritten in terms of the fixed coordinates (X,Y,Z) as:

$$V \cong k[(X^2 - Y^2)\cos 2\beta Z + (2XY)\sin 2\beta Z] \tag{A.4}$$

Alternatively

$$r^2 = x^2 + y^2$$

and $$\theta - \beta Z = \tan^{-1} \frac{y}{x}$$

and in terms of the rotating coordinates (x,y,z)

$$V \cong k(x^2 - y^2) \tag{A.5}$$

Equation (A.5) shows that the potential of the slowly twisted electrostatic quadrupole, when viewed in the rotating coordinate system, is negligibly different from the potential distribution in a classical quadrupole.

APPENDIX B

THE AXIAL VELOCITY $\dot{Z}$

The objective of this appendix is to obtain an expression for the axial velocity of the particle, in terms of the transit time, the initial axial velocity, and the values of the transverse displacements and momenta at injection. It will also be shown that the axial velocity of a particle in the structure varies only slightly from its initial value, U_{Z_o}.

The axial velocity $\dot{Z}$ is given by equations (2.32) and (2.33) as,

$$\dot{Z} = U_{Z_o}\left[1 + (\beta a)\left\{\frac{X_o}{a}\frac{P_{Y_o}}{P_{Z_o}} - \frac{Y_o}{a}\frac{P_{X_o}}{P_{Z_o}}\right\}\right] - \frac{\beta}{M}[x\,p_y - y\,p_x] \qquad \text{(B.1)}$$

But from equations (2.31)

$$\begin{aligned}\frac{\beta}{M}[x\,p_y - y\,p_x] &= \frac{\beta}{M}\left[p_z \frac{\beta\, C_2(-1)^n}{\sqrt{s}\sqrt{s-1}} \sin F_2\right]\left[C_1 \cos F_1 + \sqrt{\frac{s}{s-1}}\,(-1)^n\, C_2 \sin F_2\right] \\ &\quad + \frac{\beta}{M}\left[p_z \frac{\beta\, C_1(-1)^n}{\sqrt{s}\sqrt{s+1}} \sin F_1\right]\left[C_2 \cos F_2 - \sqrt{\frac{s}{s+1}}\,(-1)^n\, C_1 \sin F_1\right] \\ &= \frac{\beta^2 p_z C_1 C_2 (-1)^n}{M\sqrt{s}\sqrt{s-1}} \sin F_2 \cos F_1 + \frac{\beta^2 p_z}{M(s-1)}\, C_2^2 \sin^2 F_2\end{aligned}$$

$$+ \frac{\beta^2 p_z C_1 C_2 (-1)^n}{M\sqrt{s}\sqrt{s + 1}} \sin F_1 \cos F_2 + \frac{\beta^2 p_z}{M(s + 1)} C_1^2 \sin^2 F_1$$

$$= \frac{\beta^2 p_z}{2M} [\frac{C_2^2}{s - 1} (1 - \cos 2F_2) - \frac{C_1^2}{s + 1}(1 - \cos 2F_1)]$$

$$+ \frac{\beta^2 p_z}{2M} \frac{C_1 C_2 (-1)^n}{\sqrt{s}\sqrt{s - 1}} [\sin(F_1 + F_2) - \sin(F_1 - F_2)]$$

$$+ \frac{\beta^2 p_z}{2M} \frac{C_1 C_2 (-1)^n}{\sqrt{s}\sqrt{s + 1}} [\sin(F_1 + F_2) + \sin(F_1 - F_2)]$$

$$= \frac{\beta^2 p_z}{2M} [\frac{C_2^2}{s - 1} (1 - \cos 2F_2) - \frac{C_1^2}{s + 1}(1 - \cos 2F_1)]$$

$$+ \frac{\beta C_1 C_2}{2}\sqrt{\frac{2qk}{M}} [\frac{1}{\sqrt{s + 1}} + \frac{1}{\sqrt{s - 1}}]\sin(F_1 + F_2)$$

$$+ \frac{\beta C_1 C_2}{2}\sqrt{\frac{2qk}{M}} [\frac{1}{\sqrt{s + 1}} - \frac{1}{\sqrt{s - 1}}]\sin(F_1 - F_2)$$

$$= \frac{\beta^2 p_z}{2M} [\frac{C_2^2}{s - 1}(1 - \cos 2F_2) - \frac{C_1^2}{s + 1}(1 - \cos 2F_1)]$$

$$+ \frac{\beta C_1 C_2}{2\sqrt{s^2 - 1}} [(f_1 + f_2)\sin(F_1 + F_2) - (f_1 - f_2)\sin(F_1 - F_2)] \qquad (B.2)$$

Thus,

$$\dot{Z} = U_{Z_0}[1 + (\beta a)\{\frac{X_0}{a} \frac{P_{Y_0}}{P_{Z_0}} - \frac{Y_0}{a} \frac{P_{X_0}}{P_{Z_0}}\}]$$

$$+ \frac{\beta^2}{2} \frac{p_z}{M} [\frac{C_1^2}{s + 1} (1 - \cos 2F_1) - \frac{C_2^2}{s - 1} (1 - \cos 2F_2)]$$

$$-\frac{\beta C_1 C_2}{2\sqrt{s^2 - 1}}\,[(f_1 + f_2)\sin(F_1 + F_2) - (f_1 - f_2)\sin(F_1 - F_2)]$$

(B.3)

Examination of equation (B.2) shows that the following upper bound may be placed on the magnitude of the quantity $\beta(x\ p_y - y\ p_x)$:

$$\begin{aligned}
|\beta(x\ p_y - y\ p_x)| &\leq \left|\frac{\beta^2 p_z}{2}\,\frac{2C_2^2}{s - 1}\right| + \left|\frac{\beta C_1 C_2 M}{2\sqrt{s^2 - 1}}\,2f_1\right| \\
&= \left|\beta^2 p_z\,\frac{C_2^2}{s - 1}\right| + \left|\frac{\beta C_1 C_2 M}{\sqrt{s^2 - 1}}\,\sqrt{\frac{2qk}{M}}\sqrt{s + 1}\right| \\
&= \left|\beta^2 p_z\,\frac{C_2^2}{s - 1}\right| + \left|\frac{\beta^2 p_z C_1 C_2}{\sqrt{s - 1}}\,\frac{\sqrt{2qkM}}{\beta p_z}\right| \\
&= \beta^2 p_z\left[\left|\frac{C_2^2}{s - 1}\right| + \left|\frac{C_1 C_2}{\sqrt{s}\sqrt{s - 1}}\right|\right] \\
&= \beta^2 p_z\,\frac{|C_2|}{\sqrt{s}\sqrt{s - 1}}\left[|C_1| + \sqrt{\frac{s}{s - 1}}\,|C_2|\right]
\end{aligned}$$

Therefore

$$|\beta(x\ p_y - y\ p_x)|_{max} \leq \beta^2 p_z\,\frac{|C_2|_{max}}{\sqrt{s}\sqrt{s - 1}}\left[|C_1| + \sqrt{\frac{s}{s - 1}}\,|C_2|\right]_{max}$$

(B.4)

It is shown in Chapter 3 that for a particle to be confined within the aperture,

$$\left[|C_1| + \sqrt{\frac{s}{s - 1}}\,|C_2|\right]_{max} \leq a \qquad \text{(B.5)}$$

Thus, for particles confined by the structure

$$|\beta(x\ p_y - y\ p_x)| \le \beta^2 p_z \frac{a\ |C_2|_{max}}{\sqrt{s}\ \sqrt{s - 1}}$$

But from equation (B.5) it is apparent that

$$|C_2|_{max} \le a\sqrt{\frac{s - 1}{s}} \quad .$$

Thus,

$$|\beta(x\ p_y - y\ p_x)| \le \frac{\beta^2 a^2}{s} p_z \tag{B.6}$$

At Z = 0, equation (B.6) implies that

$$|\beta(X_0 P_{Y_0} - Y_0 P_{X_0})| \le \frac{\beta^2 a^2}{s} p_z \tag{B.7}$$

Equation (2.32) gives the axial velocity $\dot{Z}$ as

$$\dot{Z} = \frac{p_z}{M} [1 - \frac{\beta}{p_z}(x\ p_y - y\ p_x)]$$

$$= \frac{P_{Z_0}}{M} \frac{[1 - \frac{\beta}{p_z}(x\ p_y - y\ p_x)]}{(P_{Z_0}/p_z)} \tag{B.8}$$

where

$$\frac{P_{Z_0}}{p_z} = 1 - \frac{\beta}{p_z}(X_0\ P_{Y_0} - Y_0\ P_{X_0}) \quad .$$

Substituting this expression in equation (B.8) gives

$$\dot{Z} = U_{Z_0} \frac{[1 - \frac{\beta}{p_z}(x\,p_y - y\,p_x)]}{[1 - \frac{\beta}{p_z}(X_0\,P_{Y_0} - Y_0\,P_{X_0})]}$$

Using the inequalities (B.6) and (B.7) the axial velocity is found to be bounded by

$$U_{Z_0} \frac{[1 - \frac{(\beta a)^2}{s}]}{[1 + \frac{(\beta a)^2}{s}]} \leq \dot{Z} \leq U_{Z_0} \frac{[1 + \frac{(\beta a)^2}{s}]}{[1 - \frac{(\beta a)^2}{s}]} \qquad \text{(B.10)}$$

which for $(\beta a)^2 = 0.1$ and $s = 2$ gives

$$0.9\,U_{Z_0} \leq \dot{Z} \leq 1.1\,U_{Z_0}$$

APPENDIX C

DERIVATION OF THE MATRIX FORM OF THE ANALYTIC SOLUTION

Equation (2.46) gives the x coordinate as

$$x = A_1\, e^{jf_2 t} + A_2\, e^{-jf_2 t} - j\,\frac{f_1 M}{\beta p_z}\,[A_3\, e^{jf_1 t} - A_4\, e^{-jf_1 t}]$$

Substituting for A_1, A_2, A_3 and A_4 from equations (2.48) gives

$$x = \frac{\beta p_z}{2qkM}\,[\frac{e^{jf_2 t} + e^{-jf_2 t}}{2}]$$

$$+ \frac{\beta p_z}{Mf_2}[\frac{e^{jf_2 t} - e^{-jf_2 t}}{2j}][Y_o - \frac{\beta p_z}{2qkM}\,P_{X_o}]$$

$$+ \frac{f_1}{2qk}\,[\frac{e^{jf_1 t} - e^{-jf_1 t}}{2j}]P_{X_o}$$

$$+ [\frac{e^{jf_1 t} + e^{-jf_1 t}}{2}][X_o - \frac{\beta p}{2qkM}\,P_{Y_o}]$$

Thus,

$$x = \{\cos f_1 t\}X_o + \{\frac{\beta p_z}{\sqrt{2qkM}}\,\frac{\sin f_2 t}{\sqrt{s - 1}}\}Y_o$$

$$+ \frac{1}{\sqrt{2qkM}}\,\{\sqrt{s + 1}\,\sin f_1 t - \frac{s}{\sqrt{s - 1}}\sin f_2 t\}P_{X_o}$$

$$+ \frac{\beta p_z}{2qkM} \{\cos f_2 t - \cos f_1 t\} P_{Y_0} \qquad \text{(C.1)}$$

Similarly,

$$y = \{- \frac{\beta p_z}{\sqrt{s + 1}} \sin f_1 t\} X_0 + \{\cos f_2 t\} Y_0$$

$$+ \frac{\beta p_z}{2qkM} \{\cos f_1 t - \cos f_2 t\} P_{X_0}$$

$$+ \frac{1}{\sqrt{2qkM}} \{\frac{s}{\sqrt{s + 1}} \sin f_1 t - \sqrt{s - 1} \sin f_2 t\} P_{Y_0} \qquad \text{(C.2)}$$

$$p_x = \{- \frac{\sqrt{2qkM}}{\sqrt{s + 1}} \sin f_1 t\} X_0 + \{\cos f_1 t\} P_{X_0}$$

$$+ \{\frac{\beta p_z}{\sqrt{2qkM}} \frac{\sin f_1 t}{\sqrt{s + 1}}\} P_{Y_0} \qquad \text{(C.3)}$$

and

$$p_y = \{ 2qkM \frac{\sin f_2 t}{\sqrt{s - 1}}\} Y_0 + \{- \frac{\beta p_z}{\sqrt{2qkM}} \frac{\sin f_2 t}{\sqrt{s - 1}}\} P_{X_0}$$

$$+ \{\cos f_2 t\} P_{Y_0} \qquad \text{(C.4)}$$

Equations (C.1), (C.2), (C.3) and (C.4) can be combined in a matrix form giving equations (2.49) and (2.50).

Further consideration of equations (C.1) to (C.4) shows that they can be rearranged and the trigonometric expressions can be combined to obtain the form of the trajectory solution given by equations (2.31). Equations (C.1) to (C.4) can be rearranged to take the form

$$x = [X_0 - \frac{\beta p_z}{2qkM} P_{Y_0}]\cos f_1t + [\frac{\sqrt{s+1}}{\sqrt{2qkM}} P_{X_0}]\sin f_1t$$

$$+ [\frac{\beta p_z}{2qkM} P_{Y_0}]\cos f_2t$$

$$+ [\frac{\beta p_z}{\sqrt{2qkM}} \frac{1}{\sqrt{s-1}} Y_0 - \frac{s}{\sqrt{s-1}} \frac{1}{\sqrt{2qkM}} P_{X_0}]\sin f_2t$$

$$y = [Y_0 - \frac{\beta p_z}{2qkM} P_{X_0}]\cos f_2t - [\frac{\sqrt{s-1}}{\sqrt{2qkM}} P_{Y_0}]\sin f_2t$$

$$+ [\frac{\beta p_z}{2qkM} P_{X_0}]\cos f_1t$$

$$- [\frac{\beta p_z}{\sqrt{2qkM}} \frac{1}{\sqrt{s+1}} X_0 - \frac{s}{\sqrt{s+1}} \frac{1}{\sqrt{2qkM}} P_{Y_0}]\sin f_1t$$

$$p_x = \sqrt{2qkM}\, [\frac{P_{X_0}}{\sqrt{2qkM}} \cos f_1t - \frac{1}{\sqrt{s+1}} \{X_0 - \frac{\beta p_z}{2qkM} P_{Y_0}\}\sin f_1t]$$

$$p_y = \sqrt{2qkM}\, [\frac{P_{Y_0}}{\sqrt{2qkM}} \cos f_2t + \frac{1}{\sqrt{s-1}} \{Y_0 - \frac{\beta p_z}{2qkM} P_{X_0}\}\sin f_2t] \tag{C.5}$$

Since, $\frac{1}{2qkM} = \frac{\beta p_z}{2qkM} \frac{1}{\beta p_z} = (-1)^n \frac{\sqrt{s}}{\beta p_z}$

equations (C.5) become

$$x = D_1 \cos f_1t - D_2 \sin f_1t + \sqrt{\frac{s}{s-1}}\,(-1)^n[D_3 \sin f_2t + D_4 \cos f_2t]$$

$$y = D_3 \cos f_2t - D_4 \sin f_2t - \sqrt{\frac{s}{s+1}}\,(-1)^n[D_1 \sin f_1t + D_2 \cos f_1t]$$

$$p_x = - p_z \frac{\beta(-1)^n}{\sqrt{s}\sqrt{s+1}} [D_2 \cos f_1t + D_1 \sin f_1t]$$

$$p_y = p_z \frac{\beta(-1)^n}{\sqrt{s}\sqrt{s-1}} [D_4 \cos f_2t + D_3 \sin f_2t]$$

or

$$x = \sqrt{D_1^2 + D_2^2}\,\cos(f_1 t + \tan^{-1}\frac{D_2}{D_1})$$

$$+\sqrt{\frac{s}{s-1}}\,(-1)^n\sqrt{D_3^2 + D_4^2}\,\sin(f_2 t + \tan^{-1}\frac{D_4}{D_3})$$

$$y = \sqrt{D_3^2 + D_4^2}\,\cos(f_2 t + \tan^{-1}\frac{D_4}{D_3})$$

$$-\sqrt{\frac{s}{s+1}}\,(-1)^n\sqrt{D_1^2 + D_2^2}\,\sin(f_1 t + \tan^{-1}\frac{D_2}{D_1})$$

$$p_x = -\,p_z\,\frac{\beta(-1)^n}{\sqrt{s}\sqrt{s+1}}\sqrt{D_1^2 + D_2^2}\,\sin(f_1 t + \tan^{-1}\frac{D_2}{D_1})$$

$$p_y = p_z\,\frac{\beta(-1)^n}{\sqrt{s}\sqrt{s-1}}\sqrt{D_3^2 + D_4^2}\,\sin(f_2 t + \tan^{-1}\frac{D_4}{D_3}) \qquad (C.6)$$

where,

$$D_1 = [X_o - \frac{s}{\beta}\frac{P_{Y_o}}{p_z}]$$

$$D_2 = -\,\frac{(-1)^n\sqrt{s}\sqrt{s+1}}{\beta p_z}\,P_{X_o}$$

$$D_3 = [Y_o - \frac{s}{\beta}\frac{P_{X_o}}{p_z}]$$

$$D_4 = \frac{(-1)^n\sqrt{s}\sqrt{s-1}}{\beta p_z}\,P_{Y_o} \qquad (C.7)$$

Comparing equations (C.6) and (C.7) with equations (2.31) and (2.37) it is clear that equations (C.6) and equations (2.31) are the same and that D_1, D_2, D_3 and D_4 are related to C_1, C_2, α_1 and α_2 by

$$C_1^2 = D_1^2 + D_2^2$$

$$C_2^2 = D_3^2 + D_4^2$$

$$\alpha_1 = \tan^{-1} \frac{D_2}{D_1}$$

$$\alpha_2 = \tan^{-1} \frac{D_4}{D_3}$$

APPENDIX D

COMPUTATION OF ACCEPTANCE FOR POINT SOURCE INJECTION

Equation (3.13) sets the limits for the transverse momenta at injection, from a point source at Z = 0, as

$$|[s^2 P_{Y_0}{}^2 + s(s+1)P_{X_0}{}^2]^{1/2}| + \sqrt{\frac{s}{s-1}}\,|[s^2 P_{X_0}{}^2 + s(s-1)P_{Y_0}{}^2]^{1/2}| \le |\beta_a P_{Z_0}|$$

This equation is more easily interpreted when expressed in terms of the polar coordinates:

$$P_{T_0} = (P_{X_0}{}^2 + P_{Y_0}{}^2)^{1/2} \quad ,$$

$$\phi_{T_0} = \tan^{-1}\left(\frac{P_{Y_0}}{P_{X_0}}\right)$$

Thus, $P_{X_0} = P_{T_0} \cos \phi_{T_0}$, $P_{Y_0} = P_{T_0} \sin \phi_{T_0}$, and equation (3.13) becomes

$$\left|\frac{P_{T_0}}{P_{Z_0}}\right| \le \frac{|\beta a|}{|[s^2 + s\cos^2 \phi_{T_0}]^{1/2}| + \sqrt{\frac{s}{s-1}}\,|[s^2 - s\sin^2 \phi_{T_0}]^{1/2}|} \tag{D.1}$$

This equation was used to plot the transverse momenta acceptance diagrams shown in figure (3.5). These curves intersect the normalized $\frac{P_{X_0}}{P_{Z_0}}$ and $\frac{P_{Y_0}}{P_{Z_0}}$ axes at right angles since

$$\frac{d\left(\frac{P_{T_0}}{P_{Z_0}}\right)}{d\phi_{T_0}} = 0 \quad \text{at } \phi_{T_0} = 0, \frac{\pi}{2}, \pi, \frac{3\pi}{2} \quad .$$

It is also clear from equation (D.1) that

$$\left|\frac{P_{X_0}}{P_{Z_0}}\right|_{\max} = \frac{|\beta a|}{s} \frac{1}{\sqrt{s+1} + s/\sqrt{s-1}} \quad \text{at } \phi_{T_0} = 0, \pi$$

and

$$\left|\frac{P_{Y_0}}{P_{Z_0}}\right|_{\max} = \frac{|\beta a|}{2s} \qquad \text{at } \phi_{T_0} = \frac{\pi}{2}, \frac{3\pi}{2} \tag{D.2}$$

Consideration of these limits shows that there will be a certain value of s at which $\left|\frac{P_{X_0}}{P_{Z_0}}\right|_{\max}$ reaches a maximum value. On the other hand no such maximum exists for $\left|\frac{P_{Y_0}}{P_{Z_0}}\right|_{\max}$ and it decreases with any increase in s. In order to find the value $s = s_1$, at which $\left|\frac{P_{X_0}}{P_{Z_0}}\right|_{\max}$ has a maximum value, the expression for $\left|\frac{P_{X_0}}{P_{Z_0}}\right|_{\max}$ is differentiated with respect to s giving

$$\left.\frac{d\left|\frac{P_{X_0}}{P_{Z_0}}\right|_{\max}}{ds}\right|_{s=s_1} = \left.\frac{|\beta a|\{-\frac{d}{ds}[\sqrt{s^2+s} + \sqrt{s^3/(s-1)}]\}}{[\sqrt{s^2+s} + \sqrt{s^3/(s-1)}]^2}\right|_{s=s_1} = 0$$

or

$$\frac{2s_1 + 1}{2\sqrt{s_1^2 + s_1}} + \frac{1}{2}\sqrt{\frac{s_1 - 1}{s_1^3}} \; \frac{3s_1^2(s_1 - 1) - s_1^3}{(s_1 - 1)^3} = 0 \quad . \tag{D.3}$$

Solving equation (D.3) numerically gives $s_1 = 1.3295$. Substitution of this value of s_1 into the expression for $\left|\frac{P_{X_o}}{P_{Z_o}}\right|_{\max}$ gives

$$\left[\left|\frac{P_{X_o}}{P_{Z_o}}\right|_{\max}\right]_{\max} = 0.226|\beta a|$$

$$= 0.0714 \text{ for } (\beta a)^2 = 0.1$$

APPENDIX E

COMPUTER PROGRAMS LISTINGS

The first program in this Appendix was used for plotting the two sets of trajectories that were used for the evaluation of the analytic solution developed in Chapter 2. To obtain the first set of trajectories, the analytic trajectories, equations (2.31), (2.34) and (2.35) are used to compute the trajectory points in the rotating (x,y,z) coordinate system. Then equations (2.7) and (2.13) are used to refer these trajectories to the fixed (X,Y,Z) coordinate system. The trajectories are then plotted in this fixed (X,Y,Z) coordinate system. The second set of trajectories are computed directly in terms of the fixed (X,Y,Z) coordinate system by numerically integrating equation (2.6) using the Runge-Kutta method for numerical integration.

The Runge-Kutta method is a self starting method in which the calculation of the variables at the end of each interval depends on the values of the variables and their derivatives at the beginning of this interval. For all intervals the values of the variables are computed in the same manner by using for the initial values those at the beginning of each interval. The method may be best understood by studying Table E.1 which illustrates the steps for solving a second order differential equation in onevariable x(36). This method was easily applied to the system of differential equations, (2.6).

The second program in this Appendix computes the trajectory points of particles along a twisted electrostatic quadrupole lens structure. The structure may be a single twisted section or it may consist of two equal but oppositely twisted sections. The axial distance traversed by the particle was computed using the exact expression of equation (2.35). The value of s was determined for each particle individually in terms of the injection conditions.

TABLE E.1

Second-Order Differential Equation.

$$\boxed{\frac{d^2x}{dt^2} = f(x, \dot{x}, t)}$$

Initial conditions: $x_0, \dot{x}_0, t_0$

t	x	$\dot{x}$	$\ddot{x}$	AUXILIARY COMPUTATIONS
$t_{11} = t_0$	$x_{11} = x_0$	$\dot{x}_{11} = \dot{x}_0$	$\ddot{x}_{11} = f(x_0, \dot{x}_0, t)$	Whatever is necessary to compute $f(x, \dot{x}, t)$
$t_{12} = t_{11} + \frac{\Delta t}{2}$	$x_{12} = x_{11} + \dot{x}_{11}\frac{\Delta t}{2}$	$\dot{x}_{12} = \dot{x}_{11} + \ddot{x}_{11}\frac{\Delta t}{2}$	$\ddot{x}_{12} = f(x_{12}, \dot{x}_{12}, t_{12})$	
$t_{13} = t_{11} + \frac{\Delta t}{2}$	$x_{13} = x_{11} + \dot{x}_{12}\frac{\Delta t}{2}$	$\dot{x}_{13} = \dot{x}_{11} + \ddot{x}_{12}\frac{\Delta t}{2}$	$\ddot{x}_{13} = f(x_{13}, \dot{x}_{13}, t_{13})$	
$t_{14} = t_{11} + \Delta t$	$x_{14} = x_{11} + \dot{x}_{13}\Delta t$	$\dot{x}_{14} = \dot{x}_{11} + \ddot{x}_{13}\Delta t$	$\ddot{x}_{14} = f(x_{14}, \dot{x}_{14}, t_{14})$	
		$\Delta x_1 = \frac{\Delta t}{6}(\dot{x}_{11} + 2\dot{x}_{12} + 2\dot{x}_{13} + \dot{x}_{14})$	$\Delta \dot{x}_1 = \frac{\Delta t}{6}(\ddot{x}_{11} + 2\ddot{x}_{12} + 2\ddot{x}_{13} + \ddot{x}_{14})$	
$t_{21} = t_{11} + \Delta t$	$x_{21} = x_{11} + \Delta x_1$	$\dot{x}_{21} = \dot{x}_{11} + \Delta \dot{x}_1$	$\ddot{x}_{21} = f(x_{21}, \dot{x}_{21}, t_{21})$	
$t_{22} = t_{21} + \frac{\Delta t}{2}$	$x_{22} = x_{21} + \dot{x}_{21}\frac{\Delta t}{2}$	$\dot{x}_{22} = \dot{x}_{21} + \ddot{x}_{21}\frac{\Delta t}{2}$	$\ddot{x}_{22} = f(x_{22}, \dot{x}_{22}, t_{22})$	
$t_{23} = t_{21} + \frac{\Delta t}{2}$	$x_{23} = x_{21} + \dot{x}_{22}\frac{\Delta t}{2}$	$\dot{x}_{23} = \dot{x}_{21} + \ddot{x}_{22}\frac{\Delta t}{2}$	$\ddot{x}_{23} = f(x_{23}, \dot{x}_{23}, t_{23})$	
$t_{24} = t_{21} + \Delta t$	$x_{24} = x_{21} + \dot{x}_{23}\Delta t$	$\dot{x}_{24} = \dot{x}_{21} + \ddot{x}_{23}\Delta t$	$\ddot{x}_{24} = f(x_{24}, \dot{x}_{24}, t_{24})$	
		$\Delta x_2 = \frac{\Delta t}{6}(\dot{x}_{21} + 2\dot{x}_{22} + 2\dot{x}_{23} + \dot{x}_{24})$	$\Delta \dot{x}_2 = \frac{\Delta t}{6}(\ddot{x}_{21} + 2\ddot{x}_{22} + 2\ddot{x}_{23} + \ddot{x}_{24})$	
$t_{31} = t_{21} + \Delta t$	$x_{31} = x_{21} + \Delta x_2$	$\dot{x}_{31} = \dot{x}_{21} + \Delta \dot{x}_2$	$\ddot{x}_{31} = f(x_{31}, \dot{x}_{31}, t_{31})$	

```
C     PROGRAM TO COMPUTE AND PLOT THE APPROXIMATE ANALYTIC TRAJECTORIES
C     AND THE ACTUAL TRAJECTORIES (RUNGE- KUTTA TRAJECTORIES) OF
C     A PARTICLE ALONG THE TWISTED ELECTROSTATIC QUADRUPOLE STRUCTURE.
C     THE ACTUAL TRAJECTORIES ARE COMPUTED THROUGH NUMERICAL INTEGRATION
C     OF THE SECOND ORDER COUPLED DIFFERENTIAL EQUATIONS OF MOTION
C     USING THE RUNGE - KUTTA METHOD OF NUMERICA INTEGRATION.
      DIMENSION AX(8002),AY(8002),AZ(8002),DVAZ(8002)
      CALL PLOTS
C     CREAT ORIGIN OF THE PLOTS
      CALL PLOT(0.0,1.0,-3)
C     JIM= NUMBER OF PARTICLES WHOSE TRAJECTORIES ARE TO BE COMPUTED
C     AND PLOTTED. ONE AT A TIME.
      READ(5,16)JIM
   16 FORMAT(I2)
C     J= NUMBER OF POINTS COMPUTED ON EACH OF THE TRAJECTORIES.
C     VO= ACCELERATING POTENTIAL OF THE PARTICLES.
C     AR= RADIUS OF THE APERTURE IN METERS.
C     QM= CHARGE TO MASS RATIO (COULOMB PER KILOGRAM).
C     SOOOO= STABILITY FACTOR WHEN ( XO * PYO -YO * PXO )=0.0.
      READ(5,1)J,VO,AR,QM,SOOOO
    1 FORMAT(I4,4E12.5)
      PI=3.1415927
      JJJO=J
      AL=2.*PI*SQRT(10.0)*AR
      AJ=250.
      JJ=AJ
      V=(2.*PI*AR/AL)*(2.*PI*AR/AL)*(VO/SOOOO)
      VZO=SQRT(2.*QM*VO)
      AK=V/(AR*AR)
      HO=AL/(AJ*VZO)
      B=2.*PI/AL
      DO 555 MIN=1,JIM
C     XO , YO , ZO  THE INITIAL COORDINATES OF THE PARTICLE.
C     DXO,DYO THE INITIAL NORMALIZED TRANSVERSE MOMENTA OF THE PARTICLE.
C     DVZO  THE NORMALIZED AXIAL INJECTION VELOCITY.
      READ(5,2)XO,YO,ZO
      READ(5,2)DXO,DYO,DVZO
    2 FORMAT(3E12.6)
      XOO=XO
      YOO=YO
      ZOO=ZO
      DXOO=DXO
      DYOO=DYO
C     S THE STABILITY FACTOR OF THE PARTICLE COMPUTED ACCORDING TO ITS
C     INJECTION CONDITIONS.
      DELS=1.+B*(XO*DYO-YO*DXO)
      LEDS=1./DELS
      S=SOOOO*DELS*DELS
      FX=SQRT(2.*QM*AK*(S+1.))
      FY=SQRT(2.*QM*AK*(S-1.))
      ZZ11=ZO
      YY11=YO
      XX11=XO
      TT11=0.0
      TT=0.0
      PVZ11=DVZO
      DYYY1=DYO
      DXXX1=DXO
      MMM=1
C     COMPUTE THE CONSTANTS OF THE MOTION UI , VI , ALP1 AND ALP2.
      AP1=-SQRT(S*(S+1.))*DXO*LEDS/ABS(B)
      BP1=XO-S*DYO*LEDS/B
      IF(BP1) 309,310,311
  310 IF(AP1) 312,313,314
  312 ALP1=-PI/2.
      GO TO 320
  314 ALP1=PI/2.
      GO TO 320
  313 ALP1=0.0
      GO TO 320
  311 CP1=AP1/BP1
      ALP1=ATAN(CP1)
      GO TO 320
  309 CP1=AP1/BP1
      ALP1=ATAN(CP1)+PI
  320 AP2=SQRT(S*(S-1.))*DYO*LEDS/ABS(B)
      BP2=YO-S*DXO*LEDS/B
      IF(BP2) 409,410,411
  410 IF(AP2) 412,413,414
  412 ALP2=-PI/2.
      GO TO 420
  414 ALP2=PI/2.
      GO TO 420
  413 ALP2=0.0
      GO TO 420
  411 CP2=AP2/BP2
      ALP2=ATAN(CP2)
      GO TO 420
  409 CP2=AP2/BP2
      ALP2=ATAN(CP2)+PI
  420 UI=SQRT((XO-S*DYO*LEDS/B)**2+(S*(S+1.)*DXO*DXO*LEDS*LEDS/(B*B)))
      VI=SQRT((YO-S*DXO*LEDS/B)**2+(S*(S-1.)*DYO*DYO*LEDS*LEDS/(B*B)))
      THX20=2.*ALP1
      THY20=2.*ALP2
      THPOO=ALP1+ALP2
      THNOO=ALP1-ALP2
      IF(MMM-1)44,44,45
   45 THX=FX*TT+ALP1
      THY=FY*TT+ALP2
      THX2=2.*THX
      THY2=2.*THY
      THP12=THX+THY
      THN12=THX-THY
      RPXO=DXO
      RPYO=DYO
C     FOR EACH TIME TT COMPUTE AXIAL DISTANCE ZZ11 AND AXIAL NORMALIZED
C     VELOCITY PVZ11.
      ZZ11=VZO*TT*(1.+B*(XO*RPYO-YO*RPXO)+0.5*B*SQRT(AK*S/VO)*((UI*UI/(S
     1+1.))-(VI*VI/(S-1.))))+0.25*B*(SQRT(S/(S-1.)**3)*VI*VI*(SIN(THY2)
     2-SIN(THY20))-SQRT(S/(S+1.)**3)*UI*UI*(SIN(THX2)-SIN(THX20)))+0.5*
     3B*UI*VI*(COS(THP12)-COS(THPOO)-COS(THN12)+COS(THNOO))/
     4SQRT(S*S-1.)
      PVZ11=.5*B*B*((UI*UI/(S+1.)-VI*VI/(S-1.))+(VI*VI*COS(THY2)/(S-1.)
     1-UI*UI*COS(THX2)/(S+1.))-UI*VI*(SIN(THP12)*(1./SQRT(S*S-S)
     2+1./SQRT(S*S+S))-SIN(THN12)*(1./SQRT(S*S-S)-1./SQRT(S*S+S))))+1.
      THZ=B*ZZ11
C     COMPUTE THE ROTATING COORDINATES AND THEIR ADJOINT NORMALIZED
```

```
C     MOMENTA XXX,YYY,DXXX,DYYY.
      YYY=VI*COS(THY)-UI*SQRT(S/(S+1.))*SIN(THX)*ABS(B)/B
      XXX=UI*COS(THX)+VI*SQRT(S/(S-1.))*SIN(THY)*ABS(B)/B
      DXXX=-1.*ABS(B)*UI*SIN(THX)/SQRT(S*(S+1.))
      DYYY=ABS(B)*VI*SIN(THY)/SQRT(S*(S-1.))
C     COPUTE FIXED COORDINATES XX11,YY11.
      XX11=XXX*COS(THZ)-YYY*SIN(THZ)
      YY11=XXX*SIN(THZ)+YYY*COS(THZ)
      DXXX1=DXXX*COS(THZ)-DYYY*SIN(THZ)
      DYYY1=DXXX*SIN(THZ)+DYYY*COS(THZ)
      TT11=TT
C     STORE FIXED COORDINATES AX,AY,AZ AND NORMALIZED AXIAL VELOCITY
C     DVAZ.
   44 AX(MMM)=XX11*100.
      AY(MMM)=YY11*100.
      AZ(MMM)=ZZ11
      DVAZ(MMM)=PVZ11
      MMM=MMM+1
      TT=TT+HO
      IF(MMM-J)45,45,46
   46 MANNN=0
C     PLOT FRAMES , AXES AND WRITE SCALES ON AXES. FOR PLOTTING AX , AY
      AND DVAZ VERSUS AZ AND AX VERSUS AY ONCE FOR THE ANALYTIC
C     TRAJECTORIES COMPUTED ABOVE AND FOR THE RUNGE - KUTTA
C     TRAJECTORIES COMPUTED BELOW.
      CALL PLOT(0.0,9.25,2)
      CALL PLOT(6.0,9.25,2)
      CALL PLOT(6.0,0.0,2)
      CALL PLOT(0.0,0.0,2)
      CALL SYMBOL(0.6,0.75,0.12,'ANALYTICAL',0.0,10)
      CALL AXIS(0.5,0.5,'Z(M)',-4,5.0,0.0,1.0E10,1.0,20.0)
      CALL SYMBOL(0.43,0.35,0.08,'0.0',0.0,3)
      CALL SYMBOL(1.43,0.35,0.08,'1.5',0.0,3)
      CALL SYMBOL(2.43,0.35,0.08,'3.0',0.0,3)
      CALL SYMBOL(3.43,0.35,0.08,'4.5',0.0,3)
      CALL SYMBOL(4.43,0.35,0.08,'6.0',0.0,3)
      CALL SYMBOL(5.43,0.35,0.08,'7.5',0.0,3)
      CALL AXIS(0.5,0.75,'X(CM)',5,4.0,90.0,1.0E10,1.0,20.0)
      CALL SYMBOL(0.19,0.75,0.08,'-1.6',0.0,4)
      CALL SYMBOL(0.19,1.75,0.08,'-0.8',0.0,4)
      CALL SYMBOL(0.26,2.75,0.08,'0.0',0.0,3)
      CALL SYMBOL(0.26,3.75,0.08,'0.8',0.0,3)
      CALL SYMBOL(0.26,4.75,0.08,'1.6',0.0,3)
      CALL SYMBOL(0.6,5.0,0.12,'RUNGE-KUTTA',0.0,11)
      CALL AXIS(0.5,5.0,'X(CM)',5,4.0,90.0,1.0E10,1.0,20.0)
      CALL SYMBOL(0.19,5.00,0.08,'-1.6',0.0,4)
      CALL SYMBOL(0.19,6.00,0.08,'-0.8',0.0,4)
      CALL SYMBOL(0.26,7.0,0.08,'0.0',0.0,3)
      CALL SYMBOL(0.26,8.0,0.08,'0.8',0.0,3)
      CALL SYMBOL(0.26,9.0,0.08,'1.6',0.0,3)
      CALL PLOT(0.5,2.75,3)
      CALL PLOT(5.5,2.75,2)
      CALL PLOT(5.5,7.0,3)
      CALL PLOT(0.5,7.0,2)
      CALL PLOT(0.0,12.0,-3)
      CALL PLOT(0.0,9.25,2)
      CALL PLOT(6.0,9.25,2)
      CALL PLOT(6.0,0.0,2)
      CALL PLOT(0.0,0.0,2)
      CALL SYMBOL(0.6,0.75,0.12,'ANALYTICAL',0.0,10)
      CALL AXIS(0.5,0.5,'Z(M)',-4,5.0,0.0,1.0E10,1.0,20.0)
      CALL SYMBOL(0.43,0.35,0.08,'0.0',0.0,3)
      CALL SYMBOL(1.43,0.35,0.08,'1.5',0.0,3)
      CALL SYMBOL(2.43,0.35,0.08,'3.0',0.0,3)
      CALL SYMBOL(3.43,0.35,0.08,'4.5',0.0,3)
      CALL SYMBOL(4.43,0.35,0.08,'6.0',0.0,3)
      CALL SYMBOL(5.43,0.35,0.08,'7.5',0.0,3)
      CALL AXIS(0.5,0.75,'Y(CM)',5,4.0,90.0,1.0E10,1.0,20.0)
      CALL SYMBOL(0.19,0.75,0.08,'-1.6',0.0,4)
      CALL SYMBOL(0.19,1.75,0.08,'-0.8',0.0,4)
      CALL SYMBOL(0.26,2.75,0.08,'0.0',0.0,3)
      CALL SYMBOL(0.26,3.75,0.08,'0.8',0.0,3)
      CALL SYMBOL(0.26,4.75,0.08,'1.6',0.0,3)
      CALL SYMBOL(0.6,5.0,0.12,'RUNGE-KUTTA',0.0,11)
      CALL AXIS(0.5,5.0,'Y(CM)',5,4.0,90.0,1.0E10,1.0,20.0)
      CALL SYMBOL(0.19,5.00,0.08,'-1.6',0.0,4)
      CALL SYMBOL(0.19,6.00,0.08,'-0.8',0.0,4)
      CALL SYMBOL(0.26,7.0,0.08,'0.0',0.0,3)
      CALL SYMBOL(0.26,8.0,0.08,'0.8',0.0,3)
      CALL SYMBOL(0.26,9.0,0.08,'1.6',0.0,3)
      CALL PLOT(0.5,2.75,3)
      CALL PLOT(5.5,2.75,2)
      CALL PLOT(5.5,7.0,3)
      CALL PLOT(0.5,7.0,2)
      CALL PLOT(11.0,0.0,-3)
      CALL PLOT(0.0,9.25,2)
      CALL PLOT(6.0,9.25,2)
      CALL PLOT(6.0,0.0,2)
      CALL PLOT(0.0,0.0,2)
      CALL SYMBOL(0.6,0.75,0.12,'ANALYTICAL',0.0,10)
      CALL AXIS(0.5,0.5,'Z(M)',-4,5.0,0.0,1.0E10,1.0,20.0)
      CALL SYMBOL(0.43,0.35,0.08,'0.0',0.0,3)
      CALL SYMBOL(1.43,0.35,0.08,'1.5',0.0,3)
      CALL SYMBOL(2.43,0.35,0.08,'3.0',0.0,3)
      CALL SYMBOL(3.43,0.35,0.08,'4.5',0.0,3)
      CALL SYMBOL(4.43,0.35,0.08,'6.0',0.0,3)
      CALL SYMBOL(5.43,0.35,0.08,'7.5',0.0,3)
      CALL AXIS(0.5,0.75,'VZ/VZO',6,4.0,90.0,1.0E10,1.0,20.0)
      CALL SYMBOL(0.26,0.75,0.08,'0.0',0.0,3)
      CALL SYMBOL(0.26,1.75,0.08,'0.3',0.0,3)
      CALL SYMBOL(0.26,2.75,0.08,'0.6',0.0,3)
      CALL SYMBOL(0.26,3.75,0.08,'0.9',0.0,3)
      CALL SYMBOL(0.26,4.75,0.08,'1.2',0.0,3)
      CALL SYMBOL(0.6,5.0,0.12,'RUNGE-KUTTA',0.0,11)
      CALL AXIS(0.5,5.0,'VZ/VZO',6,4.0,90.0,1.0E10,1.0,20.0)
      CALL SYMBOL(0.26,5.00,0.08,'0.0',0.0,3)
      CALL SYMBOL(0.26,6.00,0.08,'0.3',0.0,3)
      CALL SYMBOL(0.26,7.00,0.08,'0.6',0.0,3)
      CALL SYMBOL(0.26,8.00,0.08,'0.9',0.0,3)
      CALL SYMBOL(0.26,9.00,0.08,'1.2',0.0,3)
      CALL PLOT(0.0,-12.0,-3)
      CALL PLOT(0.0,9.25,2)
      CALL PLOT(6.0,9.25,2)
      CALL PLOT(6.0,0.0,2)
      CALL PLOT(0.0,0.0,2)
      CALL SYMBOL(0.6,0.75,0.12,'ANALYTICAL',0.0,10)
      CALL AXIS(1.0,2.75,' ',1,4.0,0.0,1.0E10,1.0,20.0)
      CALL SYMBOL(5.25,2.75,0.12,'X(CM)',0.0,5)
      CALL CIRCLE(4.875,2.75,0.0,360.,1.875,1.875,0.5)
      CALL AXIS(3.0,0.75,' ',1,4.0,90.0,1.0E10,1.0,20.0)
      CALL SYMBOL(3.1,4.6,0.12,'Y(CM)',0.0,5)
      CALL AXIS(3.0,5.0,' ',1,4.0,90.0,1.0E10,1.0,20.0)
      CALL SYMBOL(3.1,8.9,0.12,'Y(CM)',0.0,5)
      CALL AXIS(1.0,7.0,' ',1,4.0,0.0,1.0E10,1.0,20.0)
      CALL SYMBOL(5.25,7.00,0.12,'X(CM)',0.0,5)
      CALL SYMBOL(0.6,5.0,0.12,'RUNGE-KUTTA',0.0,11)
      CALL CIRCLE(4.875,7.0,0.0,360.,1.875,1.875,0.5)
      CALL PLOT(-10.5,0.75,-3)
      GO TO 3333
  567 H=HC
      Z11=Z00
      Y11=Y00
      X11=X00
      MJM=1
      D1Z11=SQRT(2.*QM*VO)
      D1X11=DX00*D1Z11
      D1Y11=DY00*D1Z11
      AQM=-2.*QM*AK
      AX(MJM)=X11*100.
      AY(MJM)=Y11*100.
      VZO=D1Z11
      AZ(MJM)=Z11
      DVAZ(MJM)=D1Z11/VZO
  404 T11=0.
      TH=2.*B*Z11
      C=COS(TH)
      SO=SIN(TH)
      D2X11=AQM*(X11*C+Y11*SO)
      D2Y11=AQM*(X11*SO-Y11*C)
      D2Z11=AQM*B*(2.*X11*Y11*C+(Y11*Y11-X11*X11)*SO)
    3 T12=T11+0.5*H
      X12=X11+0.5*H*D1X11
      Y12=Y11+0.5*H*D1Y11
      Z12=Z11+0.5*H*D1Z11
      D1X12=D1X11+0.5*H*D2X11
      D1Y12=D1Y11+0.5*H*D2Y11
      D1Z12=D1Z11+0.5*H*D2Z11
      BT12=2.*B*Z12
      C12=COS(BT12)
      S12=SIN(BT12)
      D2X12=AQM*(X12*C12+Y12*S12)
      D2Y12=AQM*(X12*S12-Y12*C12)
      D2Z12=AQM*B*(2.*X12*Y12*C12+(Y12*Y12-X12*X12)*S12)
      T13=T11+0.5*H
      X13=X11+0.5*H*D1X12
      Y13=Y11+0.5*H*D1Y12
      Z13=Z11+0.5*H*D1Z12
      D1X13=D1X11+0.5*H*D2X12
      D1Y13=D1Y11+0.5*H*D2Y12
      D1Z13=D1Z11+0.5*H*D2Z12
      BT13=2.*B*Z13
      C13=COS(BT13)
      S13=SIN(BT13)
      D2X13=AQM*(X13*C13+Y13*S13)
      D2Y13=AQM*(X13*S13-Y13*C13)
      D2Z13=AQM*B*(2.*X13*Y13*C13+(Y13*Y13-X13*X13)*S13)
      T14=T11+H
      X14=X11+H*D1X13
      Y14=Y11+H*D1Y13
      Z14=Z11+H*D1Z13
      D1X14=D1X11+H*D2X13
      D1Y14=D1Y11+H*D2Y13
      D1Z14=D1Z11+H*D2Z13
      BT14=2.*B*Z14
      C14=COS(BT14)
      S14=SIN(BT14)
      D2X14=AQM*(X14*C14+Y14*S14)
      D2Y14=AQM*(X14*S14-Y14*C14)
      D2Z14=AQM*B*(2.*X14*Y14*C14+(Y14*Y14-X14*X14)*S14)
      X11A=X11
      Y11A=Y11
      Z11A=Z11
      T11=T11+H
      X11=X11+(H/6.)*(D1X11+2.*D1X12+2.*D1X13+D1X14)
      Y11=Y11+(H/6.0)*(D1Y11+2.*D1Y12+2.*D1Y13+D1Y14)
      Z11=Z11+(H/6.0)*(D1Z11+2.*D1Z12+2.*D1Z13+D1Z14)
  611 D1X11=D1X11+(H/6.0)*(D2X11+2.*D2X12+2.*D2X13+D2X14)
      D1Y11=D1Y11+(H/6.0)*(D2Y11+2.*D2Y12+2.*D2Y13+D2Y14)
      D1Z11=D1Z11+(H/6.0)*(D2Z11+2.*D2Z12+2.*D2Z13+D2Z14)
      BT11=2.*B*Z11
      C11=COS(BT11)
      S11=SIN(BT11)
      D2X11=AQM*(X11*C11+Y11*S11)
      D2Y11=AQM*(X11*S11-Y11*C11)
      D2Z11=AQM*B*(2.*X11*Y11*C11+(Y11*Y11-X11*X11)*S11)
      BT111=BT11/2.
      P1X11=D1X11/D1Z11
      P1Y11=D1Y11/D1Z11
      MJM=MJM+1
      AX(MJM)=X11*100.
      AY(MJM)=Y11*100.
      AZ(MJM)=Z11
      DVAZ(MJM)=D1Z11/VZO
 7772 IF(MJM-J)3,3,33
   33 MANNN=MANNN+1
      GO TO 3333
 3333 JJJ1=JJJ0+1
      JJJ2=JJJ1+1
      AZ(JJJ1)=0.0
      AZ(JJJ2)=1.5
      AX(JJJ1)=-1.6
      AX(JJJ2)=0.8
      AY(JJJ1)=-1.6
      AY(JJJ2)=0.8
      DVAZ(JJJ1)=0.0
      DVAZ(JJJ2)=0.3
      IF(MANNN)811,811,812
  812 CALL PLOT(0.0,4.25,-3)
  811 CALL LINE(AZ,AX,JJJ0,1,0,0)
      CALL PLOT(0.0,12.0,-3)
      CALL LINE(AZ,AY,JJJ0,1,0,0)
      CALL PLOT(11.0,0.0,-3)
      CALL LINE(AZ,DVAZ,JJJ0,1,0,0)
      CALL PLOT(0.5,-12.0,-3)
      CALL LINE(AX,AY,JJJ0,1,0,0)
      IF(MANNN)821,821,822
  821 CALL PLOT(-11.5,0.0,-3)
      GO TO 567
  822 MANKN=0
      CALL PLOT(11.0,-5.0,-3)
  555 CONTINUE
  223 CALL PLOT(0.0,0.0,999)
      WRITE(6,6666)
 6666 FORMAT(17H**PLOT FINISHED**)
      STOP
      END
```

'ILE

SECOND PROGRAM

```
C     PROGRAM FOR TRACING PARTICLES ALONG THE TWISTED LENS STRUCTURES.
C     PLOTS ARE PRODUCED FOR THE X-Z, X
C     PLOTS ARE PRODUCED FOR THE X-Z, Y-Z, PX-Z, PY-Z, PX-PY AND X-Y
C     PROGECTIONS OF THE MOTION.
C     NUM  = NO. OF (XO,YO) COORDINATES CONSIDERED.
C     KLJM = NO. OF (PXO,PYO) MOMENTA CONSIDERED FOR EACH INJECTION
C              POINT (XO,YO).
C     QM   = CHARGE-TO-MASS RATIO (COULOMB/KG.).
C     AR   = RADIUS OF APERTURE.
C     M ,N = DESIGN PARAMETERS SPECIFYING LENGTH OF THE LENS. BOTH M ,N
C    ODD OR BOTH EVEN INTEGERS AND M>N>0.
C    NNN   = PARAMETER SPECIFYING INITIAL CONDITION
C     NNN  = PARAMETER SPECIFYING DIRECTION OF TWIST OF THE ELECTRODES.
C              NNN=0 FOR COUNTER-CLOCKWISE TWIST(B POSITIVE),
C              NNN=1 FOR CLOCKWISE TWIST (B NEGATIVE).
C     MAAA = PARAMETER SPECIFYING THE STRUCTURE CONSIDERED.
C              MAAA= -1 FOR SINGLE TWISTED LENS,
C              MAAA= 0  FOR THE STRUCTURE CONSISTED OF TWO OPPOSITELY
C                         TWISTED LENS SECTIONS.
C     MTRA = 0.0 OR NEGATIVE  THE X-Y AND PX-PY CURVES ARE PLOTTED AND
C                               THE EXIT COORDINATES AND MOMENTA ARE MARKED.
C     MTRA = POSITIVE  ONLY THE EXIT COORDINATES AND MOMENTA MARKED.
C     J    = PARAMETER DEFINING THE ACCURACY IN COMPUTING THE EXIT
C              COORDINATES AND MOMENTA AT THE EXIT PLANE.IT IS THE NUMBER
C              OF DIVISIONS OF THE TIME INTERVAL BETWEEN THE TRAJECTORY
C              POINTS AS THE PARTICLE APPROACHES THE LENS EXIT.
C     VO   = ACCELERATING POTENTIAL OF THE PARTICLES.
C     AM   = NUMBER OF TRAJECTORY POINTS COMPUTED PER PERIODIC LENGTH
C              OF TWIST.
      DIMENSION AX(2000),AY(2000),AZ(2000),PX(2000),PY(2000)
      DIMENSION RRPX(30),RRPY(30),RRPZ(30)
      CALL PLOTS
      CALL PLOT(0.0,1.0,-3)
      READ(5,2001)KLJM
 2001 FORMAT(I3)
      READ(5,101)J,M,N,AM,VO,AR,QM
  101 FORMAT(3I2,4E12.6)
C     COMPUTE IMAGING VALUE OF S UGING M,N.
      BAM=M
      BAN=N
      BAP=BAM*BAM+BAN*BAN
      BAD=BAM*BAM-BAN*BAN
      SO=BAP/BAD
      PI =3.1415927
      AL =2.*PI*AR*SQRT(10.0)
C     COMPUTE LENGTH OF LENS.
      ALLENS=SQRT(BAP/8.0)*AL
      B=2.*PI/AL
      AK =B*B*(VO/SO)
      V =AK*AR*AR
      READ(5,102)NUM,NNN
      READ(5,102)MAAA,MTRA
  102 FORMAT(2I2)
      ANN =NNN
      AB =COS(PI*ANN)
C     PLOT FRAMES , AXES AND PRINT SCALE ON THE AXES AND DASHED CIRCLE
C     ON THE X-Y PLOT TO REPRESENT THE QUADRUPOLE APERTURE.
```

```
      CALL PLOT(0.0,9.25,2)
      CALL PLOT(6.0,9.25,2)
      CALL PLOT(6.0,0.0,2)
      CALL PLOT(0.0,0.0,2)
      CALL AXIS(1.0,2.75,' ',1,4.0,0.0,1.0E10,1.0,20.0)
      CALL SYMBOL(5.25,2.75,0.12,'X(CM)',0.0,5)
      CALL CIRCLE(4.875,2.75,0.0,360.,1.875,1.875,0.5)
      CALL AXIS(3.0,0.75,' ',1,4.0,90.0,1.0E10,1.0,20.0)
      CALL SYMBOL(3.1,4.6,0.12,'Y(CM)',0.0,5)
      CALL AXIS(3.0,5.0,' ',1,4.0,90.0,1.0E10,1.0,20.0)
      CALL SYMBOL(3.1,8.9,0.12,'PY/PZ',0.0,5)
      CALL AXIS(1.0,7.0,' ',1,4.0,0.0,1.0E10,1.0,20.0)
      CALL SYMBOL(5.25,7.0,0.12,'PX/PZ',0.0,5)
      CALL PLOT(0.0,12.0,-3)
      CALL PLOT(0.0,9.25,2)
      CALL PLOT(6.0,9.25,2)
      CALL PLOT(6.0,0.0,2)
      CALL PLOT(0.0,0.0,2)
      CALL AXIS(0.5,0.5,'Z(CM)',-5,5.0,0.0,1.0E10,1.0,20.0)
      CALL SYMBOL(0.43,0.35,0.08,'0.0',0.0,3)
      CALL SYMBOL(1.5,0.35,0.08,'8',0.0,1)
      CALL SYMBOL(2.5,0.35,0.08,'16',0.0,2)
      CALL SYMBOL(3.5,0.35,0.08,'24',0.0,2)
      CALL SYMBOL(4.5,0.35,0.08,'32',0.0,2)
      CALL SYMBOL(5.5,0.35,0.08,'40',0.0,2)
      CALL AXIS(0.5,0.75,'X(CM)',5,4.0,90.0,1.0E10,1.0,20.0)
      CALL SYMBOL(0.19,0.75,0.08,'-1.6',0.0,4)
      CALL SYMBOL(0.19,1.75,0.08,'-0.8',0.0,4)
      CALL SYMBOL(0.26,2.75,0.08,'0.0',0.0,3)
      CALL SYMBOL(0.26,3.75,0.08,'0.8',0.0,3)
      CALL SYMBOL(0.26,4.75,0.08,'1.6',0.0,3)
      CALL AXIS(0.5,5.0,'Y(CM)',5,4.0,90.0,1.0E10,1.0,20.0)
      CALL SYMBOL(0.19,5.0,0.08,'-1.6',0.0,4)
      CALL SYMBOL(0.19,6.0,0.08,'-0.8',0.0,4)
      CALL SYMBOL(0.19,7.0,0.08,'0.0',0.0,3)
      CALL SYMBOL(0.19,8.0,0.08,'0.8',0.0,3)
      CALL SYMBOL(0.19,9.0,0.08,'1.6',0.0,3)
      CALL PLOT(0.5,2.75,3)
      CALL PLOT(5.5,2.75,2)
      CALL PLOT(5.5,7.0,3)
      CALL PLOT(0.5,7.0,2)
      CALL PLOT(10.0,0.0,-3)
      CALL PLOT(0.0,9.25,2)
      CALL PLOT(6.0,9.25,2)
      CALL PLOT(6.0,0.0,2)
      CALL PLOT(0.0,0.0,2)
      CALL AXIS(0.5,0.5,'Z(CM)',-5,5.0,0.0,1.0E10,1.0,20.0)
      CALL SYMBOL(0.43,0.35,0.08,'0.0',0.0,3)
      CALL SYMBOL(1.5,0.35,0.08,'8',0.0,1)
      CALL SYMBOL(2.5,0.35,0.08,'16',0.0,2)
      CALL SYMBOL(3.5,0.35,0.08,'24',0.0,2)
      CALL SYMBOL(4.5,0.35,0.08,'32',0.0,2)
      CALL SYMBOL(5.5,0.35,0.08,'40',0.0,2)
      CALL AXIS(0.5,0.75,'PX/PZ',5,4.0,90.0,1.0E10,1.0,20.0)
      CALL SYMBOL(0.19,0.75,0.08,'-0.2',0.0,4)
      CALL SYMBOL(0.19,1.75,0.08,'-0.1',0.0,4)
      CALL SYMBOL(0.19,2.75,0.08,'0.0',0.0,3)
      CALL SYMBOL(0.19,3.75,0.08,'0.1',0.0,3)
      CALL SYMBOL(0.19,4.75,0.08,'0.2',0.0,3)
      CALL AXIS(0.5,5.0,'PY/PZ',5,4.0,90.0,1.0E10,1.0,20.0)
      CALL SYMBOL(0.19,5.0,0.08,'-0.2',0.0,4)
      CALL SYMBOL(0.19,6.0,0.08,'-0.1',0.0,4)
      CALL SYMBOL(0.26,7.0,0.08,'0.0',0.0,3)
      CALL SYMBOL(0.26,8.0,0.08,'0.1',0.0,3)
      CALL SYMBOL(0.26,9.0,0.08,'0.2',0.0,3)
      CALL PLOT(0.5,2.75,3)
      CALL PLOT(5.5,2.75,2)
      CALL PLOT(5.5,7.0,3)
      CALL PLOT(0.5,7.0,2)
      CALL PLOT(-10.0,-12.0,-3)
      DO 5566 IIL=1,KLJM
 5566 READ(5,103)RRPX(IIL),RRPY(IIL),RRPZ(IIL)
      DO 666 IEX=1,NUM
      READ (5,103)XO,YO,ZO
      DO 666 IABC=1,KLJM
      RPXO=RRPX(IABC)
      RPYO=RRPY(IABC)
      RPZO=RRPZ( IABC)
  103 FORMAT (3E12.6)
      PZOO =1.0
      PZO =RPZO
      ZOO=0.0
      THOOO=0.0
      I=0
C     CALCULATE S FOR THE PARTICLE ACCORDING TO ITS INJECTION CONDITIONS.
 1033 PXO=RPXO*PZO
      PYO =RPYO*PZO
      PZ=PZO*(1.+B*(XO*RPYO-YO*RPXO))
      DXO =PXO/PZ
      DYO =PYO/PZ
      S =SO*PZ*PZ
      QMK =2.*QM*AK
      FX =SQRT(QMK*(S+1.))
      FY =SQRT(QMK*(S-1.))
      VZO=SQRT(2.*QM*VO)
C     START CALCULATION OF TRAJECTORY POINTS USING ANALYTIC SOLUTION.
      H=AL/(AM*VZO)
      UI=SQRT((XO-SQRT(VO*S/AK)*PYO)**2+(VO*(S+1.)*PXO*PXO/AK))
      VI=SQRT((YO-SQRT(VO*S/AK)*PXO)**2+(VO*(S-1.)*PYO*PYO/AK))
      AP1=-SQRT(VO*(S+1.)/AK)*PXO
      BP1=(XO-SQRT(VO*S/AK)*PYO)
      IF(BP1)309,310,311
  310 IF(AP1)312,313,314
  312 ALP1=-PI/2.
      GO TO 320
  314 ALP1=PI/2.
      GO TO 320
  313 ALP1=0.0
      GO TO 320
  311 CP1=AP1/BP1
      ALP1=ATAN(CP1)
      GO TO 320
  309 CP1=AP1/BP1
      ALP1=ATAN(CP1)+PI
  320 AP2=SQRT(VO*(S-1.)/AK)*PYO
      BP2=YO-SQRT(VO*S/AK)*PXO
      IF(BP2)409,410,411
  410 IF(AP2)412,413,414
  412 ALP2=-PI/2.
      GO TO 420
  414 ALP2=PI/2.
      GO TO 420
  413 ALP2=0.0
      GO TO 420
  411 CP2=AP2/BP2
      ALP2=ATAN(CP2)
      GO TO 420
  409 CP2=AP2/BP2
      ALP2=ATAN(CP2)+PI
  420 HO=H
      KK=0
      TT=0.0
      Z11=0.0
  520 ATHX=FX*TT
      ATHY=FY*TT
      CX=COS(ATHX)
      SX=SIN(ATHX)
      CY=COS(ATHY)
      SY=SIN(ATHY)
      FACTO=SQRT(VO/AK)
      A11=CX
      A12=AB*SY*SQRT(S/(S-1.))
      A13=(SX*SQRT(S+1.)-S*SY/SQRT(S-1.))*FACTO
      A14=(AB*SQRT(S)*(CY-CX))*FACTO
      A21=-AB*SX*SQRT(S/(S+1.))
      A22=CY
      A23=-A14
      A24=((SX*S/SQRT(S+1.))-SY*SQRT(S-1.))*FACTO
      A31=-SX/SQRT(S+1.)
      A32=0.0
      A33=CX*FACTO
      A34=-A21*FACTO
      A41=0.0
      A42=SY/SQRT(S-1.)
      A43=A12*FACTO
      A44=CY*FACTO
      AX11=A11*X0+A12*Y0+A13*PXC+A14*PY0
      AY11=A21*X0+A22*Y0+A23*PXC+A24*PY0
      PX11=(A31*X0+A32*Y0+A33*PX0+A34*PY0)/FACTO
      PY11=(A41*X0+A42*Y0+A43*PX0+A44*PY0)/FACTO
      THX=ATHX+ALP1
      THY=ATHY+ALP2
      THX2=2.*THX
      THY2=2.*THY
      THP12=THX+THY
      THN12=THX-THY
      Z11A=Z11
      THX20=2.*ALP1
      THY20=2.*ALP2
      THP00=ALP1+ALP2
      THN00=THP00-2.*ALP2
      Z11=VZ0*TT*(1.+B*(X0*RPY0-Y0*RPX0)+0.5*B*SQRT(AK*S/V0)*((UI*UI/(S
     1+1.))-(VI*VI/(S-1.))))+0.25*B*(SQRT(S/(S-1.)**3)*VI*VI*(SIN(THY2)
     2-SIN(THY20))-SQRT(S/(S+1.)**3)*UI*UI*(SIN(THX2)-SIN(THX20)))+0.5*
     3B*UI*VI*(COS(THP12)-COS(THP00)-COS(THN12)+COS(THN00))/
     4SQRT(S*S-1.)
C     CHECK THE AXIAL DISTANCE TRAVERSED BY THE PARTICLE.
      IF(Z11-ALLENS)601,601,602
  602 TT=TT-H0
C     DECREASE THE TIME INCREMENT SO THE FINAL DISTANCE TRAVERSED BY THE
```

```
C      PARTICLE BE FINALLY EGUAL TC THE LENS LENGTH WITHIN THE DEGREE OF
C      ACCURACY SPECIFIED BY J.
       HO=HO/2.0
       KK=KK+1
       TT=TT+HO
       IF(J-KK)530,530,520
  601  I=I+1
       TT=TT+HO
       THOI=B*Z11+THOOO
       CCTH=COS(THOI)
       SCTH=SIN(THOI)
       AXI=AX11
       AYI=AY11
       AZI=Z11
       PXI=PX11*PZO
       PYI=PY11*PZO
       PZI=PZ-B*(AXI*PYI-AYI*PXI)
C      STORE TRAJECTORY POINTS IN TERMS OF THE FIXED COORDINATE SYSTEM.
       AX(I)=AX11*CCTH-AY11*SCTH
       AY(I)=AX11*SCTH+AY11*CCTH
       PX(I)=(PX11*CCTH-PY11*SCTH)*PZO/PZI
       PY(I)=(PX11*SCTH+PY11*CCTH)*PZO/PZI
       AZ(I)=Z11+ZOO
 6006  FORMAT(5X,5(E10.3,3X),I4)
       GO TO 520
  530  MAAA=MAAA+1
       IF(MAAA)5305,5305,5306
C      FOR THE STRUCTURE CONSTRUCTED OF TWO OPPOSITELY TWISTED SECTIONS
C      CONSIDER THETRANSEVERSE COORDINATES AND MCMENTA AT THE EXIT PLANE
C      OF THE FIRST SECTION IN THE ROTATING COORDINATE SYSTEM AS THE
C      INJECTICN CONDITICNS OF THE PARTICLE FOR THE SECOND TWISTED SECTION.
 5305  XO=AXI
       YO=AYI
       ZOO=AZI
       PZO=PZI
       VO=VO*PZI*PZI
       RPXO=PXI/PZO
       RPYO=PYI/PZO
       THOOO=B*ZOO
       B=-B
       HO=H
       GO TO 1033
 5306  I1=I+1
       I2=I+2
C      CREAT SCALES FOR PLOTTING THE TRAJECTORIES.
       AX(I1)=-0.016
       AX(I2)=0.008
       AY(I1)=AX(I1)
       AY(I2)=AX(I2)
       PX(I1)=-0.2
       PX(I2)=0.1
       PY(I1)=-0.2
       PY(I2)=0.1
       AZ(I1)=0.0
       AZ(I2)=0.08
       CALL PLOT(1.0,0.75,-3)
       ABAX1=(AX(1)-AX(I1))/AX(I2)
       ABAX2=(AX(I)-AX(I1))/AX(I2)
       ABAY1=(AY(1)-AY(I1))/AY(I2)
       ABAY2=(AY(I)-AY(I1))/AY(I2)
```

```
C     MARK ENTRY AND EXIT TRANSEVERSE COORDINATES ON THE X-Y PLANE.
      CALL SYMBOL(ABAX1,ABAY1,0.04,003,0.0,-1)
      CALL SYMBOL(ABAX2,ABAY2,0.04,011,0.0,-1)
      IF(MTRA)105,105,106
  105 CALL LINE(AX,AY,I,1,0,0)
  106 CALL PLOT(0.0,4.25,-3)
      ABPX1=(PX(1)-PX(I1))/PX(I2)
      ABPX2=(PX(I)-PX(I1))/PX(I2)
      ABPY1=(PY(1)-PY(I1))/PY(I2)
      ABPY2=(PY(I)-PY(I1))/PY(I2)
C     MARK ENTRY AND EXIT TRANSEVERSE MOMENTA ON THE PX-PY PLANE.
      CALL SYMBOL(ABPX1,ABPY1,0.04,003,0.0,-1)
      CALL SYMBOL(ABPX2,ABPY2,0.04,011,0.0,-1)
C     START PLOTTING THE TRAJECTORY PROJECTIONS.
      IF(MTRA)115,115,116
  115 CALL LINE(PX,PY,I,1,0,0)
      CALL PLOT(-0.5,7.75,-3)
      CALL LINE(AZ,AX,I,1,0,0)
      CALL PLOT(0.0,4.25,-3)
      CALL LINE(AZ,AY,I,1,0,0)
      CALL PLOT(10.0,0.0,-3)
      CALL LINE(AZ,PY,I,1,0,0)
      CALL PLOT(0.0,-4.25,-3)
      CALL LINE(AZ,PX,I,1,0,0)
      CALL PLOT(-10.5,-12.75,-3)
      GO TO 666
  116 CALL PLOT(-1.0,-5.0,-3)
  666 CONTINUE
      CALL PLOT(0.0,0.0,999)
      WRITE(6,7788)
 7788 FORMAT(10X,'***** PLOT FINISHED *****')
 3333 FORMAT(10X,'HHHHHHHH')
      STOP
      END
ILE
```

APPENDIX F

SPATIAL MODES OF THE MOTION ALONG THE TWISTED STRUCTURE

In order to express the analytic solution of the particle motion along the twisted structure in terms of the fixed (X,Y,Z) coordinates, equations (2.31) are substituted into equations (2.7). The X coordinate of the moving particle will be,

$$\begin{aligned} X &= x \cos \beta z - y \sin \beta z \\ &= [C_1 \cos F_1 + \sqrt{\frac{s}{s-1}} (-1)^n C_2 \sin F_2] \cos \beta z \\ &\quad - [C_2 \cos F_2 - \sqrt{\frac{s}{s+1}} (-1)^n C_1 \sin F_1] \sin \beta z \qquad \text{(F.1)} \end{aligned}$$

while the Y coordinate will be

$$\begin{aligned} Y &= x \sin \beta z + y \cos \beta z \\ &= [C_1 \cos F_1 + \sqrt{\frac{s}{s-1}} (-1)^n C_2 \sin F_2] \sin \beta z \\ &\quad + [C_2 \cos F_2 - \sqrt{\frac{s}{s+1}} (-1)^n C_1 \sin F_1] \cos \beta z \qquad \text{(F.2)} \end{aligned}$$

where, $F_1 = f_1 t + \alpha_1$ and $F_2 = f_2 t + \alpha_2$. Equation (F.1), after the multiplication of the trigonometric terms becomes,

$$
\begin{aligned}
X = {} & C_1 \cos(f_1 t + \alpha_1) \cos \beta z \\
& + \sqrt{\frac{s}{s + 1}} (-1)^n C_1 \sin(f_1 t + \alpha_1) \sin \beta z \\
& - C_2 \cos(f_2 t + \alpha_2) \sin \beta z \\
& + \sqrt{\frac{s}{s - 1}} (-1)^n C_2 \sin(f_2 t + \alpha_2) \cos \beta z \\
= {} & \frac{1}{2} C_1 [\{\cos(f_1 t - \beta z + \alpha_1) + \cos(f_1 t + \beta z + \alpha_1)\} \\
& + (-1)^n \sqrt{\frac{s}{s + 1}} \{\cos(f_1 t - \beta z + \alpha_1) - \cos(f_1 t + \beta z + \alpha_1)\}] \\
& - \frac{1}{2} C_2 [\{\sin(\beta z - f_2 t - \alpha_2) + \sin(\beta z + f_2 t + \alpha_2)\} \\
& + (-1)^n \sqrt{\frac{s}{s - 1}} \{\sin(f_2 t + \alpha_2 + \beta z) + \sin(f_2 t + \alpha_2 - \beta z)\} \\
= {} & \frac{1}{2} C_1 \{1 + (-1)^n \sqrt{\frac{s}{s + 1}}\} \cos(f_1 t - \beta z + \alpha_1) \\
& + \frac{1}{2} C_1 \{1 - (-1)^n \sqrt{\frac{s}{s + 1}}\} \cos(f_1 t + \beta z + \alpha_1) \\
& - \frac{1}{2} C_2 \{1 + (-1)^n \sqrt{\frac{s}{s - 1}}\} \sin(-f_2 t + \beta z - \alpha_2) \\
& - \frac{1}{2} C_2 \{1 - (-1)^n \sqrt{\frac{s}{s - 1}}\} \sin(f_2 t + \beta z + \alpha_2) \qquad \text{(F.3)}
\end{aligned}
$$

Equation (F.2), after the multiplication of the trigonometric terms becomes

$$
\begin{aligned}
Y = {} & C_1 \cos(f_1 t + \alpha_1) \sin \beta z \\
& - \sqrt{\frac{s}{s + 1}} (-1)^n C_1 \sin(f_1 t + \alpha_1) \cos \beta z
\end{aligned}
$$

$$
\begin{aligned}
&+ C_2 \cos(f_2 t + \alpha_2)\cos \beta z \\
&+ \sqrt{\frac{s}{s-1}}\,(-1)^n\, C_2 \sin(f_2 t + \alpha_2)\sin \beta z \\
= {}& \frac{1}{2} C_1 [\{\sin(f_1 t + \alpha_1 + \beta z) - \sin(f_1 t + \alpha_1 - \beta z)\} \\
&- (-1)^n \sqrt{\frac{s}{s+1}}\, \{\sin(f_1 t + \alpha_1 + \beta z) + \sin(f_1 t + \alpha_1 - \beta z)\}] \\
&+ \frac{1}{2} C_2 [\{\cos(f_2 t + \alpha_2 + \beta z) + \cos(-f_2 t - \alpha_2 + \beta z)\} \\
&+ (-1)^n \sqrt{\frac{s}{s-1}}\, \{\cos(-f_2 t - \alpha_2 + \beta z) - \cos(f_2 t + \alpha_2 + \beta z)\}] \\
= {}& - \frac{1}{2} C_1 \{1 + (-1)^n \sqrt{\frac{s}{s+1}}\} \sin(f_1 t - \beta z + \alpha_1) \\
&+ \frac{1}{2} C_1 \{1 - (-1)^n \sqrt{\frac{s}{s+1}}\} \sin(f_1 t + \beta z + \alpha_1) \\
&+ \frac{1}{2} C_2 \{1 + (-1)^n \sqrt{\frac{s}{s-1}}\} \cos(-f_2 t + \beta z - \alpha_2) \\
&+ \frac{1}{2} C_2 \{1 - (-1)^n \sqrt{\frac{s}{s-1}}\} \cos(f_2 t + \beta z + \alpha_2) \qquad \text{(F.4)}
\end{aligned}
$$